ISSN 2587-1943

#17

VOLUME 9, 1
JUNE 2025

IJIEA

JOURNAL

INTERNATIONAL JOURNAL OF INNOVATIVE ENGINEERING APPLICATIONS

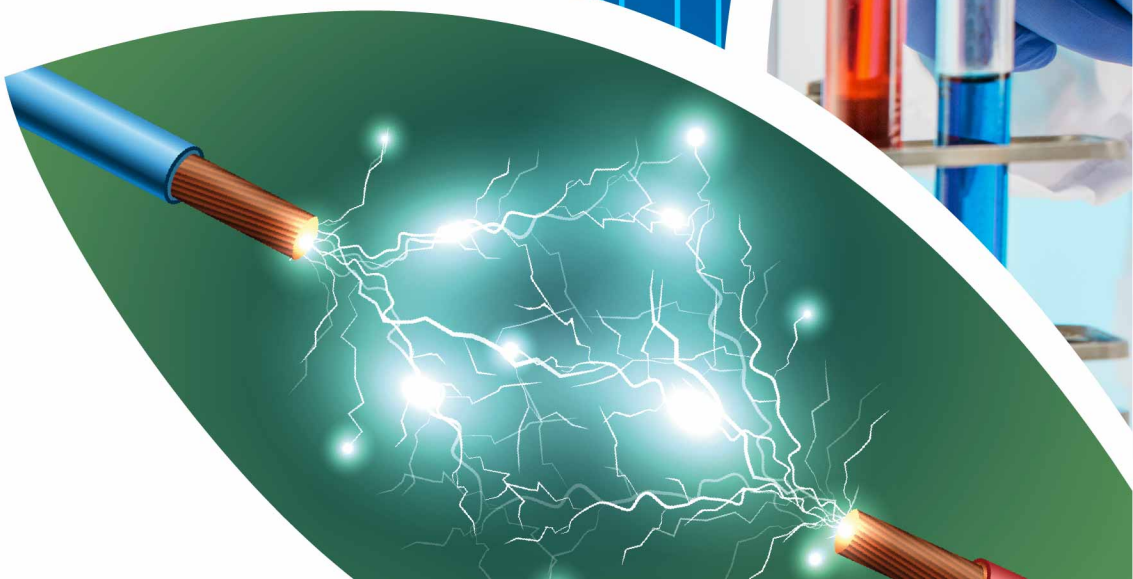

International Journal of Innovative Engineering Applications is published June and December.

Adress for the manuscripts and correspondence:

Uluslararası Yenilikçi Mühendislik Uygulamaları Dergisi
Fırat Üniversitesi Kampüsü, Teknoloji Fakültesi, Merkez–Elazığ

Tel: +90 424 237 0000/ Ext.7655
e-mail: ijieatr@gmail.com

ISSN: 2587-1943

Elazığ-2025

#17
IJIEA

IJIEA
volume 9 issue 1

CONTENTS / İÇİNDEKİLER

IJIEA
volume 9 issue 1

CONTENTS / İÇİNDEKİLER

IJIEA
volume 9 issue 1

CONTENTS / İÇİNDEKİLER

IJIEA
volume 9 issue 1

CONTENTS / İÇİNDEKİLER

International Journal of Innovative Engineering Applications

Journal homepage: https://dergipark.org.tr/ijiea

A COMPARATIVE ANALYSIS OF EFFICIENTNETB0 AND EFFICIENTNETV2 VARIANTS FOR BRAIN TUMOR CLASSIFICATION USING MRI IMAGES

Kerem Gencer*[1]

[1]*Afyon Kocatepe University, Faculty of Engineering, Department of Computer Engineering, Afyonkarahisar, Turkey*

Abstract

Original scientific paper

Accurate and early diagnosis of brain tumors is critical for effective treatment planning, yet traditional methods of analyzing Magnetic Resonance Imaging (MRI) scans are labor-intensive and prone to variability among experts. Deep learning, particularly Convolutional Neural Networks (CNNs), has emerged as a transformative tool in medical imaging by automating feature extraction and enhancing classification accuracy. This study provides a comparative analysis of EfficientNetB0 and three EfficientNetV2 variants (S, M, and L) for brain tumor classification using the Figshare Brain Tumor Dataset, which includes glioma, meningioma, and pituitary tumors. Each model was evaluated using metrics such as accuracy, precision, recall, F1-score, and ROC-AUC. The results reveal that EfficientNetV2-S outperformed other models, achieving the highest accuracy of 98.20% and delivering balanced performance across all classes. EfficientNetV2-M and EfficientNetV2-L also demonstrated strong classification capabilities, with minor trade-offs in computational efficiency. These findings highlight the potential of EfficientNetV2 architectures for automated and reliable brain tumor classification, offering significant advantages for clinical applications. Future work could focus on integrating multi-modal imaging data and optimizing models for deployment in real-time diagnostic settings.

Keywords: *Brain tumor classification, deep learning, efficientNet, EfficientNetV2, medical imaging, MRI.*

MRI GÖRÜNTÜLERİNİ KULLANARAK BEYİN TÜMÖRÜ SINIFLANDIRMASI İÇİN EFFİCİENTNETB0 VE EFFİCİENTNETV2 VARYANTLARININ KARŞILAŞTIRMALI ANALİZİ

Özet

Orijinal bilimsel makale

Beyin tümörlerinin doğru ve erken teşhisi etkili tedavi planlaması için kritik öneme sahiptir, ancak Manyetik Rezonans Görüntüleme (MRI) taramalarını analiz etmenin geleneksel yöntemleri emek yoğun olup uzmanlar arasında değişkenliğe eğilimlidir. Derin öğrenme, özellikle Evrişimsel Sinir Ağları (CNN'ler), özellik çıkarmayı otomatikleştirerek ve sınıflandırma doğruluğunu artırarak tıbbi görüntülemede dönüştürücü bir araç olarak ortaya çıkmıştır. Bu çalışma, glioma, menenjiyoma ve hipofiz tümörlerini içeren Figshare Beyin Tümörü Veri Setini kullanarak beyin tümörü sınıflandırması için EfficientNetB0 ve üç EfficientNetV2 varyantının (S, M ve L) karşılaştırmalı bir analizini sağlar. Her model doğruluk, kesinlik, geri çağırma, F1 puanı ve ROC-AUC gibi ölçütler kullanılarak değerlendirildi. Sonuçlar, EfficientNetV2-S'nin diğer modellerden daha iyi performans gösterdiğini, %98,20'lik en yüksek doğruluğu elde ettiğini ve tüm sınıflarda dengeli bir performans sağladığını ortaya koymaktadır. EfficientNetV2-M ve EfficientNetV2-L ayrıca hesaplama verimliliğinde küçük ödünlerle güçlü sınıflandırma yetenekleri gösterdi. Bu bulgular, EfficientNetV2 mimarilerinin otomatik ve güvenilir beyin tümörü sınıflandırması için potansiyelini vurgulayarak klinik uygulamalar için önemli avantajlar sunuyor. Gelecekteki çalışmalar, çok modlu görüntüleme verilerini entegre etmeye ve gerçek zamanlı tanılama ortamlarında dağıtım için modelleri optimize etmeye odaklanabilir.

Anahtar Kelimeler: *Beyin tümörü sınıflandırması, derin öğrenme, EfficientNet, EfficientNetV2, tıbbi görüntüleme, MRI.*

1 Introduction

Brain tumors represent one of the most severe and complex medical conditions, necessitating accurate and early diagnosis to ensure effective treatment planning. Magnetic Resonance Imaging (MRI) is a critical tool in diagnosing brain tumors due to its ability to provide detailed images of soft tissues [1, 2]. However, manual analysis of MRI scans is labor-intensive and prone to variability among experts, which has driven the demand for automated and reliable classification methods.

Deep learning, particularly Convolutional Neural Networks (CNNs), has become a transformative technology in medical imaging, enabling automatic

*Corresponding author.

E-mail address: keremgencer09@hotmail.com (K. Gencer)

Received 28 June 2024; Received in revised form 22 November 2024; Accepted 30 April 2025

 Doi: https://doi.org/10.46460/ijiea.1523782

feature extraction and improved classification accuracy [3, 4]. EfficientNetB0, introduced as a baseline architecture, employed a novel compound scaling method to balance depth, width, and resolution, achieving state-of-the-art performance in image classification tasks [5]. The subsequent development of EfficientNetV2 models further improved computational efficiency and accuracy by introducing advanced training techniques and optimized architectural designs [6].

Deep learning approaches, particularly CNNs, have revolutionized brain tumor classification, leveraging their ability to extract high-level features from medical imaging datasets and significantly enhancing diagnostic accuracy [7]. Emerging techniques, such as data augmentation and transfer learning, have further improved the generalization and efficiency of CNN-based models in medical image classification [8, 9].

Existing research has demonstrated the effectiveness of both EfficientNetB0 and EfficientNetV2 architectures in medical imaging applications, including brain tumor classification [10, 11]. However, comparative studies evaluating their performance on the same dataset using consistent evaluation metrics remain limited.

In recent years, advanced approaches have made significant progress in the classification of brain tumors. For example, studies on accurate brain tumor classification with optimized EfficientNet architecture have presented innovative methods to improve model performance [12]. Gencer and Gencer (2024) introduced a hybrid model that combines EfficientNetB0 with a Quantum Genetic Algorithm (QGA), achieving remarkable accuracy in brain tumor classification. Their approach demonstrated significant advantages in feature selection and computational efficiency compared to traditional methods [13]. Furthermore, a comprehensive review on transfer learning techniques and model efficiency using MRI datasets has offered potential solutions to make existing deep learning approaches more efficient [14]. Such studies contribute to the development of more reliable and generally applicable models for brain tumor classification.

This study addresses this gap by conducting a comprehensive analysis of EfficientNetB0 and EfficientNetV2 variants (S, M, and L) for the classification of brain tumors using MRI images.

- This study aims to address critical gaps in brain tumor classification research by focusing on the following key objectives:
- To systematically evaluate the performance of EfficientNetB0 and EfficientNetV2 variants (S, M, and L) in brain tumor classification.
- To investigate how advanced architectures, particularly EfficientNetV2 models, impact model generalization and computational efficiency in handling high-dimensional MRI datasets.

To compare the strengths and weaknesses of EfficientNetB0 and EfficientNetV2 variants on a consistent dataset to determine the most effective model for practical clinical applications. The Figshare Brain Tumor Dataset [15] was selected for this study due to its comprehensive MRI image collection, enabling a robust evaluation of the proposed models. The results provide insights into the trade-offs between computational complexity and classification accuracy, offering practical implications for deploying these models in clinical settings. This paper is structured as follows: Section 2 outlines the dataset, preprocessing steps, and training processes for EfficientNetB0 and EfficientNetV2 variants, with Section 2.1 focusing on the evolution and features of EfficientNet architectures. Section 3 presents the comparative performance analysis of the models using evaluation metrics such as accuracy, precision, recall, and ROC-AUC. Section 4 summarizes the study findings and highlights the clinical potential of EfficientNetV2 models for brain tumor diagnosis.

2 Materials and Methods

The Figshare Brain Tumor Dataset [15] was used in this study, consisting of MRI scans categorized into three classes: glioma, meningioma, and pituitary tumor in Table 1. The dataset, downloaded from the Figshare platform, comprises MATLAB (.mat) files containing tumor images and their corresponding labels. All images were resized to 128x128 pixels for uniformity, and grayscale images were converted into RGB format to meet the input requirements of the EfficientNet models.

Data preprocessing involved resizing images, duplicating grayscale images across three channels to simulate RGB format, and shuffling the dataset. The dataset was split into 80% training and 20% testing subsets using a stratified random split to preserve class balance.

The study utilized four EfficientNet variants: EfficientNetB0, EfficientNetV2-S, EfficientNetV2-M, and EfficientNetV2-L. EfficientNetB0 served as the baseline model, leveraging compound scaling to balance depth, width, and resolution. The EfficientNetV2 variants introduced enhancements for faster training and higher accuracy. All models used pre-trained ImageNet weights for feature extraction, followed by a classification head comprising a dense layer with 128 units and ReLU activation, a dropout layer with a 0.5 rate, and a softmax output layer for multi-class classification.

Model training employed the Adam optimizer with a learning rate of 0.001 and sparse categorical cross-entropy loss. Each model was trained for 30 epochs with a batch size of 32. Early stopping with a patience of 10 epochs was applied to mitigate overfitting, and the learning rate was reduced by a factor of 0.2 when validation loss plateaued for five consecutive epochs.

The models' performance was evaluated using several metrics, including overall accuracy, precision, recall, F1-score, and confusion matrices. The area under the Receiver Operating Characteristic curve (ROC-AUC) was calculated for each class to assess classification performance further. Additionally, training and validation loss and accuracy plots were generated to visualize model convergence.

The experimental workflow consisted of data loading and preprocessing, independent training of each EfficientNet variant, feature extraction using the trained models, and performance evaluation. Python,

TensorFlow, and Keras were the primary tools for model implementation, while OpenCV was used for image preprocessing. Scikit-learn facilitated evaluation metric calculations, and visualizations were created using Seaborn and Matplotlib.

Table 1. Dataset Details.

Collection Period	Not specified
Published By	Jun Cheng (2015)
Platform	Figshare
Total Images	3064
Image Modality	T1-weighted contrast-enhanced MRI
Tumor Types	Glioma, Meningioma, Pituitary Tumors
Number of Patients	233
Image Planes	Axial, Coronal, Sagittal
Image Size	512 × 512 pixels

2.1 EfficientNet Variants: Evolution and Comparative Features for Brain Tumor Classification

EfficientNet models represent a significant leap in the design of convolutional neural networks (CNNs) by introducing compound scaling, which balances the network's depth, width, and resolution [6]. The successes of deep architectures in deep learning have laid important groundwork, especially with the work of Simonyan and Zisserman on large-scale image recognition with deep networks [16]. The EfficientNet family has evolved to include variants such as EfficientNetB0 and its successors in the EfficientNetV2 series (S, M, and L), which offer improved accuracy and computational efficiency.

EfficientNetB0 was introduced as the baseline model, leveraging a novel scaling method to achieve state-of-the-art performance with fewer parameters and FLOPS compared to traditional architectures. It employs depthwise separable convolutions and compound scaling, which optimally scales depth, width, and resolution [6, 17]. This architecture demonstrated significant improvements in image classification tasks while maintaining computational efficiency.

EfficientNetV2-S is a smaller variant of the EfficientNetV2 family, optimized for faster training and better performance. This model incorporates several enhancements, such as Fused-MBConv layers, which reduce the complexity of mobile inverted bottleneck layers used in EfficientNetB0, and progressive learning for improved convergence [6]. EfficientNetV2-S is particularly suitable for scenarios requiring faster inference and lower memory usage.

EfficientNetV2-M strikes a balance between model size and performance. It extends the capabilities of EfficientNetV2-S by increasing the network's depth and width while maintaining the efficiency improvements introduced in the V2 architecture [6, 18]. This variant is well-suited for tasks requiring high accuracy with moderate computational resources.

EfficientNetV2-L, the largest variant in the EfficientNetV2 family, offers superior performance by scaling up the network's dimensions while incorporating the architectural optimizations of the V2 series. This model is designed for high-accuracy applications where computational resources are less constrained, such as advanced medical imaging tasks [6, 18].

The EfficientNet variants demonstrate a progressive improvement in terms of computational efficiency and accuracy. EfficientNetB0 provides a strong baseline for image classification, while the EfficientNetV2 models enhance performance through architectural optimizations and training techniques. In this study, these variants were evaluated on the Figshare Brain Tumor Dataset, comparing their accuracy, ROC-AUC scores, and confusion matrices to determine the most effective model for brain tumor classification.

3 Experimental Results and Discussions Conclusion

Table 2 evaluates the performance of EfficientNet models (EfficientNetB0 and EfficientNetV2 variants: S, M, and L) in brain tumor classification. Performance metrics include Precision, Recall, F1-Score, and overall Accuracy.It is seen that EfficientNetB0 model provides high accuracy especially on Class2 and Class3, but shows lower performance in Precision and Recall values for Class1.EfficientNetV2-S model shows a very balanced and high performance for all classes. Especially for Class3, both Precision and Recall values are 1.00, indicating that it provides perfect classification in this class. The overall accuracy of the model (98.20%) is one of the highest compared to other EfficientNetV2 variants.EfficientNetV2-M model shows similar accuracy for Class2 and Class3, while slightly lower Precision and Recall values are encountered on Class1. However, the model performs quite well in terms of overall accuracy (97.87%).The EfficientNetV2-L model has shown consistent performance in Class1 and Class2 classes, while maintaining Precision, Recall and F1-Score values at 99% levels for Class3. However, the overall accuracy of this model (97.71%) is slightly lower than the V2-S model.Overall, the EfficientNetV2-S model has the highest accuracy and stability for all classes, providing a clear superiority compared to Ef ficientNetB0.

In Figure 1, EfficientNetB0 performed less effectively compared to other models, with a low correct classification rate, especially for Class1. EfficientNetV2-S outperformed other models by showing high accuracy rates for all classes. EfficientNetV2-M showed a balanced performance in Class1 and Class3, while its false positive rates were slightly higher than EfficientNetV2-S. EfficientNetV2-L showed the best classification performance for Class2, but lagged behind other EfficientNetV2 variants in Class1. Overall, EfficientNetV2 models showed better overall performance compared to EfficientNetB0 and produced more balanced results across classes.

Table 1. Performance Comparison of EfficientNet Variants in Brain Tumor Classification.

Model	Class	Precision	Recall	F1-Score	Accuracy
EfficientNetB0	Class1	0.98	0.68	0.80	
	Class2	0.85	0.99	0.92	0.9021
	Class3	0.95	0.95	0.95	
EfficientNet V2-S	Class1	0.95	0.99	0.97	
	Class2	0.99	0.97	0.98	0.9820
	Class3	1.00	0.99	1.00	
EfficientNet V2-M	Class1	0.95	0.97	0.96	
	Class2	0.99	0.97	0.98	0.9787
	Class3	0.99	0.99	0.99	
EfficientNet V2-L	Class1	0.96	0.95	0.96	
	Class2	0.98	0.98	0.98	0.9771
	Class3	0.99	0.99	0.99	

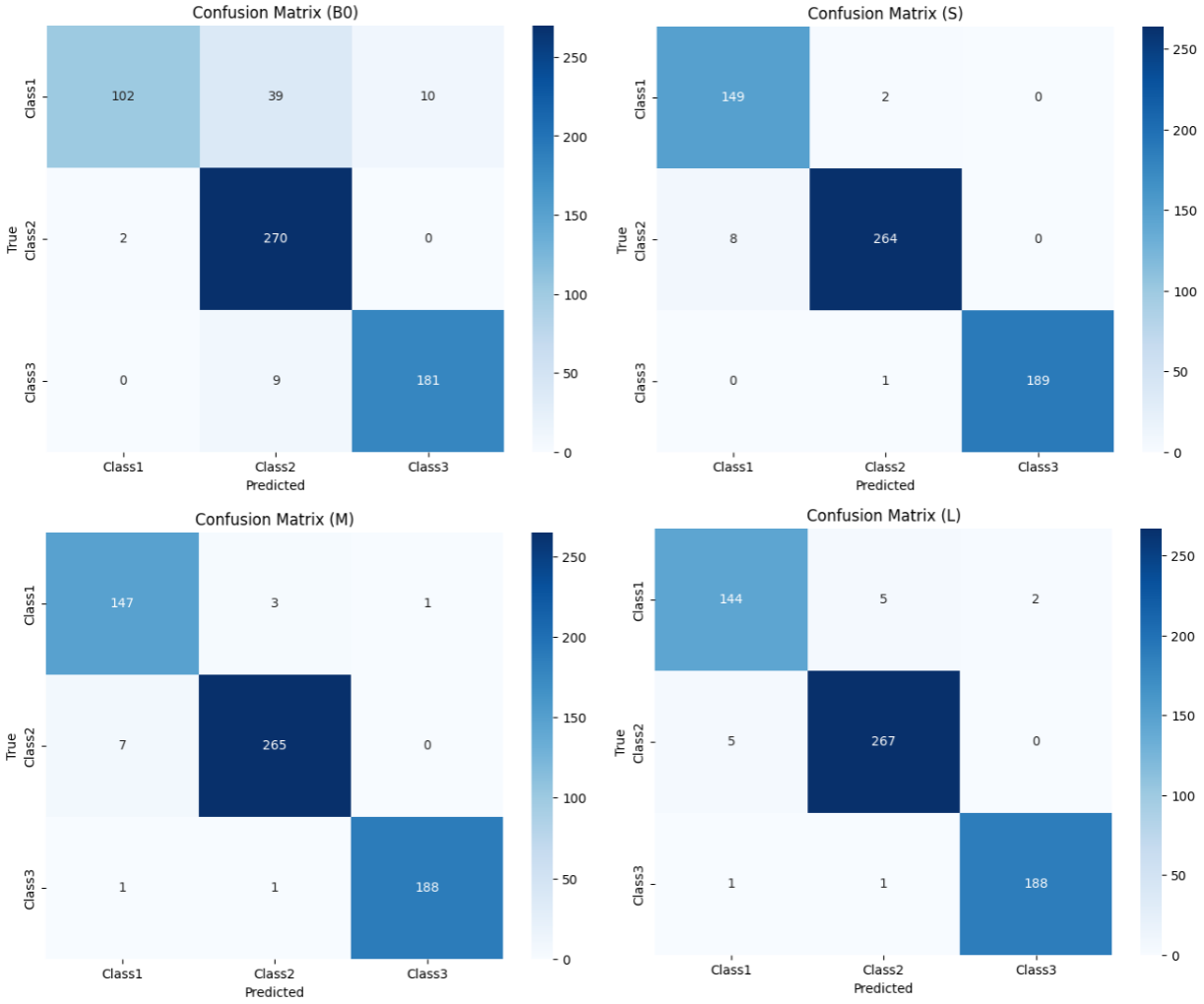

Figure 1. Confusion Matrices of EfficientNet Variants for Brain Tumor Classification.

In Figure 2, significant fluctuations were observed in the validation loss graph of the EfficientNetB0 model, indicating that the model experienced a less stable learning process.The EfficientNetV2-S model exhibited a more stable learning curve in terms of validation loss and reached high accuracy levels quickly.The EfficientNetV2-M model showed that validation loss decreased steadily and the model provided a rapid increase in validation accuracy.The validation loss graph of the EfficientNetV2-L model contained more fluctuations compared to the other EfficientNetV2 variants, but the overall accuracy level remained high.In general, the EfficientNetV2 variants showed more stable and high-performance learning compared to the EfficientNetB0 model in both loss and accuracy graphs

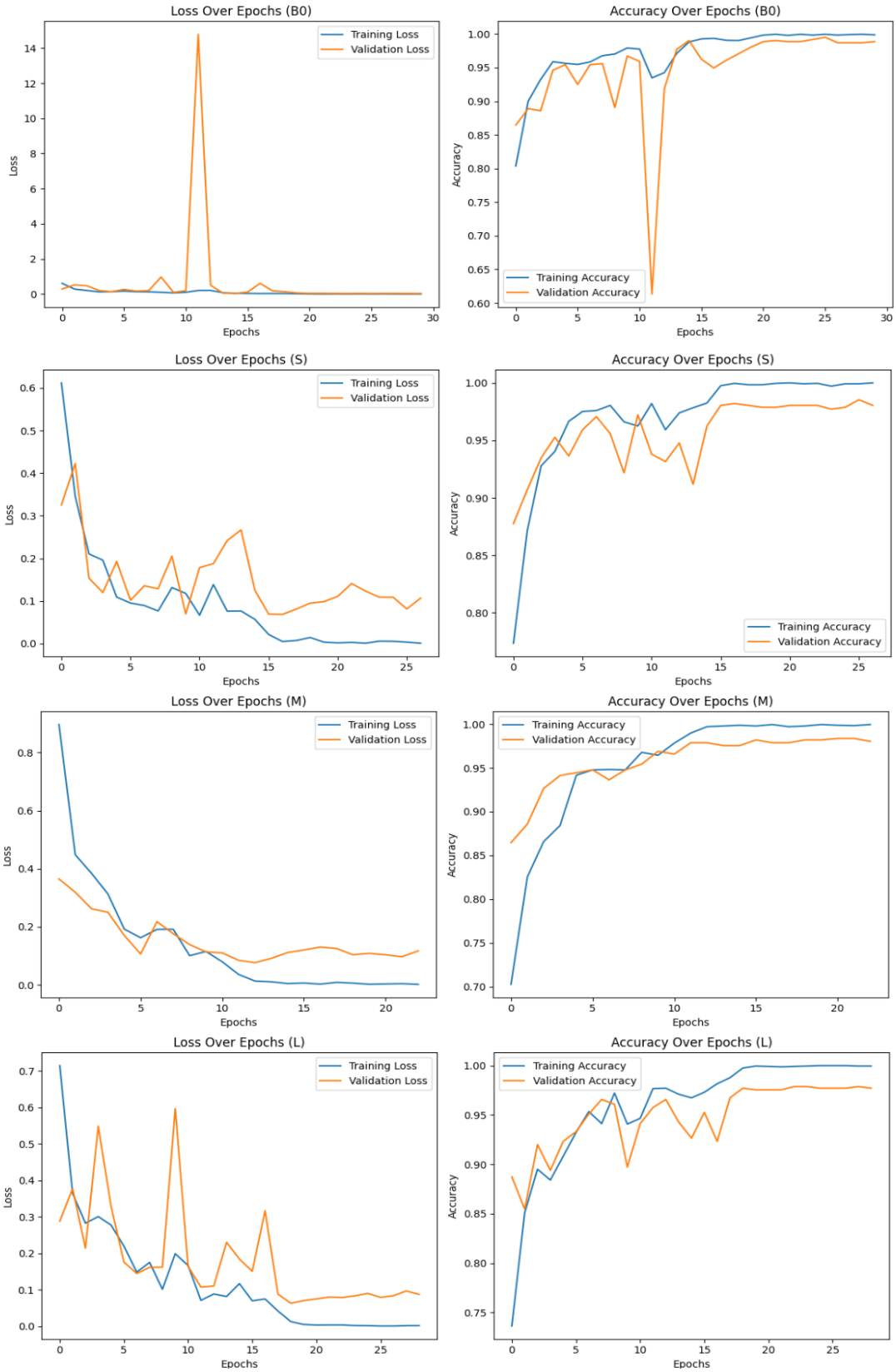

Figure 2. Loss and Accuracy Trends Across EfficientNet Variants During Training.

In Figure 3, the EfficientNetB0 model showed a slightly higher performance with AUC scores of 0.97 for Class1 and Class2 and 0.99 for Class3. EfficientNetV2-S showed excellent classification capacity by increasing the AUC values to 1.00 for all classes. EfficientNetV2-M model also showed a very strong performance with an AUC score of 1.00 for all classes. EfficientNetV2-L, like other EfficientNetV2 variants, showed a successful overall performance with an AUC value of 1.00 for each class. ROC curves clearly show that EfficientNetV2 models have a higher generalization capacity compared to EfficientNetB0 and provide superior performance in brain tumor classification.

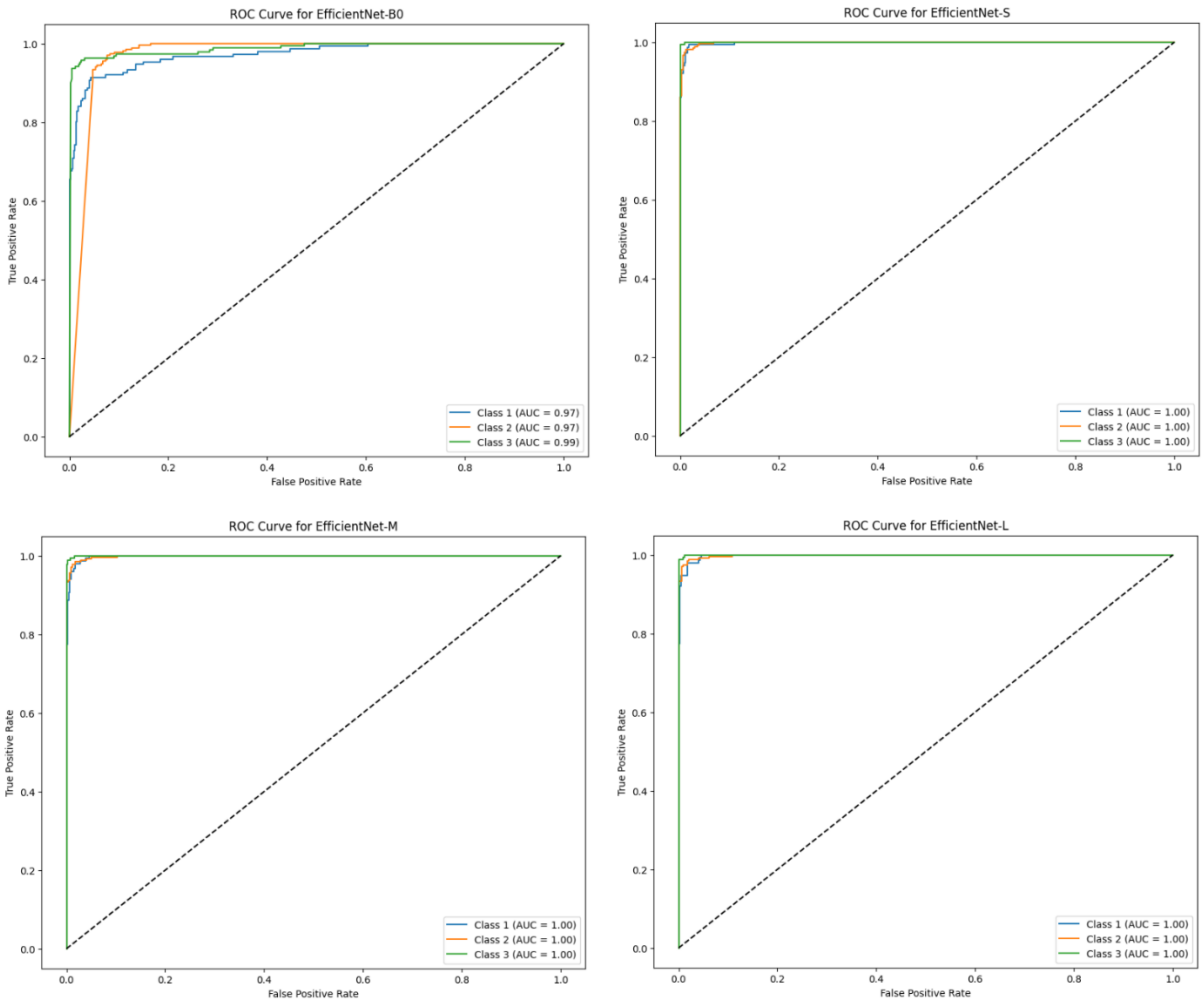

Figure 3. ROC Curves and AUC Scores for EfficientNet Variants in Brain Tumor Classification.

4 Conclusion and Future Work

Brain tumor classification using MRI images remains a critical challenge in medical imaging, demanding high accuracy and computational efficiency for practical applications. This study provides a comparative analysis of EfficientNetB0 and the EfficientNetV2 variants (S, M, and L) to address this challenge. Results indicate that while EfficientNetB0 serves as a strong baseline model, the EfficientNetV2 variants significantly outperform it in terms of accuracy, precision, recall, and AUC scores across all classes. Specifically, the EfficientNetV2-S variant emerged as the most effective model, achieving the highest accuracy (98.20%) and balanced performance across all tumor classes. EfficientNetV2-M and EfficientNetV2-L also demonstrated excellent classification capabilities, with minor trade-offs between computational complexity and performance. EfficientNetV2-S, with its advanced architectural enhancements and efficient training techniques, provides a promising solution for real-world clinical applications, offering high accuracy while minimizing computational costs. EfficientNetV2-S, with its advanced architectural enhancements and efficient training techniques, provides a promising solution for real-world clinical applications, offering high accuracy while minimizing computational costs. Overall, the results highlight the potential of EfficientNetV2 architectures for reliable and automated brain tumor classification, paving the way for their integration into diagnostic workflows. Future studies can focus on several key directions to build upon the findings of this research. Expanding the dataset to include larger and more diverse samples can improve the generalizability of the models, ensuring robust performance across different patient populations and imaging conditions. Incorporating multi-modal imaging data, such as CT scans or PET images, can enhance classification accuracy and provide a more comprehensive diagnostic approach by leveraging complementary information from various imaging techniques. Developing explainable AI methods to interpret model predictions would enable clinicians to understand and trust the decision-making process of the models, fostering their adoption in clinical workflows. Optimizing the models for deployment on edge devices, such as portable medical imaging equipment, can facilitate real-time diagnosis in resource-constrained settings, making advanced diagnostic tools accessible in remote or underserved regions. Integrating classification models with tumor segmentation techniques could create a complete diagnostic pipeline, including tumor localization and grading, thereby offering a more holistic approach to brain tumor diagnosis and treatment planning. These advancements have the potential to significantly enhance the practical utility and impact of AI-driven diagnostic systems in medical imaging.

Declaration

Ethics committee approval is not required.

References

[1] Pereira, S., Pinto, A., Alves, V., & Silva, C. A. (2016). Brain tumor segmentation using convolutional neural networks in MRI images. *IEEE Transactions on Medical Imaging, 35(5)*, 1240–1251.

[2] Akkus, Z., Galimzianova, A., Hoogi, A., Rubin, D. L., & Erickson, B. J. (2017). Deep learning for brain MRI segmentation: State of the art and future directions. *Journal of Digital Imaging, 30*, 449–459.

[3] LeCun, Y., Bengio, Y., & Hinton, G. (2015). Deep learning. Nature, 521(7553), 436–444.

[4] Litjens, G., Kooi, T., Bejnordi, B. E., Setio, A. A. A., Ciompi, F., Ghafoorian, M., ... & Sánchez, C. I. (2017). A survey on deep learning in medical image analysis. *Medical Image Analysis*, 42, 60–88.

[5] Tan, M., & Le, Q. V. (2019). EfficientNet: Rethinking model scaling for convolutional neural networks. *In Proceedings of the 36th International Conference on Machine Learning* (pp. 6105–6114).

[6] Tan, M., Le, Q. V., Shlens, J., Vasudevan, V., & Cheng, Y. (2021). EfficientNetV2: Smaller models and faster training. *In Proceedings of the IEEE/CVF Conference on Computer Vision and Pattern Recognition* (pp. 10096–10106).

[7] Ronneberger, O., Fischer, P., & Brox, T. (2015). U-Net: Convolutional networks for biomedical image segmentation. *In International Conference on Medical Image Computing and Computer-Assisted Intervention* (pp. 234–241). *Springer.*

[8] Ravi, D., Wong, C., Deligianni, F., Berthelot, M., Andreu-Perez, J., Lo, B., & Yang, G. Z. (2017). Deep learning for health informatics. *IEEE Journal of Biomedical and Health Informatics*, 21(1), 4–17.

[9] Shen, D., Wu, G., & Suk, H. I. (2017). Deep learning in medical image analysis. *Annual Review of Biomedical Engineering*, 19, 221–248.

[10] Özbay, F. A., & Özbay, E. (2023). Brain tumor detection with mRMR-based multimodal fusion of deep learning from MR images using Grad-CAM. *Iran Journal of Computer Science*, 6(3), 245–259.

[11] Yildirim, M., Akkaya, N., & Badem, H. (2023). Detection and classification of glioma, meningioma, pituitary tumor, and normal in brain magnetic resonance imaging using deep learning-based hybrid model. *Iran Journal of Computer Science*, 6(4), 455–464.

[12]Islam, M. M., Talukder, M. A., Uddin, M. A., Akhter, A., & Khalid, M. (2024). BrainNet: Precision brain tumor classification with optimized EfficientNet architecture. *International Journal of Intelligent Systems*, 2024(1), 3583612.

[13] Gencer, K., & Gencer, G. (2024). Hybrid deep learning approach for brain tumor classification using EfficientNetB0 and novel quantum genetic algorithm. *PeerJ Computer Science*, 10, e2556.

[14] Shamshad, N., Sarwr, D., Almogren, A., Saleem, K., Munawar, A., Rehman, A. U., & Bharany, S. (2024). Enhancing brain tumor classification by a comprehensive study on transfer learning techniques and model efficiency using MRI datasets. *IEEE Access.*

[15] Cheng, J. (2017). Brain tumor dataset. Figshare.

[16] Simonyan, K., & Zisserman, A. (2015). Very deep convolutional networks for large-scale image recognition. *International Conference on Learning Representations.*

[17] Howard, A. G., Zhu, M., Chen, B., Kalenichenko, D., Wang, W., Weyand, T., ... & Adam, H. (2017). MobileNets: Efficient convolutional neural networks for mobile vision applications. *arXiv preprint arXiv*:1704.04861.

[18] Dosovitskiy, A., Beyer, L., Kolesnikov, A., Weissenborn, D., Zhai, X., Unterthiner, T., ... & Houlsby, N. (2021). An image is worth 16×16 words: Transformers for image recognition at scale. *International Conference on Learning Representations.*

International Journal of Innovative Engineering Applications

Journal homepage: https://dergipark.org.tr/ijiea

CLASSIFICATION OF BRAIN TUMORS USING ARTIFICIAL INTELLIGENCE

Sedat Bayaral*[*1], Evrim Gül[2], Derya Avcı[3]

[1]*Firat University, Instutie of Science, Sofware Engineering, Elazig, Turkey*
[2]*Firat University, Faculty of Medicine, Department of Emergency Medicine, Elazig, Turkey*
[3]*Firat University, Vocational School of Technical Sciences, Department of Computer Technologies, Elazig, Turkey*

Abstract

Original scientific paper

Brain MRI is a medical image obtained by MRI, which stands for "Magnetic Resonance Imaging". Brain MRI uses magnetic fields and radio waves to create detailed images of the brain and surrounding tissues. Today, deep learning algorithms are used to detect brain tumors or classify different brain regions. In this study, feature extraction has been performed with current deep learning models using a dataset consisting of 7023 open access images obtained from patients from various parts of the world, and the results were evaluated by training Support Vector Machine (SVM) and XGBoost models with the extracted features. In this study, 4 deep learning models, VGG16, VGG19, ResNet50 and MobileNetV2, have been used for feature extraction. In order to achieve higher performance, transfer learning method is used in this study, which allows the weights of models that are pre-trained with large data sets to be used in other models. The weights of the models trained with ImageNet were included in the study to improve performance and save time. Although the original layer structures of the models are fixed, the GlobalAveragePooling2D layer has been added to the CNN models to improve performance and generalize the features extracted from deep learning models. Brain MRI images divided into 4 classes as glioma tumor, meningioma tumor, pituitary tumor and no tumor. Auxiliary functions have been used to obtain optimum values for the parameters used for training the models. Accuracy, F1-score, precision and sensitivity metrics used to evaluate the training results. When the results are evaluated, the best performance with an F1-score of 97.87% is obtained by classifying the features extracted from the ResNet50 CNN model with Support Vector Machine (SVM).

Keywords: *Artificial intelligence, machine learning, brain tumor MRI, classification.*

1 Introduction

Cells that grow uncontrollably in the skull region are called brain tumors. Early diagnosis and diagnosis of brain tumors is very important for the treatment of the disease. In recent years, various medical imaging systems have been developed to detect brain tumors. One of them, Brain MRI, is a medical imaging method also known as "Magnetic Resonance Imaging". Brain MRI uses magnetic fields and radio waves to create detailed images of the brain and surrounding tissues. These images provide important information for diagnosing and monitoring brain diseases and planning treatment. Brain tumors are complex and a professional neurosurgeon is required to identify the tumor and its type from an MRI image. Diagnosing tumors from MRI with the help of artificial intelligence systems provides time and convenience to experts.

Today, deep learning algorithms are used to detect brain tumors or classify different brain regions. Deep learning is a machine learning method that can predict subsequent inputs by feeding based on available data. The quantity and quality of data affect the performance of deep learning models. Among with other medical imaging techniques, MRI allows for clearer images. Therefore, thanks to MRI which can display tumors developing in the brain in detail, deep learning models have given more precise results, and studies in this field have attracted the attention of researchers, and many new and productive studies have been carried out in this field.

2 Related Works

The use of artificial intelligence technologies in the diagnosis of medical diseases has started to increase in recent years. Developments in medical imaging systems and the increasingly high quality and detailed images obtained from these imaging systems have attracted the attention of researchers. MRI, one of the medical imaging systems, is used to detect brain tumors. Artificial intelligence models, which can successfully segment and classify images by minimizing the error, facilitate the work of experts in the early diagnosis of the disease. Convolutional Neural Networks (CNN), one of the most popular deep learning models in image classification in recent years, are frequently used in the classification of medical images. For this reason, various studies have been conducted on tumor detection from brain MRI using artificial intelligence technologies.

*Corresponding author.
E-mail address: sedatbayaral97@hotmail.com (S. Bayaral)
Received 08 October 2024; Received in revised form 02 February 2025; Accepted 06 March 2025
 Doi: https://doi.org/10.46460/ijiea.1563426

Karamehić et al. [1] utilized a dataset of 4 classes and preprocessed the images in the dataset with the Python PIL library. After the classification process with VGG16, an accuracy of 96.9% was achieved.

Remzan et al. [2] conducted a classification study using a dataset consisting of 5712 images. In the study, 7 CNN models were incorporated through transfer learning, and feature extraction was performed using these models. The extracted features were evaluated with various machine learning classifiers, and a feature ensemble was created using the top 3 features with the best performance. Subsequently, the best-performing machine learning classifier, MLP (Multi-Layer Perceptron), was employed for brain MRI classification. The study revealed that the best features were obtained from the ResNet50, VGG19, and EfficientNetV2B1 CNN models. Finally, an accuracy of 96.67% was achieved in classification using MLP.

Pal et al. [3] conducted a classification study using a 4-class dataset. The VGG16 CNN model was employed in the study, and when the results were evaluated using the AUC (Area Under ROC Curve) metric, a success rate of 92% was recorded. The model achieved a success rate of 90% for the meningioma class, 91% for the pituitary class, 93% for the glioma class, and 89% for the non-tumor class.

Bohra et al. [4] utilized 3 CNN models for feature extraction and classified the extracted features using various machine learning algorithms. It was noted that the best results were obtained from the features extracted with the aid of the VGG16 CNN model, achieving an accuracy of 97.7%.

Hong [5] classified Brain MRI using a basic CNN model and VGG16. After 300 epochs, the basic CNN model achieved an accuracy of 67%, while VGG16 achieved an accuracy of 80%.

Latif et al. [6] performed feature extraction using the 3D Discrete Wavelet Transform and conducted classification with a Random Forest classifier, also comparing the results with various other classification algorithms. The study results indicated that high-grade glioma was detected with an average accuracy of 89.75%, while low-grade glioma was detected with an average accuracy of 86.7%.

Kibriya et al. [7] performed feature extraction using deep learning models and conducted classification with Support Vector Machine (SVM) from the machine learning models. A total of 15320 MRI images were utilized in the study, achieving an accuracy of 98% with the CNN-SVM based model.

Tandel et al. [8], compared transfer learning-based CNN models with traditional machine learning algorithms, including Decision Trees, Linear Discriminant Analysis, Naive Bayes, SVM, K-Nearest Neighbors (KNN), and ensemble methods. The comparison of the AlexNet model with these 6 machine learning algorithms revealed that deep learning was 12% more successful than machine learning.

Kumar et al. [9] utilized a dataset of 3064 brain MRI images. ResNet50 was employed for classification, resulting in mean accuracy of 97.08% with image augmentation and 97.48% without image augmentation.

Gürkahraman et al. [10] performed brain tumor detection from T1-weighted MRI. In the study, DenseNet121 with transfer learning, one of the ANN models, was utilized for feature extraction, and the obtained features were classified using SVM, KNN, and Bayesian algorithms. The results indicated that the Pearson correlation coefficient (R) of the CNN architecture increased from 88% to 96.7%, and the accuracy improved from 94.6% to 98.6% after image augmentation. The accuracy values of the SVM, KNN, and Bayesian classifiers were recorded as 99.8%, 99.1%, and 89.3%, respectively, while the Pearson correlation coefficient values were 99.5%, 98.9%, and 79%, respectively.

Taşçı [11] utilized a dataset consisting of 3443 images with 4 classes. Among the 19 pre-trained models, the features extracted from the DenseNet201 model yielded the highest accuracy. In the proposed method, 1920 features from the 'avg_pool' layer and 1000 features from the 'fc1000' layer of DenseNet201 were combined. An accuracy of 95.00% was achieved without feature selection, while an accuracy of 95.76% was obtained with mRMR feature selection.

Uysal et al. [12] utilized AlexNet, VGG16, and MobileNetV3 models for classifying a 4-class dataset. The accuracy rates of the images classified using AlexNet, VGG16, and MobileNetV3 were 94.47%, 96.875%, and 95.673%, respectively, while the F1-scores were 94%, 97%, and 96%, respectively.

Demir et al. [13] utilized a pre-trained Convolutional Neural Network model called MobileNetV2 for feature extraction. Subsequently, the ReliefF algorithm was employed for feature selection. The features extracted by MobileNetV2 and those selected by the ReliefF algorithm were fed into the classifiers separately, and the system performance was evaluated. The experimental results indicated that the highest performance was achieved with the combination of MobileNetV2 for feature extraction, ReliefF for feature selection, and the KNN classifier.

Aslan [14] utilized the KNN algorithm in combination with the MobileNetV2 deep learning model for the detection of brain tumors using MRI. In the study, the values from the fully connected layers of the pre-trained MobileNetV2 model were used as features. The KNN classification algorithm was employed to enhance the classification performance of the extracted features. In the experimental studies, an accuracy score of 96.44% was achieved with the proposed method using the KNN classifier for the detection of brain tumors.

Paul et al. [15] classified MRI using models based on Fully Connected and Convolutional Neural Networks architectures. The prediction results in one of three classes: meningioma, glioma, or pituitary. A total of 989 axial images from 191 patients were used (to avoid confusing the neural networks with three different planes containing the same diagnosis). The 512x512 images were augmented, and the models were tested. As a result of the 5-fold cross-validation evaluation, the highest performance rate was found to be a mean accuracy of 91.43%.

Srinivas [16] proposed a model combining CNN and KNN. Feature extraction was conducted using CNN models, while classification was carried out using KNN models. The BraTS 2015 and BraTS 2017 datasets were

employed in the study. As a result, an accuracy of 96.25% was achieved.

Jayade et al. [17] extracted features using the GLCM (Gray Level Co-occurrence Matrix) method and classified benign and malignant tumors with SVM and KNN classifiers. The study utilizing only the SVM classifier achieved an accuracy of 91.21%, while the study using only the KNN classifier achieved an accuracy of 79.23%. However, an accuracy of 94.13% was attained in the study conducted with the new model created by combining both classifiers.

Ayadi et al. [18] investigated the detection of three types of brain tumors. The SVM classifier was employed, achieving an accuracy of 90.27%. The results were obtained through k-fold cross-validation.

Amin et al. [19] conducted classification using T1C, T1, Flair, and T2 weighted MRI. Information with varying textures and structures was extracted from these images of different weights. In order to fuse them, Daubechies wavelet kernels and DWT were employed for more informative tumor region detection. Following this fusion process, noise removal was applied using PDDF. The BRATS 2012, BRATS 2013, BRATS 2015, BRATS 2013 leaderboard, and BRATS 2018 datasets were utilized to evaluate the proposed method. As a result of the study, the fusion of information obtained from different imaging techniques yielded more successful outcomes compared to single sequences.

Shahin et al. [20] proposed a new neural network architecture comprising 4 modules. In the first module, feature extraction is performed. In the next module, RSPA is utilized to enhance the network's features and emphasize significant regions. The next module, ASPP, is utilized for the collection and integration of features at different scales. And the last module is utilized for classification. In the study, 4 publicly available datasets containing 9581 images were utilized. Evaluation with the Cheng, Brats-small-2C, and Brats-small-4C datasets yielded accuracies of 99.78%, 99.33%, and 96.33%, respectively.

Kang et al. [21] employed transfer learning models for feature extraction and evaluated these features using 7 different machine learning algorithms. The top three feature sets that demonstrated optimal performance among the machine learning algorithms were selected and subsequently provided as input to various machine learning models for classification. The results indicated that Support Vector Machine (SVM) classifiers, particularly those utilizing radial basis function kernels, exhibited strong performance, especially in large datasets.

Guzmán et al. [22] conducted a classification study of brain MRI using 7 CNN models. The images comprised four classes: glioma, meningioma, pituitary, and tumor-free. A dataset of 7023 images was created by combining the Fighshare, SARTAJ, and Br35H datasets. Classification was performed using one traditional CNN model and six pre-trained CNN models. The models employed in the study included the traditional CNN implementation, ResNet50, InceptionV3, InceptionResNetV2, Xception, MobileNetV2, and EfficientNetB0. The best performance was achieved with InceptionV3, yielding an accuracy of 97.12%.

Tiwari et al. [23] conducted a classification study utilizing a dataset consisting of four classes: meningioma, glioma, pituitary, and tumor-free. In the study, a new CNN model was proposed, and an accuracy of 99% was achieved following the classification process with this model.

Aamir et al. [24] conducted a classification study utilizing brain MRI. Firstly, image quality enhancement was performed. In the second stage, feature extraction was carried out using two different pre-trained deep learning models. The PLS method was employed to convert these features into a hybrid feature vector form. In the third stage, top tumor locations were extracted through agglomerative clustering. Subsequently, these results were resized appropriately and fed into the main model for classification. The results indicated that the proposed model achieved a classification accuracy of 98.95% compared to existing models.

Saleh et al. [25] conducted a study to detect brain tumors and their types from MRI utilizing five pre-trained models. The models employed in the study included Xception, ResNet50, InceptionV3, VGG16, and MobileNet, with F1-score values obtained as 98.75%, 98.50%, 98.00%, 97.50%, and 97.25%, respectively. These accuracy rates are reported to have a positive impact on the early detection of tumors, potentially preventing paralysis and other disabilities.

Muhammad et al. [26] utilized VGG16 and ResNet50 models to classify brain MRI, evaluating the results based on metrics such as accuracy, sensitivity, specificity, and ROC curve analysis. The VGG16 model achieved 96% accuracy in classifying brain tumors, while the classification of malignant tumors yielded an accuracy of 94.30% when compared to the ResNet50 model. Conversely, the ResNet50 model demonstrated a classification accuracy of 93.10% for benign tumors in comparison with the VGG16 model.

Bahya et al. [27] employed machine learning algorithms to automate brain tumor detection in MRI scans, diagnosing normal and abnormal cases, including meningioma, glioma, and pituitary tumors. Feature extraction techniques such as FFT, K-means clustering, and Tamura texture analysis were utilized, along with dimensionality reduction methods. The study achieved an accuracy of 92.6% with Gradient Boosting (GB), 86% with Adaptive Boosting (ADA), and 82% with SVM for normal and abnormal classification. For specific tumor types, GB achieved 67.9%, SVM 65.3%, and ADA 59.6%. Due to its superior performance, GB was recommended as the most effective algorithm.

Dewan et al. [28] investigated brain tumor detection using MRI scans, focusing on glioma, meningioma, and pituitary tumors. Feature extraction was performed using the Gray Level Co-occurrence Matrix (GLCM) method, and the extracted features were classified using machine learning algorithms, including KNN, SVM, Decision Tree, Naïve Bayes, Logistic Regression, and Random Forest. Among these, Random Forest achieved the highest accuracy of 91.04%. The proposed approach effectively distinguishes between different tumor types and normal cases, aiding in early diagnosis and treatment planning.

Akter et al. [29] proposed a deep learning-based approach for automatic brain tumor classification and

segmentation using MRI scans. A CNN-based model was developed for classifying brain images into four categories, while a U-Net-based model was employed for tumor segmentation. The study utilized six benchmark datasets to evaluate the impact of segmentation on classification performance. Two classification methods were assessed based on accuracy, recall, precision, and AUC. The proposed model outperformed existing pre-trained models, achieving a highest accuracy of 98.7% on a merged dataset and 98.8% with segmentation. The results suggest that this framework could be effectively used in clinical settings for automatic brain tumor detection and segmentation.

N. et al. [30] developed a multiclass classification framework for brain tumor detection using a standard CNN architecture and transfer learning. The study classified meningioma, glioma, pituitary tumors, and normal cases by utilizing pre-trained models such as VGG16, AlexNet, and ResNet50, which were fine-tuned on a balanced dataset. Various optimizers, including Adam, AdaDelta, and SGD, were evaluated to enhance performance. The highest accuracy of 99.83% was achieved using VGG16 with the AdaDelta optimizer, while ResNet50 had the lowest accuracy of 70%. The custom CNN model demonstrated the lowest loss of 0.04%. The findings highlight the potential of deep learning-based models in improving brain tumor diagnosis and treatment planning.

Filatov et al. [31] addressed the challenge of manual brain tumor diagnosis by utilizing pretrained convolutional neural networks (CNN) for automated classification. The study classified three tumor types along with non-tumor MRI images using models such as ResNet50, EfficientNetB1, EfficientNetB7, and EfficientNetV2B1. Among these, EfficientNet demonstrated strong performance due to its scalable nature, with EfficientNetB1 achieving the highest accuracy—87.67% for training and 89.55% for validation. The findings highlight the potential of deep learning in reducing diagnostic errors and improving brain tumor classification.

Islam et al. [32] investigated the effectiveness of deep transfer learning architectures in brain tumor diagnosis using MRI scans. The study applied four pretrained models—InceptionV3, VGG19, DenseNet121, and MobileNet—on a dataset compiled from three benchmark sources: Figshare, SARTAJ, and Br35H. The dataset consisted of four classes: pituitary tumor, meningioma, glioma, and no tumor, with image augmentation applied to balance class distributions. Experimental results demonstrated that MobileNet achieved the highest accuracy of 99.60%, outperforming other models. These findings emphasize the potential of transfer learning in enhancing brain tumor classification accuracy.

Ullah et al. [33] explored the classification of brain tumors using deep learning-based methods on MRI images. The study addressed the challenge of dataset imbalance, which can bias classifier performance, by generating synthetic images using a sparse autoencoder network. Two pretrained neural networks were fine-tuned with Bayesian optimization, and deep features were extracted from the global average pooling layer. To enhance feature selection, the study proposed an improved Quantum Theory-based Marine Predator Optimization algorithm (QTbMPA) for selecting the most relevant features from both networks. The selected features were fused using a serial-based approach and classified with neural network classifiers. Experimental results on an augmented Figshare dataset demonstrated an accuracy of 99.80%, with a sensitivity of 99.83% and a precision of 99.83%, highlighting the effectiveness of the proposed framework.

Rasheed et al. [34] investigated the classification of brain tumors using deep learning techniques on MRI images. The study leveraged convolutional neural networks (CNNs) combined with a hybrid attention mechanism to classify glioma, meningioma, pituitary tumors, and non-tumor cases. Benchmark datasets were utilized to evaluate the proposed method against established pre-trained models such as Xception, ResNet50V2, DenseNet201, ResNet101V2, and DenseNet169. Experimental results demonstrated superior performance, achieving a classification accuracy of 98.33%, with a precision of 98.30%, recall of 98.30%, and an F1-score of 98.20%. These findings highlight the effectiveness of the hybrid attention-based CNN approach in improving brain tumor classification accuracy and generalization, making it a valuable tool for medical diagnostics.

3 Artificial Intelligence

Artificial intelligence is the branch of science that enables human intelligence to fulfill various tasks by imitating human intelligence by machine. It is aimed to realize the learning process carried out by cells called neurons in humans by computers based on a mathematical basis. Today, it is used extensively in strategic games such as chess and go, speech recognition, driverless cars, personal assistants and many other fields. Although artificial intelligence is a general term, it is divided into many sub-branches such as Artificial Neural Networks, Machine Learning, Image Processing, Natural Language Processing, Expert Systems.

3.1 Machine Learning

Machine learning is a sub-branch of Artificial Intelligence. Machine learning involves computers discovering how to perform tasks without being explicitly programmed to do so. It involves computers learning from data provided to them to perform certain tasks. For simple tasks assigned to computers, it is possible to program algorithms that tell the machine how to perform all the steps needed to solve the problem at hand; no learning is required on the computer's side. For more advanced tasks, it can be difficult for a human to manually create the necessary algorithms. In practice, it may be more effective to help the machine develop its own algorithm, rather than having human programmers determine every necessary step.

The discipline of machine learning uses various approaches to teach computers to perform tasks for which there is no fully satisfactory algorithm. In cases where there are many possible answers, one approach is to label some of the correct answers as valid. This can then be used

as training data to develop the algorithm(s) the computer uses to find the correct answers. For example, the MNIST dataset of handwritten digits is often used to train the system for the task of numeric character recognition.

3.2 Deep Learning

Deep Learning, a subfield of machine learning, is a field of study that covers artificial neural networks and similar machine learning algorithms that contain one or more hidden layers.

In other words, it is the use of at least one artificial neural network (ANN) and many algorithms to obtain new data from the data at hand.

Deep learning can be performed supervised, semi-supervised or unsupervised. Deep neural networks have also shown successful results with a reinforcement learning approach. Neural networks are inspired by information processing and distributed communication nodes in biological systems. Neural networks have several differences from biological brains. In particular, neural networks tend to be static and symbolic, whereas the biological brain of most living organisms is dynamic (plastic) and analog.

4 Materials and Methods

The training process consists of four stages: preprocessing the images, splitting the data into training and test sets, utilizing CNN models for feature extraction by structuring their layers, and selecting the optimal hyperparameters.

The dataset contains images with a resolution of 1615×840. Since the input sizes of the CNN models used for feature extraction vary, the images have been resized to match the respective input dimensions of the models as a preprocessing step. No additional processing has been applied. Subsequently, the data has been divided into two parts: training and test sets.

The training data has been used for feature extraction to select the best parameters, subsequently, machine learning models have been trained using these optimal parameters and tested with test data. In the study, feature extraction has been performed using 4 CNN (Convolutional Neural Network) models, classification has been performed with SVM and XGBoost machine learning algorithms and performance comparison has been conducted. Figure 1 shows the flow diagram of the model.

While the basic architecture of the CNN models used in the study is kept constant, the upper layers have been removed and a GlobalAveragePooling2D layer has been added. The GlobalAveragePooling2D layer summarizes the features obtained after convolution and pooling layers and provides more general feature extraction by reducing the number of features. This results in computational and time savings.

Auxiliary functions have been employed to determine the parameters that the machine learning models achieve optimal performance. For parameter optimization, the RandomSearchCV class from the sklearn library, a Python programming language library, has been utilized. The RandomSearchCV class is used to optimize the parameters used in machine learning models. Manually finding the optimal parameter set and combination that yields the best performance in machine learning models is a time-consuming process. The RandomSearchCV class divides the available dataset into parts with the K-Fold method and evaluates the performance of the machine learning model by making random selections from the list of parameters to be optimized and displays the parameter group with the highest performance. In this study, RandomSearchCV has been used to find the most optimal parameters for the features extracted from CNN models to work effectively with machine learning algorithms. Configured with 5 K-fold and 20 iterations, a total of 100 iterations have been performed, and the model has been trained using the optimal values found by the RandomSearchCV class, with the results being reported.

Another parameter optimization class, GridSearchCV, has not been preferred in this study as it tries all possible combinations and causes a long processing time due to the large size of the attributes obtained from the dataset used in the study.

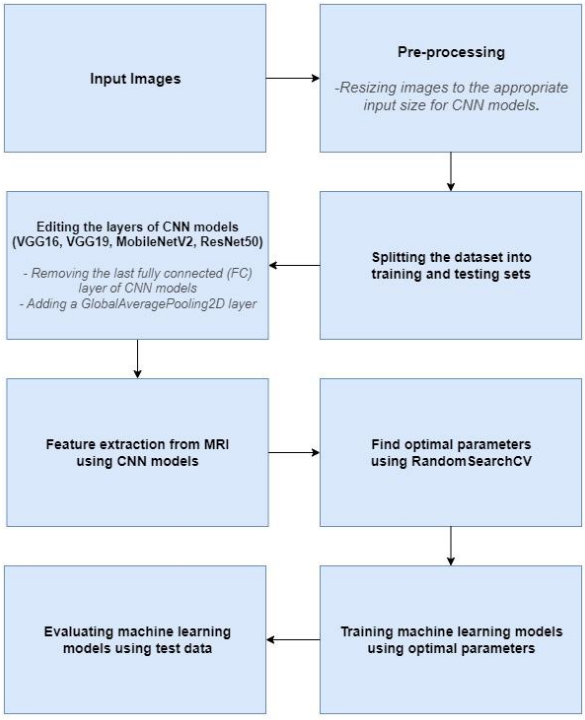

Figure 1. Model training flowchart.

4.1 Dataset

The dataset used in the study has been obtained from the Kaggle [35]. The dataset has 4 classes as glioma, meningioma, pituitary and non-tumor and contains 7023 images in jpeg format. Table 1 shows the distribution of classes in the dataset. Figure 2 shows sample images from the dataset. This dataset has been created by merging figshare, SARTAJ, and Br35H datasets. Since the images are of varying sizes, so all images have been standardized before training. The dataset has been split into two parts, 80% training and 20% testing.

Table 1. Number of classes in the dataset.

Glioma	Meningioma	Pituitary	No Tumor	Total
1621	1645	1757	2000	7023

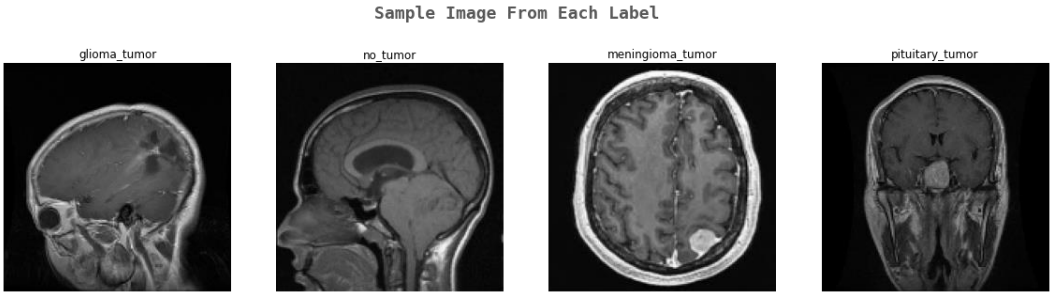

Figure 2. Sample MRI images from the dataset.

4.2 Evaluation Metrics

Accuracy, Sensitivity, Precision and F1-score metrics are used to evaluate the models after training. These metrics are calculated based on the values of TP (Positive True), TN (Negative True), FP (Positive False), FN (Negative False).

A confusion matrix is a table used to evaluate the performance of a classification model. It is used to evaluate two classes of cases (positive and negative). In particular, it is the basis for calculating performance metrics such as recall and precision. Considering a two-class case, it includes four main categories:

- True Positive (TP): The case where true positive instances are correctly identified. Instances that the model labels as positive are indeed positive.
- True Negative (TN): The case where true negative instances are correctly identified. Instances that the model labels as negative are indeed negative.
- False Positive (FP): The case where true negative instances are incorrectly identified as positive. The model labeled samples as positive when they should have been negative.
- False Negative (FN): The case where true positive instances are incorrectly identified as negative. The model labeled samples that should have been positive as negative.

The confusion matrix is used to gain a more detailed understand of which classes the model performs better or worse. It also provides as the foundation for calculating metrics such as the F1-score.

Recall measures the extent to which the model misses true positives (true positives). In particular, it is used for situations that are important to detect. For example, in a model that detects a disease, a low recall value may indicate that some of the people who are actually sick are not detected. Recall ranges from 0 to 1, with 1 representing an ideal situation.

Precision measures how many of the samples that the model labels as positive are actually positive. It is used when it is important to limit false positives. For example, in a spam email filtering application, high precision prevents the user from mistakenly marking important emails as spam. Precision ranges from 0 to 1, with 1 representing an ideal situation.

The F1-score provides a balance by taking the harmonic mean of recall and precision. This balance is particularly important when the data is unbalanced or when false positive and false negative errors are of equal importance. The F1-score is useful when the model needs to balance both false positive and false negative errors. The F1-score value ranges from 0 to 1, with 1 representing an ideal situation.

4.3 Support Vector Machines (SVM)

Support Vector Machines are a versatile and powerful machine learning model. It can perform both linear or non-linear classification, and can also be applied in regression tasks. It is mostly used in classification processes. It is one of the most popular models in machine learning. It is highly suitable for classifying small or medium-sized complex data sets. An SVM uses a hyperplane to separate points on a plane. This hyperplane can be a point, a line, a 3D plane or more multidimensional planes. The primary objective of the SVM model is to separate these points while maximizing the margin of the decision boundary. It uses a set of parameters to achieve this.

4.3.1 Kernel Parameter

SVM does not only work with 2-dimensional data. It can also work with multidimensional data using various kernels, a technique known as the kernel trick. For example, data that cannot be separated in 2 dimensions can be transformed into separable data by mapping it to 3 or more dimensions. The SVM classifier in the scikit-learn library used in the study uses 4 kernels: Linear Kernel, Poly Kernel, RBF Kernel and Sigmoid Kernel.

Linear Kernel aims to separate classes on a 2D plane with a single linear boundary. The area between two classes is called margin. The higher the margin value, the better and more accurate the performance of the classifier. The mathematical representation of the Linear Kernel is given in Equation 1. It computes the dot product of two feature vectors, x_1 and x_2. Here, x_1 and x_2 represent data points in the feature space. The dot product measures their similarity in a linear space. A higher dot product value indicates that the two data points are more similar.

Poly Kernel (Polynomial Kernel) is used to separate data that cannot be explained in 2 dimensions. The higher the polynomial degree, the better the fit to the data. High polynomial degree can lead to over-fitting. The

mathematical representation of the Poly Kernel is given in Equation 2. It takes two feature vectors, x_1 and x_2, and applies a polynomial transformation. Here, x_1 and x_2 represent data points in the feature space. The parameter γ scales the dot product, affecting the influence of input features. The term r is a constant that shifts the polynomial function, and d determines the polynomial degree. A larger d increases complexity, making the model more flexible but also more prone to overfitting.

RBF (Radial Base Function), another kernel used to separate high-dimensional data, transforms the attributes by calculating the distance to the specified reference points and performs re-separation in this way. The mathematical representation of the RBF Kernel is given in Equation 3. It calculates the similarity between two feature vectors, x_1 and x_2, based on their squared Euclidean distance. The parameter γ controls the spread of the function, determining how much influence each data point has. A higher γ makes the model more sensitive to nearby points, capturing fine details but increasing the risk of overfitting, while a lower γ results in a smoother decision boundary.

Sigmoid kernel, although adapted for SVM, is an imported function from Artificial Neural Networks. By its nature, it is highly error-prone and is not widely used in practice. It is disadvantageous in that positive values are difficult to obtain and may cause uneven updating of weights in backpropagation. Although it is not commonly preferred in research, it has been included in this study to assess its impact. The mathematical representation of the Sigmoid Kernel is given in Equation 4. It calculates the similarity between two feature vectors, x_1 and x_2, by applying the hyperbolic tangent function to their dot product. The parameter γ controls the influence of the dot product, and r is a constant that shifts the output. The function is sensitive to changes in γ, with higher values leading to a more complex decision boundary, while r adjusts the overall scaling of the function.

$$K(x_1, x_2) = x_1^T x_2 \quad (1)$$

$$K(x_1, x_2) = (\gamma \cdot x_1^T x_2 + r)^d \quad (2)$$

$$K(x_1, x_2) = \exp(-\gamma \cdot \|x_1 - x_2\|^2) \quad (3)$$

$$K(x_1, x_2) = \tanh(\gamma \cdot x_1^T x_2 + r) \quad (4)$$

4.3.2 C Parameter

The goal of the SVM model is to find the optimal hyperplane. Maintaining the decision boundary as wide as possible while finding the hyperplane is crucial for the generalization performance of the model. However, if one insists on keeping the attributes on the correct side and outside this hyperplane with the calculated hyperplane, this is called hard classification (hard margin). However, allowing a few attributes that can be missed is called soft margin. The parameter C can be used to help determine this margin when building the SVM model. This parameter is effective if a Linear Kernel is used for the SVM classifier. The lower the C parameter is chosen, the higher the level at which the model is able to sift through these outlier features. So a low C value leads to soft classification, while a high C value leads to hard classification. A high C value can lead to overfitting of the model

As shown in Figure 3, when the C parameter is set to a low value, outliers are more tolerant of being outside the hyperplane and soft classification is performed, which leads to a wider calculation of the decision boundary of the two classes separated by the hyperplane. As can be seen in the same figure, if the C parameter is set to a high value, the area separated by the hyperplane is narrower and has the effect of covering more attributes. This situation can lead to overfitting and may cause a decrease in generalization performance. To select the optimal C value, hyperparameter tuning techniques should be employed.

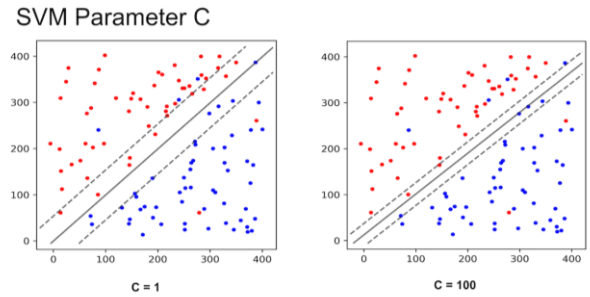

Figure 3. The effect of C parameter in SVM Classifier.

4.3.3 Gamma Parameter

The gamma parameter, used for class separation with the Radial Basis Function, adjust the degree of curvature of the bell curve generated by the function. A high gamma value makes the bell curve more curved, which can cause the model to overfit. A low gamma value makes the bell curve flatter, but can lead to under-learning. When used in combination with a C value, the performance of class separation can be improved. If an SVM model utilizing the RBF Kernel is over-fitting, it is recommended to decrease the gamma value and if it is under-fitting, it is recommended to increase the gamma value. Figure 4 shows the effect of C and gamma parameters on class distinction.

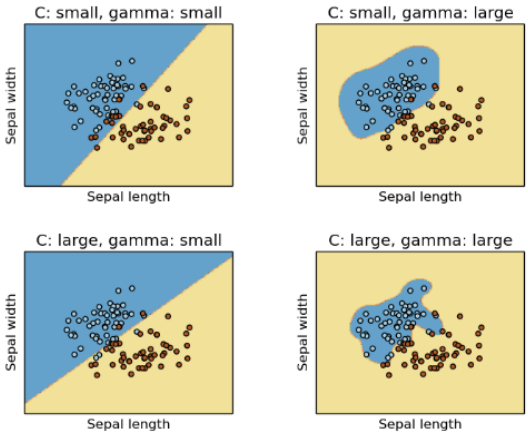

Figure 4. Effect of C and Gamma values on class distinction.

4.4 XGBoost

XGBoost is a machine learning technique built upon the Gradient Boosting algorithm, which is based on the boosting algorithm, one of the ensemble algorithms. The boosting algorithm consists of a set of algorithms that try to optimize an ensemble of a set of weak learners. Each model aims to make better predictions based on the shortcomings of the previous model. Thus, strong learners are formed from multiple weak learners. Decision trees are also utilized as weak learners in the structure of the system.

Gradient Boosting is a boosting algorithm that seeks to minimize errors through gradient descent. It calculates the gradient of the loss function at each iteration. XGBoost also includes L1 (Lasso) and L2 (Ridge) regularization techniques to prevent overfitting. By controlling the complexity of the trees, these techniques enhance the generalizability of the model.

XGBoost is used in many tasks such as regression and classification. It is one of the most widely popular machine learning algorithms today.

4.4.1 Max Depth Parameter

Depending on the type of problem and dataset, more complex relationships can be learned by increasing the depth of the decision trees used in the XGBoost algorithm. However, deeper trees may lead to over-fitting. Therefore, random or grid search methods can be employed for optimal selection.

4.4.2 Learning Rate

In the XGBoost algorithm, the prediction of each tree is sequentially added to the overall sum. By weighting the contribution of each tree, the learning rate can be slowed down. This is called shrinkage. The XGBoost algorithm uses a learning rate coefficient to achieve this. In general, choosing a low learning rate allows the model to learn more robustly, although training may take longer.

4.4.3 Subsample

During training, a random subset of the dataset is selected for training each tree. By training the model on different subsets, this approach helps prevent overfitting.

4.4.4 N Estimators

Each tree used in the XGBoost algorithm is referred to as an estimator. Predicting the optimal number of trees, can be challenging. A small number of estimators can lead to under-fitting, while a large number can lead to over-fitting. The ideal number of estimators can only be chosen using techniques such as random or grid search. The search is terminated when there is no improvement in the performance of the model after a certain point. Figure 5 shows the effect of the N Estimators parameter on the model performance.

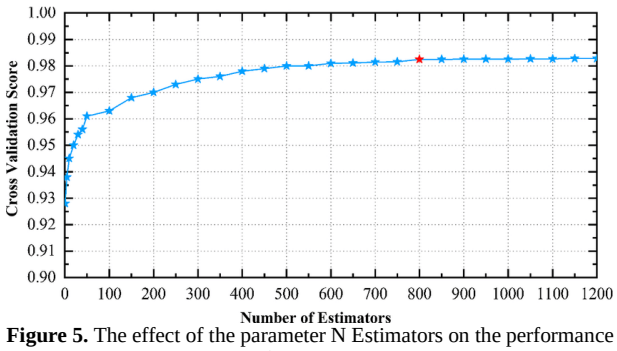

Figure 5. The effect of the parameter N Estimators on the performance of the model.

4.5 RandomSearchCV

When models are created, they are initialized with various hyperparameters. The models operate, learn, and make predictions based on these hyperparameters. It is clear that hyperparameters are present at every stage of the models, so the correct choice of parameters will directly affect the performance of the model. The right choice of hyperparameters depends on the problem and the data set. A set of hyperparameters that works well for one model may not be appropriate for another.

For hyperparameters that vary from model to model, various methods have been developed to select the most appropriate hyperparameter. RandomSearchCV is one of these methods. The RandomSearchCV class is included in the scikit-learn library. The purpose of this class is to test the performance of the model by randomly selecting the hyperparameters of the model over a specified range. In this way, it is aimed to obtain suitable values in a short time since the entire range specified for the hyperparameters is not scanned. RandomSearchCV utilizes the cross-validation method, where instead of using the entire dataset, a portion of the dataset used for training, and the remaining part for testing. Thus, it more accurately measures the fit of the parameter set for the model.

Unlike the RandomSearchCV class, the GridSearchCV class searches over the entire specified range. This requires a long time to select the suitable parameters. Since the GridSearchCV class searches over all possibilities, it is considered the most reliable method. However, considering the costs and time constraints, the RandomSearchCV class is more advantageous. In this study, RandomSearchCV class has been employed to select suitable hyperparameters for the machine learning models used in this study.

5 Results and Discussion

In this study, Accuracy, Sensitivity, Precision and F1-score metrics, which are used to evaluate the learning success of a model, are taken into consideration. First, features have been extracted from the 4 CNN models respectively and these features have been given to SVM and XGBoost machine learning models separately. In SVM model training, the optimum values of C and gamma parameters have been determined with RandomSearchCV. At the same time, 4 kernels used in SVM models have been tested respectively to determine the kernel with the best performance. The optimum values

of max_depth, learning rate, subsample, n_estimators parameters of the XGBoost model have been also determined by RandomSearchCV. The results of feature extraction from CNN models and subsequent classification with machine learning models are listed in Table 2. Following the evaluation of the models with the test data, cofusion matrices have been generated. Figure 6, 7, 8 and 9 illustrate the cofusion matrices produced as a result of testing the features obtained separately from 4 CNN models in the SVM model according to the kernel selection. Similarly, the cofusion matrices generated by testing the features obtained from 4 CNN models in the XGBoost model are given in Figure 10, 11, 12 and 13.

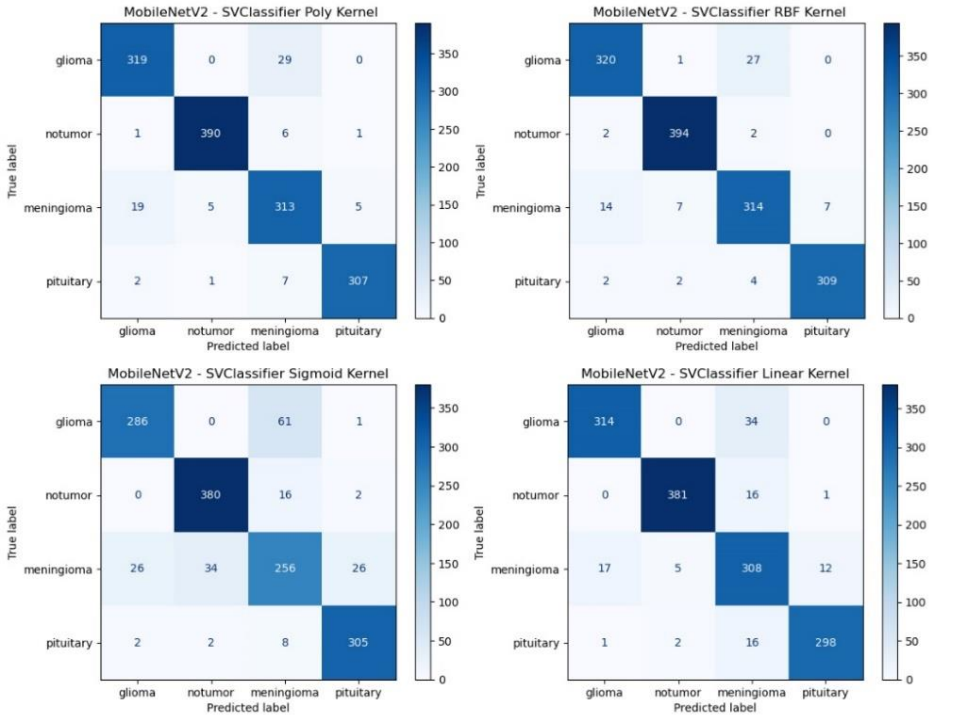

Figure 6. Cofusion Matrices of MobileNetV2 SVM Classifier.

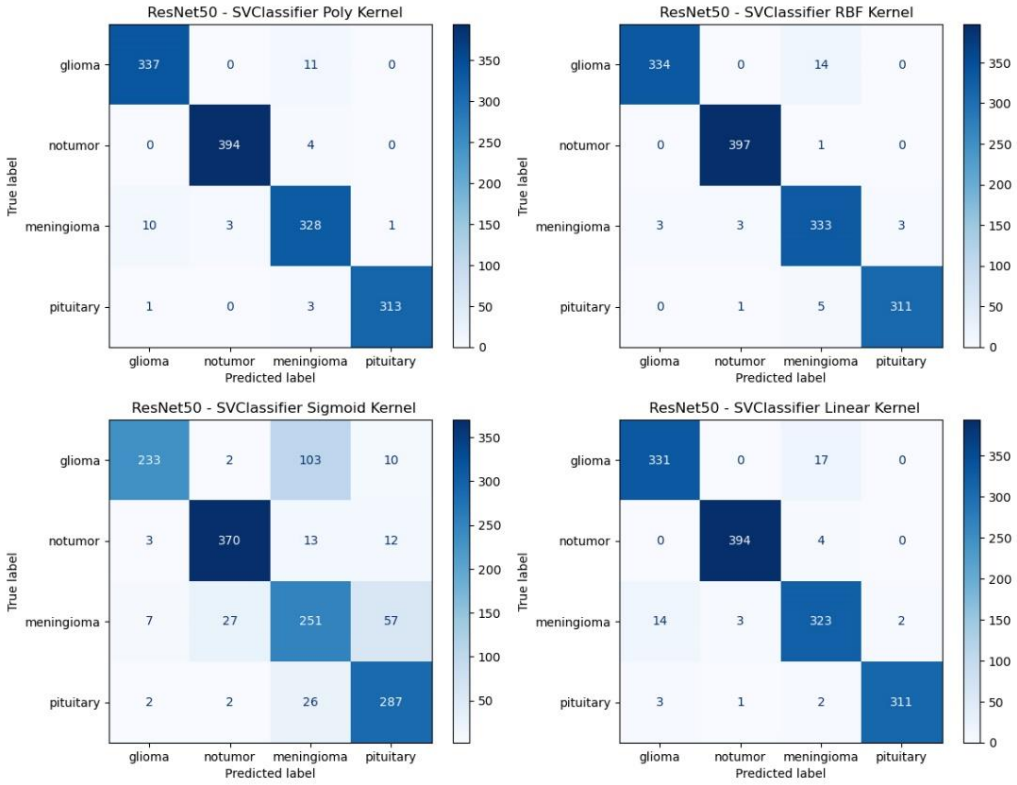

Figure 7. Cofusion Matrices of ResNet50 SVM Classifier.

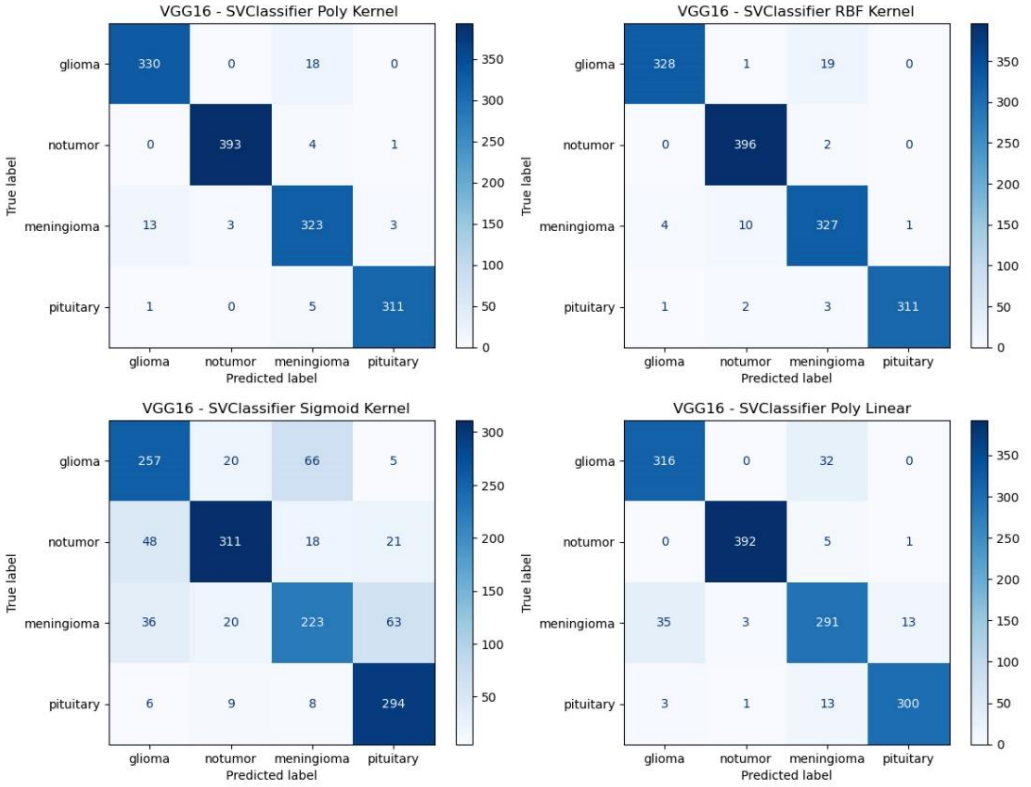

Figure 8. Cofusion Matrices of VGG16 SVM Classifier.

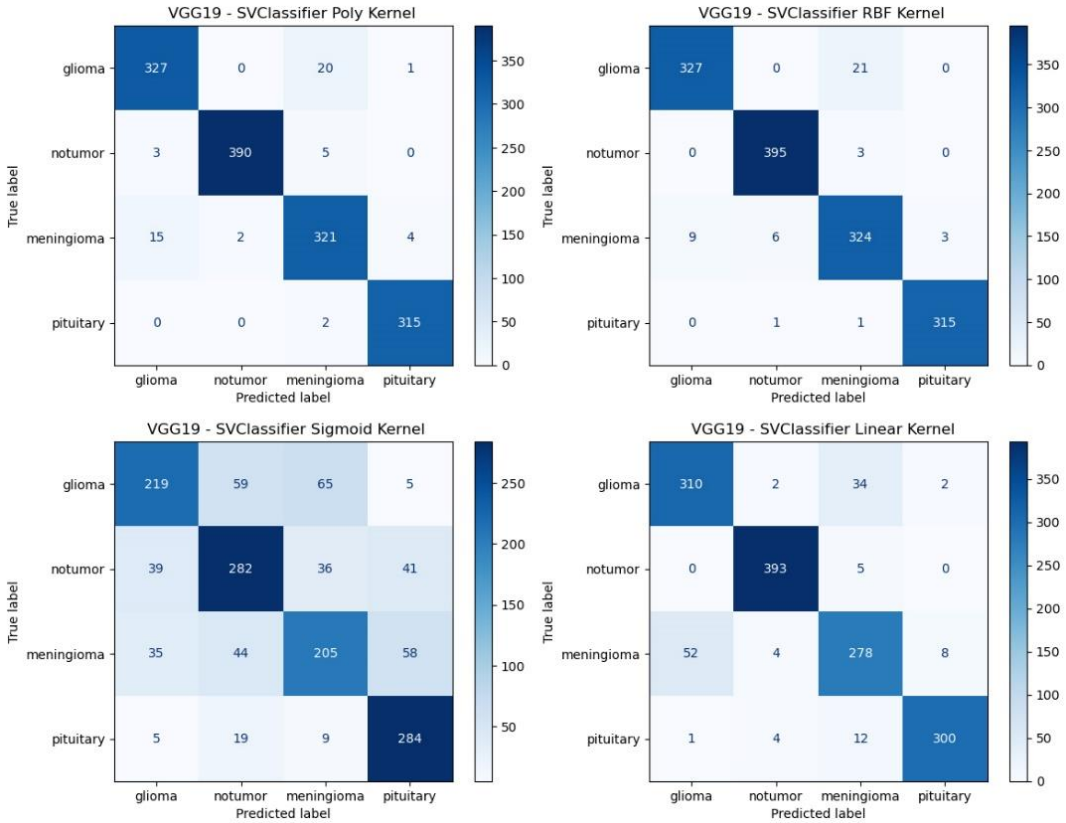

Figure 9. Cofusion Matrices of VGG19 SVM Classifier.

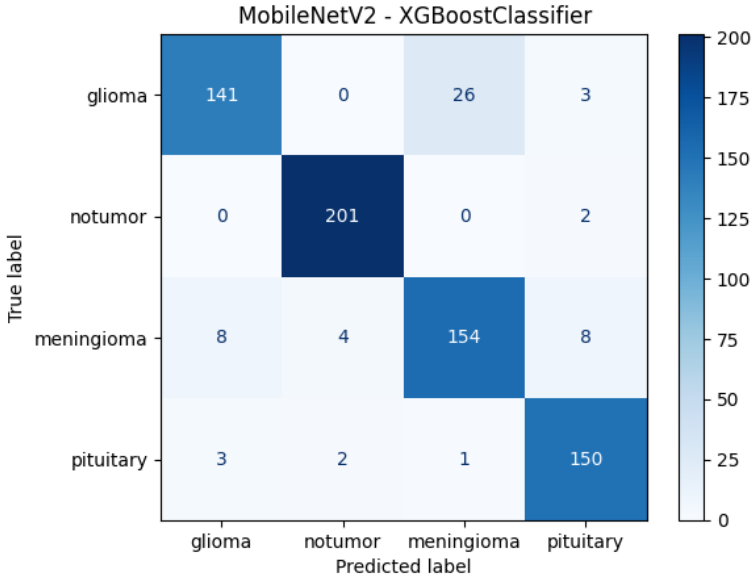

Figure 10. Confusion Matrices of MobileNetV2 XGBoost Classifier.

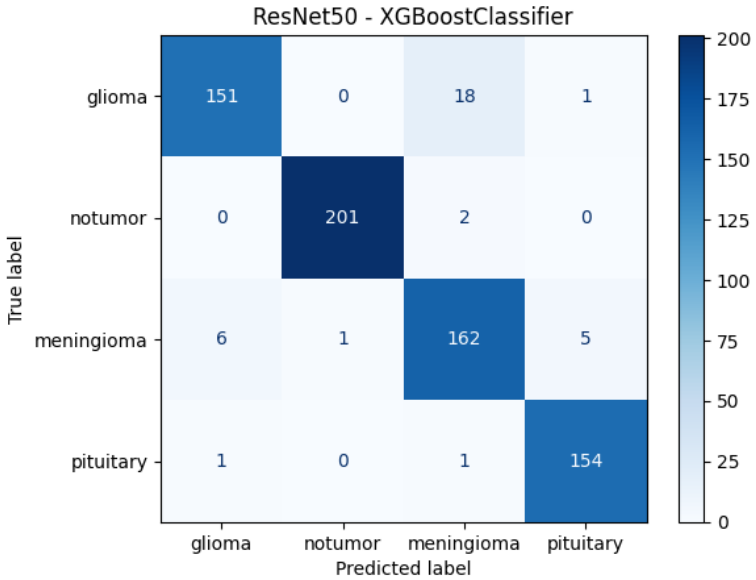

Figure 11. Confusion Matrices of ResNet50 XGBoost Classifier.

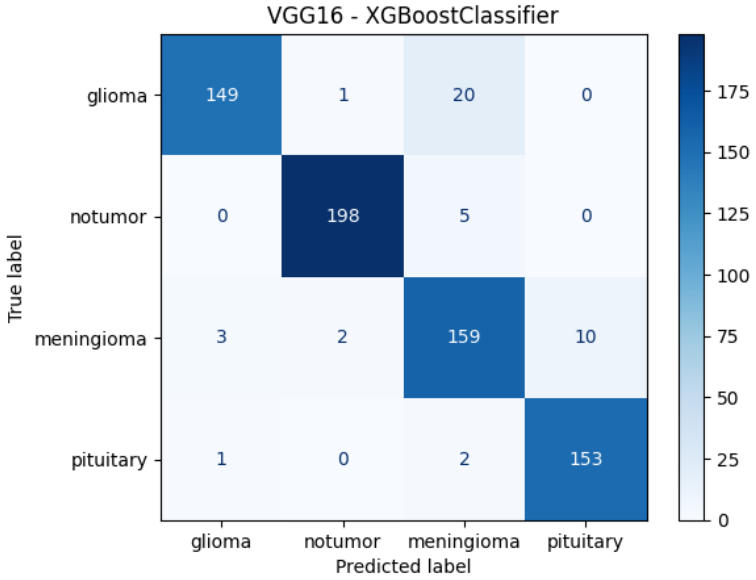

Figure 12. Confusion Matrices of VGG16 XGBoost Classifier.

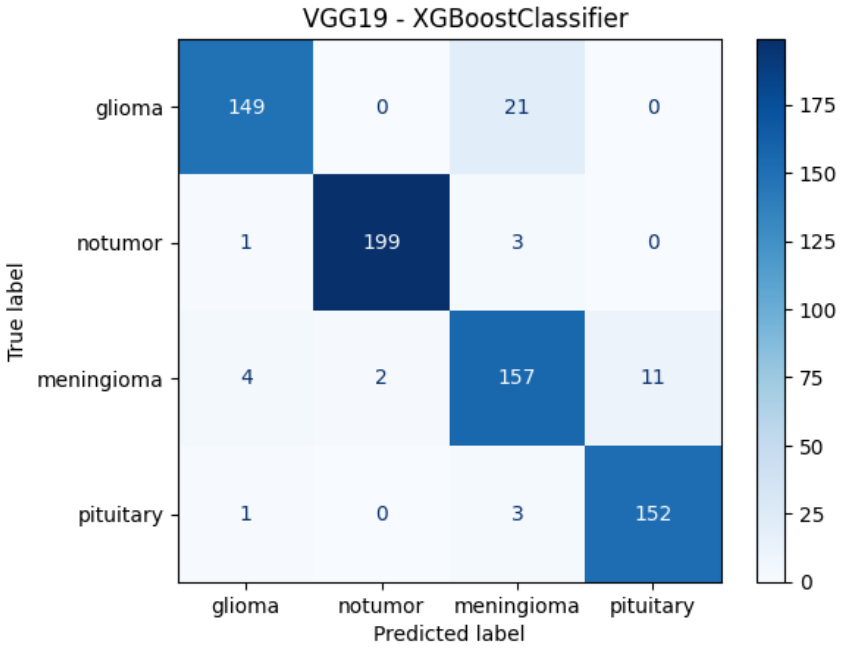

Figure 13. Confusion Matrices of VGG19 XGBoost Classifier.

Table 2. Test results of CNN models and machine learning models after training.

Method	Accuracy	Precision	Recall	F1-Score
CNN (MobileNetV2) + SVM (Poly Kernel)	0.9459	0.9466	0.9459	0.9461
CNN (MobileNetV2) + SVM (RBF Kernel)	0.9688	0.9517	0.9516	0.9515
CNN (MobileNetV2) + SVM (Sigmoid Kernel)	0.8733	0.8731	0.8733	0.8724
CNN (MobileNetV2) + SVM (Linear Kernel)	0.9259	0.9291	0.9260	0.9269
CNN (ResNet50) + SVM (Poly Kernel)	0.9765	0.9766	0.9765	0.9766
CNN (ResNet50) + SVM (RBF Kernel)	**0.9786**	**0.9790**	**0.9786**	**0.9787**
CNN (ResNet50) + SVM (Sigmoid Kernel)	0.8120	0.8293	0.8121	0.8129
CNN (ResNet50) + SVM (Linear Kernel)	0.9672	0.9674	0.9673	0.9673
CNN (VGG16) + SVM (Poly Kernel)	0.9658	0.9661	0.9658	0.9659
CNN (VGG16) + SVM (RBF Kernel)	0.9693	0.9699	0.9694	0.9694
CNN (VGG16) + SVM (Sigmoid Kernel)	0.7722	0.7737	0.7722	0.7704
CNN (VGG16) + SVM (Linear Kernel)	0.9245	0.9248	0.9246	0.9247
CNN (VGG19) + SVM (Poly Kernel)	0.9629	0.9632	0.9630	0.9631
CNN (VGG19) + SVM (RBF Kernel)	0.9686	0.9689	0.9687	0.9687
CNN (VGG19) + SVM (Sigmoid Kernel)	0.7046	0.7033	0.7046	0.7008
CNN (VGG19) + SVM (Linear Kernel)	0.9117	0.9118	0.9117	0.9116
CNN (MobileNetV2) + XGBoost	0.9189	0.9288	0.9275	0.9270
CNN (ResNet50) + XGBoost	0.9502	0.9486	0.9474	0.9474
CNN (VGG16) + XGBoost	0.9374	0.9400	0.9388	0.9389
CNN (VGG19) + XGBoost	0.9345	0.9382	0.9360	0.9361

As a result of the evaluation of the results, it has been observed that the best results have been obtained with the SVM classifier with the RBF kernel of the features obtained from the ResNet50 CNN model with 97.87% F1-score performance.

When evaluating the features extracted from the four CNN models, it has been observed that the best performances have been achieved across all CNN models utilizing the RBF kernel. Conversely, the performance with the Sigmoid kernel has been consistently lower across all CNN models.

Through the application of transfer learning, features from the ResNet50 model have been obtained quickly and effectively and have been classified with high accuracy by the SVM classifier. The best performance for the XGBoost classifier is 94.74% with the features obtained from the ResNet50 CNN model.

Table 3 presents a comparison of this study with other studies in the literature that utilize the same dataset. The results indicate that the classification performance achieved using SVM in this study demonstrates a higher accuracy rate compared to studies that employ CNN for feature extraction followed by classification with machine learning algorithms. However, studies that perform end-to-end feature extraction and classification using CNN models have reported superior performance.

Table 3. Comparison of results with other studies that utilized the same dataset.

Researchs	Methods	Evaluation Metrics	Rates
Karamehić et al. [1] (2023)	VGG16 CNN model	Accuracy	96.9%
Remzan et al. [2] (2023)	CNN models (ResNet50, VGG19, EfficientNetV2B1) for feature extraction, MLP classifier	Accuracy	96.67% (MLP classification)
Pal et al. [3] (2023)	VGG16 CNN model	Accuracy	92% (Overall) 90% (Meningioma) 91% (Pituitary) 93% (Glioma) 89% (Non-tumor)
Guzmán et al. [22] (2023)	CNN models (ResNet50, InceptionV3, InceptionResNetV2, Xception, MobileNetV2, EfficientNetB0)	Accuracy	97.12% (InceptionV3)
Bahya et al. [27] (2023)	FFT, K-means clustering, Tamura texture analysis, Gradient Boosting (GB), SVM, AdaBoost, SVM	Accuracy	Normal/Abnormal Classification: 92.6% (Gradient Boosting) 86% (ADA) 82% (SVM) Tumor Classification: GB: 67.9% SVM: 65.3% ADA: 59.6%
Dewan et al. [28] (2023)	GLCM for feature extraction, KNN, SVM, Decision Tree, Naïve Bayes, Logistic Regression, Random Forest for classification	Accuracy	91.04% (Random Forest)
Akter et al. [29] (2024)	CNN for classification, U-Net for segmentation, Benchmark datasets	Accuracy, Recall, Precision, AUC	98.7% (Merged dataset), 98.8% (with segmentation)
N. et al. [30] (2023)	CNN, Transfer learning (VGG16, AlexNet, ResNet50), Optimizers (Adam, AdaDelta, SGD)	Accuracy	99.83% (VGG16 with AdaDelta)
Filatov et al. [31] (2022)	CNN (ResNet50, EfficientNetB1, EfficientNetB7, EfficientNetV2B1)	Accuracy	EfficientNetB1: 87.67% (training) 89.55% (validation)
Islam et al. [32] (2023)	Transfer learning (InceptionV3, VGG19, DenseNet121, MobileNet)	Accuracy	99.60% (MobileNet)
Ullah et al. [33] (2024)	Sparse autoencoder network, Bayesian optimization, Quantum Theory-based Marine Predator Optimization (QTbMPA)	Accuracy, Sensitivity, Precision	99.80% (Accuracy) 99.83% (Sensitivity) 99.83% (Precision)
Rasheed et al. [34] (2024)	CNN with hybrid attention mechanism, Benchmark datasets	Accuracy, Precision, Recall, F1-score	98.33% (Accuracy) 98.30% (Precision) 98.30% (Recall) 98.20% (F1-score)
This study (2024)	Feature extraction with VGG16, VGG19, ResNet50 and MobileNetV2, classification with SVM and XGBoost	Accuracy, Precision, Recall, F1-score	XGBoost: 95.02% (Accuracy) 94.86% (Precision) 94.74% (Recall) 94.74% (F1-score) SVM: 97.86% (Accuracy) 97.90% (Precision) 97.86% (Recall) 97.87% (F1-Score)

In this study, the GlobalAveragePooling2D layer added to the final layer of the CNN models has reduced both computational and time costs. All parameters have been tested using the RandomSearchCV class, and both positive and negative outcomes have been reported. Thus, the effects of the added layers and auxiliary classes have been evaluated through the conducted tests.

No augmentation has been applied in this study, and no enhancements have been made to the images. Additionally, CNN models have been used for feature extraction without fine-tuning on MRI images. In future studies, it is anticipated that image enhancements, fine-tuning of CNN models using MRI images for more effective feature extraction, and the use of data augmentation may improve the performance of machine learning algorithms

Declaration

Ethics committee approval is not required.

References

[1] Karamehić, S., & Jukić, S. (2023). Brain tumor detection and classification using VGG16 Deep learning algorithm and Python Imaging Library. Bioengineering Studies, 4(2), 1-13.

[2] Remzan, N., Hachimi, Y. E., Tahiry, K., & Farchi, A. (2023). Ensemble learning based-features extraction for brain MR images classification with machine learning classifiers. *Multimedia Tools and Applications.*

[3] Pal, S. S., Raymahapatra, P., Paul, S., Dolui, S., Chaudhuri, A. K., & Das, S. (2023). A novel brain tumor classification model using machine learning techniques. *International Journal of Engineering Technology and Management Sciences, 7*(2), 87–98.

[4] Bohra, M., & Gupta, S. (2022). Pre-trained CNN models and machine learning techniques for brain tumor analysis. In *2022 2nd International Conference on Emerging Frontiers in Electrical and Electronic Technologies (ICEFEET)* (pp. 1–6).

[5] Hong, J. (2021). Feasibility evaluation of brain tumor magnetic resonance imaging classification using convolutional neural network model. *Journal of the Korean Society of MR Technology, 31*(1), 17–23.

[6] Latif, G., Bashar, A., Iskandar, D. N. F. A., Mohammad, N., Brahim, G. B., & Alghazo, J. M. (2023). Multiclass tumor identification using combined texture and statistical features. *Medical & Biological Engineering & Computing, 61*(1), 45–59.

[7] Kibriya, H., Masood, M., Nawaz, M., Rafique, R., & Rehman, S. (2021). Multiclass brain tumor classification using convolutional neural network and support vector machine. *Conference Proceedings*, 1–4.

[8] Tandel, G. S., Balestrieri, A., Jujaray, T., Khanna, N. N., Saba, L., & Suri, J. S. (2020). Multiclass magnetic resonance imaging brain tumor classification using artificial intelligence paradigm. *Computers in Biology and Medicine, 122*, 103804.

[9] Kumar, R., Kakarla, J., Isunuri, B., & Singh, M. (2021). Multi-class brain tumor classification using residual network and global average pooling. *Multimedia Tools and Applications, 80.*

[10] Gurkahraman, K., & Karakış, R. (2021). Veri çoğaltma kullanılarak derin öğrenme ile beyin tümörlerinin sınıflandırılması. *Gazi Üniversitesi Mühendislik Mimarlık Fakültesi Dergisi, 36*(2), 997–1012.

[11] Tasci, B. (2022). Beyin MR görüntülerinden mRMR tabanlı beyin tümörlerinin sınıflandırması. *Journal of Scientific Reports-B*(006), 1–9.

[12] Uysal, F., & Erkan, M. (2023). Evrişimsel sinir ağları temelli derin öğrenme modelleri kullanılarak beyin tümörü manyetik rezonans görüntülerinin sınıflandırılması. *EMO Bilimsel Dergi, 13*(2), 19–27.

[13] Demir, K., Arı, B., & Demir, F. (2023). Detection of brain tumor with a pre-trained deep learning model based on feature selection using MR images. *Firat University Journal of Experimental and Computational Engineering, 2*(1), 23–31.

[14] Aslan, M. (2022). Derin öğrenme tabanlı otomatik beyin tümör tespiti. *Fırat Üniversitesi Mühendislik Bilimleri Dergisi, 34*(1), 399–407.

[15] Paul, J. S., Plassard, A. J., Landman, B. A., & Fabbri, D. (2017). Deep learning for brain tumor classification. In A. Krol & B. Gimi (Eds.), *Medical Imaging 2017: Biomedical Applications in Molecular, Structural, and Functional Imaging* (p. 1013710). SPIE.

[16] Srinivas, B., & Rao, G. S. (2019). A hybrid CNN-KNN model for MRI brain tumor classification. *International Journal of Recent Technology and Engineering, 8*(2), 5230–5235..

[17] Jayade, S., Ingole, D. T., & Ingole, M. D. (2019). MRI brain tumor classification using hybrid classifier. In *2019 International Conference on Innovative Trends and Advances in Engineering and Technology (ICITAET)* (pp. 201–205).

[18] Ayadi, W., Charfi, I., Elhamzi, W., & Atri, M. (2022). Brain tumor classification based on hybrid approach. *The Visual Computer, 38*(1), 107–117.

[19] Amin, J., Sharif, M., Gul, N., Yasmin, M., & Shad, S. A. (2020). Brain tumor classification based on DWT fusion of MRI sequences using convolutional neural network. *Pattern Recognition Letters, 129*, 115–122.

[20] Shahin, A. I., Aly, W., & Aly, S. (2023). MBTFCN: A novel modular fully convolutional network for MRI brain tumor multi-classification. *Expert Systems with Applications, 212*, 118776.

[21] Kang, J., Ullah, Z., & Gwak, J. (2021). MRI-based brain tumor classification using ensemble of deep features and machine learning classifiers. *Sensors, 21*(6), Article 6.

[22] M Gómez-Guzmán, M. A., et al. (2023). Classifying brain tumors on magnetic resonance imaging by using convolutional neural networks. *Electronics, 12*(4).

[23] Tiwari, P., et al. (2022). CNN based multiclass brain tumor detection using medical imaging. *Computational Intelligence and Neuroscience, 2022*, 1830010.

[24] Aamir, M., et al. (2022). A deep learning approach for brain tumor classification using MRI images. *Computers and Electrical Engineering, 101*, 108105.

[25] Saleh, A., Sukaik, R., & Abu-Naser, S. S. (2020). Brain tumor classification using deep learning. In *2020 International Conference on Assistive and Rehabilitation Technologies (iCareTech)* (pp. 131–136).

[26] Muhammad, L. J., Badi, I., Haruna, A. A., Mohammed, I. A., & Dada, O. S. (2022). Deep learning models for classification of brain tumor with magnetic resonance imaging images dataset. In K. Raza (Ed.), *Computational Intelligence in Oncology* (pp. 159–176). Springer Singapore.

[27] Bahya, T. M., & Hussein, N. (2023). Machine learning techniques to classify brain tumor. In *2023 6th International Conference on Engineering Technology and its Applications (IICETA)* (pp. 609–614).

[28] Dewan, J., Thepade, S., Deshmukh, P., Deshmukh, S., Katpale, P., & Gandole, K. (2023). Brain tumor type identification from MR images using texture features and machine learning techniques. *Research Square.*

[29] Akter, A., et al. (2024). Robust clinical applicable CNN and U-Net based algorithm for MRI classification and segmentation for brain tumor. *Expert Systems with Applications, 238*, 122347.

[30] V. N., S. K., Kodipalli, A., Rao, T., & K. S. (2023). Comparative study of customized CNN model and transfer learning for brain tumor classification. In *2023 International Conference on Network, Multimedia and Information Technology (NMITCON)* (pp. 1–6).

[31] Filatov, D., & Yar, G. N. A. H. (2022). Brain tumor diagnosis and classification via pre-trained convolutional neural networks. *arXiv preprint arXiv:2208.00768*.

[32] Islam, M. M., Barua, P., Rahman, M., Ahammed, T., Akter, L., & Uddin, J. (2023). Transfer learning architectures with fine-tuning for brain tumor classification using magnetic resonance imaging. *Healthcare Analytics, 4*, 100270.

[33] Ullah, M. S., Khan, M. A., Masood, A., Mzoughi, O., Saidani, O., & Alturki, N. (2024). Brain tumor classification from MRI scans: A framework of hybrid deep learning model with Bayesian optimization and quantum theory-based marine predator algorithm. *Frontiers in Oncology, 14*.

[34] Rasheed, Z., Ma, Y.-K., Ullah, I., Al-Khasawneh, M., Almutairi, S. S., & Abohashrh, M. (2024). Integrating convolutional neural networks with attention mechanisms for magnetic resonance imaging-based classification of brain tumors. *Bioengineering, 11*(7), Article 7.

[35] Brain Tumor MRI Dataset. (2024). Retrieved June 15, 2024, from https://www.kaggle.com/datasets/masoudnickparvar/brain-tumor-mri-dataset.

International Journal of Innovative Engineering Applications

Journal homepage: https://dergipark.org.tr/ijiea

OPTIMIZING BIG DATA MANAGEMENT ON MICROSOFT SQL SERVER: ENHANCING PERFORMANCE THROUGH NORMALIZATION AND ADVANCED ANALYTICAL TECHNIQUES

***Süleyman Burak Altınışık*[1], *Turgay Tugay Bilgin*[*2]**

[1]*Department of Project Management, Mert Software Electronics, Bursa, Turkey*
[2]*Department of Computer Engineering, Faculty of Enginerring and Natural Sciences, Bursa Technical University, Bursa, Turkey*

Abstract

Original scientific paper

This study investigates Big Data management challenges and solutions in cable manufacturing using Microsoft SQL Server (MSSQL), focusing on performance optimization, normalization, and advanced analytical techniques. Addressing the 4Vs of Big Data, our case study collects data from 45 TAGs at one-minute intervals, generating approximately 56 million daily records. We employ OPC technology for data acquisition, strategic normalization processes, and advanced MSSQL optimization techniques. Normalization significantly reduced data redundancy, decreasing the dataset from 56 million to 283 rows per day and improving query execution times from over 40 minutes to less than 0.1 seconds for complex analytical queries. We also propose a database-independent software development approach to balance cost and performance. This research contributes practical insights into performance optimization, scalability, and cost-effective solutions for organizations managing large-scale data processing challenges in industrial settings, offering a blueprint for efficient Big Data management that balances technical performance with economic considerations.

Keywords: *Big data management, data normalization, cable manufacturing, performance optimization.*

MİCROSOFT SQL SERVER' DA BÜYÜK VERİ YÖNETİMİNİN OPTİMİZASYONU: NORMALİZASYON VE İLERİ ANALİTİK TEKNİKLER İLE PERFORMANSININ ARTIRILMASI

Özet

Orijinal bilimsel makale

Bu çalışma, kablo üretim sektöründe Microsoft SQL Server (MSSQL) kullanarak Büyük Veri yönetimi zorluklarını ve çözümlerini incelemekte, performans optimizasyonu, normalizasyon ve ileri düzey analitik tekniklere odaklanmaktadır. Büyük Veri'nin 4V'sini ele alan örnek olay incelemesinde, 45 TAG'dan bir dakikalık aralıklarla veri toplanmakta ve günlük yaklaşık 56 milyon kayıt oluşturulmaktadır. Veri toplamak için OPC teknolojisini, stratejik normalizasyon süreçlerini ve ileri düzey MSSQL optimizasyon tekniklerini kullanmaktayız. Normalizasyon, veri tekrarını önemli ölçüde azaltmış, veri setini günde 56 milyondan 283 satıra düşürmüş ve karmaşık analitik sorgular için sorgu yürütme sürelerini 40 dakikadan 0.1 saniyenin altına indirmiştir. Ayrıca, maliyet ve performans dengesini sağlamak için veritabanından bağımsız yazılım geliştirme yaklaşımı önermekteyiz. Bu araştırma, endüstriyel ortamlarda büyük ölçekli veri işleme zorluklarıyla karşılaşan organizasyonlar için performans optimizasyonu, ölçeklenebilirlik ve maliyet etkin çözümler konusunda pratik bilgiler sunmakta, teknik performans ile ekonomik hususlar arasında denge kuran etkili bir Büyük Veri yönetimi için bir yol haritası sunmaktadır.

Anahtar Kelimeler: *Büyük veri yönetimi, veri normalizasyonu, kablo üretimi, performans optimizasyonu.*

1 Introduction

The rapid evolution of Big Data has transformed data management and analytics, creating new opportunities and challenges for organizations across industries and academia [1]. With data volumes growing exponentially, effectively managing, processing, and analyzing large datasets has become a crucial skill [2]. This growth is characterized by the "4Vs" of Big Data: Volume, Velocity, Variety, and Veracity. These dimensions increase the complexity of handling data, requiring innovative solutions for storage, processing, and analysis [3].

Despite advancements in database technologies, balancing technical performance and economic feasibility remains a significant challenge [4]. Traditional database

*Corresponding author.
E-mail address: turgay.bilgin@btu.edu.tr (T. T. Bilgin)
Received 09 October 2024; Received in revised form 23January 2025; Accepted 10 February 2025
 Doi: https://doi.org/10.46460/ijiea.1563777

management systems (DBMSs) often fall short in addressing the demands of modern data environments, particularly in scenarios where real-time data processing is essential [5]. Microsoft SQL Server (MSSQL) has emerged as a reliable platform for managing complex data operations due to its advanced querying capabilities, indexing methods, and robust data processing mechanisms [6]. However, its adaptability and cost-effectiveness in Big Data applications continue to be key areas of investigation.

One underexplored aspect of Big Data management is the role of data normalization in enhancing database performance. Data normalization minimizes redundancy and improves data integrity, making it a foundational principle in database design [7]. However, its application in high-velocity data environments, such as those requiring real-time processing, has not been sufficiently addressed. Current research often prioritizes technical innovations like query optimization, indexing strategies, and hardware upgrades [8]. Yet, the potential of normalization to improve performance while conserving resources remains inadequately examined.

Another critical gap involves the economic implications of database-dependent software systems. Organizations adopting such systems often face challenges related to vendor lock-in, limited database portability, and higher long-term maintenance costs [9]. These constraints can hinder flexibility and scalability, especially for businesses transitioning between database platforms. Addressing this issue requires database-independent software development strategies that ensure seamless integration across different systems while maintaining cost-effectiveness and operational flexibility [10].

This study aims to address these gaps by exploring how MSSQL can be optimized using data normalization techniques and how database-independent software design can alleviate economic burdens. The research hypothesizes that combining MSSQL's technical strengths with effective normalization strategies can significantly enhance performance in Big Data environments. Furthermore, adopting database-independent approaches can improve cost-efficiency and scalability by enabling interoperability across various DBMSs.

To test these hypotheses, this study examines data collected in milliseconds from 45 TAGs in a cable manufacturing plant. This high-velocity data environment represents the challenges of managing and analyzing large-scale, real-time production data. By implementing data normalization techniques within MSSQL, the research evaluates the impact on performance, scalability, and resource utilization. Additionally, it investigates the advantages of database-independent software in reducing costs and ensuring adaptability in industrial settings.

The findings of this research aim to provide actionable insights into balancing technical and economic considerations in Big Data management. By focusing on normalization as a cost-effective optimization tool and database independence as a strategy for flexibility, the study contributes to both academic literature and practical applications. These insights are particularly relevant for industrial environments, where real-time data analysis is essential for maintaining production quality and operational efficiency.

This study not only addresses gaps in the current literature but also offers practical solutions for organizations grappling with the complexities of Big Data. By combining theoretical exploration with real-world application, it provides a comprehensive perspective on effective strategies for managing large-scale data operations.

2 Literature Review

Several effective techniques have been identified for optimizing SQL Server performance in Big Data environments [5]. Key strategies include indexing, partitioning, sharding, and caching, which collectively enhance query performance and resource utilization [15]. Advanced query optimization methods, such as multi-level indexing and query rewriting, have achieved significant success by reducing data access and execution times by approximately 40% and 35%, respectively [6]. Additionally, implementing a query caching mechanism can further improve data access performance by prioritizing frequently used data and reducing execution times [17]. Innovative approaches, such as genetic algorithms, have demonstrated adaptability and efficiency in managing complex queries in the context of Big Data, effectively optimizing query performance [18]. While these techniques offer significant improvements, their implementation may vary depending on specific database architectures and workloads, necessitating a tailored approach to achieve optimal results [20]. In conclusion, a versatile strategy that combines these techniques is crucial for effectively managing the challenges SQL Server faces in Big Data environments.

Database performance optimization, particularly in SQL-based systems, has been extensively studied. Myalapalli et al. (2015) examined various SQL tuning techniques, such as indexing and query optimization, demonstrating their significant impact on reducing query execution times in large-scale databases [15]. Pedrozo and Vaz (2014) developed a tool for automatic index selection, which is critical in database management systems handling large volumes of data [16]. This tool optimizes query performance by automatically selecting the most efficient indexes based on query patterns, thereby significantly reducing computational load.

In the field of data warehousing, Correia et al. (2018) discussed the implementation of Fast Online Analytical Processing (OLAP) techniques in Big Data environments [17]. Their study emphasizes the necessity of real-time data processing capabilities for timely decision-making processes in large enterprises. They also address the challenges of maintaining high performance in the context of large data volumes. Sulistiani et al. (2020) explored the application of Agile methodologies in the development of OLAP systems for sales data analysis [18]. Their work demonstrated the effectiveness of the Agile approach in adapting to changing business needs and improving overall system response times.

The debate between normalization and denormalization in database design remains a critical topic. Erdinc et al. (2018) analyzed the impact of database

design on software performance by comparing normalization and denormalization strategies [19]. They found that normalization reduces data redundancy and ensures data integrity; however, denormalization can significantly enhance query performance in certain scenarios by reducing the need for complex join operations [21]. Milicev (2021) introduced the concept of hyper models for the denormalization of transactional relational databases, offering a flexible framework for balancing performance and data consistency [22]. This approach provides a versatile solution for optimizing databases in environments where performance is a critical factor.

In addition to these studies, Alshemaimri et al. (2021) conducted a comprehensive survey on problematic database code snippets in software systems, highlighting how these issues negatively impact database performance [20]. Their work underscores the importance of code quality and its direct effect on database efficiency.

The role of SQL in big data processing has extended beyond the limitations of traditional databases to meet modern data analytics requirements. Silva et al. (2016) analyzed the transition of SQL from traditional databases to big data platforms and examined the challenges that arise during this process. The importance of techniques developed to optimize SQL for large-scale data workloads was emphasized [28].

A study by Santos et al. (2017) focused on the performance of SQL-on-Hadoop solutions. It examined how data warehouses could be optimized on low-performance hardware using SQL-on-Hadoop. The study demonstrated that effective data processing is achievable even on cost-effective infrastructures through SQL query optimization [26].

Real-time data analytics has emerged as a critical requirement in big data environments. Yang et al. (2014) introduced Druid, a real-time analytical data store designed to enhance speed and efficiency in query processing. The study provided significant insights into managing and analyzing high-velocity data streams [27].

Rahman et al. (2024) explored advanced optimization techniques to improve real-time query performance in SQL databases for big data analytics. The study evaluated the impact of indexing, query caching, and parallel processing techniques on handling large-scale data workloads [29].

Optimizing SQL in big data processing plays a crucial role in enhancing system performance. Uzzaman et al. (2024) reviewed best practices and techniques for optimizing SQL databases to handle big data workloads. The study highlighted innovative approaches in storage management and query planning [30].

Panwar (2024) proposed the use of advanced stored procedures to improve the capacity of SQL Server for processing big data. The study demonstrated how stored procedures optimize query operations, reducing both processing time and resource consumption under heavy data loads [32].

Performance comparisons of big data analytics platforms have been widely discussed in the literature. Pirzadeh et al. (2017) conducted a comprehensive evaluation of various big data analytics platforms. The study highlighted the advantages and limitations of SQL-based systems in query processing [31].

Ordonez (2013) questioned whether big data analytics could be performed directly within a DBMS and discussed the advantages of such an approach. The study noted that performing analytics at the database level reduces data transfer costs but poses challenges in performance optimization [33].

3 Methodology

This study utilized a comprehensive approach to examine Big Data management strategies within a cable manufacturing environment, focusing on the capabilities of Microsoft SQL Server. Data collection was carried out using OPC technology, which captured information from 45 TAGs across various production stages at a millisecond-level frequency [3][8]. The system architecture ensured efficient and reliable data transfer from production sensors to the MSSQL database, enabling seamless data ingestion and storage [5]. The dataset was carefully selected based on its relevance to critical production parameters, such as temperature, speed, and diameter. These factors were chosen for their importance in monitoring production quality and operational efficiency. The selection process also aimed to ensure the dataset's representativeness, making it applicable to other industrial scenarios.

The sensors are integrated with the machine and transmit data to the database via the integrated KEPSERVER using OPC technology. A Microsoft service within the database continuously monitors the KEPSERVER and transfers millisecond-level records to the database. As shown in Figure 1, signals obtained from the machine are transferred to the KEPSERVER. A Windows service, specifically designed to transfer OPC data to the database located on the local server, continuously monitors the KEPSERVER and transfers any changed tag values to the database. This structure is as seen in figure 1.

A structured data normalization process was implemented to enhance database performance and maintain data integrity. Two techniques were primarily employed: z-score normalization and min-max scaling. Z-score normalization was used to standardize variables by centering them around the mean and scaling to unit variance, which is particularly useful for data following a Gaussian distribution. Min-max scaling, on the other hand, rescaled data to a range of [0, 1], making it suitable for bounded datasets. These methods ensured uniformity across the dataset while preserving relationships between variables. Additionally, denormalization was selectively applied to improve query efficiency in read-intensive scenarios, such as generating reports. This approach balanced the benefits of normalization, including reduced redundancy and improved consistency, with the performance advantages of denormalized structures for specific use cases.

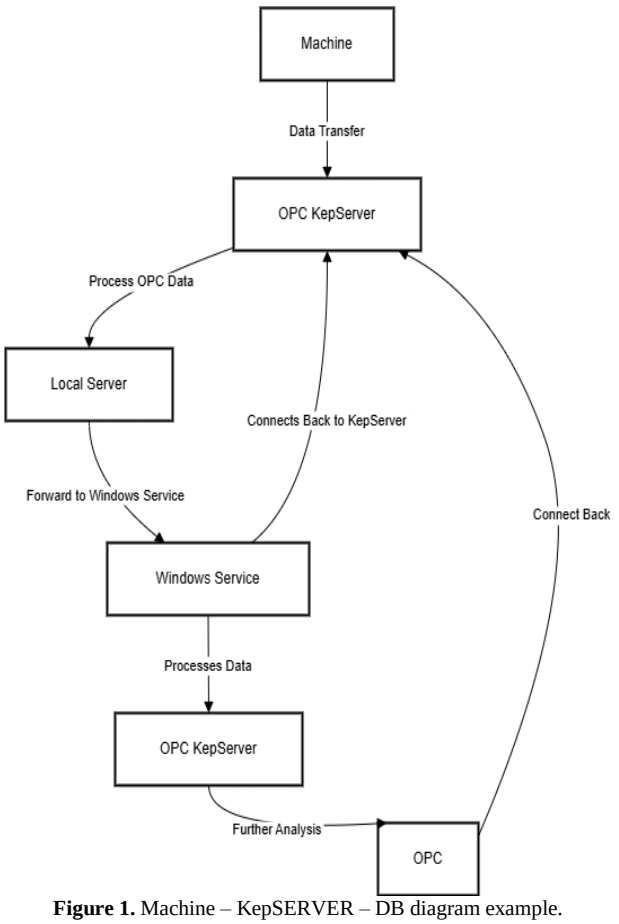

Figure 1. Machine – KepSERVER – DB diagram example.

The data processing phase involved the design and execution of optimized SQL queries to group and analyze the collected data [13]. These queries were tailored to extract statistical metrics, such as mean values, variances, and trend patterns, which are essential for monitoring production processes. Performance improvement techniques, including the use of indexed views, data partitioning, and execution plan analysis, were applied to minimize query execution times and optimize system resource usage.

To address challenges related to vendor lock-in and database portability, a database-independent software development strategy was adopted. This approach involved creating abstraction layers to decouple application logic from database-specific functionalities, allowing compatibility with various DBMS platforms. By implementing this strategy, the study demonstrated enhanced flexibility and potential cost savings, which are critical for scalable Big Data solutions.

The evaluation of the implemented methods relied on performance metrics such as query execution times, CPU usage, and memory consumption. These metrics provided measurable insights into system efficiency. Security protocols, including access controls and data encryption, were incorporated to ensure data reliability. Moreover, data integrity checks, such as consistency constraints and validation rules, were performed to maintain accuracy. Statistical analyses were conducted on the processed data to extract meaningful insights. Techniques such as regression analysis and anomaly detection were utilized to identify trends and outliers, contributing to improved production quality and decision-making.

To ensure transparency and reproducibility, future research should provide more detailed technical explanations of the normalization processes and algorithms employed. For instance, specifying the formulas, software tools, or custom scripts used would enhance methodological clarity. Additionally, further elaboration on the criteria for dataset selection could improve the study's generalizability to other industrial contexts. By addressing these aspects, this research contributes to advancing practical Big Data management strategies while balancing technical efficiency with economic feasibility.

3.1 Data Collection Process

The data collection process, a critical component of this study, was designed to ensure accurate, reliable, and continuous data gathering from various stages of the cable production line [8]. This process utilizes OPC (OLE for Process Control) technology, a standard that facilitates data exchange between devices and software in industrial automation systems [9].

OPC technology is used to collect data from numerous sensors, measurement devices, and control systems on the production line [10]. This approach enables the consolidation of data from different production lines and devices into a single centralized Microsoft SQL Server (MSSQL) database [11]. The OPC server regularly pulls data from the sensors and devices, and a Windows service on the OPC server ensures that this information is recorded in the MSSQL database in a specified format [12].

Data is collected from 45 TAGs in milliseconds, capturing critical parameters of the cable production process [8]. These parameters are essential for the efficient monitoring and analysis of the production process [15].

These data points are collected from various stages of the production process, reflecting the current state of the system. The collected data is critical for monitoring and optimizing the production line, identifying potential issues, and conducting quality control procedures.

Data collection intervals, data volume, and collection methods are key factors that influence the overall performance of the system [7]. These factors are carefully evaluated to balance the need for comprehensive data with system efficiency and resource utilization [8]. This data collection process forms the foundation for subsequent data processing, analysis, and performance optimization steps in the study, enabling a comprehensive investigation of Big Data management in the context of cable production [11].

Table 1. Key data collected during cable production process by chamber.

Data	Description	Chamber
Metre	Measures the length of the produced cable and is used to monitor the total production quantity. This data is critical for determining how long the production line has been operational and the volume of products manufactured.	1
HatHizi (Line Speed)	Monitors the speed of the cable production line. This data is used to evaluate the efficiency of the production process and ensure that the line operates at an optimal speed.	1
SicakCapReel (Hot Diameter)	Measures the diameter of the cable during production. This data is an important factor influencing the cable's physical properties and final quality.	1
SogukCapReel (Cold Diameter)	Monitors the diameter of the cable after production. This measurement ensures that the final dimensions and shape stability of the cable are maintained.	1
Spark	Tracks sparks that occur during production. This data helps detect electrical issues in the production process.	1
VidaDevri (Screw RPM)	Measures the rotational speed of the screw mechanism used in the cable production line. This data directly affects the cable's quality and is monitored to ensure process stability.	1
1BolgeReel - 6BolgeReel	Monitors the measurements in different regions of the cable production line. These data are essential for tracking and optimizing changes occurring in various regions of the production line.	2

3.1.1 Implementation of OPC Technology

In this study, the implementation of OPC (OLE for Process Control) technology constitutes a critical component of the data collection process [9]. OPC serves as a standardized interface for industrial automation systems, facilitating seamless communication between various hardware devices and software applications involved in the cable production process [12].

In our setup, OPC technology is used to establish a robust and efficient data collection system [10]. The implementation consists of several key components:

- **OPC Server:** A dedicated OPC server was set up to mediate between the physical devices on the production line and the data collection software. This server is responsible for reading data in real-time from various sensors, measurement devices, and control systems [13].
- **Device Integration:** Each of the 45 TAGs designated for data collection is configured to communicate with the OPC server [8]. These TAGs represent different parameters at various stages of production, such as cable length, line speed, hot diameter, and cold diameter [14].
- **Data Formatting:** The OPC server is programmed to format the collected data into a standard structure compatible with the Microsoft SQL Server database. This ensures consistency in data representation and facilitates ease of processing and analysis in subsequent stages [11] [16]. A Windows service on the OPC server accesses the SQL Server and is programmed to record the data in a structure that fits the database architecture. This minimizes resource usage on the OPC server [12].
- **Communication Protocol:** The implementation uses standard OPC protocols such as OPC DA (Data Access) or OPC UA (Unified Architecture), depending on the specific requirements of the devices and systems in use [9] [10]. These protocols ensure reliable and secure data transmission from the production site to the database [11].
- **Data Buffering:** To address potential network interruptions or database outages, a data buffering mechanism is included in the OPC implementation [12]. This prevents data loss during temporary communication failures [15].
- **Time Synchronization:** The OPC server is synchronized with a central time source to provide accurate timestamps for all collected data points. This is crucial for maintaining data integrity and enabling time-based analyses [8].
- **Security Measures:** The OPC implementation includes security features such as encryption and authentication to protect the data transmission process from unauthorized access or interference [17].
- **Scalability:** The OPC configuration is designed to be scalable, allowing new TAGs or devices to be added easily as the production system expands or evolves [18].

By leveraging OPC technology in this manner, we establish a reliable and efficient data collection infrastructure that forms the foundation of our Big Data management strategy [10]. This implementation enables us to capture comprehensive and real-time data from the cable production process, providing the raw data necessary for subsequent processing and analysis stages [8] [14].

3.1.2 Data Collection in Cable Manufacturing

The data collection process in cable manufacturing is designed to capture comprehensive information on various aspects of the production process [7]. This process aims to provide a holistic view of cable manufacturing operations by gathering data from critical points along the production line. The data collection system utilizes 45 TAGs distributed across these production areas. Each TAG corresponds to a specific sensor or measurement device on the production line. These TAGs are configured to transmit data at regular intervals, ensuring a continuous flow of information about the production process [12].

Data flows into the system in real-time in millisecond format, contributing to the formation of Big Data [13]. The collected data is instantly transmitted to the centralized Microsoft SQL Server database via the OPC infrastructure. This real-time data transfer allows production managers and analysts to access up-to-date information about the production process.

Various measures are implemented to ensure data integrity and reliability:

- **Sensor Calibration**: Regular calibration of sensors and measurement devices is essential to maintain accuracy [14].
- **Data Validation**: Automated checks are employed to identify and flag anomalous readings.
- **Redundancy**: Critical measurements are typically captured by multiple sensors to ensure data continuity in case of sensor failure.

This approach provides a rich dataset for subsequent analysis and optimization efforts. By collecting detailed information on production parameters, the system offers in-depth insights into production efficiency, product quality, and areas with potential for improvement within the cable manufacturing process.

3.1.3 Data Collection Intervals

In cable manufacturing, the effective management of Big Data systems critically relies on the determination and implementation of appropriate data collection intervals. This study adopts a carefully considered approach to data collection scheduling that balances the need for detailed information with system efficiency and resource management [11].

The primary data collection interval has been set to one minute. This interval was selected after considering several factors:

1. **Dynamics of the Production Process**: A one-minute interval is well-aligned with the typical rate of change in cable manufacturing parameters. It is frequent enough to capture significant fluctuations in production conditions while avoiding the omission of critical events.
2. **Data Volume Management**: Shorter intervals may provide more detailed data but also significantly increase the volume of collected data. A one-minute interval maintains a manageable level of data volume for storage and processing, while still providing adequate detail.
3. **System Resource Utilization**: More frequent data collection increases the load on both the OPC server and the SQL database. The chosen interval helps to optimize the use of system resources [15].
4. **Analysis Requirements**: A one-minute interval provides sufficient resolution for most analytical needs, including trend analysis, quality control, and production optimization.

However, the system is designed with the flexibility to adjust collection intervals based on specific production scenarios:

1. **Critical Process Stages:** During critical stages of production or when new processes are being tested, the system allows for a temporary increase in collection frequency, potentially reducing intervals to as short as one minute.
2. **Low Activity Periods:** During periods of low production activity or machine downtime, the collection interval can be extended to reduce unnecessary data accumulation [18].
3. **Event-Triggered Collection:** In addition to regular intervals, the system is configured to capture data instantaneously when specific thresholds are exceeded or particular events occur. This ensures that critical information is not missed between regular collection points.
4. **Adaptive Intervals:** The system includes an adaptive mechanism that automatically adjusts collection intervals based on the rate of change in key parameters. This allows for more frequent data collection during periods of high variability and less frequent collection during stable periods [17].

The implementation of these data collection intervals includes:

1. **Configuration of the OPC Server:** Configuring the OPC server to retrieve data from sensors at specified intervals.
2. **Synchronization of Data Communication:** Ensuring that data transmission to the SQL database is synchronized with these intervals.
3. **Timestamping:** Applying timestamps to each data point to ensure accurate temporal analysis.

By carefully managing the data collection intervals, the system ensures comprehensive and efficient capture of production data. This approach facilitates detailed and reliable monitoring and analysis of the cable production process.

3.1.4 System Architecture

The architecture of the data collection system is designed to ensure efficient collection, transmission, and storage of data from the cable production process. This system integrates various components to provide a seamless flow of data from the production line to analytical tools. The architecture consists of the following key components:

1. **Sensors and Measurement Devices:** These devices are distributed along the production line and capture various parameters such as cable length, line speed, hot diameter, and cold diameter. They serve as primary data sources that continuously monitor the production process.
2. **OPC Server:** This server acts as an intermediary between physical devices and the database. It collects data from sensors and measurement devices and standardizes the data format to ensure consistent data representation.
3. **Windows Service:** This service is located on the OPC server and is designed to write the standardized data to the SQL Server. It continuously performs connection checks and validations. In the event of a disruption, it temporarily stores data in a local directory on the OPC server at one-minute intervals to maintain data integrity. Once the connection is reestablished, it sequentially reads the data and continues writing to the SQL Server.
4. **Microsoft SQL Server Database:** This is the central repository where all collected data is stored. It is designed to handle large volumes of data efficiently, supporting rapid data retrieval and complex queries.
5. **Monitoring and Control Interface:** This component provides a user-friendly interface for real-time monitoring of the production process. It allows operators and managers to view current production parameters and historical data.

In this architecture, the data flow follows a specific path:

1. **Data Origin:** Data originates from sensors and measurement devices on the production line.
2. **Data Collection:** The OPC server collects this data at regular intervals (typically every minute).
3. **Data Transmission:** The collected data is then transmitted to the Microsoft SQL Server database for storage.
4. **Data Retrieval:** The monitoring and control interface retrieves data from the database to display real-time and historical information.

This architecture is designed with several key features:

1. **Scalability:** The system can accommodate additional sensors or increased data collection rates as production needs evolve [18].
2. **Reliability:** Redundancy measures are in place to ensure continuous data collection even in the event of component failures.
3. **Security:** Data transmission and storage incorporate encryption and access control measures to protect sensitive production information [17].
4. **Performance Optimization:** The architecture is optimized to handle high-frequency data collection and storage operations without compromising system performance.
5. **Integration Capability:** The system is designed to easily integrate with other enterprise systems, such as ERP or quality management software, to facilitate comprehensive data analysis and decision-making processes [20].

This robust system architecture provides efficient and reliable data collection in the cable manufacturing environment, forming the foundation for effective Big Data management. By enabling real-time monitoring, historical analysis, and data-driven decision-making processes, it contributes to improvements in production efficiency and quality control.

3.2 Data Processing

The data processing phase is one of the fundamental components of this study and focuses on transforming raw data into meaningful and actionable information [5]. This process leverages the capabilities of Microsoft SQL Server to efficiently handle large volumes of data and derive valuable insights from the cable manufacturing process [13].

At the core of data processing is a complex SQL query structure that performs multiple operations simultaneously. This query is designed to process data collected from various stages of the production line, such as Chamber 1 and Chamber 2, and to generate comprehensive production metrics for each reel [6]. The key components of data processing are given below:

1. **Data Relational Mapping:** The query establishes relationships between different tables in the database, particularly focusing on the relationships between the "Reel" and "ReelReadings" tables [12]. This relationship is based on matching the ReelID values and ensures the aggregation of all relevant data for each reel.
2. **Data Grouping:** Data is grouped by ReelID, allowing for the analysis of production metrics for each reel. This grouping is essential for understanding the performance and characteristics of each production unit.
3. **Statistical Calculations:** For each reel, the query computes several statistical measures:
   - Minimum, maximum, and average values of meter readings
   - Minimum, maximum, and average values of line speed
   - Minimum, maximum, and average values of hot diameter
   - Minimum, maximum, and average values of cold diameter
4. **Time-Based Filtering:** The query includes a time-based filter, typically using the StartDate and

EndDate fields from the Reel table, to focus on specific production periods [16].

5. **Data Aggregation:** Results are consolidated to provide a comprehensive view of production metrics for each reel.

The SQL query utilized in the data processing phase is designed to group the data collected during cable production meaningfully and perform various statistical calculations. This query establishes relationships between different tables, integrates relevant data, and extracts key statistical information such as minimum, maximum, and average values. The primary aim of the query is to provide detailed insights into the various stages of the production process and the events occurring at these stages by conducting statistical analyses on the collected production data.

This data processing procedure facilitates in-depth analyses of the different stages of the cable production process and enables an understanding of the performance of these stages. The statistical information obtained is crucial for optimizing the production process and for quality control.

```
CREATE PROCEDURE [dbo].[PROC_OPC] @COMPANYID INT, @CPERIODID INT, @SD DATE, @ED DATE
AS BEGIN

DECLARE @STARTDATE DATE, @ENDDATE DATE
SET @STARTDATE = @SD--Parameter Sniffing
SET @ENDDATE = @ED

DECLARE @OPC TABLE(RECEIPTID INT)

INSERT INTO @OPC
SELECT DISTINCT RECEIPTID FROM OPCMMAVALUES WHERE COMPANYID = @COMPANYID
    AND TRANSDATE BETWEEN @STARTDATE AND @ENDDATE

INSERT INTO OPCMMAVALUES
SELECT PR.COMPANYID,
       PR.PWORKSTATIONID,
       PR.RECEIPTID,
       DP.OPCTAGDEFID,
       PR.PID,
       PR.TRANSDATE,
       ISNULL(MIN(TAGVALUEFLOAT),0) MINVALUE,
       ISNULL(MAX(TAGVALUEFLOAT),0) MAXVALUE,
       ISNULL(AVG(TAGVALUEFLOAT),0) AVGVALUE,
       GETDATE() INSERTDATE
FROM PRECEIPTOT PR WITH(NOLOCK, INDEX(IX_PRECEIPTOT_6))
    INNER JOIN PIDRECEIPT P WITH(NOLOCK, INDEX(IX_PIDRECEIPT_5))
        ON PR.COMPANYID = P.COMPANYID AND PR.RECEIPTID = P.PRORECEIPTID
    INNER JOIN PORT_DEFINITION DP WITH(NOLOCK)
        ON PR.COMPANYID = DP.COMPANYID AND PR.PWORKSTATIONID = DP.PWORKSTATIONID
    INNER JOIN OPCTAGRESULT OP WITH(NOLOCK, INDEX(IX_OPCTAGRESULT_1))
        ON DP.COMPANYID = OP.COMPANYID AND DP.OPCTAGDEFID = OP.OPCTAGDEFID
            AND OP.INSERTDATE BETWEEN P.JOBSTARTTIME AND P.INSERTDATE
WHERE PR.COMPANYID = @COMPANYID
      AND PR.CPERIODID = @CPERIODID
      AND PR.TRANSDATE BETWEEN @STARTDATE AND @ENDDATE
      AND PR.RECEIPTID NOT IN (SELECT * FROM @OPC)
GROUP BY PR.COMPANYID,
    PR.PWORKSTATIONID,
    PR.PID,
    PR.TRANSDATE,
    PR.RECEIPTID,
    DP.OPCTAGDEFID
ORDER BY PWORKSTATIONID,
    RECEIPTID
END
```

Figure 2. Analysis query.

To understand the operation of the SQL query, it is important to examine the functions of the tables used and the logic of the query. Below is a detailed explanation of these tables and the query logic:

- **PRECEIPTOT (PR) Table**: This table contains transaction records related to the production process. Fields such as PR.COMPANYID, PR.PWORKSTATIONID, PR.RECEIPTID, and PR.TRANSDATE indicate the company, workstation, and time period in which the production process occurred. This table plays a central role in the data processing phase.
- **PRECEIPTOM (PM) Table**: This table is linked to the PR table and contains details of the processes within the production workflow. The PR.COMPANYID and PR.RECEIPTID fields establish the relationship between these two tables.
- **STOCK (S) Table**: This table provides information about the inventory used in production. It is connected to the PM table and provides details about the materials used during the production process.
- **PORT_DEFINITION (DP) Table**: This table contains definitions of the data collected via OPC. The PR.COMPANYID and PR.PWORKSTATIONID fields link this table to the PR table. The DP.OPCTAGDEFID field specifies a unique identifier for each measurement point.
- **OPCTAGRESULT (OP) Table**: This table includes real-time data collected through OPC. The DP.OPCTAGDEFID and OP.INSERTDATE fields link this table to the DP table. It stores data collected within specific time periods.

The query combines records from the PR table with corresponding records in the PM, S, DP, and OP tables. This join operation is performed using the INNER JOIN command. INNER JOIN ensures that only records with matches in both tables are retrieved, allowing for the processing of relevant data only.

One of the primary functions of the query is to calculate the minimum, maximum, and average values of data collected within a specific time frame (between PR.WORKSTARTTIME and PR.INSERTDATE). These statistical calculations make the data more meaningful and enable the evaluation of performance at various stages of the production process.

An important phase of the query is data grouping. This grouping process allows for the aggregation of data based on specific fields and facilitates statistical analysis within these groups. The GROUP BY clause used in the query enables the grouping of data by fields such as PR.COMPANYID, PR.PWORKSTATIONID, PR.PID, PR.TRANSDATE, PR.RECEIPTID, and DP.OPCTAGDEFID. This grouping allows for the segregation of data from different stages of the production process and makes it possible to perform comparisons between these stages. For example, comparing data collected at different time intervals on the same production line can help identify deviations in the production process and determine the causes of these deviations.

The processed data provides valuable insights into production efficiency, quality control, and areas with potential for improvement in the cable manufacturing process. Additionally, it enables the identification of trends, anomalies, and correlations among various production parameters. These insights contribute to optimizing the production process, addressing quality issues, and enhancing overall operational efficiency.

3.3 Query Optimization Techniques

Optimizing the data processing phase is crucial for efficiently handling large data sets and maximizing system performance. To minimize lock contention and enhance concurrency, the WITH(NOLOCK) hint has been strategically employed in queries. This technique allows read operations to bypass locks held by other transactions, significantly reducing query wait times. By decreasing database locking, this method facilitates faster query execution and improves overall system performance. However, it is important to note that this approach might occasionally read uncommitted data. This trade-off is considered acceptable in real-time monitoring scenarios where immediate data access is more critical than absolute consistency.

A comprehensive indexing strategy has been implemented to optimize query performance. Key indexes such as IX_PRECEIPTOT_6 and IX_OPCTAGRESULT have been created on frequently queried columns as shown in Figure 3. These indexes are regularly maintained and adjusted according to query patterns and performance metrics.

```
3  CREATE NONCLUSTERED COLUMNSTORE INDEX IX_OPCTAGRESULT_1
4   ON OPCTAGRESULT (OPCTAGDEFID, INSERTDATE, TAGVALUEFLOAT)
5
```

Figure 3. Create index.

For fact tables with a large number of rows, columnstore indexes have been applied. These indexes provide significant performance improvements for analytical queries that scan large sections of the table.

4. Performance Analysis

Efficient data processing in industrial environments managing large data sets is critical due to its direct impact on operational efficiency and cost-effectiveness. In the context of cable production, reducing data processing times enhances both production line efficiency and overall system performance. This section highlights significant performance improvements achieved through normalization and other optimization techniques by examining their impact on data processing.

4.1 Impact of Normalization on Data Processing

At the beginning of the data processing phase, the system collected data from 45 TAGs at one-minute intervals, resulting in approximately 13,500 records per interval. During peak production periods, data was collected from 81 machines and 824 TAGs, creating a substantial data load. On a single day, this data extraction process accumulated approximately 56 million rows in the database, placing significant pressure on system resources.

According to Table 2, as the number of records increased from 10,000 to 56 million, the corresponding size of the dataset grew from 551 MB to over 3 TB, further intensifying the pressure on the system.

Table 2. Growth of Dataset Size and Record Count Impact on System Load

Sequence ID	Record Count	Size (megabyte)
1	10.000	551
2	25.000	1380
3	50.000	2765
4	100.000	5546
5	200.000	11136
6	300.000	16815
7	400.000	22622
8	500.000	28595
9	1.000.000	57647
10	1.500.000	87508
11	2.000.000	118428
12	2.500.000	150640
13	3.000.000	184383
14	4.000.000	250638
15	5.000.000	320316
16	6.000.000	393989
17	7.000.000	944520
18	12.000.000	1111568
19	25.000.000	1290530
20	56.000.000	3000000

The total data processing time extended to approximately 40 minutes and 45 seconds, illustrating the challenges of processing such large datasets in real-time (refer to Figure 4 for the SQL query used in the pre-normalization data analysis).

```
2  DECLARE @COMPANYID INT = 7
3  DECLARE @STARTDATE DATETIME
4  DECLARE @ENDDATE DATETIME
5
6  SELECT COUNT(1)
7  FROM OPCTAGRESULT WITH(NOLOCK, INDEX(IX_OPCTAGRESULT))
8  WHERE COMPANYID = @COMPANYID AND
9      INSERTDATE >= @STARTDATE AND
10     INSERTDATE <= @ENDDATE
```

Figure 4. Pre-normalization query.

To address these inefficiencies, a comprehensive normalization process was implemented. Normalization significantly reduced the dataset size by eliminating redundancy and unnecessary data points. For every 1-minute interval, the number of rows decreased from 13,500 to just 45. This reduction dramatically improved query performance, reducing the daily dataset to only 283 rows and lowering the query processing time to an impressive 0.1 seconds (see Figure 5 for the SQL query used in the post-normalization analysis). The application of normalization clearly demonstrated its ability to optimize large-scale data processing, resulting in faster query times and more efficient system resource usage.

```
DECLARE @COMPANYID INT = 7
DECLARE @TRANSDATE DATE

SELECT *
FROM OPCMMAVALUES WITH(NOLOCK, INDEX(IX_OPCMMAVALUES_1))
WHERE COMPANYID = @COMPANYID AND
    TRANSDATE = @TRANSDATE
```

Figure 5. Post-Normalization query.

4.2 Performance Improvements

Normalization led to significant performance enhancements overall [19]. Before normalization, processing the dataset consisting of 56 million rows (as indicated in Table 1, over 3 TB) took more than 40 minutes, causing substantial delays in critical operations. After normalization, the reduced dataset allowed query processing times to fall below one second. This dramatic reduction in both data size and processing time underscores the value of normalization as a performance optimization strategy [21].

In addition to faster query times, the reduction in data size also optimized disk I/O operations, which are crucial in large-scale databases [22]. Normalization enabled more efficient data retrieval, thereby improving overall system performance and reducing storage demands. As a result, the system was able to achieve higher query throughput without performance degradation, thereby enhancing scalability and operational capacity.

4.2.1 Resource Utilization and System Optimization

Normalization and optimization techniques have significantly improved query performance while enhancing resource utilization. By eliminating redundant and repetitive data, the load on critical resources such as CPU, memory, and disk I/O has been substantially reduced [20]. These improvements have made data processing more efficient and minimized the operational burden on the system. In industrial environments requiring high data processing capacities, such as cable manufacturing, these advancements have directly contributed to maintaining production efficiency and reducing operational costs.

As shown in Figure 6, prior to normalization, the database often experienced performance bottlenecks caused by excessive resource consumption due to large datasets. For example, during query execution, CPU usage averaged 88%, memory usage reached 84%, and disk I/O utilization was negligible at 1 MB. However, as demonstrated in Figure 7, significant improvements were observed after normalization: CPU usage decreased to 20%, memory usage dropped to 37%, and disk I/O utilization slightly increased to 6 MB. These measurements were obtained using SQL Server Profiler, clearly indicating improved resource utilization.

These optimizations have enabled the system to process data more effectively, reduced the risk of resource exhaustion, and increased its capacity to handle growing data volumes. Furthermore, the system's scalability has been enhanced without requiring additional resources, contributing to its long-term sustainability.

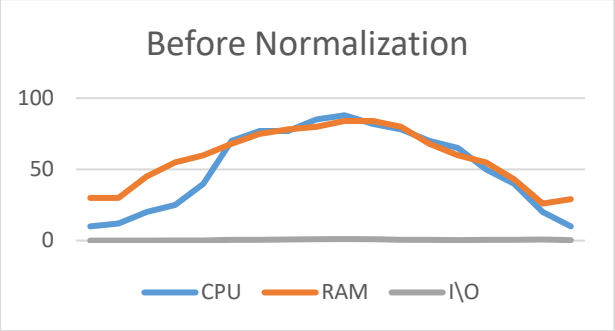

Figure 6. Before Normalization – Resource Usage

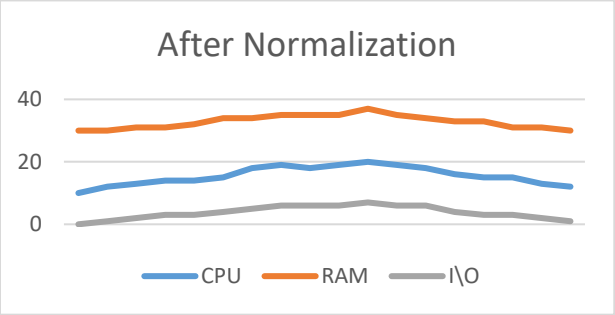

Figure 7. Before Normalization – Resource Usage

4.2.2 Reduction in Query Times

Normalization has had a profound impact on reducing query execution times. Initially, querying large datasets could take up to 40 minutes, significantly affecting the system's response capability and real-time data acquisition. After the implementation of normalization, the reduction in data size directly led to a significant decrease in query times.

Table 3 presents a comparison of query execution times before and after normalization. For instance, prior to optimization, querying 1 million records took approximately 12 seconds, whereas after optimization, the same query was processed in just 0.91 seconds. This dramatic reduction in query time demonstrates the effectiveness of normalization and other optimization techniques in enhancing system performance.

Table 3. Execution times of SQL queries.

Sequence ID	Before Norm. (secs)	After Norm. (secs)
1	0,4	0,001
2	0,5	0,003
3	1,3	0,005
4	1,4	0,008
5	2,6	0,011
6	3,3	0,016
7	4,1	0,032
8	5,2	0,04
9	8,4	0,82
10	12	0,91
11	14,6	1,02
12	16,7	1,13
13	22,3	1,54
14	29,5	1,82
15	39,9	2,01
16	44,5	2,26
17	51,1	2,41
18	289	2,92
19	612	3,47
20	1835	3,88

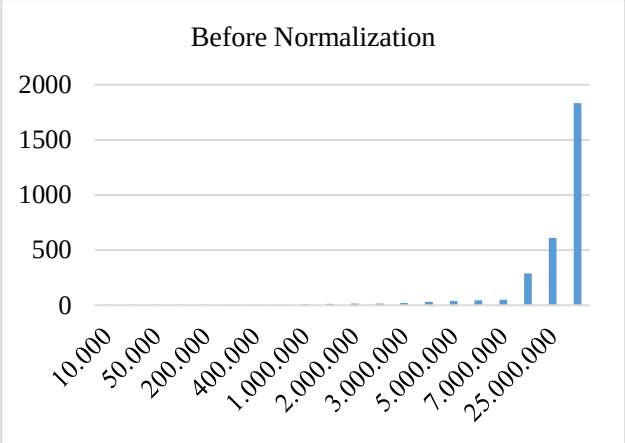

Figure 8. Before normalization.

Figure 8 further illustrates the stark difference in query performance before and after optimization. The system's ability to handle more queries in parallel with reduced latency has increased overall data processing capacity and enabled the handling of larger datasets without compromising performance.

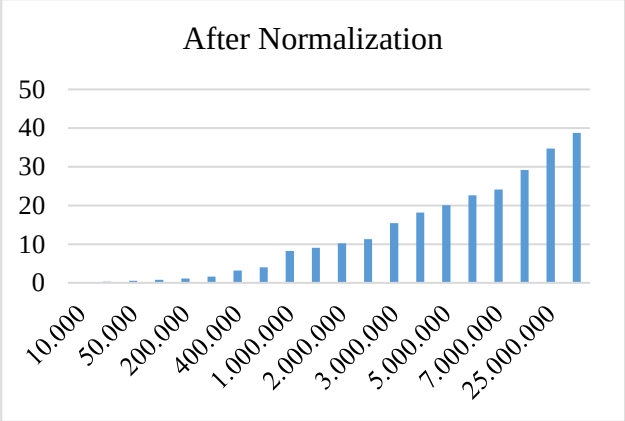

Figure 9. After normalization.

The reduction in query times is crucial in real-time production environments, as timely data analysis is essential for decision-making and process optimization [17]. Faster query execution also enables the system to handle multiple queries simultaneously, thereby enhancing overall operational efficiency.

4.3 Strategic Importance of Normalization

In this study, normalization has enabled the system to allocate resources more efficiently by reducing the overall dataset size, which has directly contributed to faster processing times and improved resource utilization [19]. The long-term benefit of normalization lies in its ability to scale the system as data volumes increase, without compromising performance or requiring significant additional resources. As demonstrated in Table 2 and Figures 8 and 9, normalization has had a tangible impact on reducing query execution times and improving system operations.

However, normalization is not a one-time solution; it should be part of a continuous data management strategy [21]. As data sets evolve and expand, regular review and adjustment of the normalization process are necessary to ensure sustained performance gains. In dynamic industrial environments like cable production, this approach helps maintain operational efficiency, supports scalability, and lays the groundwork for more advanced data analysis techniques.

In conclusion, the strategic importance of normalization lies in its ability to optimize both short-term performance and long-term sustainability [22]. By integrating normalization as a fundamental part of the data management process, organizations can ensure that their systems remain responsive and scalable in the face of increasing data complexity.

5 Results and Recommendations

Effective data management is crucial for modern industrial processes, where the ability to process large datasets directly impacts operational efficiency and business competitiveness [23]. This study examined the optimization of database performance through normalization and indexing techniques on Microsoft SQL Server (MSSQL). The results highlight both the strengths and limitations of MSSQL in managing large-scale data and provide insights for its application in industrial environments.

One of MSSQL's key strengths is its advanced indexing capabilities, particularly the use of non-clustered indexes on fields such as DATE and TAGID. These indexes significantly reduce data access times, enhancing query performance. This feature is especially beneficial for managing frequent queries on large datasets. The flexibility of MSSQL in performance optimization, such as the WITH(NOLOCK) query hint, further improves efficiency by minimizing locking during query execution. This makes MSSQL a valuable tool for large-scale data processing.

MSSQL also excels in data security and integrity, offering robust tools for auditing, error management, and security. These features ensure consistent and reliable data storage, minimizing the risks of data loss or corruption. Its scalability allows MSSQL to grow with increasing data volumes, supporting long-term data management strategies in expanding industrial environments. This scalability is particularly relevant for real-time data collection systems, such as those used in production lines, where large amounts of sensor data are generated continuously.

However, the study identifies several limitations of MSSQL. The high licensing costs of its advanced features pose a financial challenge, especially for small and medium-sized enterprises (SMEs). These costs can make it difficult for organizations with limited budgets to adopt MSSQL for large-scale applications. Additionally, as databases increase in size and complexity, MSSQL may experience performance degradation, requiring regular maintenance and optimization. Index fragmentation is a common issue that requires frequent monitoring. Fragmented indexes must be reorganized or rebuilt based on their fragmentation levels to maintain optimal query performance.

Another limitation is MSSQL's restricted support for distributed data management [24]. In scenarios requiring the management of large datasets across multiple

geographic locations or systems, MSSQL's limited capabilities in distributed databases and clustering solutions can hinder its effectiveness. Alternative platforms, such as cloud-based or open-source solutions, may offer more suitable options for such use cases. Exploring these alternatives could reveal opportunities for improving scalability and flexibility in distributed environments.

Normalization, while improving data integrity and reducing redundancy, presents its own challenges. It can introduce additional complexity and computational overhead during query execution, particularly in environments requiring real-time data access. These trade-offs, such as increased response times for complex queries or challenges in maintaining normalized forms during rapid data updates, should be acknowledged. A deeper understanding of these trade-offs could guide the development of hybrid approaches that balance normalization and denormalization to achieve optimal performance.

The findings of this study are not limited to the cable manufacturing sector but are applicable to other industries with similar production processes. In sectors such as healthcare, logistics, and finance, where real-time data collection and processing are critical, MSSQL's optimization techniques can be adapted to meet specific operational needs. Key factors such as the volume of data collected, the number of tags (TAGs) used, and data collection intervals play a crucial role in determining the success of database management strategies. Further exploration of these industries could help generalize the findings and provide industry-specific recommendations.

With the increasing adoption of machine learning and advanced analytics, MSSQL's role in supporting these technologies is becoming increasingly important. Predictive modeling and analytics require clean, consistent, and enriched datasets. MSSQL's compatibility with programming languages such as R and Python enables seamless integration of machine learning models directly into the database environment. Future research should explore how MSSQL can be optimized to streamline data preparation and enhance its support for advanced analytics workflows.

Dynamic optimization techniques that adapt to workload changes in real time could further enhance MSSQL's performance. For example, machine learning algorithms could be employed to monitor query execution patterns and dynamically optimize indexes, queries, and data structures. These approaches could improve resource management and ensure consistent performance, even in high-demand environments.

Finally, MSSQL's potential in federated learning scenarios should be explored. Federated learning allows for distributed data management while maintaining data privacy, making it a suitable option for industries where data security is critical. Additionally, MSSQL's integration with visualization tools like Power BI and Tableau offers significant potential for enhancing reporting and decision-making processes.

This study highlights the strengths of MSSQL in indexing, query optimization, and data integrity while also addressing its limitations in cost, distributed management, and normalization trade-offs. Acknowledging the overhead and complexity introduced by normalization helps present a more balanced view. The insights gained provide a foundation for future research to explore alternative platforms, hybrid optimization techniques, and advanced analytics workflows. These advancements could lead to more scalable, adaptable, and cost-effective data management solutions for modern industrial applications.

5.1 General Evaluation of Our Processes

This study aimed to optimize MSSQL performance for managing large-scale data by employing data processing and normalization techniques. By simplifying data workflows, the approach successfully reduced processing times and enhanced overall system efficiency. The SQL queries designed for this purpose utilized non-clustered indexing, which significantly decreased data access times and improved query execution speeds, particularly in scenarios involving datasets with millions of rows. Among the optimization strategies applied, normalization emerged as the most impactful. By reducing redundancy, minimizing dataset size, and retaining only essential information, normalization not only enhanced data integrity but also optimized resource utilization. This led to shorter query times and more responsive system performance. However, the normalization process introduced certain trade-offs, such as increased complexity in real-time data access and added processing overhead, which need to be carefully considered when implementing such strategies.

5.2 Recommendations for Future Work

To sustain the benefits of normalization and indexing in MSSQL, continuous monitoring and optimization are essential. Index fragmentation is a common issue that can degrade query performance over time, particularly in large and dynamic databases. Regular maintenance is necessary to rebuild fragmented indexes and ensure consistent query efficiency. Similarly, normalization, which organizes data into structured formats, must be revisited periodically to adapt to evolving datasets and changing system requirements. This approach ensures that the performance improvements achieved during initial implementation are preserved and even enhanced.

Future studies should explore the applicability of these techniques to alternative database platforms. MSSQL, while effective in managing large datasets, has certain limitations in distributed data management and clustering environments. Research into open-source systems such as PostgreSQL or cloud-based solutions like Amazon Aurora and Google BigQuery could reveal how these platforms address similar optimization challenges. Comparative analyses would provide valuable insights into the scalability, flexibility, and cost-effectiveness of normalization and indexing across various systems. Additionally, studying hybrid approaches that balance normalization and denormalization could address some of the trade-offs identified in this study, particularly in scenarios requiring real-time data access.

As industries increasingly adopt machine learning and advanced analytics, the role of MSSQL in supporting

these technologies becomes more significant. Predictive modeling, classification, and other advanced analytics require clean, consistent, and well-managed datasets. Preparing MSSQL infrastructure to handle such workflows should be a key area of focus. Research could examine how data cleansing and enrichment processes within MSSQL can be automated to streamline data preparation for machine learning applications.

Furthermore, integrating MSSQL with programming languages like R and Python could enable the efficient implementation of machine learning models directly within the database environment. This integration offers significant potential for predictive and prescriptive analytics, especially in industries like manufacturing, healthcare, and finance.

Dynamic optimization techniques also deserve further investigation. These methods, which adapt in real time to workload changes, could improve both query performance and resource management in MSSQL. For example, machine learning-based algorithms could monitor query execution patterns and dynamically optimize indexes, queries, and data structures. These advancements would ensure that MSSQL remains efficient even in high-demand environments with fluctuating workloads.

Finally, the role of MSSQL in federated learning scenarios should be explored. As data privacy and security become increasingly critical, federated learning offers a promising approach for distributed data management without sharing sensitive data. MSSQL's ability to manage large datasets while maintaining strong privacy controls makes it a suitable candidate for such architectures. Future research could focus on optimizing MSSQL for federated learning workflows, ensuring data privacy and security while enabling efficient data handling and processing. Additionally, its integration with data visualization tools like Power BI and Tableau could enhance reporting capabilities, enabling organizations to make data-driven decisions more effectively.

In conclusion, addressing these areas in future research will not only enhance the scalability, flexibility, and efficiency of MSSQL but also ensure its continued relevance in the evolving landscape of industrial data management.

Declaration

Ethics committee approval is not required.

References

[1] Malik, P. K., Sharma, R., Singh, R., Gehlot, A., Satapathy, S. C., Alnumay, W. S., Pelusi, D., Ghosh, U., & Nayak, J. (2021). Industrial internet of things and its applications in industry 4.0: *State of the art. Computer Communications,* 166, 125–139.

[2] Ghasemaghaei, M. (2021). Understanding the impact of big data on firm performance: The necessity of conceptually differentiating among big data characteristics. *International Journal of Information Management,* 57, 102055

[3] Fan, C., Yan, D., Xiao, F., Li, A., An, J., & Kang, X. (2021). Advanced data analytics for enhancing building performances: From data-driven to big data-driven approaches. *Building Simulation,* 14(1), 3–24.

[4] Naeem, M., Jamal, T., Diaz-Martinez, J., Butt, S. A., Montesano, N., Tariq, M. I., De-la Hoz-Franco, E., & De-La-Hoz-Valdiris, E. (2022). Trends and future perspective challenges in big data. *In Advances in Intelligent Data Analysis and Applications* (pp. 309–325). Springer.

[5] Ranjan, J., & Foropon, C. (2021). Big data analytics in building the competitive intelligence of organizations. *International Journal of Information Management,* 56, 102231.

[6] Larrea, M. L., & Urribarri, D. K. (2021). Visualization technique for comparison of time-based large data sets. *In Conference on Cloud Computing, Big Data & Emerging Topics* (pp. 179–187). Springer.

[7] Dinneen, J. D., & Brauner, C. (2017). Information-not-thing: Further problems with and alternatives to the belief that information is physical.

[8] Vaitis, M., Feidas, H., Symeonidis, P., Kopsachilis, V., Dalaperas, D., Koukourouvli, N., Simos, D., & Taskaris, S. (2019). Development of a spatial database and web-GIS for the climate of Greece. *Earth Science Informatics*, 12(1), 97–115.

[9] Amin, M., Romney, G. W., Dey, P., & Sinha, B. (2019). Teaching relational database normalization in an innovative way. *Journal of Computing Sciences in Colleges*, 35(2), 48–56.

[10] Alqithami, S. (2021). A serious-gamification blueprint towards a normalized attention. *Brain Informatics*, 8(1), 1–13.

[11] Oditis, I., Bicevska, Z., Bicevskis, J., & Karnitis, G. (2018). Implementation of NoSQL-based data warehouse. *Baltic Journal of Modern Computing*, 6(1), 45–55.

[12] Hrubaru, I., Talabă, G., & Fotache, M. (2019). A basic testbed for JSON data processing in SQL data servers. *In Proceedings of the 20th International Conference on Computer Systems and Technologies* (pp. 278–283).

[13] Chung, Y. G., Haldoupis, E., Bucior, B. J., Haranczyk, M., Lee, S., Zhang, H., Vogiatzis, K. D., Milisavljevic, M., Ling, S., Camp, J. S., et al. (2019). Advances, updates, and analytics for the computation-ready, experimental metal–organic framework database: Core MOF 2019. *Journal of Chemical & Engineering Data,* 64(12), 5985–5998.

[14] Bouros, P., & Mamoulis, N. (2019). Spatial joins: What's next? *SIGSPATIAL Special*, 11(1), 13–21.

[15] Myalapalli, V. K., Totakura, T. P., & Geloth, S. (2015). Augmenting database performance via SQL tuning. *In 2015 International Conference on Energy Systems and Applications* (pp. 13–18). IEEE.

[16] Pedrozo, W. G., & Vaz, M. S. M. G. (2014). A tool for automatic index selection in database management systems. *In 2014 International Symposium on Computer, Consumer and Control* (pp. 1061–1064). IEEE.

[17] Correia, J., Santos, M. Y., Costa, C., & Andrade, C. (2018). Fast online analytical processing for big data warehousing. *In 2018 International Conference on Intelligent Systems* (IS) (pp. 435–442). IEEE.

[18] Sulistiani, H., Setiawansyah, S., & Darwis, D. (2020). Penerapan metode agile untuk pengembangan online analytical processing (OLAP) pada data penjualan (Studi kasus: CV Adilia Lestari). *Jurnal CoreIT: Jurnal Hasil Penelitian Ilmu Komputer dan Teknologi Informasi,* 6(1), 50–56.

[19] Erdinç, H. N., Buluş, N., & Erdoğan, C. (2018). Veritabanı tasarımının yazılım performansına etkisi: Normalizasyona karşı denormalizasyon. *Süleyman Demirel Üniversitesi Fen Bilimleri Enstitüsü Dergisi*, 22(2), 887–895.

[20] Alshemaimri, B., Elmasri, R., Alsahfi, T., & Almotairi, M. (2021). A survey of problematic database code fragments in software systems. *Engineering Reports,* 3(10), e12441.

[21] Milicev, D. (2021). Hyper-relations: A model for denormalization of transactional relational databases. *IEEE Transactions on Knowledge and Data Engineering.*

[22] Chaparro-Cruz, I. N., & Montoya-Zegarra, J. A. (2021). Borde: Boundary and sub-region denormalization for semantic brain image synthesis. *In 2021 34th SIBGRAPI Conference on Graphics, Patterns and Images (SIBGRAPI)* (pp. 81–88). IEEE.

[23] Costa, R. L. D. C., Moreira, J., Pintor, P., dos Santos, V., & Lifschitz, S. (2021). A survey on data-driven performance tuning for big data analytics platforms. *Big Data Research,* 25, 100206.

[24] Chillón, A. H., Ruiz, D. S., & Molina, J. G. (2021). Towards a taxonomy of schema changes for NoSQL databases: The Orion language. *In International Conference on Conceptual Modeling* (pp. 176–185). Springer.

[25] Gupta, E., Sural, S., Vaidya, J., & Atluri, V. (2021). Attribute-based access control for NoSQL databases. *In Proceedings of the Eleventh ACM Conference on Data and Application Security and Privacy* (pp. 317–319).

[26] Santos, M. Y., Costa, C., Galvão, J., Andrade, C., Martinho, B. A., Lima, F. V., & Costa, E. (2017, July). Evaluating SQL-on-Hadoop for big data warehousing on not-so-good hardware. *In Proceedings of the 21st International Database Engineering & Applications Symposium* (pp. 242-252).

[27] Yang, F., Tschetter, E., Léauté, X., Ray, N., Merlino, G., & Ganguli, D. (2014, June). Druid: A real-time analytical data store. *In Proceedings of the 2014 ACM SIGMOD international conference on Management of data* (pp. 157-168).

[28] Silva, Y. N., Almeida, I., & Queiroz, M. (2016, February). SQL: From traditional databases to big data. *In Proceedings of the 47th ACM Technical Symposium on Computing Science Education* (pp. 413-418).

[29] Rahman, M. M., Islam, S., Kamruzzaman, M., & Joy, Z. H. (2024). Advanced Query Optimization in SQL Databases For Real-Time Big Data Analytics. *Academic Journal on Business Administration, Innovation & Sustainability*, 4(3), 1-14.

[30] Uzzaman, A., Jim, M. M. I., Nishat, N., & Nahar, J. (2024). Optimizing SQL databases for big data workloads: techniques and best practices. *Academic Journal on Business Administration, Innovation & Sustainability*, 4(3), 15-29.

[31] Pirzadeh, P., Carey, M., & Westmann, T. (2017, December). A performance study of big data analytics platforms. *In 2017 IEEE international conference on big data* (big data) (pp. 2911-2920). IEEE.

[32] Panwar, V. (2024). Optimizing Big Data Processing in SQL Server through Advanced Utilization of Stored Procedures. *Journal Homepage: http://www. ijmra. us,* 14(02).

[33] Ordonez, C. (2013, October). Can we analyze big data inside a DBMS?. *In Proceedings of the sixteenth international workshop on Data warehousing and OLAP* (pp. 85-92)

.

International Journal of Innovative Engineering Applications

Journal homepage: https://dergipark.org.tr/ijiea

ALTITUDE CONTROL OF QUADROTOR BASED ON METAHEURISTIC METHODS

***Muhammed Kivanc Kurnaz*[1], *Yagmur Olmez*[2], *Gonca Ozmen Koca*[*1]**

[1]*Fırat University, Faculty of Technology, Department of Mechatronics Engineering, Elazig, 23200, Turkiye*
[2]*Malatya Turgut Ozal University, Faculty of Engineering and Natural Sciences, Department of Electrical and Electronics Engineering, Malatya, 44210, Turkiye*

Abstract

Original scientific paper

Quadrotor, which is used in many fields and is still a challenge to control, has a complex kinematic and dynamic system, and its flight performance depends on many variables that need to be controlled simultaneously. In this study, the effective determination of PID parameters for altitude control of quadrotors, which presents a complex control problem, has been tested comparatively with innovative metaheuristic approaches. Among the strong metaheuristic algorithms, the Crow Search Algorithm (CSA), Particle Swarm Optimization Algorithm (PSO), Golden Jackal Optimization Algorithm (GJO), and Jellyfish Search Algorithm (JSA) were comparatively analyzed for the determination of PID parameters. The parameters obtained with CSA caused the minimum steady-state error with the value of 6.9580e-04 in the closed-loop control system. A minimum overshoot was also obtained with the parameters optimized with CSA. When these results are evaluated, it can be said that CSA performs better than other altitude control algorithms, considering the quadrotor's stable and accurate positioning performance.

Keywords: *Crow search algorithm; golden jackal optimization algorithm; jellyfish search algorithm; parameter optimization; particle swarm optimization algorithm; quadrotor.*

1 Introduction

An unmanned aerial vehicle (UAV) is a motorized aircraft that can adjust its speed and direction through sensors and software methods without needing a pilot. With the development of technology, UAVs have begun to be used in areas that may pose a threat to human health, especially in military defense and operations, and in search and rescue activities during and after natural disasters.

UAVs can be classified into two main groups. These are fixed-wing and rotatıng wing UAVs. The main advantages of fixed-wing UAVs are that they are more aerodynamically efficient, can stay in the air for a long time, have a longer flight distance, and are easier to control compared to other similar aircraft. But today, the trend towards rotary-wing unmanned aerial vehicles has increased due to changing technological conditions, costs, difficult terrain conditions, and the need for fixed-wing unmanned aerial vehicles to have runways or launch systems for takeoff and landing. Another great advantage of rotary-wing unmanned aerial vehicles is that they provide the opportunity to rise from the ground. In other words, it includes vertical take-off and take-off (VTOL) features [1].

Systems with highly complicated kinematics and dynamics, such as quadrotors, are difficult to control. One of the traditional control methods, PID control, is used very often. There are various ways in which PID control parameters can be tuned. Ziegler-Nichols (ZN) and tuning methods can be easily applied [2]. However, these methods are time-consuming. Because many trials are required to determine the space where the system is stable and therefore it is difficult to provide movements of the quadrotor in the desired direction. In experimental studies, this uncertainty may cause damages and losses. Recently, metaheuristic methods have been progressively applied to find the optimum value of PID parameters [3]. Metaheuristic optimization methods are applied to problems with large solution spaces in engineering fields by studying the animals' behavior that move in flocks to meet their needs such as food and shelter. In this field, many algorithms such as Ant Colony Optimization (ACO based on the movements of ants to find food, and Particle Swarm Optimization (PSO) algorithms inspired by the movements of birds in flocks, can be given as examples [4]. It has been shown in previous studies that these metaheuristic algorithms give more efficient results in controlling the quadrotor than traditional methods.

In this study, the Crow Search Algorithm (CSA), Particle Swarm Optimization Algorithm (PSO), Golden Jackal Optimization Algorithm (GJO), and Jellyfish Search Algorithm (JSA), which are metaheuristic algorithms, are compared. The algorithms used in this study aim to analyze the performance of the proposed control framework by minimizing the error and determining the best parameter values in the solution space without sticking to the local optimum in the altitude control of the quadrotor.

*Corresponding author.
E-mail address: gonca.ozmen@gmail.com (G. Ozmen)
Received 14 October 2024; Received in revised form 06 February 2025; Accepted 24 February 2025
 Doi: https://doi.org/10.46460/ijiea.1564844

The organization of the paper can be introduced as follows: Section 2 represents the dynamic model of the PMD. Section 3 describes the CSA, PSO, GJO, and JSA algorithms for height control of the quadrotor. Experimental analysis is introduced in Section 4. Finally, Section 5 presents the conclusion of the analysis.

1.1 Related Works

Kapnopoulos et al. achieved attitude and position control of a quadrotor based on PID and Model Predictive Control (MPC) methods. Cooperative Particle Swarm Optimization (PSO) was used to determine the parameters of the control methods. In PSO, they used two different swarms for position control and attitude control. Two swarms work cooperatively to explore the search space more efficiently. By performing simulation studies on different trajectories, they compared the cooperative PSO algorithm with GA and standard PSO and showed that their method was better [5]. Hermouche et al. controlled a quadrotor with PID in their study. They used and compared meta-heuristic algorithms as; GOA, GWO, PSO, WOA, ALO, HHO, and SSA to determine PID parameters. Using four different objective functions, they obtained minimum error with SAE and STAE, minimum overshoot with WOA_STA, fastest optimization with SAE and STA, and best altitude with DA_SAE [6]. Sahrir et al. used PSO-based PID control for altitude and attitude stabilization of a quadcopter. They evaluated PSO roll, pitch, and yaw performance utilizing IAE, ISE, ITAE, and ITSE cost functions. Among these cost functions, ITSE gave a superior result in tracking. They also compared ZN-PID and PSO-PID in the presence of wind as a disturbance input and observed that PSO-PID gives better results during roll motion [7]. Belge et al. obtained a hybrid algorithm with Harris Hawk Optimization (HHO)-Grey Wolf Optimization (GWO), which is one of the metaheuristic algorithms for payload hold and release in unmanned aerial vehicles in their study. They compared HHO-GWO with PSO optimization by performing path planning. They examined the effect of changing mass on the system [8]. Gün first obtained the parameters of the PID control method by Ziegler Nicholes and the trying-error method to minimize the energy consumption of the quadrotor in his study, Then, he trained the coefficients using PSO, differential evolutionary algorithm (DE), gravity search algorithm (GSA), charged system search (CSS) algorithm. As a result of the comparison, he observed that DE-PID consumes less energy of the quadrotor compared to other algorithms [9]. Alqudsi et al. used the trajectory generation and optimization algorithm (TGO) to create an unobstructed trajectory over predetermined points. With this algorithm, they aimed to reach the waypoints on the quadrotor's trajectory in minimum time and create new trajectories. The proposed algorithm is compared with constrained quadratic programming (CQP) and unconstrained quadratic programming (UQP) [10]. Meraihi et al. conducted extensive research on the Crow Search algorithm by compiling the work developed on it and combined with different algorithms. They identified several engineering applications for CSA [11]. Sheta et al. used the PID control method to ensure the desired orientation and position of the quadrotor. They used meta-heuristic algorithms PSO, CSA, GA, and the traditional ZN method to determine the PID parameters. They evaluated the results in terms of performance criteria using a multi-objective fitness function. Among the algorithms used, they observed that the parameters obtained with PSO showed the best performance in motion control of the quadrotor [3]. Farzaneh et al. obtained a dynamic model of a quadrotor. They used a neural network as the main control method for the quadrotor system. They conducted simulation and experimental studies to test the performance of the system. The performance of the neural network model is superior to the PID model of the quadrotor [12]
.

Table 1. Summary of recent studies based on control structures developed for quadrotor control.

Authors	Method	Aim	Experimental/ Simulation	Obtained Results	Tuning Method
Sheta et al [3]	PID	Position control	Simulation	PSO-optimized parameters yield impressive control results in quadcopter control, surpassing those of GA and CSA.	PSO, GA, CSA
Kapnopoulos et al. [5]	MPC, PID	Attitude & Position control	Simulation	Trajectory tracking was successfully achieved with MPC and PID.	PSO
Hermouche et al. [6]	PID	Altitude control	Simulation	A PID model with metaheuristics for four objectives was comparatively investigated on the quadrotor.	DA, GOA, WOA, GWO, PSO, ALO, HHO, SSA
Sahrir et al. [7]	PID	Altitude & Position control	Simulation	Altitude and attitude stabilization of a quadrotor is achieved with the PID controller, whose parameters are optimized with PSO.	PSO
Belge et al. [8]	PID	Path planning	Simulation	A fast and safe path planning is provided with HHO and GWO methods.	HHO, GWO
Gün [9]	PID	Attitude control	Simulation	The PID control parameters have the best results optimized with DE	DE, PSO, GSA, CSS
Alqudsi et al. [10]	-	Trajectory tracking	Simulation	A new trajectory producer with an optimizer is created to produce adaptable and collision-free routes.	TGO
Farzaneh et al [12]	NN, PID	Attitude & Position control	Simulation/ Experimental	Optimal Neural Network Controller has an effective performance for the Stabilization of a Quadrotor.	Enumerative Optimization
Proposed study	PID	Altitude control	Simulation	A successful control method has been developed for quadrotors using a CSA-based PID, achieving a minimum steady-state error of 6.9580e-04.	CSA, PSO, GJO, and JSA

1.2 Literature Gaps

Although the quadrotor is a complex kinematic and dynamic system with six degrees of freedom (6-DOF), it is controlled by changing the speed of four rotors, i.e. propellers. The flight performance of the quadrotor depends on many variables, and many variables need to be controlled simultaneously. This makes it difficult to control such a complex system. Generally, classical

control methods or modern control algorithms are used to control a quadrotor. Classical control methods are not sufficient for the targeted performance of such a complex system, and since these variables are directly effective in the movement of the aircraft, the parameters must be selected most appropriately. By using an efficient optimization method, suitable parameters can be found much more efficiently and in a short time interval in large search spaces. On the other hand, modern optimization methods may also be insufficient because of model uncertainties. In these cases, more effective results are obtained by using hybrid algorithms for such unstable systems. Thus, the performance of the quadrotor can be improved, energy efficiency can be achieved, and more precise control can be achieved.

1.3 Literature Gaps Motivation and Proposed Method

Our motivation is to realize the altitude control of the quadrotor based on meta-heuristics, which are widely used in the control of unmanned aerial vehicles. Firstly, the dynamic model of the quadrotor, which is a nonlinear system, is obtained. While obtaining the mathematical model, it is taken into account that the PMD has a diagonal structure, and the z-axis is downward based on the right-hand rule starting from the center of gravity of the quadrotor. Secondly, the PID control method was used for the height control of the quadrotor. While calculating the PID control parameters, 4 different metaheuristic algorithms were used to provide more efficient results and more stable movement of the system.

To evaluate the proposed algorithms, the performance criteria of the system such as maximum overshoot, rise time, and settling time are tested and compared. In this paper, 4 different algorithms are used for tuning the parameters of the PID for the height control of a nonlinear quadrotor with a complex structure.

2 Modelling Of Parot Mambo Drone

In this section, the mathematical modeling of the quadrotor, the reference coordinate systems to be used in the model, and the kinematic and dynamic model according to the Newton-Euler motion equations are defined by accepting some assumptions. According to the Newton-Euler motion equations, the kinematic and dynamic model is defined by accepting some assumptions below.

- The propellers and structure of the drone are rigid.
- It has a symmetrical structure.
- The thrust and drag forces continue with the square of the propeller velocity.
- The center of gravity comes across with the beginning of the body frames.
- Four propellers operate under the same conditions. The amount of thrust (b) and the amount of torque (d) are the same for all.

To obtain the mathematical model of the quadrotor, the kinematic and dynamic equations of the vehicle must be found. To obtain equations, coordinate systems must also be determined. These are the body coordinate system x_b, y_b, z_b, and the fixed location coordinate system x_e, y_e, z_e. The specified axis sets are shown on the drone in Fig. 1.

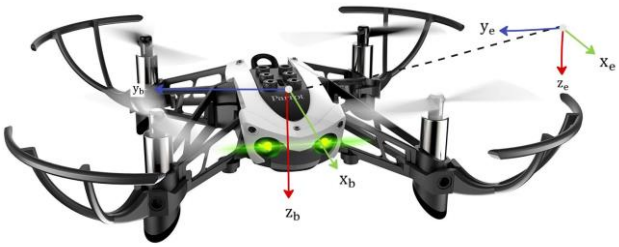

Figure 1. Parrot Mambo Drone and its coordinate system

The quadrotors, schematically shown in Figure 2, are available for two different configurations: x (cross) and + (plus). The vehicle in the plus (+) configuration has a more acrobatic configuration, while the vehicle in the x (cross) configuration is more stable. The plus (+) vehicle uses two rotors to move in the x and y directions, while the cross (x) vehicle uses four rotors. For example, in the 'cross' quadrotor, the speed of rotors 1 and 2 (3 and 4) increases (decreases) at the same time throughout the pitch action. The quadrotor used in this study has a cross (x) configuration. The direction of the rotations is clockwise for the 1st and 3rd rotors and counterclockwise for the 2nd and 4th rotors.

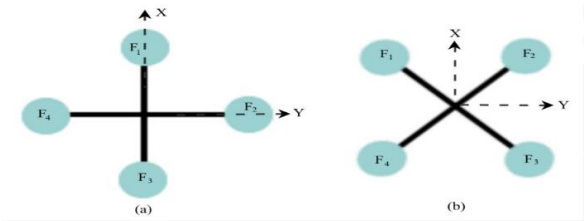

Figure 2 a 'Plus' configuration **b** 'Cross' configuration

If the relationship between two coordinate systems is expressed as r_e in the E frame, and r_b in the B frame, Equation 1 emerges.

$$r_e = R^{(E,B)} r_b \tag{1}$$

where, $R^{(E,B)}$ is the transformation matrix. Equation 2.1 expresses the conversion from B to E coordinate system. A certain order is followed to perform these transformations. First, the transformation should be made with the help of the z-axis yaw (ψ) angle, then with the help of the y-axis pitch (θ) angle, and then with the help of the x-axis roll (φ) angle. As a result of the transformation, Equation 2 emerges.

$$R = \begin{bmatrix} \cos\psi\cos\theta & -\sin\psi\cos\phi + \cos\psi\sin\theta\sin\phi & \cos\psi\sin\theta\cos\phi + \sin\psi\sin\phi \\ \sin\psi\cos\theta & \sin\psi\sin\theta\sin\phi + \cos\psi\cos\phi & \sin\psi\sin\theta\cos\phi - \sin\phi\cos\psi \\ -\sin\theta & \cos\theta\sin\phi & \cos\theta\cos\phi \end{bmatrix} \tag{2}$$

Euler angles; roll (ϕ), pitch (θ), and yaw (ψ) compose the orientation of the quadrotor. If a rigid body is not in motion, that is, it is stationary, its inertia is its mass but if it is in motion, its moment of inertia arises against the change in rotation movements around itself. The angular moment acting on the body coordinate system is obtained by Eq. 3.

$$M_B = J\dot{\omega} + \omega x J\omega \tag{3}$$

Where J is the diagonal inertia matrix of the drone, ω is the angular speed vector, and M_B is the moment affecting the body axis assembly. If the moment M_B acting on the body axis set is denoted by L, M, N and the rotation moment on the x_b, y_b, and z_b axes, respectively.

$$M_B = \begin{bmatrix} L \\ M \\ N \end{bmatrix} = \begin{bmatrix} I_{xx} & 0 & 0 \\ 0 & I_{yy} & 0 \\ 0 & 0 & I_{zz} \end{bmatrix} \begin{bmatrix} \dot{p} \\ \dot{q} \\ \dot{r} \end{bmatrix} + \begin{bmatrix} p \\ q \\ r \end{bmatrix} x \begin{bmatrix} I_{xx} & 0 & 0 \\ 0 & I_{yy} & 0 \\ 0 & 0 & I_{zz} \end{bmatrix} \begin{bmatrix} p \\ q \\ r \end{bmatrix} \tag{4}$$

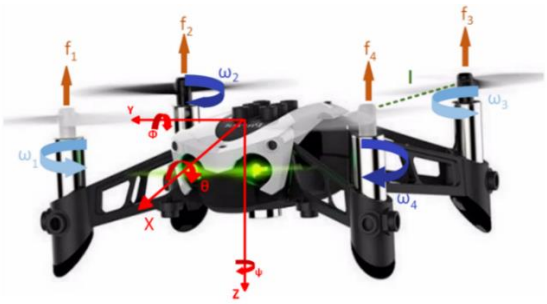

Figure 3. Rotor rotation directions and distances on the quadrotor.

If the moment on the x_b axis is obtained concerning the gravity center of the quadrotor, the moment on the y_b axis is acquired concerning the gravity center of the drone. The moment on the z_b axis is calculated from the rotor torque, the following equations are obtained.

$$\begin{aligned} L_{(roll)} &= l(b\Omega_2^2 - b\Omega_4^2) \\ M_{(pitch)} &= l(b\Omega_3^2 - b\Omega_1^2) \\ N_{(yaw)} &= d(\Omega_1^2 + \Omega_3^2 - \Omega_2^2 - \Omega_4^2) \end{aligned} \tag{5}$$

Here, Ω is the angular speed of the rotor, b is the aerodynamic force constant, l is the distance between the center of mass and the rotors, and d is the aerodynamic moment constant. Based on Equations 4 and 5, the translation and rotation equations are obtained as follows.

$$\begin{aligned} \ddot{\phi} &= \frac{(I_{yy} - I_{zz})}{I_{xx}} \dot{\psi}\dot{\theta} - \frac{J_r}{I_{xx}}(\Omega_r)\dot{\theta} + \frac{l}{I_{xx}} U_2 \\ \ddot{\theta} &= \frac{(I_{zz} - I_{xx})}{I_{yy}} \dot{\psi}\dot{\phi} + \frac{J_r}{I_{yy}}(\Omega_r)\dot{\phi} + \frac{l}{I_{yy}} U_3 \\ \ddot{\psi} &= \frac{(I_{xx} - I_{yy})}{I_{zz}} \dot{\theta}\dot{\phi} + \frac{l}{I_{zz}} U_4 \end{aligned} \tag{6}$$

Each rotor speed is obtained by Equation 6.

$$\begin{bmatrix} U_1 \\ U_2 \\ U_3 \\ U_4 \end{bmatrix} = \begin{bmatrix} b & b & b & b \\ 0 & bl & 0 & -bl \\ -bl & 0 & bl & 0 \\ d & -d & d & -d \end{bmatrix} \begin{bmatrix} \Omega_1^2 \\ \Omega_2^2 \\ \Omega_3^2 \\ \Omega_4^2 \end{bmatrix} \tag{8}$$

3 Control of Parrot Mambo DRONE

PID (Proportional-Integral-Derivate) control is a widely used control method for the control of aircraft. PID provides the appropriate control signal (u(t)) for a closed-loop control system by passing the error through proportional, integral, and derivative components.

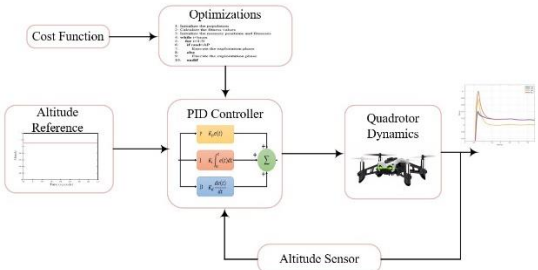

Figure 4. Altitude control of the quadrotor with optimal PID-tuned algorithms.

The control signal of the PID is given as Eq. (9).

$$u(t) = K_p e_z + K_i \int e_z dt + K_d \frac{de_z}{dt} \tag{9}$$

where u(t) is the control output signal. k_p, k_i, and k_d are proportional, integral, and derivative gains, respectively. e(t) is a closed-loop error.

PID control is highly preferred in linear systems as well as in nonlinear systems [13]. This method can be adapted to many systems and is a control method used in industrial applications and automatic control applications since it contains fewer variables compared to other methods. There are many methods to determine PID control parameters. They can be adjusted by using various methods such as trial and error, Ziegler-Nichols, Cohen-Coon, or metaheuristic optimization algorithms.

3.1 Crow Search Algorithm

The crow search algorithm was created by modeling some intelligent behaviors of crows. It was presented by Azkarzadeh in 2016 as a nature-inspired method [14]. Unlike other birds, crows can remember where they hide their food and can obtain more food by following other crows. In this algorithm, crows have two different movement strategies. These are: (1) protecting the location of their food and (2) learning where other crows hide their food. Based on this scenario, the motion equations of crows are created as given in Eqs. (10) - (11). At the t^{th} iteration, j-th crow is required to go to its hiding position and i-th crow agrees to follow j-crow. In the first scenario, if j^{th} crow is not hip to that the i^{th} crow is following him then i-th crow changes its position according to Eq. (10).

$$x_i(t+1) = x_i(t) + rand_i \; x \; fl_i(t) \; x \; (m_j(t) - x_i(t+1)) \tag{10}$$

where x_i denotes the position of i-th crow. fl and m_j represent the flight length and the hiding place of the j-th crow. In the second scenario, j-th crow is aware that i-th crow is following it and updates the next positions by using the following equation:

$$x_i(t+1) = lb + rand * (ub - lb) \quad (11)$$

Algorithm 1. Pseudo code of the Crow Search Algorithm

1. Define fl, AP, N, d, and maxIt.
2. Initialize X and Mem
3. Calculate fitness values of the crows
4. Determine the best and worst ones
5. **while** t < maxIter
    a. **for** i=1:N
        i. Select j-th crow, randomly.
        ii. **if** rand < AP
            1. Generate Xnew with Eq. (10)
        iii. Else
            1. Generate Xnew with Eq. (11)
        iv. Endif
        v. Calculate fitness value of Xnew as f(Xnew)
        vi. if f(Xnew(i)) < f(X(i))
            1. Update X(i) with Xnew(i)
        vii. Endif
    b. Endfor
6. **Endwhile**

** X: Initial population, fl: flight length, AP: awareness probability, N: number of the crows, d: dimension, maxIt: maximum number of the iteration, Mem: crows' memories set, Xnew: new solution.

3.2 Particle Swarm Optimization Algorithm

Particle Swarm Optimization is one of the oldest and most widely used optimization methods. Kennedy developed the algorithm by modeling the animals' behaviors in the flock [15]. In PSO, the positions of the particles are updated based on global and local optimal solutions. The following equations are presented for the updating of the particles' velocities and positions:

$$velocity(t+1) = velocity(t) + r_1\ x\ c_1\ x(p_{best} - x(t)) + r_2\ x\ c_2\ x\ (g_{best} - x(t)) \quad (12)$$

$$x_i(t+1) = x_i(t) + velocity(t+1) \quad (13)$$

where, $velocity$ and x represent velocities and the positions of the particles, respectively. c_1 and c_2 denote the acceleration parameters. P_{best} and g_{best} are the local best and global best solutions in the particles' population. r_1 and r_2 show two random values. The pseudo-code of the PSO is presented in Algorithm 2.

Algorithm 2. Pseudo code of the Particle Swarm Optimization

1. Define v and x
2. Initialize N, d, and maxIt
3. Calculate the fitness values of the particles
4. Assign x as p_{best}
5. Determine g_{best}
6. **while** t < maxIter
    a. Update x and v of the particles with Eq. (12-13)
    b. Calculate fitness values of the particles
    c. **for** i=1:N
        i. if f(Xnew(i)) < f(p_{best}(i))
            1. Update p_{best}(i)
        ii. Endif
    d. Endfor
    e. Determine g_{best}
7. **Endwhile**

** v: velocities of the particles, x: positions of the particles, N: number of the crows, d: dimension, maxIt: maximum number of the iteration, P_{best}: local best solution, and g_{best}: global best solution.

3.3 Golden Jackal Optimization Algorithm

Golden Jackal Optimization is presented by Chopra and Ansari in 2022 [16]. A newly introduced nature-inspired metaheuristic algorithm is developed by modeling the habits of the jackals during hunting. The exploration phase is the searching for the prey stage and it is led by the male jackal. The male jackal finds the prey and the female jackal follows him. In this stage, positions of the male and female jackals are obtained by using Eqs. (14-15).

$$x_m(t+1) = x_m(t) - E.|x_m(t) - rl.p(t)| \quad (14)$$

$$x_{fm}(t+1) = x_f(t) - E.\left|x_f(t) - rl.p(t)\right| \quad (15)$$

The positions of the preys are updated by using the following function (Eq. (16)):

$$p(t+1) = \frac{x_m(t+1) + x_{fm}(t+1)}{2} \quad (16)$$

In the exploitation phase, the jackals harass the prey and decrease their evading energy of them. The prey with decreased energy is surrounded and is easily hunted by the jackals. The behavior of the jackals is modeled by the following equations:

$$x_m(t+1) = x_m(t) - E.|rl.x_m(t) - p(t)| \quad (17)$$

$$x_{fm}(t+1) = x_f(t) - E.\left|rl.x_f(t) - p(t)\right| \quad (18)$$

Where rl represents a vector based on the Levy function. The evading energy of the prey is calculated as: $E = E_0 + E_1$. Where, E_0 and E_1 represent the initial and the decreasing energy of the prey, respectively. The initial and the decreasing energy is calculated as: $E_0 = 2\ x\ r - 1$ and $E_1 = c\ x\ (1 - it/maxIt)$. Where, r and c denote the random and a constant number, respectively.

Algorithm 3. Pseudo code of the Golden Jackal Optimization Algorithm

1. Define N, d, maxIt
2. Initialize P
3. **while** t < maxIter
   a. Calculate fitness values of the preys
   b. Assign the best and the second best preys as X_m and X_{fm}
   c. **for** i=1:N
      i. Update E
      ii. Update rl
      iii. **if** E < 1
         1. Update X with Eq. (17)
      iv. **Else**
         1. Update X with Eq. (18)
      v. **endif**
      vi. Calculate fitness values of the X population
   d. **endfor**
4. **endwhile**

** P: Prey population, X_1: Male jackal's position, X_1: Female jackal's position, E: Evading energy, rl: Vector based on Levy movement function,

3.4 Jellyfish Search Algorithm

The Jellyfish Search Algorithm (JSA) is one of the population-based methods which is introduced by Chou and Truong in 2021 [17]. The method is created by modeling the behavior of the jellyfish population. JSA consists of two stages: exploitation and exploration. In the exploration stage, the jellyfish society follows the ocean current to find plenty of nutrients. This movement is realized by using Eq. (19):

$$x_i(t+1) = x_i(t) + r_1 \; x \; ocr \tag{19}$$

$$ocr = x^* - df \tag{20}$$

$$df = \beta \; x \; r_2 \; x \; \mu \tag{21}$$

Where ocr represents the ocean current. r_1 and r_2 are the random values in the range of (0, 1). β and μ denote the distribution coefficient and the mean of the jellyfish population, respectively. In the exploitation stage, the jellyfish search the space by using two different movement strategies, which are called passive (Type A) and active (Type B) movement strategies. In the Type A, the jellyfish move around their positions. The equation of the Type A is realized with the following equation:

$$x_i(t+1) = x_i(t) + \Upsilon \; x \; r_3 \; x \; (ub - lb) \tag{22}$$

Where, ub and lb are upper and lower bounds, respectively. Υ is a motion constant and must be bigger than zero. r_3 is a random value. While forming jellyfish blooms, they aim to move to places where there is plenty of food. This motion is realized in Type B motion strategy and it is modeled mathematically as given in Eq. (23).

$$x_i(t+1) = x_i(t) + Step \tag{23}$$

$$step = r \; x \; D \tag{24}$$

$$D = \begin{cases} x_i - x_j & if \; f(x_i) \geq f(x_j) \\ x_j - x_i & if \; f(x_i) < f(x_j) \end{cases} \tag{25}$$

Where, D and Step represent the direction vector and the length of the motion, respectively. In this algorithm, a time control strategy is used to select the motion type. Eq. (26) introduces the time control strategy:

$$c = 2 \; x \; r \; x \left(1 - \frac{t}{T}\right) - 1 \tag{26}$$

Where t and T are current and the maximum number of the iterations. C is the time control function.

Algorithm 4. Pseudo code of the Jellyfish Search Algorithm

1. Define N, d, and maxIt
2. Initialize X
3. Calculate the fitness values of the
4. **while** t < maxIter
   a. Determine X^*
   b. **for** i=1:N
      i. Calculate c(t) with Eq. (26)
      ii. **if** c(t) ≥ 0.5
         1. Calculate ocr with Eq. (20)
         2. Update X with Eq. (18)
      iii. **Else**
         1. if rand < c(t)
            a. Update X with Eq. (22)
         2. Else
            a. Update X with Eq. (23)
         3. Endif
      iv. **Endif**
      v. Calculate fitness values of the X population
   c. **Endfor**
5. **Endwhile**

X: Jellyfish population, X^*: Best jellyfish, c(t): Time control parameter, ocr: ocean current function

4 Experimental Studies and Results

In this section, the results of parameter tuning with CSA, PSO, GJO, and JSA algorithms for altitude control of the quadrotor using PID control and various analyses calculated as a result of these algorithms are presented. The quadrotor used in this study is the Mambo Mini Drone (PMD) produced by Parrot. There are 4 sensors on the quadrotor. These are the inertial measurement unit (IMU), pressure sensor, ultrasonic sensor, and camera.

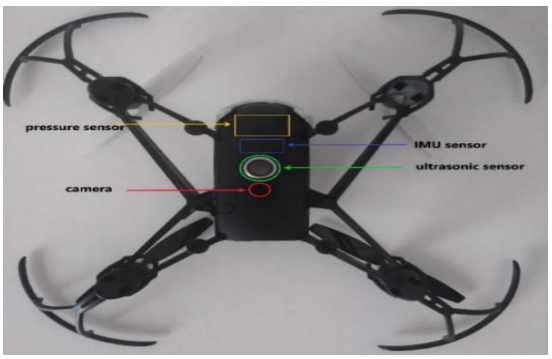

Figure 5. Illustration of sensors on the quadrotor [18].

Table 2 presents the physical parameters of the PMD. These parameters were used to create the mathematical model and control model of the quadrotor.

Table 2. Physical parameters of Parrot Mambo Drone.

Description	Parameter	Unit	Value
Mass	m	kg	0.063
Length of an arm	l	m	0.0624
Drag coefficient	d	Nms^2	78.26e-5
Thrust coefficient	b	Ns^2	0.0107
Inertia Moment along x-axis	l_{xx}	kgm^2	5.82e-5
Inertia Moment along y-axis	l_{yy}	kgm^2	7.16e-5
Inertia Moment along z-axis	l_{zz}	kgm^2	0.0001
Rotor Moment of Inertia	J_r	kgm^2	0.1021e-6

In the experiments conducted to optimize the PID control parameters, by obtaining with CSA, PSO, GJO, and JSA were used as shown in Table 3.

Table 3. Optimization parameters of the CSA, PSO, GJO, and JSA.

Algorithm	Parameter	Symbol	Value
CSA	Number of dimensions	pd	3
	Number of populations	N	50
	Number of iterations	T	250
	Awareness probability	AP	0.1
	Flight length	fl	2
	Lower bound	u	0
	Upper bound	l	100
PSO	Number of dimensions	b	3
	Number of populations	n	50
	Number of iterations	k	250
	Cognitive parameter	c_1	0.12
	Social parameter	c_2	1.2
	Lower bound	down	0
	Upper bound	up	100
GJO	Number of dimensions	dim	3
	Number of populations	n	50
	Number of iterations	iter	250
	Lower bound	lb	0
	Upper bound	ub	100
JSA	Number of dimensions	nd	3
	Number of populations	nPop	50
	Number of iterations	MaxIt	250
	Lower bound	Lb	0
	Upper bound	Ub	100

The PID control parameter values Kp, Ki, and Kd obtained by CSA, PSO, GJO, and JSA for the input shown as thrust (z) to the system as the height control of the quadrotor are presented in Table 4.

Table 4. Optimal PID parameters.

Algorithms	K_p	K_i	K_d
CSA	99.4685	10.0842	16.7308
PSO	89.3500	10.1010	13.7640
GJO	91.2160	0.0676	13.9287
JSA	99.6977	10.1872	16.6593

Figure 5 presents the errors of the quadrotor because of the altitude control of each meta-heuristic algorithm. When we closely examine the peak values of the error values, the PSO algorithm reached the peak error value of 0.1 in 0.0996 seconds. PSO algorithm was followed by GJO which reached 0.074 peak error value in 0.076 seconds, JSA which reached 0.041 peak error value in 0.04096 seconds, and CSA which reached 0.0375 peak error value in 0.03652 seconds. Considering these results, the peak error value of the CSA algorithm was lower than the other algorithms.

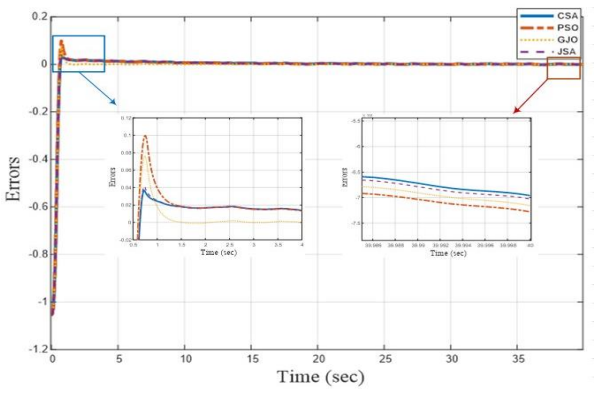

Figure 6. Errors for altitude control of quadrotor.

The overshoot, rise, and settling times of a quadrotor because of PID height control parameters optimized with CSA, PSO, GJO, JSA algorithms-based PIDs, and classic PID are shown in Table 5. Each value here refers to the effectiveness of the quadrotor in controlling the height movement. The overshoot value achieved using the PSO algorithm is notably higher than that of the other algorithms, particularly the CSA and JSA algorithms. The rising time is roughly similar across all algorithms. The GJO algorithm produced the best settling time, while the settling times for the CSA, PSO, and JSA algorithms are nearly identical. Furthermore, the classic PID controller demonstrated poorer performance regarding overshoot, rise time, and settling time.

Table 5. Performance criteria for each algorithm.

Algorithms	Overshoot (%)	Rising Time (s)	Settling Time (s)	Error
CSA	3.1439	0.3976	1.1207	6.9580e-04
PSO	8.8823	0.3824	1.2677	7.2764e-04
GJO	6.7353	0.3875	0.9760	7.1542e-04
JSA	3.5585	0.3963	1.1320	7.0231e-04
Classic PID	12.5471	1.2513	11.3126	7.0162e-04

In this respect, it is shown that the desired altitude control of the quadrotor can be achieved with meta-heuristic algorithms. These results prove the suitability of the optimization approach of a highly nonlinear system with a complex structure such as a quadrotor by using meta-heuristic algorithms in this study.

To further analyze the performances of the algorithms, the convergence curves of CSA, PSO, GJO, and JSA are compared in Figure 7. Since the adjustment of the parameters of the control methods is a minimization problem, the point where the cost function value is minimum is seen as the point where the optimal parameters are. This means the quadrotor can reach the given reference altitude with the highest accuracy. Convergence curves up to 250 iterations were created for the PID altitude control of the quadrotor using CSA, PSO, GJO, and JSA-based approaches. Figure 7 shows that JSA and CSA produce competitive results. In other words, these algorithms converge to the optimum point the fastest among the considering methods. In addition, JSA and CSA methods have competitive results.

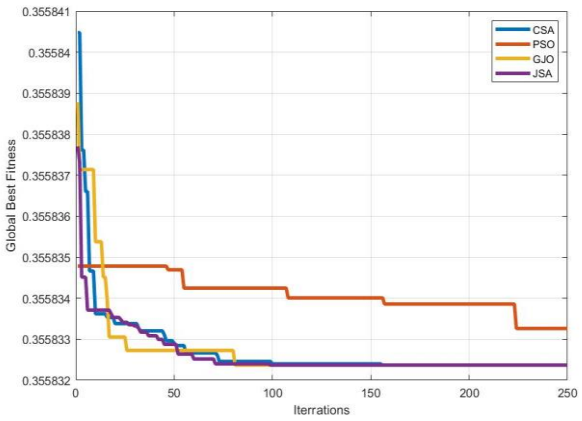

Figure 7. Convergence curves of CSA, PSO, GJO, and JSA.

It is also obviously seen that PSO has a much larger error compared to CSA, GJO, and JSA. The proposed control approach based on CSA, PSO, GJO, and JSA provides adequate performance for the altitude control of the quadrotor for these methods, as shown in the convergence curves in Figure 8.

Examining the convergence behavior of the algorithms to the optimal point is quite effective in the qualitative evaluation of the algorithms. For this purpose, when the convergence curves of the considered methods are examined, it can be concluded that the JSA and CSA methods are qualitatively more adequate than the other algorithms for this problem. The altitude response of the quadrotor is represented in Fig. 8. Previous results in Fig. 6., Fig. 7 and Table 5 prove that the superior control performance is provided by using CSA to optimize the control parameters of PID.

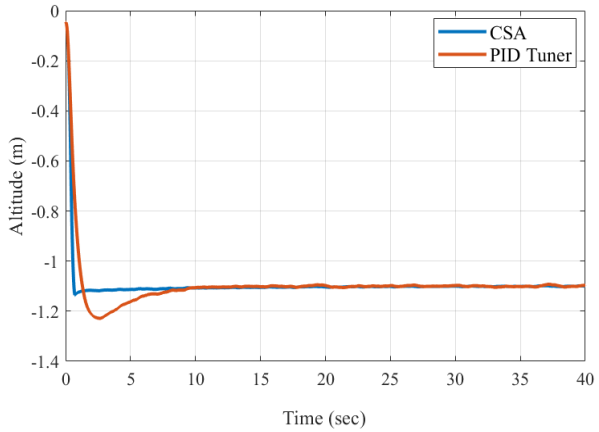

Figure 8. Altitude response of the quadrotor.

The altitude response in Fig. 8. shows that the CSA-optimized PID produces a faster and more stable output than the tuner-optimized PID. The Euler angles of the quadrotor are also given in Fig.9.

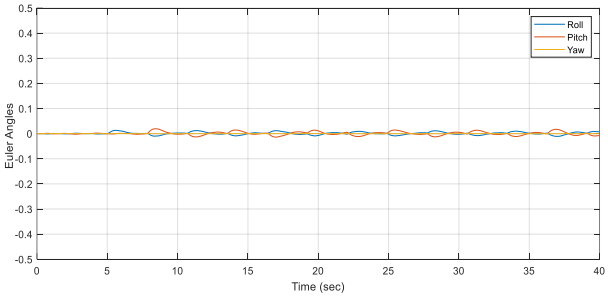

Figure 9. Euler angles of the quadrotor.

The drone will be more stationary during takeoff the closer the roll, pitch, and yaw angle oscillation and error rate are near zero. The references of these three angles roll, pitch, and yaw are therefore regarded as zero.

5 Conclusion

The quadrotor, a type of unmanned aerial vehicle with a complex system, can be effectively controlled using optimization methods, even though it is often challenging to manage with conventional techniques. This characteristic makes it a popular choice for evaluating performance in various engineering problem-solving scenarios.

This study provides an overview of four optimization algorithms: the Crow Search Algorithm (CSA), Particle Swarm Optimization Algorithm (PSO), Golden Jackal Optimization Algorithm (GJO), and Jellyfish Search Algorithm (JSA). These algorithms are utilized to fine-tune the dynamic equations of a quadrotor model and the PID control parameters used for altitude control. A comparison of each metaheuristic algorithm used in controlling the system is presented. In this context, the results obtained from the error performance of each algorithm are analyzed and evaluated. The CSA algorithm achieved the target altitude with the smallest error compared to the others. Following the CSA algorithm in performance are the JSA, GJO, and PSO algorithms, respectively. The convergence curves of these algorithms provide a clearer representation of their control processes. To better analyze the performance of the quadrotor, we examined the maximum overshoot, rise time, and settling time. Among the algorithms tested, the CSA demonstrated the lowest maximum overshoot, measuring at 3.1499, followed by the JSA, GJO, and PSO algorithms in that order. Upon analyzing the rising times, it becomes evident that the results demonstrate a striking similarity. It is seen that the PSO has reached the reference point in a shorter time, followed by GJO, JSA, and finally CSA. Based on the analyses conducted, the PID parameters for altitude control of the quadrotor were optimized using various metaheuristic algorithms, and comparative studies were carried out.

The results obtained using the PID tuner served as the reference point. Based on the overshoot metric, the improvement percentages for each method were as follows: the CSA method showed an improvement of 74.94%, the PSO method improved by 29.21%, the GJO method increased by 46.32%, and the JSA method achieved a 71.64% increase. In terms of rising time, the improvement percentages were as follows: the CSA method showed a 68.23% improvement, the PSO method had a 69.44% increase, the GJO method improved by 69.03%, and the JSA method reported a 68.33% enhancement. Regarding settling time, the improvement percentages were as follows: the CSA method showed a 90.09% improvement, the PSO method increased by 88.79%, the GJO method improved by 91.37%, and the JSA method reported an enhancement of 89.99%.

Future research will focus on position control and trajectory tracking analyses of the quadrotor. Additionally, hybrid metaheuristic algorithms will be employed to achieve more stable control.

Declaration

This study is derived from the thesis titled “Realization of image processing-based trajectory tracking algorithm on Parrot Mambo drone with MATLAB” of the first author (Muhammed Kivanc Kurnaz).

This study was supported by the Scientific Research Projects unit of the Firat University (FUBAP) under the grant number TEKF.21.12. The authors thank the FUBAP for their support.

References

[1] Okasha, M.; Kralev, J.; Islam, M. (2022). Design and Experimental Comparison of PID, LQR, and MPC Stabilizing Controllers for Parrot Mambo Mini-Drone, *Aerospace*, Vol. 9, No. 6, 298.

[2] Khodja, M. A.; Tadjine, M.; Boucherit, M. S.; Benzaoui, M. (2017). Experimental dynamics identification and control of a quadcopter, *2017 6th International Conference on Systems and Control, ICSC 2017*, IEEE, 498–502.

[3] Sheta, A.; Braik, M.; Maddi, D. R.; Mahdy, A.; Aljahdali, S.; Turabieh, H. (2021). Optimization of PID controller to stabilize quadcopter movements using meta-heuristic search algorithms, *Applied Sciences (Switzerland)*, Vol. 11, No. 14.

[4] Derrouaoui, S. H.; Bouzid, Y.; Guiatni, M. (2021). PSO Based Optimal Gain Scheduling Backstepping Flight Controller Design for a Transformable Quadrotor, *Journal of Intelligent and Robotic Systems: Theory and Applications*, Vol. 102, No. 3.

[5] Kapnopoulos, A.; Alexandridis, A. (2022). A cooperative particle swarm optimization approach for tuning an MPC-based quadrotor trajectory tracking scheme, *Aerospace Science and Technology*, Vol. 127, 107725.

[6] Hermouche, B.; Zennir, Y.; Kamsu Foguem, B. (2023). Influence of meta-heuristic algorithms on the optimization of quadrotor altitude PID controller, *Journal of the Brazilian Society of Mechanical Sciences and Engineering*, Vol. 45, No. 10, 1–19.

[7] Sahrir, N. H.; Basri, M. A. M. (2023). PSO–PID Controller for Quadcopter UAV: Index Performance Comparison, *Arabian Journal for Science and Engineering*, Vol. 48, No. 11, 15241–15255.

[8] Belge, E.; Altan, A.; Hacıoğlu, R. (2022). Metaheuristic Optimization-Based Path Planning and Tracking of Quadcopter for Payload Hold-Release Mission, *Electronics (Switzerland)*, Vol. 11, No. 8.

[9] Gün, A. (2023). Attitude control of a quadrotor using PID controller based on differential evolution algorithm, *Expert Systems with Applications*, Vol. 229, No. PB, 120518.

[10] Alqudsi, Y.; Makaraci, M.; Kassem, A.; El-Bayoumi, G. (2023). A numerically-stable trajectory generation and optimization algorithm for autonomous quadrotor UAVs, *Robotics and Autonomous Systems*, Vol. 170, No. January 2021, 104532.

[11] Meraihi, Y.; Gabis, A. B.; Ramdane-Cherif, A.; Acheli, D. (2021). A comprehensive survey of Crow Search Algorithm and its applications, *Artificial Intelligence Review*, Vol. 54, No. 4, 2669–2716.

[12]Farzaneh, M. M.; Tavakolpour-Saleh, A. R. (2022). Stabilization of a quadrotor system using an optimal neural network controller, *Journal of the Brazilian Society of Mechanical Sciences and Engineering*, Vol. 44, No. 1, 1–12.

[13]Chang, W.-D.; Shih, S.-P. (2010). PID controller design of nonlinear systems using an improved particle swarm optimization approach, *Communications in Nonlinear Science and Numerical Simulation*, Vol. 15, No. 11, 3632–3639.

[14]Askarzadeh, A. (2016). A novel metaheuristic method for solving constrained engineering optimization problems: crow search algorithm. *Computers & structures*, *169*, 1-12.

[15]Kennedy, J., & Eberhart, R. (1995, November). Particle swarm optimization. In *Proceedings of ICNN'95-international conference on neural networks* (Vol. 4, pp. 1942-1948). ieee.

[16]Chopra, N., & Ansari, M. M. (2022). Golden jackal optimization: A novel nature-inspired optimizer for engineering applications. *Expert Systems with Applications*, *198*, 116924.

[17]Chou, J. S., & Truong, D. N. (2021). A novel metaheuristic optimizer inspired by the behavior of jellyfish in the ocean. *Applied Mathematics and Computation*, *389*, 125535.

[18]Kurnaz, M. K. (2023). Realization of image processing-based trajectory tracking algorithm on Parrot Mambo drone with MATLAB. Master's Thesis, https://tez.yok.gov.tr/.

International Journal of Innovative Engineering Applications

Journal homepage: https://dergipark.org.tr/ijiea

EVALUATION OF THE ENERGY PERFORMANCE OF ADOBE STRUCTURES CONSTRUCTED USING MODERN TECHNIQUES FOR A SUSTAINABLE FUTURE: THE CASE OF ELAZIĞ

***Muhammed Emin Demirtaş*[*1], *Ayça Gülten*[1]**

[1]*Fırat University, Faculty of Architecture, Department of Architecture, Elazığ, Turkey*

Abstract

Original scientific paper

Natural materials offer significant advantages in terms of energy efficiency in buildings. Materials such as earth, adobe, and stone stand out due to their high thermal mass, which enables them to provide cooling during the summer and retain heat during the winter. Among these natural materials, earth-derived materials are also notable for their low energy costs. This research evaluates the energy performance of a building constructed using the rammed earth technique in the Keban district of Elazığ. As a case study, the "Women's Education and Production Center Project," designed and implemented by Architect Özgül Öztürk in the Keban district of Elazığ, is examined. Comparisons are made with the energy performance that would result if the same building were constructed using concrete and sandwich panel materials. This study aims to analyze the energy performance of rammed earth, concrete, and sandwich panel materials and to determine the environmental impacts of these materials. In this context, the study focuses on alternative materials that could contribute to future sustainable construction. In this research, energy performance analysis was conducted using Revit. This program examined the thermal insulation capacities and energy consumption rates of buildings constructed with different materials. The results of the study indicate that rammed earth material is superior in energy efficiency. These evaluations also highlight the contributions of natural and breathable materials, such as rammed earth, to the environmental sustainability of buildings. It is considered that such materials could emerge as a sustainable alternative in future construction.

Keywords: *Adobe, breathable material, energy performance, natural material, rammed earth, sustainable material.*

SÜRDÜRÜLEBİLİR BİR GELECEK İÇİN MODERN TEKNİKLER KULLANILARAK İNŞA EDİLEN KERPİÇ YAPILARIN ENERJİ PERFORMANSININ DEĞERLENDİRİLMESİ: ELAZIĞ ÖRNEĞİ

Özet

Orijinal bilimsel makale

Doğal malzemeler, yapıların enerji verimliliği açısından önemli avantajlar sunmaktadır. Toprak, kerpiç ve taş gibi doğal malzemeler, yüksek termal kütleleri sayesinde, yaz aylarında serinlik sağlama ve kış aylarında ise ısı tutma özellikleri ile öne çıkmaktadır. Bu doğal malzemelerden biri olan toprak türevli malzemeler, düşük enerji maliyetleri ile de dikkat çekmektedir. Bu çalışma, Elazığ'ın Keban ilçesinde sıkıştırılmış toprak tekniği ile inşa edilmiş bir yapının enerji performansını değerlendirmektedir. Değerlendirilecek yapı örneği olarak, Mimar Özgül Öztürk'ün Elazığ'ın Keban ilçesinde projelendirdiği ve uyguladığı "Kadın Eğitim ve Üretim Merkezi Projesi" ele alınmaktadır. Aynı yapının beton ve sandviç panel ile inşa edilmesi durumunda ortaya çıkacak enerji performansı ile karşılaştırmalar yapılmıştır. Çalışmanın amacı, sıkıştırılmış toprak, beton ve sandviç panel malzemelerin enerji performanslarını analiz etmek ve bu malzemelerin çevresel etkilerini belirlemektir. Bu bağlamda, gelecekteki sürdürülebilir yapılaşmaya katkı sunacak alternatif malzemeler üzerinde durulmuştur. Araştırmada, Revit ile enerji performans analizi yapılmıştır. Bu program aracılığıyla, farklı malzemelerle inşa edilen yapıların ısı yalıtım kapasiteleri, enerji tüketim oranları incelenmiştir. Analiz sonuçları, sıkıştırılmış toprak malzemenin enerji verimliliği açısından daha üstün olduğunu göstermektedir. Bu değerlendirmeler ile sıkıştırılmış toprak gibi doğal ve nefes alan malzemelerin, yapıların çevresel sürdürülebilirliğine katkıları da vurgulanmaktadır. Bu tür malzemelerin, gelecekteki yapılaşmada sürdürülebilir bir alternatif olarak öne çıkabileceği değerlendirilmektedir.

Anahtar Kelimeler: *Kerpiç, nefes alan malzeme, enerji performansı, doğal malzeme, sıkıştırılmış toprak, sürdürülebilir malzeme.*

*Corresponding author.

E-mail address: emindemirtas23@gmail.com (M. E. Demirtaş)

Received 11 November 2024; Received in revised form 08 April 2025; Accepted 28 April 2025

 Doi: https://doi.org/10.46460/ijiea.1583130

1 Introduction

Rapid urbanization and industrialization worldwide have led to the rapid depletion of natural resources and a significant increase in environmental impacts. Modern construction processes, particularly the intensive use of industrial materials, have resulted in high energy consumption and carbon emissions. The widespread use of concrete, steel, and glass materials has caused high carbon emissions, negatively affecting the environment. This situation has adversely affected the balance of global ecosystems and made the necessity for sustainable construction even more pressing [1]. In this context, the importance of sustainability in the construction industry has increased and continues to grow globally. The environmental impacts of material choices in the construction sector and energy efficiency are at the heart of global sustainability discussions. As a result, the rapid depletion of energy resources and increasing environmental degradation have brought natural materials back into focus. The concept of sustainability not only requires the conservation of natural resources but also calls for solutions that enhance energy efficiency and ensure the preservation of ecological balance in the future.

Compared to industrial materials, natural materials such as earth and adobe require less energy during production and minimize carbon emissions. The ability of these materials to be safely returned to nature without causing harm and their lack of negative environmental impact presents a significant advantage for the construction sector. Furthermore, these materials are biologically biodegradable and minimize waste production. These characteristics further emphasize the necessity of using earth-derived materials in sustainable construction processes.

Earth-derived materials are significant among sustainable building materials due to their structures, which minimize environmental impacts and have low energy consumption. Materials such as adobe and rammed earth, part of traditional construction techniques, are re-evaluated in modern construction processes. Thanks to their high thermal mass, these materials help balance indoor temperatures, reducing energy consumption. By providing cooling in the summer and retaining heat in the winter, these materials increase the energy efficiency of buildings while keeping energy consumption at a minimum [2]. Furthermore, using local resources for earth-derived materials reduces transportation costs and diminishes environmental impacts. These properties make earth-derived materials a significant alternative for ecological sustainability in modern construction. In this context, the importance of environmental and contemporary adobe applications is increasingly recognized.

In Turkey, industrialization and urbanization have led to a decline in the use of natural materials, resulting in the widespread adoption of industrial materials. Materials such as concrete and steel are commonly preferred in construction but create negative environmental impacts. This situation has led to issues related to energy efficiency and ecological sustainability, emphasizing the need to re-evaluate natural materials. Materials such as earth and adobe, which hold significant importance in Turkey's architectural history, have been overlooked in modern construction processes but should be reconsidered, especially in terms of energy efficiency and environmental sustainability. Elazığ serves as an important example in this regard. With its rich cultural and architectural heritage, Elazığ has long been known for buildings constructed with natural materials by various civilizations throughout history. The environmentally friendly materials used in these buildings, such as adobe and rammed earth, are essential to the city's architectural identity. However, in modern construction processes, industrial alternatives have replaced these materials, leading to a construction approach that is distant from sustainability. In future sustainable construction projects, re-evaluating these traditional materials is critical to preserve the historical identity of cities and build energy-efficient structures with low environmental impact.

The literature contains some studies related to ecological, next-generation adobe. In their research, Leblebiciler and Akıncı addressed this topic, aiming to enhance the quality of ecological adobe production by adding various reinforcing materials to adobe. In their studies, they showed that an adobe sample containing 6% pumice, 10% plaster, 2% slaked lime, 10% volcanic tuff, and 3% organic fibers (flax) exhibited a pressure strength increase from 1075 pascals to 5532 pascals. Its thermal conductivity coefficient decreased from 0.64 W/mK to 0.42 W/mK compared to a sample of pure earth. These findings indicate that contemporary ecological adobe has high-pressure strength and, with its low thermal conductivity, can be used in modern buildings as a next-generation material [3]. Akbaş et al. thoroughly examined adobe construction techniques in their study and subsequently evaluated adobe based on the criteria of national and international certifications related to sustainability and ecological materials. In this context, a detailed table was created to assess the extent to which adobe meets these certification criteria. The researchers argued that adobe should be included in the "green material" category and conducted a comprehensive discussion [4]. Coşkun aimed to develop an alternative to the widely used alker pounding technique in modern technology by utilizing gypsum-added adobe for wall construction in his study. In this context, an experimental study assessed the applicability of the sprayed concrete technique, commonly used in concrete, for gypsum-added adobe materials regarding compressive strength [5]. In his study, Yardımlı investigated contemporary adobe structures within environmental approaches, analyzing how some of these eco-friendly buildings utilize the advantages of adobe material while others do not. He emphasized the ongoing need to explore environmentally sustainable materials and highlighted the ecological benefits of adobe constructions. He also suggested that alternative methods should be explored for recycling and utilizing waste materials [6]. Akkaş's study focuses on using adobe as a sustainable building material. It is emphasized that adobe can be utilized in masonry structures and as panel walls in reinforced concrete and steel structures. Through experimental investigations, suitable additives and curing conditions have been determined to increase the mechanical strength of adobe, and the results suggest that a wider potential for its use in

the construction sector has been demonstrated [7]. In the study, Kıvrak investigates the effects of silica fume on adobe material's mechanical and physical properties. The clay soil was mixed with silica fume to produce adobe. The results of the experiments suggest that adding silica fume positively impacts all properties of the adobe [8]. Koç examines the role of earth materials in ecological design to reduce the impacts of increasing urbanization on the environment. It is emphasized that excavation soil should be utilized in construction, and earth construction techniques and regulations from different countries are compared. The study presents recommendations for Turkey's development of new earth construction regulations [9]. Binici et al. investigated the reasons behind the collapse of rubble stone and adobe structures with earthen mortar during the 2010 Elazığ earthquake. It is noted that heavy stones contributed to fatalities during earthquakes and that using fiber-reinforced adobe could reduce the extent of damage. The study examines the engineering properties of adobe enhanced with plastic and textile fibers, pumice, gypsum, and cement and finds that fiber-reinforced adobe possesses economic, energy-saving, and improved mechanical properties [10]. In his study, Ataç investigates the integration of adobe material with biomaterials in sustainable architecture. Compressed earth structures are associated with digital design and mycorrhizal fungi, exploring the contribution of bioengineering and construction disciplines to architectural design processes [11]. Yavaş, in his study, addresses the history, physical, and mechanical properties of adobe material, aiming to reassess this material in terms of earthquake safety. He particularly critiques the 2018 Turkey Building Earthquake Regulation, which does not permit adobe buildings, and offers recommendations for including adobe structures in the regulations with certain limitations. The study provides a detailed examination of the calculations related to the structural safety of adobe buildings and earthquake safety standards [12]. In their study, Binici et al. found the earthquake resistance of limestone used in rural areas of Turkey inadequate. They investigated the mechanical properties of materials to be used in adobe production. The study argues that using waste materials such as fiber, wheat straw, polystyrene, pumice, and clay in adobe production provides economic benefits, energy savings, and improved mechanical properties [13]. As for Özgünler, in his study, he emphasizes that the high energy consumption of the construction industry contributes to global warming and discusses the importance of environmentally friendly renewable energy sources and sustainable building materials. By stating that traditional earth-based materials are produced with low energy and are environmentally friendly, he has conducted laboratory studies on the sustainability of these materials. The study highlights the ecological values of earth-based building materials and their potential to ensure rural sustainability [14].

In the studies reviewed in the literature, no research has been found that analyzes, with numerical data, the potential for adobe structures built using modern construction methods to exhibit better energy performance compared to contemporary building materials. Therefore, this paper provides a unique contribution compared to other studies in the literature. The study analyzed the energy performance of an ecological adobe building using a simulation program. Additionally, the performance of this building was simulated in comparison to reinforced concrete and container structures. Based on the obtained numerical data, it was concluded that adobe structures built with modern construction techniques could demonstrate better energy performance compared to other materials commonly used in the construction industry.

2 Sustainable Material: Adobe

In recent years, sustainability has gained more importance due to increasing environmental pollution and the conservation of energy resources. Numerous institutions, councils, and agencies have conducted studies to explain this concept. These studies suggest that "Sustainability is the continuity of systems and processes" [15].

The concept of sustainability is also of great importance in the construction process of buildings. In the construction sector, while environmental pollution increases, the conservation of energy resources should be a primary goal. Sustainable building materials are composed of components that do not pose a risk to human and environmental health and can be recycled and reused [16]. Sustainable building materials minimize energy consumption during production and use, and they are materials that do not pose a risk to the environment or human health from waste generated during raw material production, processing, use, maintenance, and repair stages [17]. The building materials are expected to be high-quality, environmentally friendly, aesthetically pleasing, and cost-effective. Additionally, materials that do not harm human health should be preferred.

With the advancement of technology, new construction materials have started to be preferred over earth and earth-derived materials, which have been used for long periods. Despite this, earth and earth-derived materials continue to be used in many areas. To this day, earth has primarily been utilized as adobe, a building material.

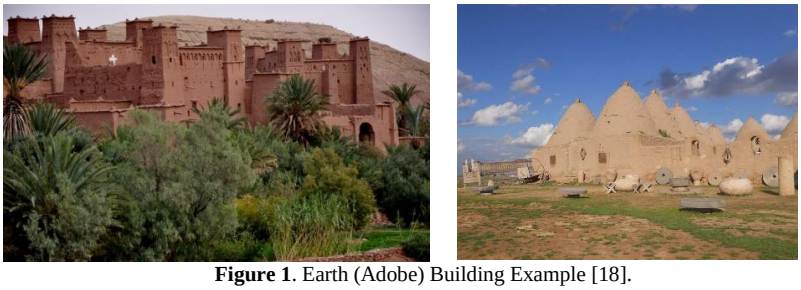

Figure 1. Earth (Adobe) Building Example [18].

Adobe is one of the world's oldest and most widely used building materials. Due to its accessibility and ease of processing, people have preferred this material since ancient times. The environmental impact of adobe is minimal [19].

Figure 2. Regions where Adobe is widely used around the world.

Adobe has many advantages and disadvantages.
Advantages:

- Its porous structure helps maintain the humidity levels of the interior space.
- It regulates heat and moisture balance through its thermal insulation properties.
- Storing heating energy contributes to maintaining a stable temperature for extended periods.
- Low production cost and the absence of the need for specialized facilities make it an economical option.
- It does not require mechanical energy during production and use stages.
- It is a recyclable material that does not harm the environment.
- Using earth obtained from excavation reduces transportation costs.

Disadvantages:

- It has high water sensitivity.
- It has low compressive strength.
- It requires annual maintenance.

All these properties make adobe a cost-effective and environmentally friendly option [5].

Adobe is a natural and healthy building material and stands out as an important construction material that contributes to preserving the global ecological balance and energy savings during both its production process and usage phase. In this context, adobe is a sustainable building material.

With its ability to regulate indoor air comfort, heat retention properties, and breathability, Adobe provides users with a refreshing living space. However, over time, it has faced tough competition from contemporary production techniques and has struggled to replace the energy-intensive reinforced concrete construction method. This situation poses risks regarding sustainable construction techniques and the preservation of cultural heritage for future generations [4].

It is essential to consider adobe as a prominent option among contemporary building materials to address the risks posed by this situation. The disadvantages of adobe must be minimized, and its advantages should be optimized more effectively.

There are two main approaches to using adobe in building construction: traditional and contemporary. Traditional adobe construction methods include the rammed earth technique and adobe block production. The rammed earth method involves the manual shaping of a damp earth mixture, combined with straw or plant fibers, without molds; this process allows for forming organic geometries. On the other hand, adobe block production involves pouring the earth mixture into molds and allowing it to dry in the sun, resulting in durable blocks. Among the contemporary adobe construction methods are rammed earth blocks, the tamping method, the spraying method, the holistic construction technique, and the unit construction technique. Rammed earth blocks are structural elements obtained by compressing a low-water mixture under pressure. The tamping method is based on mechanically compacting the earth mixture, while the spraying method involves surface coating using specialized machines. The holistic construction technique increases material efficiency by combining tamping and rammed earth methods, while the unit construction technique facilitates the construction of modular structures [6], [21].

In this context, considering earth materials in different forms and enhancing their water resistance have been crucial steps in meeting user expectations, thus contributing positively to the widespread adoption of earth materials in the future, particularly in terms of sustainability [4]. Adobe, through its use in various forms of earth materials and its application with more contemporary construction techniques, has gained characteristics that make it preferable as a modern building material. Alker is one of the most popular Adobe forms today. Alker is the process of reinforcing traditional adobe by adding plaster.

When lime is added to traditional adobe material, the water absorption rate of the material decreases, preventing the material from disintegrating due to the effect of water. Additionally, the setting time of the plaster is extended, and the workability of the mixture is improved. The addition of plaster to traditional adobe prevents the material from undergoing shrinkage. The evaporating water leaves space for air pockets, enhancing the adobe material's heat storage capacity [2].

Alker delivers the expected performance efficiently with its water absorption, heat storage, and other physical properties. The rapid setting of plaster in alker prevents deformation, shrinkage, and cracking that may occur during clay drying while also enhancing compressive strength [2].

3 Materials and Methods

In this research, the necessity of sustainable materials, the importance of adobe and natural building materials, contemporary adobe techniques, and the rationale for the use of different forms of these materials are explained in detail.

Subsequently, the "Women's Education and Production Center Project" designed and implemented by Architect Özgül Öztürk in Keban is explained in detail

through a practical application of how energy performance analysis is conducted using Autodesk Revit software. For energy performance analysis, the building to be analyzed in this study was selected, and one of the calculation methods, Revit software, was utilized to obtain the necessary calculations. Based on the analysis provided by the software, the building's annual cooling and heating loads are calculated. Additionally, to validate the accuracy of the analysis, heat gain and heat loss calculations were made using the relevant formulas to determine the building's annual cooling and heating loads, and a verification process was carried out with the obtained results.

In the final stage of the energy analysis, separate analyses were conducted for alternative materials, such as non-natural concrete or sandwich panels, to assess how the energy performance of the building would change if these materials were used instead of the rammed earth material. The analysis results were compared, and based on these comparisons, the necessity of sustainable materials, the importance of rammed earth and other natural building materials, contemporary rammed earth methods, and the reasons for using different forms of these materials were highlighted.

3.1 Building Analysis

In this study, the energy performance of the Women's Education and Production Center, an ecological building example constructed using the compressed earth technique in the Keban district of Elâzığ as part of the "Anadolu Meleği" project by Architect Özgül Öztürk, is being examined.

3.1.1 Women's Education and Production Center Project

The Women's Education and Production Center is an ecological architectural example realized by architect Özgül Öztürk within the framework of the "Anadolu Meleği" project. This project was initiated following Öztürk's winning of the first prize in the 2016 "Women of the Earth" competition, organized by the Yves Rocher Foundation and the French Institute. The project aims to revitalize rural architecture and create an environmentally friendly structure utilizing natural materials. Furthermore, this building cooperates with women's educational and production processes [22]. The structure has been constructed using the compressed earth technique. This technique is evident in the exterior images presented in Figure 3.

Figure 3. Exterior forms of the building.

This ecological building, constructed in Keban in 2019, aims to increase women's participation in production processes by combining local architectural elements with modern ecological techniques. The short-term goals of the project are to support natural life, facilitate women's social and economic participation, and transform rural areas into attractive centers. In the medium term, the development of ecotourism is targeted, while in the long term, the project aims to promote women's entrepreneurship and enhance economic activities in rural areas [22].

Figure 4. Interior forms of the building [22].

The building is a single-story structure with five windows and one fireplace. The entrance door and windows are made of wood, with a preference for using natural materials. Immediately to the left of the entrance is a kitchen counter, and a cabinet used for storage is directly opposite the entrance. Inside are seating areas designed in a divan style and made from recycled materials. The lintels, located at the upper level of the windows, provide structural support to the building. At the same time, the materials used in the interior are observed to possess warm and breathable characteristics (Figure 4).

3.1.2 Creating the Structure in Revit and Energy Analysis Settings

Autodesk Revit is an object-based software grounded in three-dimensional modeling techniques. This program is used for the design of buildings. It digitally presents the physical and functional characteristics of the designed structure and then stores this information for future use. This information repository can be accessed by all disciplines [23]. Based on this data, energy performance analysis of these designs can be conducted using the program. Users can optimize building designs based on the program's output, and necessary adjustments can be made in the digital environment by considering environmental impacts before the designs are constructed.

For the analyses performed in Revit software to yield accurate results, the building model must be created entirely and precisely. The properties of the materials used in the design must be thoroughly defined in the software, thereby preventing any potential errors or deficiencies in the analysis results [24].

In this context, after the plan drawings of the building, whose measurements have been taken (Figure 5), were completed, a detailed modeling process was carried out using Autodesk Revit software to conduct an energy performance analysis.

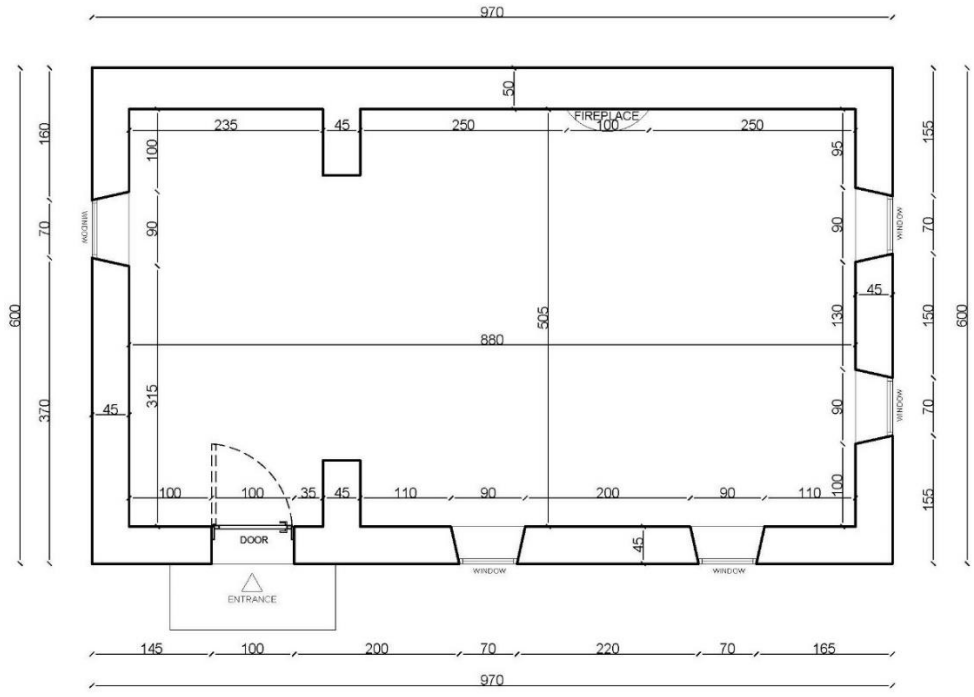

figure 5. Architectural plan of the building.

The current condition of the building and all architectural details were created through three-dimensional modeling in the digital environment (Figure 6). This enabled the analysis and evaluation processes to be conducted based on the building's digital model.

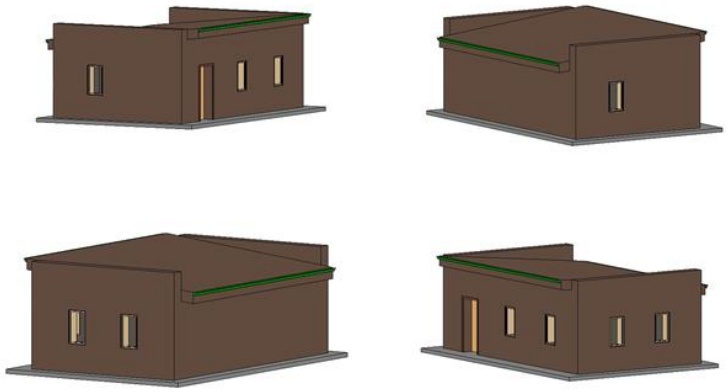

Figure 6. Three-dimensional model of the building created with autodesk revit.

In this process, the properties of the materials used in the building were defined in detail and comprehensively in the program using intelligent objects (Figure 7). This operation was carried out to obtain accurate and reliable results in the energy analysis [25].

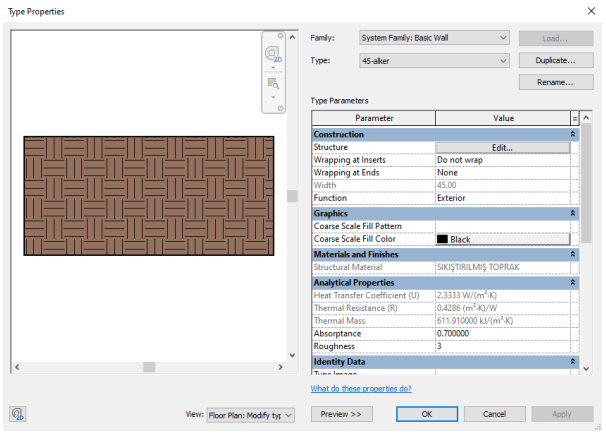

Figure 7. Building exterior wall layers detailed modeling window.

The U-values for each building component are pre-defined in the program and can be adjusted by the user when necessary (Figure 8). This allows for the integration of energy performance values appropriate to the building layers during the modeling process [25].

Mutlu's study specifies the rammed earth's thermal conductivity coefficient (λ) as 1.05 W/mK (Figure 8). In this project, based on the data obtained from the mentioned study, the thermal conductivity coefficient of rammed earth has been assumed to be the same value [26].

Additionally, two different models were created to compare natural and artificial materials, assuming that the buildings were designed with non-natural materials instead of earth-derived materials. In the first model, the building walls were created with layers consisting of 3 cm plaster, 20 cm reinforced concrete, and 2 cm plaster. In the second model, the walls were structured with layers of 0.5 cm aluminum sheet, 4 cm XPS, and 0.5 cm aluminum sheet. The energy performance analyses for both models were conducted using the Revit program.

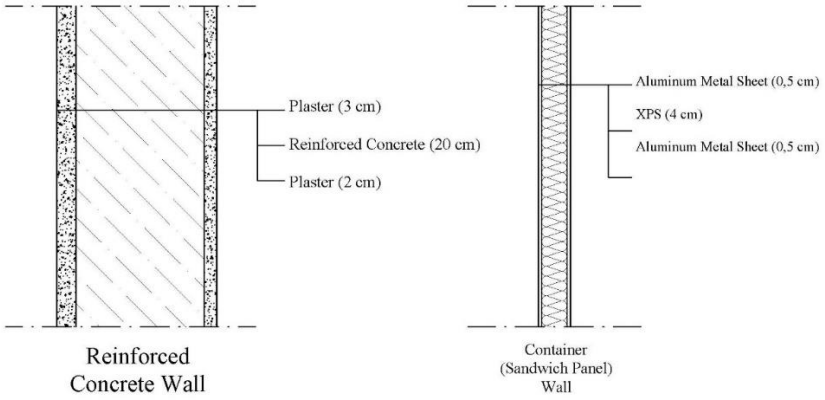

Figure 8. Wall sections for the case of designing the building with non-natural materials.

The materials' thermal conductivity coefficients (λ) for these two models are provided in Table 1 below, based on the data obtained from TS 825 and Balcıoğlu's study [27], [28].

Table 1. Thermal conductivity coefficients (λ) of the building materials used in the models [27], [28].

Building Material	**Thermal Conductivity Coefficient (λ)**
Plaster	1,60 (W/mK)
Reinforced concrete	2,50 (W/mK)
Aluminum	204 (W/mK)
Extruded Polystyrene Foam (XPS)	0,030 (W/mK)

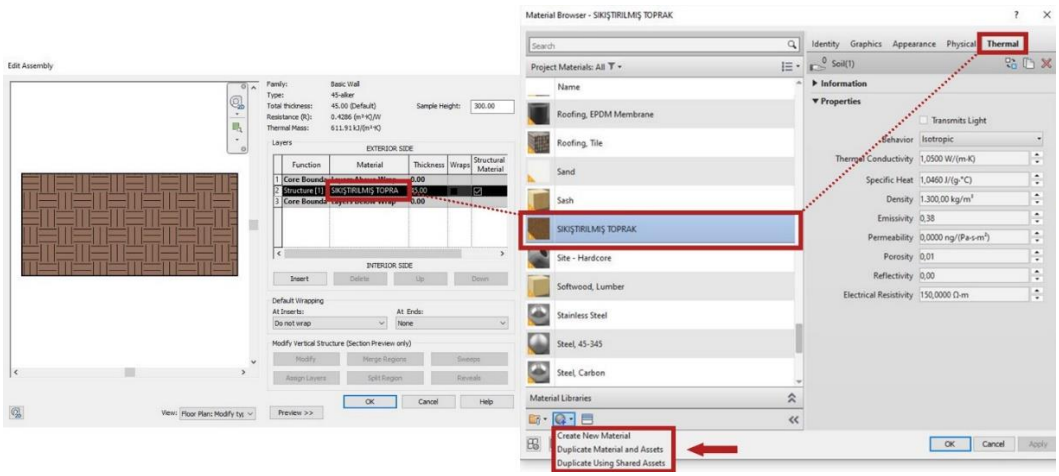

Figure 9. Creation of the detailed building model in Revit, showing the building component layers and thermal properties.

Materials not available in the software can be added using the "Create New Material" option, or a new material can be created by duplicating the properties of existing materials with the "Duplicate" option (Figure 9). In this study, since the building material for the energy analysis is not included in the material database, the materials were explicitly defined and added to the model.

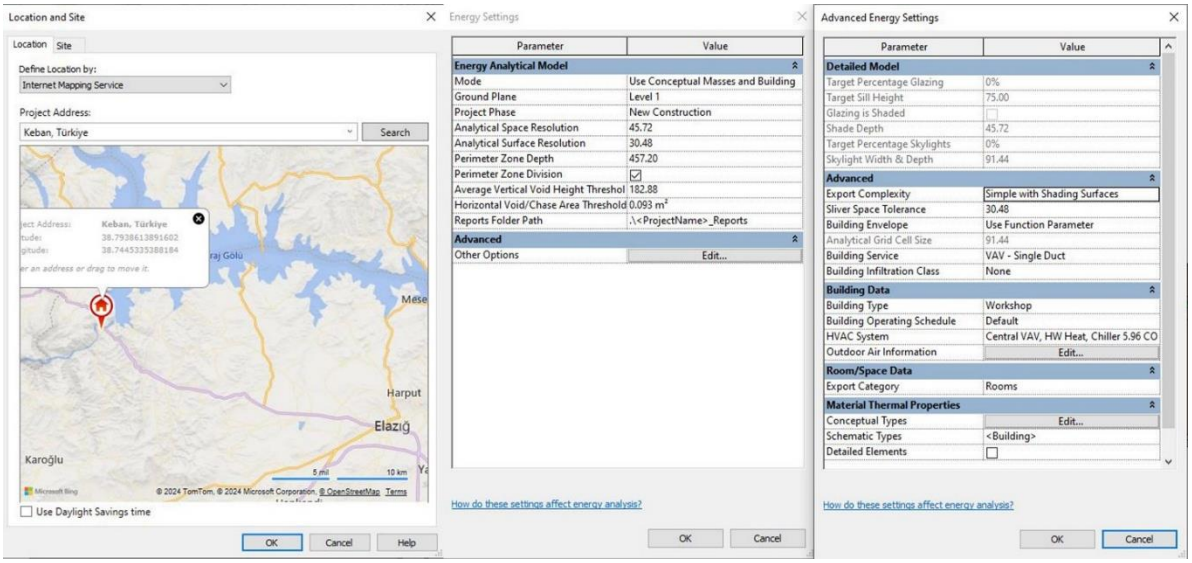

Figure 10. Building details window in revit.

After the model was created, energy definitions were made in the Revit software. In the "Analyze" tab, parameters such as the building's location, type, and daily usage range were defined, and the necessary adjustments were made to ensure that the energy analysis would provide accurate results (Figure 10).

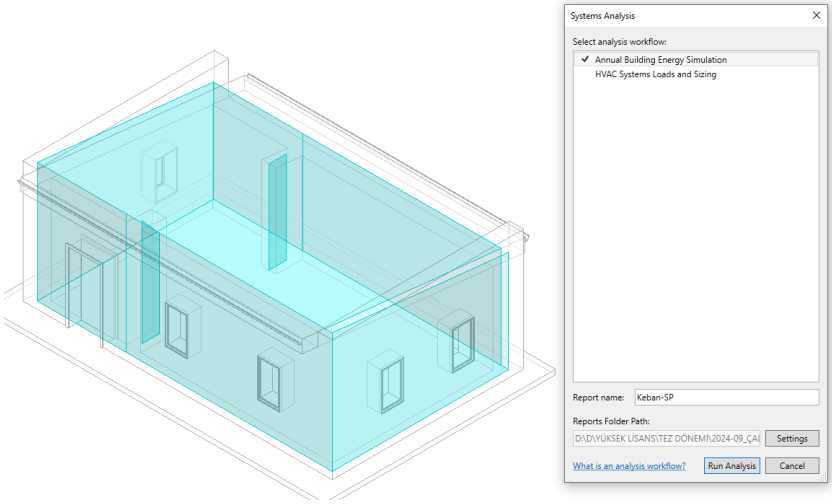

Figure 11. *Analysis window in revit.*

In the final step, by clicking on the "Systems Analysis" option in the "Energy Optimization" toolbar under the "Analyze" tab, selecting "Annual Building Energy Simulation," and then giving the "Run Analysis" command, the software performs the building energy analysis (Figure 11).

3.2 Validation Study

The building's annual cooling and heating loads were calculated using the relevant formulas for heat gain and heat loss to validate the results of Autodesk Revit software. A verification study was conducted by comparing the results obtained from Revit with these calculations.

The thermal conductivity values and other data obtained from the literature were used in the accuracy study of the research. Koçu's study states that adobe structures with wall thicknesses ranging from 50-70 cm in cold climate regions meet the required thermal conductivity coefficient of U = 0.50 W/m²K, as specified in the TS 825 standard [29]. Daily heat losses and gains were calculated by processing the areas of building component surfaces, lighting, appliance information, and user numbers; the thermal conductivity coefficients of building elements; and the "U" values of windows and doors into the "Microsoft Excel" program, using relevant formulas.

The required climate data were obtained from the Turkish State Meteorological Service website, and the relevant data are shown in Table 2.

Table 2. Heating and cooling degree days for the Keban district of Elaziğ in 2023 [30].

Centre	D/D	Jan	Feb	Mar	Apr	May	Jun	Jul	Aug	Sep	Oct	Nov	Dec	Annual
ELAZIĞ KEBAN (2023)	HDD	469	466	241	140	14					6	176	355	1867
	T≤15 °C	31	28	31	23	3					2	23	31	172
	CDD						66	211	276	107				660
	T>22 °C						25	31	31	28				115

(D/D = Degree-Day, HDD = Heating Degree-Day, CDD = Cooling Degree-Day, T≤15°C = Number of days with temperature ≤15°C, T>22°C = Number of days with temperature >22°C).

Heating Degree Days (HDD) measure the severity of cold weather conditions during a specific period, considering the outdoor and indoor temperatures. Cooling Degree Days (CDD) determine the severity of hot weather conditions, considering only the outdoor temperatures. These calculations are based on threshold temperatures of 15°C for heating and 22°C for cooling [31].

The results obtained in the verification study are presented in Table 3.

Table 3. Daily heat loss and gain.

Daily Heat Loss	2.993 W
Daily Heat Gain	5.796 W

The daily heat loss of 2,993 W represents the energy exchange with the outdoor conditions, while the daily heat gain of 5,796 W represents the energy inputs from both the indoor and outdoor environments of the building. These values are used to calculate the annual heating and cooling loads.

After the heat gain and heat loss values are determined in watts (W), they need to be converted to kilowatt-hours (kWh) to calculate the annual heating and cooling loads (kW=W/1000). Then, the energy amount in kilowatt-hours (kWh) is calculated by multiplying the power (kW) by the time (in hours) (kWh=kW×hour). In this calculation process, the heating and cooling degree days for the year 2023, shown in Table 2, are taken into account, with 172 days assumed for the heating system and 115 days for the cooling system. Additionally, a daily usage duration of 9 hours is considered for both systems. The calculation made based on these values is shown in Table 4.

Table 4. Annual heating and cooling loads calculated from the data obtained from heat loss and gain.

Annual Heating Load Required	4.633 kWh
Annual Cooling Load Required	5.999 kWh

Table 4 presents the annual heating and cooling loads calculated based on heat loss and gain. The annual heating load has been determined as 4,633 kWh while the annual cooling load is 5,999 kWh.

Table 5. Difference between Annual Cooling and heating loads.

	With the Formula-Based Calculation Method	With Revit	DIFFERENCE (Percentage)
Annual Heating Load Required	4.633 kWh	4250 kWh	% 9.01
Annual Cooling Load Required	5.999 kWh	5625 kWh	% 6.65

Table 5 presents the findings obtained from the heating-cooling load analysis and total loads, compared with the results derived from the Revit software. In this context, the small difference in kWh confirms the accuracy and validity of the calculations. This supports the reliability and precision of the applied analysis methods.

4 Findings and Evaluation

The building was modeled using Revit software, and the necessary analysis settings were input to perform the required analyses.

Table 6. Annual and maximum values (rammed earth - current state).

	Annual Value (kWh)	Maximum Value (W)	Day of Maximum Value
Heating	4250	9973	11 JANUARY
Cooling	5625	4375	20 JULY
Total Energy Load of the Building	9875		

Table 6 presents the annual energy consumption and maximum energy loads of a building constructed using rammed earth. The building consumes 4250 kWh of energy annually for heating and 5625 kWh for cooling. The maximum energy demand for the heating system occurred on January 11, reaching 9973 W. This indicates that the low temperatures in the winter months increase the heating load. The highest demand for the cooling system was recorded on July 20, with a value of 4375 W. The hot weather conditions during the summer months increased the building's cooling needs, and this load coincided with the hottest hours of the day. In total, the building consumes 9875 kWh of energy annually.

Similarly, the building's heat gain and heat loss calculations were performed using the relevant formulas in Excel, and based on these data, the building's annual cooling and heating loads were determined.

Furthermore, as a result of the analyses conducted for the comparison of natural and artificial materials, the results obtained for the building designed with reinforced concrete are presented in Table 7, while the results for the building designed with container (sandwich panel) are provided in Table 8.

Table 7. Annual and maximum values (in the case of reinforced concrete).

	Annual Value (kWh)	Maximum Value (W)	Day of Maximum Value
Heating	4966	11008	11 JANUARY
Cooling	6847	5363	01 AUGUST
Total Energy Load of the Building	11813		

Table 7 presents the annual energy consumption and maximum energy loads of the building, assuming it is constructed using reinforced concrete materials. The building consumes 4966 kWh for annual heating and 6847 kWh for cooling. The maximum energy demand of the heating system was recorded as 11008 W on January 11th. The highest demand for the cooling system occurred on August 1st, with a value of 5363 W. In total, the building consumes 11813 kWh of energy annually.

Table 8. Annual and maximum values (in the case of container construction).

	Annual Value (kWh)	Maximum Value (W)	Day of Maximum Value
Heating	5016	11643	11 JANUARY
Cooling	7053	5487	01 AUGUST
Total Energy Load of the Building	12069		

Table 8 presents the annual energy consumption and maximum energy loads of the building, assuming it is constructed using container materials. The building consumes 5016 kWh for annual heating and 7053 kWh for cooling. The maximum energy demand of the heating system was recorded as 11643 W on January 11th. The highest demand for the cooling system occurred on August 1st, with a value of 5487 W. In total, the building consumes 12069 kWh of energy annually.

The annual heating and cooling loads and the annual energy consumption for different building materials are presented together in Table 9.

Table 9. Annual heating and cooling loads and annual energy consumption of the same building using different building materials.

	Annual Heating Load (kWh)	Annual Cooling Load (kWh)	Total Annual Energy Load (kWh)
Rammed Earth	4250	5625	9875
Reinforced Concrete	4966	6847	11813
Container (Sandwich Panel)	5016	7053	12069

The natural building material, rammed earth, records a total energy consumption of 9875 kWh with lower heating (4250 kWh) and cooling (5625 kWh) loads, while reinforced concrete and container structures show higher energy consumptions of 11813 kWh and 12069 kWh, respectively, exhibiting lower efficiency compared to natural materials. These data clearly indicate that natural materials are more advantageous in terms of energy efficiency. The analysis shows that buildings designed with industrial materials such as reinforced concrete and sandwich panels, as opposed to natural materials, exhibited higher energy consumption during heating and cooling periods, based on wall thicknesses determined according to market standards.

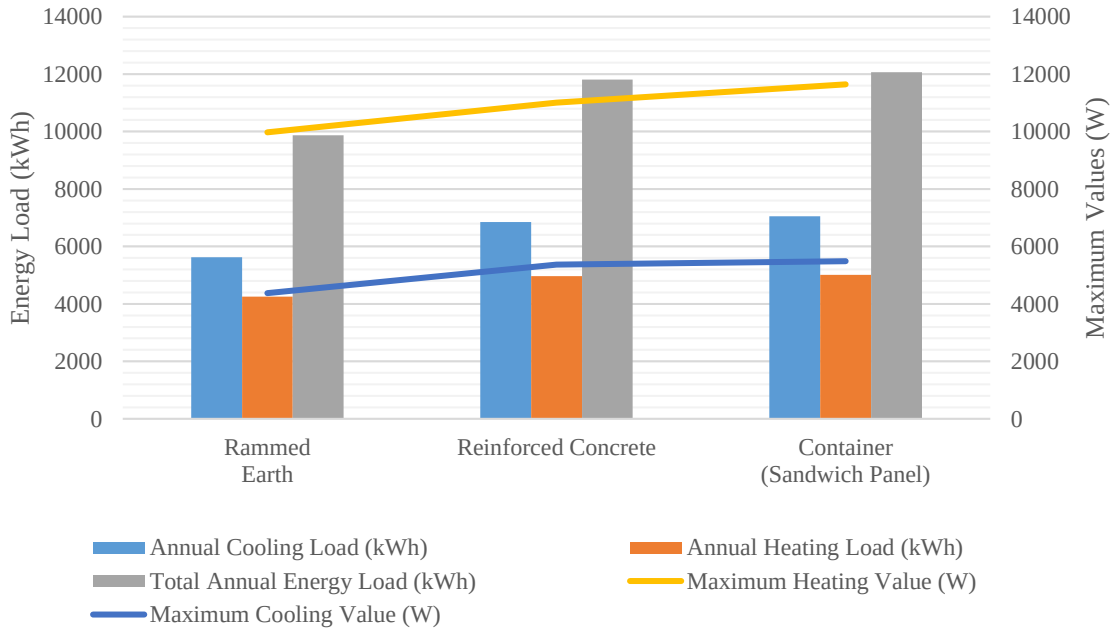

Figure 12. Annual energy load and maximum values.

In addition to the rammed earth material currently used in the structure, the annual heating and cooling load amounts, total annual energy load, and maximum heating and cooling values obtained when reinforced concrete and container materials are used, are collectively presented in Figure 12. As seen, the rammed earth material exhibits the lowest values for both maximum heating and cooling demand. The maximum heating value is determined to be 9973 W, while the maximum cooling value is recorded as 4375 W. In the case of reinforced concrete, the structure demonstrates a higher energy requirement with a maximum heating demand of 11008 W and a maximum cooling value of 5363 W. When constructed with container material, the structure exhibits the highest energy consumption with a maximum heating demand of 11643 W, and the maximum cooling value is measured as 5487 W. These data demonstrate that rammed earth is more advantageous in terms of energy efficiency compared to other materials.

5 Conclusion

The rapidly advancing industrialization process today has led to the widespread use of industrial and non-natural materials in the construction sector. The preference for materials such as concrete, steel, and glass, which consume significant energy and resources, results in high levels of carbon emissions, severely threatening environmental sustainability. These materials increase energy consumption during the production phase and throughout the entire life cycle of buildings, contributing to the deepening of global warming and other environmental issues.

In Turkey, as in the rest of the world, the processes of industrialization and urbanization have led to a shift from natural materials to industrial alternatives. Especially in large cities, reinforced concrete and steel structures have become dominant, resulting in increased energy consumption and adverse environmental impacts. Although Turkey's rich architectural heritage is based on traditional building materials and techniques, modern construction processes often overlook these elements. Particularly in terms of energy efficiency and sustainability, it is essential to reconsider the use of natural materials and integrate them into current building policies. In this context, the study emphasizes, based on the data obtained through literature review, the importance of sustainable materials and the need to readdress issues related to energy efficiency.

Additionally, in the study, the energy performance analysis of a building constructed using contemporary adobe techniques was conducted with the help of Revit software. The findings revealed that earth-based natural materials, such as adobe, offer significant advantages in terms of energy efficiency. The study also calculated the energy performance of the building when designed separately with reinforced concrete and sandwich panel materials, using Revit software. These results were evaluated by comparing them with the building's existing condition. As a natural building material, rammed earth exhibited significantly lower energy loads during both heating and cooling processes, demonstrating clear efficiency in total energy consumption. In contrast, reinforced concrete and container buildings displayed less efficient performance with higher energy consumption compared to natural materials. Furthermore, the study found that the maximum energy consumption levels of buildings constructed with non-natural materials were higher than those built with natural materials. Notably, reinforced concrete and sandwich panel buildings consumed significantly more energy during cooling periods, indicating that these materials are less suitable in terms of energy efficiency. When all the findings were considered, the study concluded that buildings constructed using contemporary adobe techniques could emerge as more energy-efficient, with lower energy requirements in both heating and cooling processes. This highlights the importance of natural materials for environmental sustainability. Additionally, modern adobe applications, such as rammed earth, should be regarded as a healthier and more environmentally friendly alternative to industrial materials.

This research highlights the need for a re-evaluation of natural materials, which have been frequently used in traditional building practices throughout history, in the context of the modern construction industry. In the past, structures built with environmentally friendly materials such as adobe and mud brick have held significant places in the identity of cities. These traditional building techniques not only provided low-cost solutions by utilizing local resources, but also resulted in buildings with high energy efficiency. Based on the findings of this study, it is evident that modern adobe techniques, such as rammed earth, offer a more environmentally friendly and health-conscious alternative compared to industrial materials. The re-evaluation of these materials holds significant potential for constructing sustainable buildings and improving energy efficiency. In this regard, the broader use of natural materials in the construction sector will yield both economic and ecological benefits. Furthermore, it will not only contribute to environmental sustainability but also aid in preserving the historical identity of the city.

In conclusion, this study emphasizes the importance of re-evaluating natural materials (particularly alternatives such as adobe and rammed earth) in the context of the modern construction industry. The advantages of traditional construction techniques in terms of energy efficiency and environmental sustainability should not be overlooked in contemporary building processes. The findings indicate that natural materials provide a more efficient and environmentally friendly option compared to industrial alternatives in terms of energy performance. In this context, the broader adoption of natural materials in the construction sector will contribute to the preservation of the historical identity of cities, offering both economic and ecological benefits. The integration of traditional building materials with contemporary construction techniques will contribute to the creation of a sustainable future, and this process will play a critical role in shaping future building policies.

Declaration

The authors declare that the ethics committee approval is not required for this study.

Acknowledgments

There is no conflict of interest among the authors. Furthermore, we would like to express our gratitude to Architect Özgül Öztürk for her valuable contributions to the realization of this study.

References

[1] Tufan, M. Z., & Özel, C. (2018). Sürdürülebilirlik kavramı ve yapı malzemeleri için sürdürülebilirlik kriterleri. *International Journal of Sustainable Engineering and Technology*, 2(1), 6–13.

[2] Kafesçioğlu, R. (1980). *Yapı malzemesi olarak kerpicin alçı ile stabilizasyonu* (TÜBİTAK MAG 505). İstanbul.

[3] Leblebiciler, Y., & Akıncı, A. (2021). Ekolojik yeni nesil kerpiç. *Journal of Science Harmony*, 4(2), 12–19.

[4] Akbaş, M. F., Aslan, M., & Arpacıoğlu, Ü. (2022). Yeşil malzeme bağlamında kerpiç. *EKSEN Dokuz Eylül University Journal of the Faculty of Architecture,* 3(2), 72–88.

[5] Coşkun, K. (2005). *Alker (alçı katkılı kerpiç) teknolojisinin püskürtme beton (shotcrete) tekniği ile uygulanabilirliğinin basınç dayanımı açısından deneysel değerlendirmesi* (Doctoral dissertation,), Istanbul Technical University).

[6] Yardımlı, S. (2021). Çevreci yaklaşımlarda malzeme ve yapım tekniği; çağdaş kerpiç yapılar. *Urban Academy - Journal of Urban Culture and Management,* 14(2), 389–413.

[7] Akkaş, F. (2011). *Lif katkılı kerpiç panel duvar üretilme olanaklarının araştırılması* (Master's dissertation, Istanbul Technical University.)

[8] Kıvrak, J. (2007). *Silis dumanı katkılı kerpiçlerin mekanik ve fiziksel özelliklerinin araştırılması* (Master's dissertation, Gazi University).

[9] Koç, Z. G. (2017). *Ekotasarım kapsamında toprak yapım sistemleri ve yönetmeliklerin irdelenmesi* (Master's dissertation, Yildiz Technical University).

[10] Binici, H., Durgun, M. Y., & Yardım, Y. (2010). Kerpiç yapılar depreme dayanıksız mıdır? Avantajları ve dezavantajları nelerdir? *KSU Journal of Engineering Sciences,* 13(2).

[11] Ataç, A. (2019). *Mimarlıkta biyomalzemelerin kullanımı: Sıkıştırılmış toprak blokların performansının mikorizal mantar kullanılarak geliştirilmesi* (Master's dissertation, Istanbul Bilgi University).

[12] Teloğlu Yavaş, A. N. (2021*). Kerpiç binaların ağırlık yükleri ve deprem etkileri altında davranışı ve yurdumuzdaki uygulanışı* (Master's dissertation, Fatih Sultan Mehmet University).

[13] Binici, H., Aksoğan, O., & Kaplan, H. (2005). Kerpiç üretiminde alternatif malzemelerin kullanımı. *Pamukkale University Journal of Engineering Sciences,* 11(2).

[14] Özgünler, M. (2017). Kırsal sürdürülebilirlik bağlamında geleneksel köy evlerinde kullanılan toprak esaslı yapı malzemelerinin incelenmesi. *Süleyman Demirel University Journal of Architectural and Applications,* 2(2).

[15] Aydın, S. (2017). *İletişim yaklaşımıyla sürdürülebilirlik kavramı, yeşil kavramı ve yerel küresel yansımaları ile ilgili bir inceleme örneği* (Master's dissertation, Istanbul University)

[16] Çüçen, A., & Solak, A. (2023). Sürdürülebilir yapı malzemeleri üzerine bir araştırma. *Journal of Technical Science,* 13(1), 1–8.

[17] Sayar, Z., Gültekin, A. B., & Dikmen, Ç. B. (2009, May 13–15). Sürdürülebilir mimarlık kapsamında ahşap ve PVC doğramaların değerlendirilmesi. In *5th International Advanced Technology Symposium (IATS'09)* (pp. 2067–2072). Karabük, Türkiye.

[18] Gaiadergi. *Doğa dostu kerpicin faydaları ve dünyadaki kerpiç yapılar.* Retrieved September 30, 2024, from https://gaiadergi.com/doga-dostu-kerpicin-faydalari-ve-dunyadaki-kerpic-yapilar/

[19] Güneri, M. (2023). *Ayçiçeği sapı ilavesi ile kerpiç malzemenin fiziksel ve mekanik özelliklerinin araştırılması* (Master's dissertation, Trakya University).

[20] De Sensi, B. (2003). Terracruda, la diffusione dell'architettura di terra *(Soil, the dissemination of earth architecture)*.

[21] Perker, Z. S., & Akkuş, K. (2019). Toprak yapı malzemesi ile mimarlık: Çağdaş uygulamalar üzerine bir değerlendirme. *Online Journal of Art & Design, 7(4).*

[22] [22]Döngüsel Tasarım. *Anadolu meleği.* Retrieved September 30, 2024, from https://donguseltasarim.com/portfolio/anadolu-melegi/

[23] Özcan, H. (2010). *Yapı bilgi sistemleri ve mimarlıktaki yeri* (Doctoral dissertation, Istanbul Technical University).

[24] Steneng, C. V. (2020). *Implementation of Revit add-in for analysis of heating plant P&ID* (Master's dissertation, Oslo Metropolitan University)

[25] Gülaçmaz, Ö., Başdemir, H., & Gülaçmaz, E. (2022). Mevcut bir eğitim yapısında enerji verimliliğini iyileştirmeye yönelik bir analiz. *Duzce University Science and Technology Journal,* 10(1), 325–341.

[26] Mutlu, G., & Tuna Kayılı, M. (2020). Geleneksel yatay taşıyıcı düzlemlerin ısıl geçirgenlik değerlerinin günümüz koşullarında irdelenmesi. *European Journal of Science and Technology,* (20), 614–622.

[27] Balcıoğlu, A. (2013). *Geleneksel ve modern bağ evi örneklerinin soğutma enerjisi korunumunda etkili olan tasarım değişkenleri açısından değerlendirilmesi* (Master's dissertation, Istanbul Technical University).

[28] Turkish Standards Institution. (2008). *TS-825: Binalarda ısı yalıtım kuralları*. Ankara, Türkiye.

[29] Koçu, N. (2012). Sürdürülebilir malzeme bağlamında 'kerpiç' ve çatı–cephe uygulamaları (Konya–Çavuş Kasabası örneği). In *6th National Roof and Facade Symposium* (pp. 12–13).

[30] Turkish State Meteorological Service. *Gün derece verileri*. Retrieved September 30, 2024, from https://www.mgm.gov.tr/veridegerlendirme/gun-derece.aspx?g=merkez&m=23-04&y=2023&a=09/

[31] Şensoy, S., Sağır, R., Eken, M., & Ulupınar, Y. (2007). *Türkiye uzun yıllar ısıtma ve soğutma gün dereceleri*. Ankara: State Meteorological Service General Directorate.

International Journal of Innovative Engineering Applications

Journal homepage: https://dergipark.org.tr/ijiea

ASSESSMENT OF THE PROBLEMS FACED BY CONSTRUCTION EQUIPMENT OPERATORS ACTIVELY WORKING IN THE FIELD AND RISK ANALYSIS OF ACTIVELY USED EQUIPMENT

Muhammed Mustafa Uyar*[*1], Ahmet Beyzade Demirpolat[2]

[1]*Department of Motor Vehicles and Transportation Technologies, Arapgir Vocational School,Malatya Turgut Özal University, Malatya, Turkey*
[2]*Department of Electronics and Automation, Arapgir Vocational School, Malatya Turgut Özal University, Malatya, Turkey*

Abstract

Original scientific paper

When research and statistics on operators actively working in the field are carefully examined, it becomes clear how serious the consequences of accidents caused by construction machinery can be. Workplace accidents caused by construction machinery and the issues they encounter rank among the top categories of accidents resulting in death or the loss of the ability to continue working when compared to other workplace accidents in the industry. To minimize workplace accidents and issues that may arise due to operator negligence when using machinery actively on the job site, certain precautions must be taken. To minimize these situations, the following measures are listed: timely maintenance of machinery, increasing the rest periods for both the machinery and the operator, increasing training and practical exercises, conducting a site survey before work begins, and implementing workplace safety measures. In our study, research and technical analyses were conducted on the problems encountered by operators actively working in the field in order to enable them to work more efficiently. Additionally, risk analyses of construction machinery actively used in the field were conducted, and the results were examined. Six types of construction machinery were included in the risk analysis conducted in our study. For forklifts, the importance level was 1 and the risk value was 20, with the highest risk activity identified as hazards arising from trucks, trailers, and workers entering the forklift work area. As a result of our study, the importance of operator training, the organization of the work site, the importance of periodic maintenance of construction equipment, and the importance of controlling the effects of work-related stress have been highlighted.

Keywords: *Construction machinery, operator, occupational health and safety, occupational accident factors, risk analysis.*

SAHADA AKTİF OLARAK ÇALIŞAN İŞ MAKİNELERİ OPERATÖRLERİNİN KARŞILAŞTIKLARI SORUNLARIN DEĞERLENDİRİLMESİ VE AKTİF OLARAK KULLANILAN EKİPMANLARIN RİSK ANALİZİ

Özet

Orijinal bilimsel makale

Sektörde sahada aktif çalışan operatörlere yönelik araştırmalar ve istatistikler dikkatli bir şekilde incelendiğinde, iş makinaları kaynaklı kazaların ne denli ciddi sonuçlara yol açmış olduğu görülmektedir. İş makinaları kaynaklı iş kazaları ve karşılaştıkları sorunlar, neticeleri itibari ile sektördeki öteki iş kazaları ile karşılaştırıldığında ölümle veya devamlı iş yapabilme kabiliyetini kaybetme ile sonuçlanan kaza çeşitleri arasında üst sıralarda yer almaktadır. İş sahasında aktif bir şekilde kullanılan makinaların operatörlerin dikkatsizliği sonucu doğabilecek iş kazaları ve karşılaşabileceği sorunları minimum düzeye indirebilmek için birtakım tedbirler almak zarureti ortaya çıkmıştır. Bu durumları minimuma indirmek için; makine bakımlarının zamanında yapılması, makinenin ve operatörün dinlenme zamanlarının arttırılması, eğitimlerin ve uygulamaların çoğaltılması, çalışma öncesi zemin etüdünün yapılması ve çalışma sahasındaki iş güvenliği tedbirlerinin alınması olarak sıralanmaktadır. Çalışmamızda başlıca etken olarak sahada aktif çalışan operatörlerin daha verimli çalışabilmesi için karşılaştıkları sorunlara yönelik araştırmalar ve teknik incelemeler yapılmıştır. Ek olarak sahada aktif olarak kullanılan iş makinelerinin risk analizleri yapılmış ve sonuçları incelenmiştir. Çalışmamızda yapılan risk analizinde 6 tane iş makinesine yer verilmiştir. Bu iş makinelerinden forkliftler için önem derecesinin 1 olduğu ve risk değerinin 20 olduğu değerler ile en yüksek olan aktivite forklift çalışma alanına kamyon, tır ve çalışanların girmesinden kaynaklı tehlikeler olarak görülmektedir. Çalışmamızın sonucu olarak operatör eğitimlerinin önemi, çalışma sahasının düzeni, iş makinasının periyodik bakımlarının önemi ve iş stresi etkisinin kontrolünün önemi ortaya çıkmıştır.

Anahtar Kelimeler: *İş makineleri, operatör, iş sağlığı ve güvenliği, iş kazası etkenleri, risk Analizi.*

*Corresponding author.
E-mail address: muhammed.uyar@ozal.edu.tr (M. M. Uyar)
Received 01 January 2025; Received in revised form 16 March 2025; Accepted 07 April 2025
 Doi: https://doi.org/10.46460/ijiea.1611365

1 Introduction

Construction machinery, which is one of the biggest requirements of our age, is of great importance in working areas within the developing heavy industry. Developments in construction machinery lead to an increase in studies in the energy sector. In this context, there are alternative fuel production studies that can meet the needs of construction equipment [1-3]. With advancing technology,, it is seen that the accidents that operators using construction machinery are exposed to can be reduced and largely prevented by the importance of operator training and the organization of the work site. In terms of the number of occupational accidents and their severe consequences, accidents on construction machinery are in the first place worldwide [4]. In order to minimize the negativities that occur in construction machinery, work organization is of great importance in terms of the risks that will arise during the work and the measures to be taken. Today, occupational health and safety comes to the forefront in all sectors [5]. The material losses of occupational accidents show that many studies in Europe have reached a grave economic loss dimension [6]. In our country, unlike industrialized countries, there is no decrease in the rate of occupational accidents, but fluctuations from year to year are noteworthy. This is an indication that the necessary precautions are not taken and the lack of education is at the highest level [7]. If the causes of accidents caused by construction machinery are examined, it is seen that approximately 50% of the accidents are caused by the faulty behaviors of the operators and working in the work site without taking the necessary precautions [8]. It is seen as a result of researches that the main cause of accidents is errors caused by lack of training [9]. Due to the unfavorable conditions of the working environment of construction machinery maintenance and repair, accident and injury risks that require occupational health and safety measures may arise. In cases where risks cannot be completely eliminated, it is important to use personal protective equipment suitable for maintenance [10]. As a result of literature reviews and researches on construction machinery, it is possible to summarize the main measures to be taken in order to prevent possible occupational accidents under three main headings as operator training, taking necessary occupational safety measures in the work area, and performing periodic maintenance and repair of construction machinery on time [11]. Reducing and controlling risks is the most important part of an effective occupational health and safety work [12]. Based on these literature researches, in order to eliminate the deficiency in the literature and to contribute, researches and technical examinations were carried out on the problems faced by the operators working actively in the field in order to work more efficiently as the main factor in our study. As a contribution to the literature, our study contributed to the literature in terms of addressing the problems of construction equipment operators working actively in the field and statistically evaluating all the problems experienced not only in terms of occupational safety. In addition to our study, risk analyzes of the construction machinery actively used in the field were made and the results were examined. When the results of our study are examined, it is seen that the most work accidents are experienced in loaders, the reason for this is that the daily working hours are more than 8 hours and the break times are not sufficient. Lack of certification and training of operators, irregularities in the working area, lack of periodic maintenance and scrapping of work machines were seen as the main causes of occupational accidents. When the types of accidents were analyzed, it was determined that 17.4% of the accidents occurred as a result of material fall. Problems arising from inadequate performance of work machines were evaluated at a rate of 16.5%. Failure to comply with occupational safety rules accounted for 13% of the accidents. Problems caused by encountering irregular working area in the work site were determined at a rate of 18.7%. Problems arising from overheating and overloading of work machines were identified at a rate of 13%. Finally, problems caused by work pressure and stress in the workplace were determined as 21.4%. When we look at the occupational safety and health statistics that emerged as a result of research on working with construction machinery in our country, it shows improvement compared to previous years. Our study contributed to the literature by addressing the problems of construction equipment operators actively working in the field and statistically evaluating all the problems experienced not only in terms of occupational safety. As a result of our study, the importance of operator training, the organization of the work area, the importance of periodic maintenance of the work machine and the importance of controlling the effect of work stress have emerged. In the risk analysis study, the highest activity for forklifts with a severity level of 1 and a risk value of 20 is seen as the hazards caused by trucks, trucks and employees entering the forklift work area. For cranes, the highest activity with a severity level of 1 and a risk value of 15 is seen as the hazards arising from the crane getting off the rails and going off the road in the crane gantry walk from the activities of crane use in stacking. For Container Stacking (Rtg Spreader), the activity with a rating of 1 and a risk value of 16, the highest activity is hazards from the rollers in the Mayna lifting system. For Handling Work Machine, the activity with a rating of 1 and a risk value of 15, the highest activity is the hazards caused by the employees entering under the load lifted by the machine. For Stacker Work Machine, the highest activity with a degree of 1 and a risk value of 20 is seen as the dangers arising from the fast maneuvering of the stacker operators with the work machine in the field and exceeding the specified speed limit. For Tractor Work Machine, the activity with a degree of 1 and a risk value of 16, the highest activity is seen as hazards caused by limbs hitting the moving rotating parts of the tractor in operation, getting stuck, etc. A schematic view of our study is given in Figure 1.

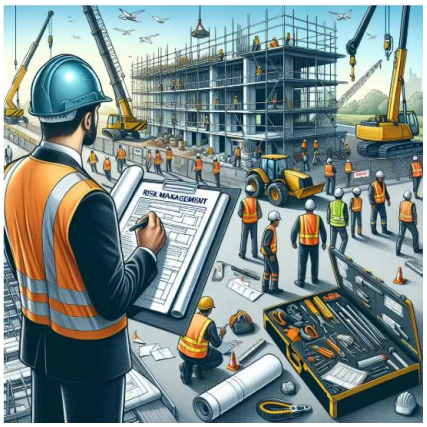

Figure 1. Schematic view showing our study.

2 Statistical Data

Many people lose their lives or become incapacitated due to the problems experienced by operators. In this study, a research was conducted on those working as active operators in the field and statistical data were analyzed.The variety of construction machines actively used in the fields and the proportions of these machines with the highest accident risk are given in Figure 2.

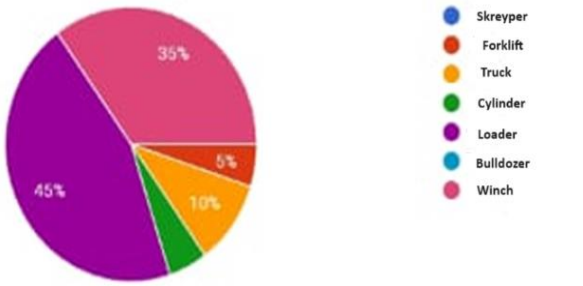

Figure 2. Ratios of the most accident-prone construction equipment active in the field.

There are machines available for different jobs used in different projects. The distribution of construction machinery accidents according to project types is shown in Figure 3 below.

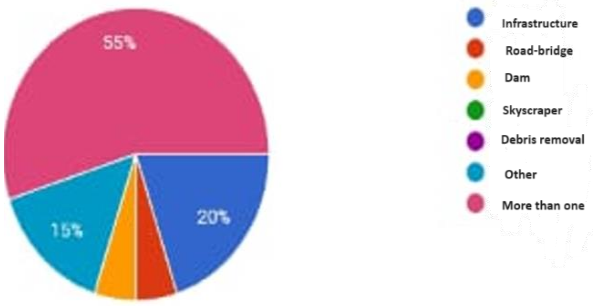

Figure 3. Distribution of construction equipment accidents according to project types.

Experience is an important factor in reducing work accidents. Apart from the experience in the use of construction machinery, knowing the machine is as important as using it. Below, the experience of the operators on the basis of years is given statistically in Figure 4[10].

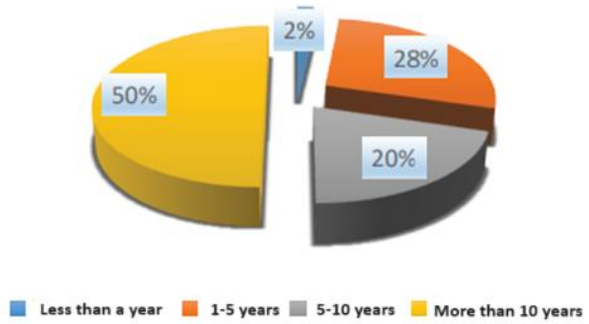

Figure 4. Years of experience of construction equipment operators.

The starting times and breaks of the operators at the work site are important parameters for the healthy execution of the work. Figure 5, Figure 6 and Figure 7 below show the starting times of the operators, the duration of their daily work and the number of breaks they take at intervals of hours, respectively.

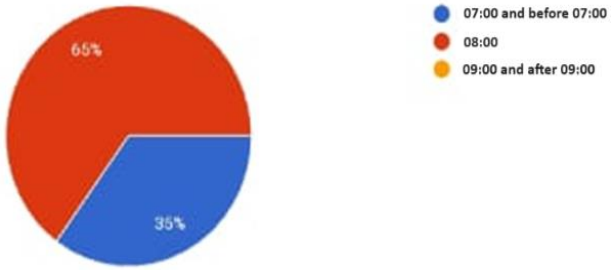

Figure 5. Starting times of construction equipment operators.

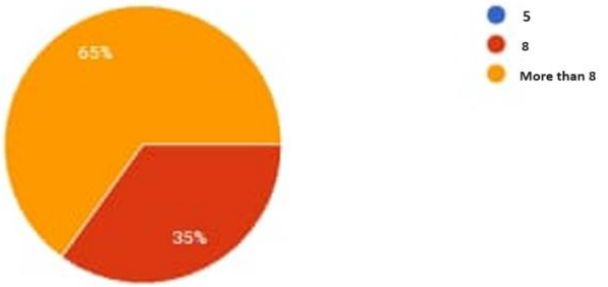

Figure 6. Daily working hours of construction equipment operators.

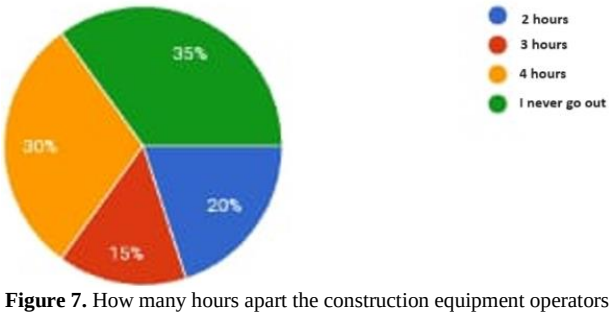

Figure 7. How many hours apart the construction equipment operators take breaks.

In line with these examinations, it is concluded that the operators do not allocate much time for rest, their daily working hours are long and working in this direction increases the possibility of accidents.

The educational status of the operators using construction machinery, their occupational health and

safety training, whether they have occupational safety certificates and driver's licenses, and from whom they received their operator training, the issues that may be effective in the formation of occupational accidents are examined in figures 8, 9, 10 and 11.

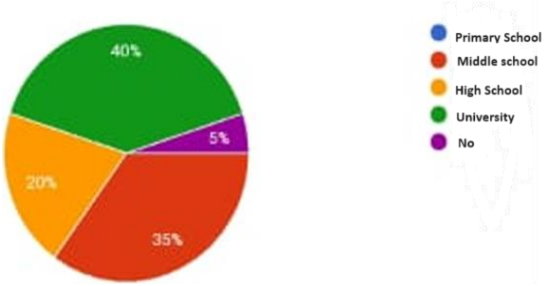

Figure 8. Education level of construction equipment operators.

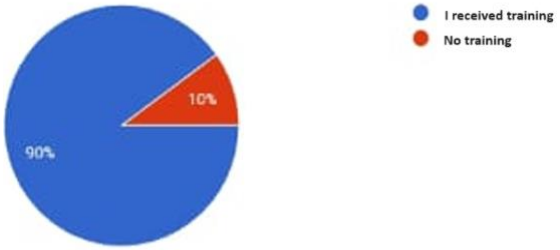

Figure 9. Occupational health and safety trainings received by construction equipment operators.

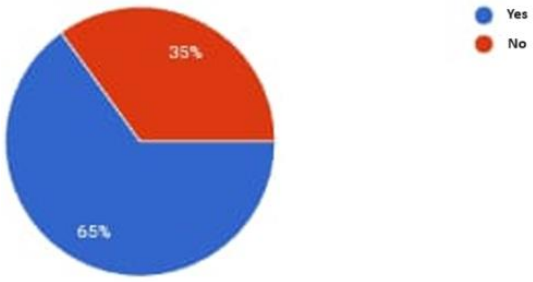

Figure 10. Whether construction equipment operators have occupational safety certificates and driving licenses.

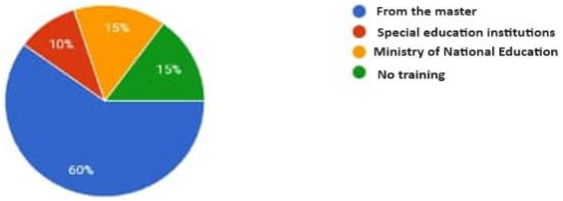

Figure 11. From whom the construction equipment operators received their operator training.

In line with these examinations, it is seen that it is important to have an operator's license. Thanks to the authorized institutions, this number is increasing day by day. It is important that the document that people using construction machinery must have belongs to the relevant machine model. It is wrong for an operator with a Backhoe-Loader work machine license to use another machine on the construction site. Each construction machine requires a different driver's license. The training received through the courses provided by authorized institutions ensures that machines of different models are used by people who have received training on that model. A driver's license is only a document related to machine use. Apart from this, it is important that each operator receives training on the use of the machine, its maintenance and OHS rules that must be followed during use. When the types of accidents that occur in construction machinery are examined, the most common accidents were tried to be determined. The aim here is to determine the most common types of accidents and to further increase the precautions. The leading accident types are given in Figure 12.

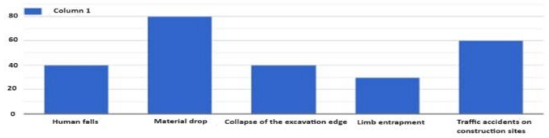

Figure 12. Types of accidents on construction equipment.

When the problems arising from the insufficient performance of the construction machinery were evaluated as 1 being the least and 5 being the most, the responses were analyzed. The statistical percentages are given in Figure 13.

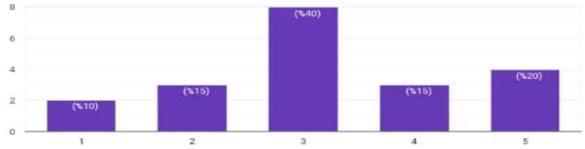

Figure 13. Problems caused by inadequate performance of construction equipment.

The responses of the operators to the problems that occur in case of non-compliance with occupational safety rules were analyzed when 1 is the least and 5 is the most. The statistical percentages are given in Figure 14.

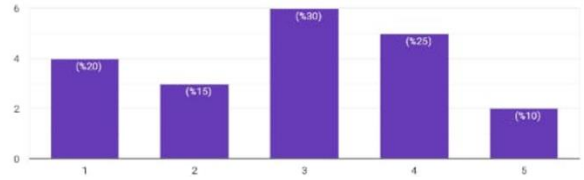

Figure 14. Accidents that occur when occupational safety rules are not followed.

Problems related to the work area, which operators encounter irregularly, without ground surveys, without taking the necessary precautions in the work areas, were examined. The measures to be taken against these problems were considered among the most important issues to protect worker health. When the problems occurring in case of encountering an irregular working area at the work site were evaluated as 1 being the least and 5 being the most, the answers encountered were examined. The statistical percentages are given in Figure 15.

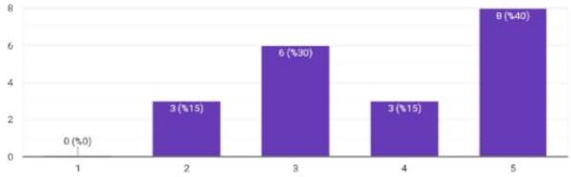

Figure 15. Encounters with irregular workspace at the worksite.

Problems related to work pressure and stress have been examined by their employers in the workplaces of the operators. The measures to be taken against these problems are important for the worker to carry out the work in a healthy way and to make healthy decisions. When the problems occurring in case of encountering work pressure and stress in the workplace were evaluated as 1 being the least and 5 being the most, the answers encountered were examined. The statistical percentages are given in Figure 16.

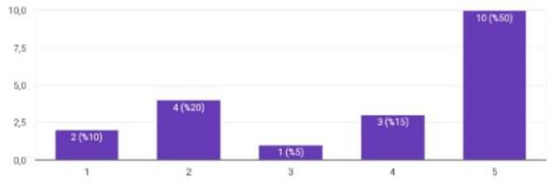

Figure 16. Work pressure and stress in the workplace

Occupational accidents caused by mechanical failures that may occur due to overheating and overloading of construction machinery are among the other important issues examined. When the problems occurring in case of overheating and overloading of construction machinery were evaluated as 1 being the least and 5 being the most, the responses were analyzed. The statistical percentages are given in Figure 17.

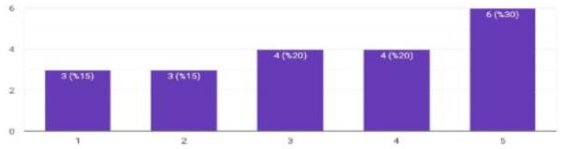

Figure 17. Overheating and overloading of construction equipment.

3 Risk Analysis

One of the most important causes of occupational accidents is the lack or incomplete risk analysis in critical areas. Risk assessment is defined as "the necessary studies to be carried out in order to identify the hazards that exist in the workplace or that may come from outside, to analyze and grade the factors that cause these hazards to turn into risks and the risks arising from hazards and to decide on control measures". With Risk Analysis Studies on Construction Machinery, serious consequences such as injury, loss of limbs, damage to the heart and respiratory systems and death can be prevented. In this respect, risk analysis of 6 construction machines was carried out in our study. In the risk analysis method applied as an example to the study to determine the risks, the matrix method was selected. The reason for choosing this method is that the results of possible risks can be graded. In the event of the realization of the hazard, the severity of the harm or damage that this hazard will cause to people, workplace and environment can be evaluated. According to the magnitude of the risk value, i.e. the height, the urgency of the measures to be taken and what can be done as a precaution is determined and the risk analysis study is completed.

3.1 Risk Analysis Study on Forklifts

In the risk analysis study, the highest activity for forklifts with an importance level of 1 and a risk value of 20 is seen as the hazards caused by trucks, trucks and employees entering the forklift work area. Risk analysis study on forklifts is given in Table 1.

Table 1. Risk analysis study on forklifts.

Activity	Danger	Root Cause of Danger	Risks Arising from Hazard	Impacts	Exposed Persons	Probability	Violence	Risk	Degree of Importance
Loading and unloading	Trucks, trucks and employees entering the forklift work area	Uncontrolled entry of employees and vehicles into the forklift work area	Risk of collision of forklifts and vehicles, risk of crushing workers	Material damage accident, loss of life, injury	Truck and lorry drivers, container yard workers	4	5	20	1
Maintenance, repair and control works	Diesel engine electrical connections	Starting work without taking the necessary safety precautions	Risk of electric shock	Injury	Forklift machine operators, electricians, engine mechanics	2	4	8	2
Maintenance, repair and control works	Moving rotating parts of a diesel generator in operation	Movable rotating parts	Risk of injury or entrapment of limbs due to contact of body parts	Injury	Engine mechanics, electricians	3	3	9	2
Maintenance, repair and control works	Electrical circuits on the forklift work machine	Exposure to electric current	Risk of electric shock	Injury	Electricity masters	2	4	8	2
Maintenance, repair and control works	Pin removal operations on machine connection points	Throwing of parts on the machine	Damage to employees due to swinging and dislocation of apparatus	Injury	Workshop masters, engine mechanics	3	3	9	2
Tire change	Tire changes on machines	High air pressure inside the tire, components that allow the tires to be fixed	Risk of crushing the worker during tire removal	Injury	Engine mechanics, external service	4	3	12	2
Loading and unloading	Risk of falling load carried by forklift crushing the worker	Failure to load the load safely onto the work machine	Falling of the transported or suspended load, crushing the employee as a result of its movement, overturning of the forklift	Loss of life, injury	Forklift operator, chock and pointer worker	3	5	15	1

3.2 Risk Analysis Study on Cranes

For Cranes, the highest activity with a rating of 1 and a risk value of 15 is the use of cranes in stacking activities. Risk analysis study on Cranes is given in Table 2

Table 2. Risk analysis study on Cranes.

Activity	Danger	Root Cause of Danger	Risks Arising from Hazard	Impacts	Exposed Persons	Probability	Violence	Risk	Degree of Importance
Stacking	Rope and rope pulleys	Failure to check the ropes, entry of employees or drivers into the crane working area	Risk of rope breakage, risk of damage to the ropes by falling parts as a result of rope pulleys breaking	Loss of life, injury, material damage	Porch workers, truck drivers who load and unload cargo at the porch	2	5	10	2
Stacking	Control and maintenance work to be carried out at the crane top	Starting work without taking safety precautions	Risk of falling from height	Loss of life, injury	Engine mechanics, electricians and external service personnel performing periodic checks	3	5	15	1
Stacking Crane Usage	Crane derails during gantry walk and goes off the road	Deformation of the crane rails, disintegration of the bearing inside the crane wheels, fast movement of the crane when loaded	Risk of braking failure due to crane inertia, risk of damage to vehicles and cargo, risk of crushing workers	Accident with loss of life, injury and property damage	Crane operators, truck drivers and shed workers	3	5	15	1
Stacking Crane Usage	Using the crane at an inappropriate speed	Failure of the crane operator to comply with the specified written instructions	Risk of the crane going off the road and harming people working around it, risk of damage to crane mechanical parts	Accident with loss of life, injury and property damage	Crane operators, truck drivers and shed workers	2	5	8	2
Stacking Crane Usage	Stairs to reach the load lifting crane platform	Contamination of stairs with dust and slippery materials, damaged stair guards and steps	Fall risk	Injury	Engine mechanics, electricians and external service personnel carrying out the inspection process	3	3	9	2
Stacking Crane Usage	Using the crane above its carrying capacity, lifting loads exceeding the maximum carrying capacity	Failure of the operator to comply with the specified crane operating instructions	Risk of damage to lifting equipment such as ropes, hooks, etc. as a result of damage to the load and damage to the surrounding area	Loss of life, injury, property damage accident	Crane operators, truck drivers and shed workers	3	5	15	1
Stacking Crane Usage	Planned maintenance and malfunctions not being eliminated on time	Inappropriate planned and breakdown maintenance	Risk of serious accidents due to improper operation of the system as a result of improper maintenance	Accidents involving loss of life, injury, property damage	Crane operators, truck drivers, truck drivers and shed workers	2	5	10	2
Using Cranes for Stacking	Leaving loads on the crane walkway, parking vehicles	Failure to comply with the specified stacking plan, failure to comply with the specified safety rules by vehicle drivers and failure to supervise this situation by employees	Risk of crane derailment due to collision and damage to the surrounding area	Accidents involving loss of life, injury, property damage	Crane operators, truck drivers, truck drivers and shed workers	2	5	10	2
Loading crane use in stacking	Crane monorail mechanism and other construction, suspended load on the crane	Uncontrolled entry of employees into the crane movement and working area, incomplete planned and breakdown maintenance works	Risk of falling parts, falling suspended load, crushing the worker as a result of movement	Loss of life, injury	Crane operators, truck drivers, truck drivers and shed workers	3	5	15	1

3.3 Risk Analysis Study on Container Stacking (Rtg Spreader) Work Machine

For Container Stacking (Rtg Spreader), with a rating of 1 and a risk value of 16, the highest activity is seen as hazards arising from the rollers in the Mayna heave system. Risk analysis study on Container Stacking (Rtg Spreader) Work Machine is given in Table 3.

Table 3. Risk analysis study on container stacking (Rtg Spreader) work machine.

Activity	Danger	Root Cause of Danger	Risks Arising from Hazard	Impacts	Exposed Persons	Probability	Violence	Risk	Degree of Importance
Container stacking and loading	Vehicles and workers entering work machine walkways	Failure to sweep construction equipment walkways	Risk of collision of construction machinery and vehicles and crushing of workers	Material damage accident, loss of life, injury	Truck and lorry drivers, container yard workers	3	5	15	1
Container stacking and loading	Construction equipment system	Failure of the signaling system feeding the Agss system to work properly	Risk of the machine going off the road, hitting surrounding vehicles	Loss of life, injury	Construction equipment operators, vehicle drivers, port workers	2	5	10	2
Container stacking and loading	Diesel generator exhaust circuit	High temperature and toxic gases	Risk of injury and poisoning from the engine	Risk of injury from burns, risk of poisoning from inhalation of toxic exhaust gases	Operators, electricians, engine mechanics	3	5	15	1
Container stacking and loading	Reels in the Mayna heave system	Rotary moving parts, part drop into rtg working area	Risk of limb entrapment, risk of eye damage from fragments,	Injury	Port site workers, operators, truck drivers, tallymen	4	4	16	1
Container stacking and loading	Rtg Spreader	380 volt electrically moving chains and other rotating moving parts, falling parts of the spreader components into the rtg work area	Risk of electric shock during work, risk of limb entrapment in moving parts, risk of falling of broken parts	Injury	Engine mechanics, electricians, truck and truck drivers	3	4	12	2
Container stacking and loading	Planned maintenance and malfunctions not being eliminated on time	Inappropriate planned maintenance and troubleshooting	Risk of serious accidents due to improper maintenance	Accidents involving loss of life, injury, property damage	Rtgoperator, truck and lorry drivers	3	5	15	1

3.4 Handling Work Machine Risk Analysis Study

For the Handling Work Machine, the highest activity with a rating of 1 and a risk value of 15 is seen as the hazards arising from workers entering under the load lifted by the machine. Risk analysis study on Handling Work Machine is given in Table 4.

Table 4. Risk analysis study on handling work machine.

Activity	Danger	Root Cause of Danger	Risks Arising from Hazard	Impacts	Exposed Persons	Probability	Violence	Risk	Degree of Importance
Loading and Unloading	Trucks, trucks and employees entering the handling machine work area	Personnel violating the working area of the crane	Risk of collision of machines and vehicles, risk of crushing workers	Material damage accident, loss of life, injury	Truck and lorry drivers, scaffolders, engine mechanics and electricians	3	5	15	1
Use of construction machinery for unloading and loading loads	Batteries on the construction machine	Splashing of acidic liquid in batteries into the body and eyes	Risk of acid in the eyes during battery inspection, risk of battery explosion, risk of electric shock	Loss of limb, injury	Electrical craftsmen, engine mechanics	3	2	6	3
Operations related to the electricity system	Handling machine electrical circuits	Starting work without taking appropriate precautions	Risk of electric shock	Injury	Electricity masters	3	2	6	3
Maintenance work	Maintenance work to be carried out in the hydraulic system of the handling machine	High hydraulic pressure, high hydraulic oil temperature	Risk of pressurized hydraulic fluid penetrating the skin, getting into the eyes	Injury	Motor mekanik ve elektrik ustaları	2	3	6	3
Maintenance and control works	Work to be done on the machine boom system	Height at which injury is likely in the event of a fall	Risk of falling due to working at height	Injury, loss of life	Engine mechanics, workshop foremen and electricians	2	5	10	2
Unloading and loading of cargo	Fast maneuvering of the handling machine operators with the work machine in the field	Exceeding the speed limits set at the port	Risk of collision with vehicles, risk of crushing the workers on board, risk of dropping the load on the scaffold, vehicles and ship	Loss of life, injury, material damagePort dock workers, truck-truck drivers, motor mechanics, ship workers	Port dock workers, truck-truck drivers, motor mechanics, ship workers	2	5	10	2
Loading and Unloading	Workers under the load lifted by the machine	Personnel violating the working area of the crane	Risk of burden on employees	Loss of life, injury	Port site workers, truck drivers, subcontractor employees	3	5	15	1
Part replacement	Replacements of attachments attached to the boom end of a handling machine	Unsuitable working environment	Risk of staff slip and fall	Injury	Engine mechanics	3	4	8	2
Loading and Unloading	Suspended load on crane	Personnel violating the working area of the crane	Risk of the suspended load falling, crushing the worker as a result of its movement	Loss of life, injury	Crane operators, truck drivers, truck drivers and shed workers	2	5	10	2

3.5 Stacker Work Machine Risk Analysis Study

For the Stacker Work Machine, the highest activity with a degree of 1 and a risk value of 20 is seen as the hazards arising from the fast maneuvering of the Stacker operators with the work machine in the field and exceeding the specified speed limit. Risk analysis study on Stacker Work Machine is given in Table 5
.

Table 5. Risk analysis study on stacker work machine.

Activity	Danger	Root Cause of Danger	Risks Arising from Hazard	Impacts	Exposed Persons	Probability	Violence	Risk	Degree of Importance
Use of cranes in stacking	Trucks, lorries and employees entering the stacker work area	Occupation of stacker workspace	Risk of collision with vehicles and crushing of workers by construction equipment	Material damage accident, loss of life, injury	Truck and lorry drivers, container yard workers	3	5	15	1
Use of cranes in stacking	Stacker operators maneuvering fast with the work machine in the field, exceeding the set speed limit	Exceeding the set speed limit	Risk of accidents, risk of crushing personnel in the work area, risk of hitting cargo and containers	Loss of life, injury, material damage	Field workers, truck drivers	4	5	20	1
Use of cranes in stacking	The presence of workers or vehicles in the blind spot of the work machine during reverse maneuvering	Failure to see the area where the rear weight is located during reverse maneuvering with the construction machine	Risk of crushing of employees, risk of collision with passenger vehicles	Accident with material damage, loss of life	Field workers, truck drivers, passenger car drivers	3	5	15	1
Use of cranes in stacking	Lamps indicating the position of the spreader twistlocks not working properly	Use of construction machinery without repairing the faults	Risk of dropping the container, risk of damage to machinery and equipment	Accident with material damage, injury	Truck drivers, stacker operator	2	5	10	2

3.6 Tractor Work Machine Risk Analysis Study

For the Tractor Work Machine, the highest activity with a rating of 1 and a risk value of 16 is seen as hazards arising from the impact of limbs on the moving rotating parts of the tractor in operation, getting stuck, etc. Risk analysis study on Tractor Work Machine is given in Table 6.

Table 6. Risk analysis study on tractor work machine.

Activity	Danger	Root Cause of Danger	Risks Arising from Hazard	Impacts	Exposed Persons	Probability	Violence	Risk	Degree of Importance
Fueling the tractor	Tractor fuel tank and fuel in the tank	Starting the fueling process without taking safety precautions	Explosion, fire	Loss of life, injury, property damage	Tractor operator, fuel dispenser, field workers, vehicle drivers	3	4	12	2
Maintenance work	Impact, jamming, etc. of limbs on moving rotating parts of the tractor in operation.	Rotary moving parts	Risk of injury or entrapment of limbs due to contact of body parts	Injury	Engine mechanics, Electricity masters	4	4	16	1
Maintenance work	Electrical circuits on the tractor work machine	Exposure to electric shock	Risk of electric shock	Injury	Electricity masters	3	4	12	2
Maintenance work to be performed on the tractor by the technical department	Pin removal operations on machine connection points	Hand tools used in maintenance or parts removed such as pins, bearings, etc.	Damage to the personnel performing the work due to swinging, dislocation, etc. of the apparatus used	Injury	Workshop masters, engine mechanics	2	4	8	2
Material transportation	Tractor water tanker attachment	Rapid maneuvering, the employee climbing on the tanker doing control work without taking the necessary safety precautions	Risk of overturning of the tanker, risk of falling of personnel climbing on the tank	Injury due to fall, accident with material damage	Tractor operator	2	4	8	2

4 Conclusions

Construction machinery has an importance that cannot be ignored today in working areas. The danger posed by construction machinery used in the industrial sector, which is the locomotive of the world economy, should not be overlooked. Operators with professional competence should be employed in construction sites, and construction machinery personnel working in construction sites should have an operator certificate related to the construction machinery they use. Operators should be trained on the dangers arising from machinery. The content of the trainings should cover accidents at world standards and emphasize the precautions to be taken. In addition, the contents of these trainings should also include occupational safety solutions applied at world standards. Occupational accidents are an important cost factor for employees and businesses and negatively affect employee and organizational productivity. Material and moral losses as a result of occupational accidents also cause great damage to the national economy. For this reason, it is necessary to identify the causes of occupational accidents in enterprises, to take the necessary measures and to supervise them in order to work effectively and efficiently in a healthier and peaceful environment. When the results of our study are examined, it is seen that the most occupational accidents are experienced in loaders, the reason for this is that the daily working hours are more than 8 hours and the break times are not sufficient. Lack of certification and training of operators, irregularities in the working area, periodic maintenance and scrapping of work machines were seen as the main causes of occupational accidents. When the accident types were analyzed, it was determined that 17.4% of the accidents were caused by falling materials. Problems caused by inadequate performance of work machines were evaluated at a rate of 16.5%. Accidents occurring in case of non-compliance with occupational safety rules were determined at a rate of 13%. Problems caused by encountering irregular working area at the work site were determined at a rate of 18.7%. Problems arising from overheating and overloading of work machines were found to be 13%. Finally, problems caused by work pressure and stress in the workplace were found to be 21.4%. When we look at the statistics on occupational safety and health that emerged as a result of research on

working with construction machinery in our country, it shows improvement compared to previous years. Our study contributed to the literature by addressing the problems of construction equipment operators who are actively working in the field and statistically evaluating all the problems experienced not only in terms of occupational safety. As a result of our study, the importance of operator trainings, the organization of the working area, the importance of periodic maintenance of the work machine and the importance of controlling the effect of work stress have emerged. In the risk analysis study, the highest activity for forklifts with a severity level of 1 and a risk value of 20 is seen as the hazards caused by trucks, trucks and employees entering the forklift work area. For cranes, the highest activity with a severity level of 1 and a risk value of 15 is seen as the hazards arising from the crane getting off the rails and going off the road in the crane gantry walk from the activities of crane use in stacking. For Container Stacking (Rtg Spreader), the activity with a rating of 1 and a risk value of 16, the highest activity is hazards from the rollers in the Mayna lifting system. For Handling Work Machine, the activity with a rating of 1 and a risk value of 15, the highest activity is the hazards caused by the employees entering under the load lifted by the machine. For Stacker Work Machine, the highest activity with a degree of 1 and a risk value of 20 is seen as the dangers arising from the fast maneuvering of the stacker operators with the work machine in the field and exceeding the specified speed limit. For Tractor Work Machine, the activity with a degree of 1 and a risk value of 16, the highest activity is seen as hazards caused by limbs hitting the moving rotating parts of the tractor in operation, getting stuck, etc.

Declaration

Ethics committee approval is not required.

References

[1] Hazar, H., & Uyar, M. (2015). Experimental investigation of isopropyl alcohol (IPA)/diesel blends in a diesel engine for improved exhaust emissions. *International Journal of Automotive Engineering and Technologies, 4*(1), 1–6.

[2] Uyar, M., & Aydın, H. (2022). Production of low sulfur diesel-like fuel from crude oil wastes by pyrolytic distillation and its usage in a diesel engine. *Energy, 244*, 122683.

[3] Hazar, H., Uyar, M., Aydın, H., & Şap, E. (2016). The effects of apricot seed oil biodiesel with some additives on performance and emissions of a diesel engine. *International Journal of Automotive Engineering and Technologies, 5*(3), 102–114.

[4] Ercan, A. (2010). Evaluation of worker health and safety in the construction sector in Turkey. *Politeknik Journal, 13*(1), 49–53.

[5] Gürcanlı, G. E. (2008). The current situation in occupational safety in the world and Turkey and the construction sector. *TMMOB Ölçü Magazine*, February 2008, 90–98.

[6] Yalçın, E., & Taçgın, E. (2016). Construction sector and occupational safety measures in excavation applications. *Chamber of Civil Engineers (İMO) Bursa Bulletin*, (65), 9–11.

[7] Vocational Qualification Authority. (2011). *National occupational standard: Construction machinery maintenance and repairer – Level 4* (Reference Code: 09UMS0010-4). Official Gazette, 26 May 2015, No: 29367.

[8] Altınöz, H., Uzun, M., Bahadır, Y., Sarmusak, F., & Karagöz, Y. (2011). Occupational accidents frequently encountered in the use of construction machinery and precautions to be taken. In *3rd Occupational Health and Safety Symposium, Çanakkale*.

[9] Gürcanlı, E. (2013). Turkish Medical Association Occupational Health and Safety Association. *İş Güvenliği Dergisi*, (48), 20–29.

[10] Pehlivan, M., Özakın, B., & Çakmak, A. (2017). The importance and future of construction equipment operator program in Turkey. *Mehmet Akif Ersoy University Journal of Institute of Science and Technology, 8*(Special 1), 140–145.

[11] Yakar, H., & Taçgın, E. (2019). Evaluations and suggestions for reducing occupational accidents encountered in the use of construction machinery. *Engineer and Machinery, 60*(697), 303–326.

[12] Taşkıran, N. (2019). *Cognitive work analysis: A study on hydraulic backhoe and operator interaction* (Master's dissertation, Gazi University).

[13] Xu, Z., & Da, Q. L. (2003). An overview of operators for aggregating information. *International Journal of Intelligent Systems, 18*(9), 953–969.

International Journal of Innovative Engineering Applications

Journal homepage: https://dergipark.org.tr/ijiea

REPLACING ARCHITECTS AND URBAN DESIGNERS WITH AI APPLICATIONS TO REACH MORE AESTHETIC DESIGNS

Azadeh Rezafar*[1]

[1]*Istanbul Arel University, Faculty of Architecture, Department of Architecture, Tepekent Campus, Istanbul, Turkey*

Abstract

Original scientific paper

Artificial intelligence (AI), one of the most advanced technologies available today, is quickly changing our lives. It has only been in the last few years that the general public has had access to a multitude of new artificial intelligence technologies that enable anyone to work with it and produce literature and art at a speed and quality never before imaginable. AI is also increasingly transforming the domains of urban planning and design. Its integration into various fields facilitates the resolution of complex issues and raises the efficiency of planning and design processes. Despite being mentioned, there has also been much controversy around this situation. Indeed, AI design has a few well-known and noteworthy advantages, such as rapid and inexpensive data analysis. However, to what extent can AI produce aesthetically appealing designs? To create more aesthetically pleasing designs, this research aims to examine the usability of the designs produced by artificial intelligence utilizing concept data rather than the designs of architects and designers. It is evident from this that, AI can never fully grasp the human creativity, intuitive thinking, and cultural sensitivity that form the soul of architecture and design; true innovation and meaningful design can only emerge from the dynamic collaboration between the power of technology and the vision of architects and designers.

Keywords: *AI-generated design, technology, design, aesthetic, architecture and urban planning.*

DAHA ESTETİK TASARIMLARA ULAŞMAK İÇİN MİMARLARI VE KENTSEL TASARIMCILARI YAPAY ZEKA UYGULAMALARIYLA DEĞİŞTİRMEK

Özet

Orijinal bilimsel makale

Günümüzdeki en yeni teknolojilerden biri olan yapay zeka (YZ), hayatımızı hızlı bir şekilde değiştirmektedir. Daha önce hiç hayal edilemeyen bir hız ve kalitede edebiyat ve sanat üretimini sağlayan çok sayıda yeni yapay zeka teknolojisine erişimi, ancak son birkaç yılda gerçekleşmiştir. YZ ayrıca şehir planlama ve tasarım alanlarında daha fazla değişimleri sağlamaktadır. Çeşitli alanlara entegrasyonu, tasarım ve planlama süreçlerinin verimliliğini artmakta ve karmaşık sorunların çözümünü kolaylaştırmaktadır. Bu konu çok sayıda tartışmayıda beraberinde getirmektedir. YZ tasarımının, hızlı ve ekonomik veri analizi gibi birçok tanınmış ve önemli avantajı sağlamaktadır. Ancak YZ ne kadar estetik tasarımlar yapabilir? Bu araştırma, mimarların ve tasarımcıların tasarımları yerine konsept verilerini kullanarak, yapay zeka ile daha estetk tasarımların üretilebilirliğini incelemeyi amaçlamaktadır. Buradan da anlaşılacağı üzere, yapay zekâ, mimarlık ve tasarımın ruhunu oluşturan insan yaratıcılığını, sezgisel düşünceyi ve kültürel duyarlılığı asla tam olarak kavrayamaz; gerçek yenilik ve anlamlı tasarım, ancak teknolojinin gücü ile mimarların ve tasarımcıların vizyonu arasındaki dinamik işbirliğinden doğabilir.

Anahtar Kelimeler: *Yapay zekayla üretilen tasarım, teknoloji, tasarım, estetik, mimarlık ve şehir planlama.*

1 Introduction

Cities offer both physical and spiritual platforms and infrastructures that enable people to reach their full potential. As a result, these individuals produce commodities and services that raise the general public's standard of living [1]. Since the extraordinary increase in urbanization worldwide, which is predicted to reach roughly 68% by 2050 [2], cities are coming under greater pressure from governmental, social, economic, and environmental perspectives. Consequently, resilience and sustainable urban development have gained significant attention, in recent years[3]. This shift has prompted designers and urban planners to prioritize sustainability and a sense of identity in their projects, recognizing that these elements are essential for creating livable urban

*Corresponding author.

E-mail address: azadehrezafar@arel.edu.tr (A. Rezafar)

Received 06 February 2025; Received in revised form 13 April 2025; Accepted 09 May 2025

 Doi: https://doi.org/10.46460/ijiea.1634363

environments[4]. To create more resilient, responsive, sustainable, and informed urban design and planning, leveraging big data analysis is needed. In other words, decision-making that is better informed, more effective, and more responsive is made possible by the growing integration of data analysis into urban planning and architecture. However, the architectural and urban design industries have not yet included many sources of information in their workflow, despite the vast amount of urban data available to them[5].

Especially, developing countries are strained by this, particularly regarding time and financial resources. Growing computational power and developing computational technologies, like artificial intelligence (AI), open up new ways to address urban problems[6]. Particularly the long-standing sustainable development issues of social justice, economic growth, and environmental preservation[7] are among these problems. Artificial Intelligence (AI) is poised to become a primary tool for local governments to achieve sustainable and intelligent growth due to its sophisticated capabilities[8]. AI improves decision-making in urban design, building performance, and transportation optimization through data analysis. This technology is increasingly being used to increase efficiency and sustainability in urban planning and architecture. AI has clear impacts on urban planning because it can be used to predict what people want or how they will behave [9]. Governments worldwide are racing to establish dominance in artificial intelligence through strategic national initiatives. For instance, the AI strategy put forward by the German government also anticipates that AI will be crucial to sustainable development[10]. The state participates in these strategies in three ways: first, as a regulator, establishing the legal framework for the development and application of AI; second, as a facilitator, constructing infrastructure or granting access to public data to AI companies; and third, as an AI user, utilizing AI in public administration or to deliver public services[11]. Likewise, an AI strategy that acknowledges the current global trend toward smart cities and smart urban infrastructure was announced by the Australian government in 2019[12]. So, a field of increasing interest and investigation is the incorporation of Artificial Intelligence into the architectural and urban design process. So, AI in architecture transcends being merely a design tool, instead functioning as a transformative technological force that restructures the entire architectural ecosystem, creating new methodologies, professional roles, and knowledge frameworks while fundamentally altering the relationship between architects, clients, and the built environment.

In addition to this Artificial Intelligence has emerged as a noteworthy tool in the fields of aesthetic architecture and picture production, providing novel avenues for design innovation, visualization, and creative artistic expression[13]. AI technologies are changing how artists work, creating new human-machine collaborations that expand artistic possibilities and aesthetics [14]. With just a basic natural language command, users may now create images or text thanks to a multitude of AI technologies that have been made public in the past year alone[15]. It is generally accepted that AI is capable of analyzing architectural designs to assess aesthetic aspects according to predetermined standards like balance, symmetry, and proportion. On the other hand, the literature reveals the parameters such as order, balance and harmony, proportions, rhythms, scale, character and identity, and the meaning of architecture (intellectual, formal, and spiritual ideas) that create aesthetic pleasure in architecture and designs [16]. Architects can improve their designs and attain desired aesthetic results by using this method. The aesthetic parameters and the basis on which these parameters are decided are outside the scope of this article. Analyzing the parameters one by one is the subject of another article. However, the literature-based aesthetic parameters given here are also accepted within the scope of this article.

Artificial intelligence tools can examine patterns in architectural tastes and styles by analyzing information from sources like design journals and social media. This makes it easier for architects to keep up with and apply design trends to their work. Nonetheless, the question now comes up, can AI replace architects and urban designers in reaching more aesthetic designs? So, in addition to AI data analysis, can it also perform aesthetic analysis? This article does not criticize or endorse the role of artificial intelligence in architecture and urban design areas. On the contrary, this article aims to analyze how artificial intelligence is used in architectural design processes and reveal its strengths and weaknesses. Finally, it tries to offer suggestions that can be improved for the future.

The background of the literature is covered in the second section. The section has presented the idea of AI, and its visual effect in the design area. The research plan, which combined a case study and a survey of the literature, is described in section three. Three legendary architectural projects in Istanbul/ Turkey have been selected in this case. The first one is a public place/ regional place. The second and third are residential apartment designs. The projects, which are classified as architectural projects with a design concept rather than contractor work, were chosen for their potential in modern architectural design.

The concepts of these projects, which were gathered from the literature and/or their original sites were used as prompts for generating digital images from short descriptive texts[17], for AI design. So it was important that selecting the cases must have design concepts. The findings of the study are discussed in section four under the topics of AI's advantages and disadvantages, and suggestions for improvement.

As a result, AI and designers must work together, thus it's important to address who makes design decisions.

2 Research Plan

Figure 1 depicts the process of conducting research. This study's methodology employed a descriptive-analytical approach. The theoretical investigation, which was compiled from books, relevant scientific websites, research articles, and studies, was made visible through the use of this technique. The approach contrasts theoretical concepts related to the cases of study. Four steps form the basis of the research, as Figure 1 illustrates. Research questions, a literature review, research of the case studies, and comparison and conclusion are these steps.

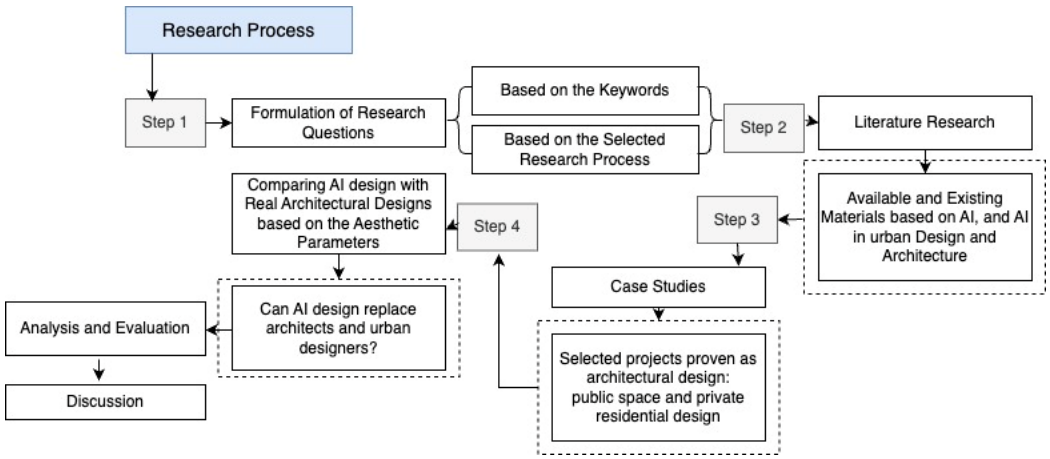

Figure 1.The research process (by author, 2024).

3 Literature Background

3.1 AI in Contrast to Conventional Techniques and Tools

Within the fields of science, business, and technology, terminology like artificial intelligence and cognitive technologies are already widely used. In general, nonetheless, they arouse various connotations in society, where their primary source of knowledge is science fiction cinema[18]. AI originated in the 1940s and was first mentioned in a short science fiction narrative written by Isaac Asimov. The landmark book "Computing Machinery and Intelligence" by Alan Turing, who developed the concept of computing intelligent machines, was published in 1950 and is currently regarded as the standard for determining an artificial system's level of intelligence. Irving John Good made predictions regarding artificial intelligence that might surpass human intelligence as early as 1966[19]. Since then, artificial intelligence has achieved milestone after milestone and is still advancing at a rapid rate. Later, more research was conducted, particularly in the 1980s when Japan began making significant investments in artificial intelligence[20]. The foundation of artificial intelligence is the creation of autonomous agents with the ability to think and plan toward an objective without underlying environmental knowledge[21]. AI already influences and interacts with people's everyday lives on an almost daily basis[22]. AI is among the most revolutionary technologies of our day. Because AI provides smart governance options and platforms that are both efficient and effective, it has become an essential component of urban services in recent years[23]. Artificial Intelligence is predicted to change how governments run, how people live, and how economies function overall. On the nature and scope of AI's influence, however, there is disagreement. On the one hand, it might improve economic development and productivity while raising public service efficiency. However, it can also make labor market imbalances worse and make national and international disparities worse[24]. According to Gummesson (2023) [25], Since artificial intelligence is still in its infancy and evolving, it is famously hard to define without changing our understanding of what constitutes AI. As of right now, there isn't a single, widely agreed-upon definition for "artificial intelligence"[26]. But the definition is accepted and used as software that, given goals, produces recommendations, predicts, content, or decisions that affect their surroundings is referred to as artificial intelligence[27]. This acceptance is also used within the scope of research. It is referred to as a buzzword frequently employed in scholarly and public conversations by Palmini and Cugurullo (2023) [28]. In a broad sense, it refers to scientific endeavors to teach machines self-learning or to automate cognitive functions like planning, language, pattern identification, and text or speech recognition[29]. In conclusion, different definitions of artificial intelligence have been offered by scientists and researchers over time, reflecting advancements in technology. Artificial Intelligence (AI) has been defined as a broad range of tools, applications, and methods that allow computer systems to learn, reason, solve problems, interact with their surroundings, and make decisions that are on par with or better than those of humans[30]. The advent of AI, as a kind of text-to-image technology, has significantly changed the architectural design process because designers are now able to create intricate, creative, and futuristic designs with it[31].

3.2 Visual Information of AI and the Architectural Designs' Imagination

Generative AI applications are growing in popularity in highly creative domains like research, design, and art, and text-to-image AI-based systems have drawn a lot of interest lately [32] . Visual representations facilitate easier comprehension and interpretation of design concepts, intents, and needs by giving designers and stakeholders a shared language. This enhances communication and collaboration[33]. Researchers observed that "AI was found to bring a distinct perspective that opens up new avenues for artistic expression," providing a novel and creative approach to the process of designing[34]. The capacity to provide original and novel design concepts is one of the main advantages of integrating AI into architecture and urban design, besides technological advantages like building management systems [35]. Artificial Intelligence has the capability to generate design solutions that surpass conventional architectural thinking through the utilization of generative design methodologies and machine learning algorithms [36]. Images/ illustrations played a significant and long-

lasting role in the study of cities by offering insightful information on the physical environment. Images have made it easier for academics to observe, record, and evaluate the layout, aesthetics, and functionality of urban environments since the eighteenth century[37]. Even with these improvements, it is still difficult to figure out which text prompts to use to get the correct images. Text-to-image generative models use user-inputted word prompts to create images. During this procedure, variances may appear in the output images even when the prompts have the same content (see Table 8). The generative process' underlying complexity and the interpretability of textual descriptions are the causes of this diversity[38]. In this research, three cases are selected. The projects were selected to test the architectural understanding capability of artificial intelligence in various contexts. Different prompts were used for two of the selected cases. Whereas for the last one, the same prompt was used. Nevertheless, different images emerged from all the results.

4 Case Studies

The research aims to determine the similarities or differences between the selected case studies, and the AI design results by using design concepts of the selected cases as prompt data for AI design. While it is impossible to say for sure which AI is and will be most useful to architects and planners in practice, both as a technological and design tool, there are several AI tools and potential capabilities that are predicted to be used worldwide. For the aim of the research, the Leonardo.ai program was used. An advanced AI art generator of Leonardo AI, which is a web-based platform, offers a wide range of models and tools for producing excellent visual art[39]. Maybe some other programs such as Midjourney.ai or stable difussion.ai provide and create more aesthetical and real models but these programs are dollar-based which is difficult and expensive for countries such as Turkey to buy and use. Leonardo AI is used in this research because of its free nature and its detailed and realistic rendering capability in visualizing architectural concepts and designs.

4.1 Public Space Design/Religious Space

Traditional mosque architecture has developed over centuries in Islamic architecture in nations like Turkey, where Islam is the predominant religion. Most of Turkey's mosque inventory is "Ottoman-type" mosques[40]. Since the military intervention in 1980, there has been an increase in political and social conservatism in Turkey[41]. Consequently, mosque architecture has attracted interest from the general public and experts. During this time, some mosque designs transformed from the formalized, commercialized, and traditional style to modern and contemporary mosque architecture by famous Turkish architects. One of these designs is the Sancaklar Mosque in Istanbul. Regarding the link between form and function, spatial organization, general architectural features, traditional courtyard design, and the use of common components in mosque architecture, the chosen sample highlights a creative and modern design trend in Turkey[42], which has been honored with awards for its unconventional architectural philosophy, unique physical and thematic formation, and ability to challenge our preconceived notions of mosques[43]. By rejecting any obvious resemblance to the historical mosque type and the usage of any traditional mosque features, the Sancaklar Mosque represents a substantial attempt to break free from the dominant formal traditions seen in the majority of existing mosques[44].

The purpose of this study is not to compare traditional and modern mosque architecture. It is to evaluate the redesign of modern and transformed mosque architecture, which has been proven in the literature, using artificial intelligence. Therefore, the definition, history, and details of mosque architecture are outside the scope of this study. Only what is required for a mosque design, and the concept of the selected case study are included in the scope of the research. In light of this circumstance, a quote mentioning the Sancaklar Mosque will be adequate to ensure the veracity of the chosen case study;

Uğur Tanyeli mentioned that [the architect] simply ignored the prevailing language of contemporary mosque architecture and poetically reconceptualized it[45].

Design Concepts/ AI Prompts

The mosque is situated in a neighborhood with numerous gated communities, with a view of Büyükçekmece Lake. Given that, a mosque lacks a set shape and that a prayer room can be anywhere that is clean, the Project distanced itself from discussions centered on form to concentrate only on the fundamentals of a holy space. Pleasure, both mental and physical, was paramount. The goal of the design was to depict the most basic forms of matter and light, as well as an inner world devoid of all cultural constraints. The building was intended to vanish off the site's slope, anchor to the earth as though it had always been there, and eliminate any temporal and cultural connections[46]. The mosque's overall design, which is characterized as unassuming and modest, stands out due to its prismatic minaret and domeless cover. It blends in well with the surrounding landscape.

In the scope of this research, the design concept of the selected case which represented form, shape, and visual designs, was obtained through a literature study and presented to AI as a prompt in four steps. Contemporary mosque cover, image phenomenon, form, character, and courtyard design have been the focus of this study, plan type and spatial organizations, pulpit, mihrab, and congregational area are outside the scope of the study.

Trying to get closer to the real design concept by increasing the details as prompt in each trial by AI. Thus, the second trial presents a more concrete design. Each trial offers four different design samples. In the next attempt, everything was written in detail, but the project was much different from the real design. This shows that when you write too much and in detail to the AI, it gets confused and can produce absurd results. In the last stage a prompt that emphasized more detail was written but slightly more important concepts, which gave good results, but since it did not fully perceive the environment and context, it created a design independent of the environment.

Table 1. Public space design concepts by the architect (Photos by the author, July 2024).

Design Concepts of the Selected Public Space	
Architect/ Urban Designer	**Real Design**
- Modern -Underground - integrate with the topography -focuse solely on the essence of the religious space by removing itself from conversations that are form-based - on a sloping, rural land - simple and impressive - beyond shape-based patterns - appeals to physical and emotional perceptions - Steps that gradually descend with the slope of the land - With the splits and cracks along the Gibla wall allow daylight to penetrate into the prayer hall. -Represent purest form of light and matter, just as a primary inner world free from all cultural burdens. - Garden surrounded by horizontal courtyard walls and vertical prismatic mass of stone -A green roof -Rural plants	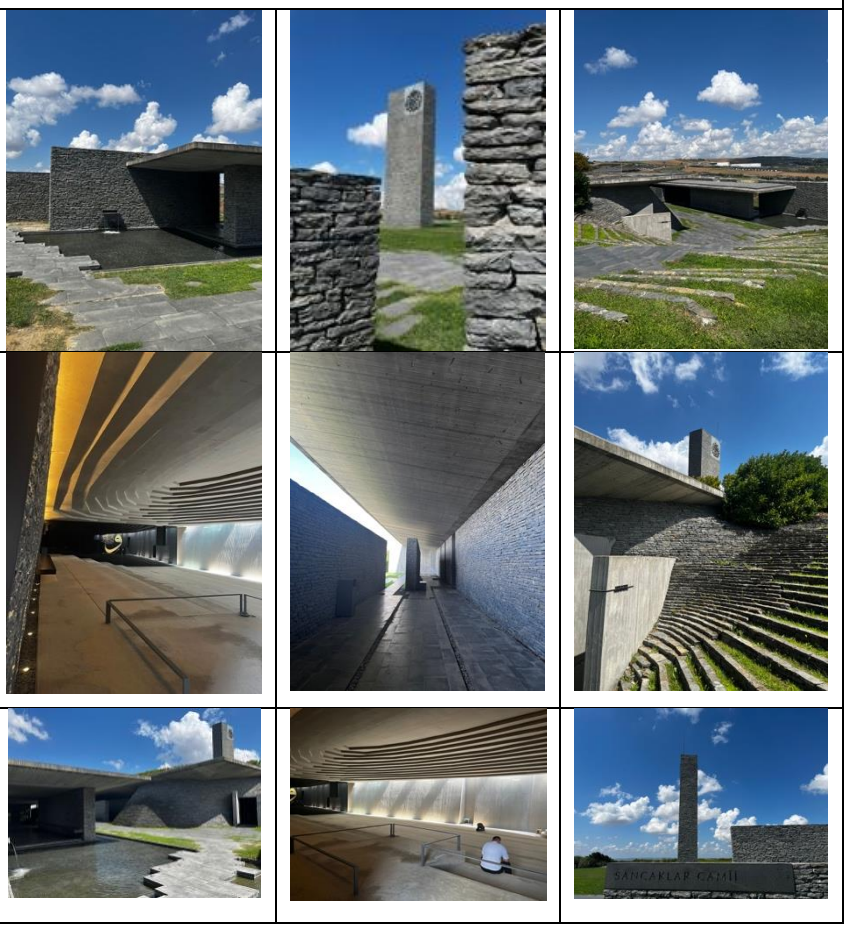

Table 2. Public space design by AI[47].

Textual Inputs		**Initial Image**	
AI Prompt 1	**AI Prompt 2**	**AI Design 1**	**AI Design 2**
-modern mosque - buried underground - the mosque integrate with the topography - the mosque be on a sloping, rural land - It should be located in a meadow landscape separated by a highway next to the mosque. - it be simple and impressive. - it go beyond shape-based patterns and create a mosque that appeals to physical and emotional perceptions. - Steps that gradually descend with the slope of the land - The slits and cracks along the qibla wall allow daylight to penetrate into the prayer hall.	-modern mosque - buried underground - the mosque integrate with the topography - the mosque be on a sloping, rural land - mosque overlook the meadow view - be simple and impressive - only concrete material and gray stones be used on the facade - it go beyond the shape-based patterns and create a mosque that appeals to physical and emotional perceptions -enter the mosque with the steps going down with the slope. -the daylight leak into the prayer hall through the slits and cracks along the qibla Wall - the roof of the mosque be a green terrace roof - people walk and take photographs on the roof - the mosque be entered from below with the stone stairs created by natural slopes from the side of the roof. - Outside the mosque, there is a long, rectangular structure. Include a minaret.		

Table 2 (Continued). Public space design by AI[48].

Textual Inputs		Initial Image	
AI Prompt 3	**AI Prompt 4**	**AI Design 3**	**AI Design 4**
- Mosque with modern and minimalist features. 1. Integration with Natural Materials and Topography: - Constructed using local natural stone, integrated with the topography. - The structure should harmonize with the environment, appearing as if it is part of the natural landscape. 2. Exterior and Facade Design: - Preserving the natural texture of local stone on the facades. - A minimalist and modern aesthetic for the exteriors. - Combined use of natural stone walls and concrete surfaces. 3. Use of Light and Space: - Ensuring natural light enters the interior through large windows and skylights. - Design elements that highlight the reflections and shadows of light in the space. 4. Interior Layout and Minimalist Design: - A minimalist interior design approach with minimal decoration and clean lines. - Geometric forms and simple decorative elements. - Use of natural stone walls and local materials in the prayer area. 5. Religious Elements of the Space: - A simple and modern mihrab on the qibla wall. - A minimalist minbar design. - A spacious, open, and airy arrangement in the main prayer area. 6. Landscape and Environmental Design: - A large courtyard integrated with the landscape. - Natural vegetation and green areas in the courtyard. - Simple yet striking abluti	- create an exact replica of the Sancaklar Mosque Natural, local stones and concrete materials used throughout the structure. The mosque is naturally set into the terrain, integrated with its surroundings. A simple, austere, and minimalist design approach. Large windows and skylights allowing ample natural light into the interior. Organic and modern forms in both interior and exterior spaces. Minimalist interior arrangements, minimal decoration, clean lines, and geometric shapes. A simple and modern mihrab on the qibla wall, minimalist minbar. A large courtyard integrated with the landscape, natural vegetation, and green areas. Simple yet striking ablution areas near the entrance. Acoustic solutions to ensure a quiet and serene worship environment. Creating a spiritual and peaceful atmosphere with natural stone walls and local materials. A modern and unique aesthetic that differs from traditional mosque designs.	  	     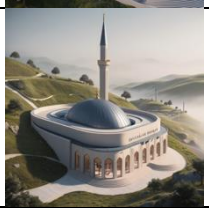

4.2 Residential Building Design/ Apartment-Loft Buildings

Loft structures, an alternate response to the homelessness crisis of the 1970s in the United States, were developed and gradually implemented in Turkey as well. These buildings were once abandoned industrial buildings converted to residential or commercial spaces[49]. Loft living has just become accessible in Istanbul, and there have been a few instances of loft designs being exhibited[50]. In this research, two examples of loft apartments in Galata are selected. The first one is the Micro Loft Bulut Project, located on a total gross area of 45 m^2 in Beyoğlu, Istanbul[51]. The building's topography was chosen to maximize opportunities in the least area and adapt to shifting occupant patterns and behavior[52]. A two-story detached house that had been abandoned was the site of the structure with its distinctive staircase[53]. It is neither forced, contrived, or of a nature that overlooks or disregards the relationship that the apartment establishes with its chaotic surroundings, which are made up of stacks of buildings dominated by uncertainties and secret backyards / inner gardens squeezed in between[54].

The artificial intelligence trial of this project can be considered more successful than other projects. The results did not make a whole difference in some trials. It perceived the desired things better. Assuming that the original design was very abstract and the concept was clearer and less emotional, we can accept that the trials are close to reality. The second residential building is the Galata Apartment, which is also situated inside the traditional housing texture in Istanbul. The primary objective of the design is to create a façade that is both distinctly contemporary and unique, while also harmonizing with the surrounding area's tone and material utilization[57]. Because of its location, the building was constructed with a layered façade that would maximize daylighting while simultaneously offering privacy. The building's interior design was to produce volumes and surfaces that would allow for maximum utilization in a serene, contemporary style[58].

Table 3. Residential Building design concepts by the architect[55] (Photos by the author August 2024).

Design Concepts of the Selected Apartment Design			
Architect/ Urban Designer	**Real Design**		
-Intended and designed to be a microloft - The staircase home, which makes up the entire street facade, was viewed as a vertical extension of the anonymity on the street within the property because of the lot's very small size (gross area of 45 m2). - This open-front staircase house has landings that serve as balconies viewing the ground floor apartments and common areas at different periods. -The hue blue on the front façade draws attention to the staircase house's unusual placement.			

Table 4. Residential Building Design by AI[56].

AI Prompt 1	**AI Prompt 2**	**AI Design 1**	**AI Design 2**
-Design a unique, modern structure that replaced an old two-story detached house. -The plot is very small, about 45 square meters. The building features an open staircase that forms the entire street-facing facade, designed to continue the street's anonymity vertically. -The staircase landings sometimes function as communal spaces and sometimes as balconies for the apartments they serve, facing the street. -The staircase facade is highlighted in a vibrant blue color, making it stand out. -In the back, overlooking a small garden, the blue color reappears in the form of sunshades. -The overall aesthetic should emphasize the building's integration into the narrow urban space, with the blue elements providing a striking contrast against the surrounding environment.	-The building is built on a very narrow, 45 square meter plot, replacing a dilapidated two-story detached house. -The design is innovative, with the entire street-facing facade dominated by an open, external staircase. -This staircase, painted in a striking blue, runs vertically along the front of the building, serving as a communal space and as balconies for the apartments at each level. -The blue facade creates a bold contrast against the urban environment, drawing attention to the building's unique architecture. -In the rear, the blue color reappears through sunshades overlooking a small, lush garden. -The setting should include surrounding buildings, typical of the neighborhood, with narrow streets and a mix of old and new architectural styles, to emphasize the building's integration into its urban context.	 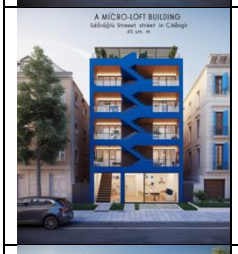  	   

Table 5. Residential Building design concepts by the architect (Photos by the author August 2024).

Design Concepts of the Selected Apartment Design			
Architect/ Urban Designer	**Real Design**		
- Located in one of the most historical areas of the city, within the historical housing texture. - The structure has a relatively small project area of 71 m². - creating a facade that is characteristically contemporary and original, but compatible with the tone and material usage in the immediate vicinity within the historical texture. - In this context, a layered facade design was adopted in this area. - Allow maximum daylight but would also provide the privacy environment that a residential structure should have. - In the interior design of the building, a calm, simple and modern design was aimed to create surfaces and volumes that allow maximum use.			

Table 6. Residential Building design by AI[59].

AI Prompt 1	**AI Prompt 2**	**AI Design 1**	**AI Design 2**
-Located in one of Istanbul's most historic districts, Pera. -The design should capture the modern yet harmonious integration of the building within its historic surroundings. 1.Environment: Surrounding the building are narrow streets and historic stone buildings, primarily 1st-degree protected historical structures. 2.Building Characteristics: Facade Design: The building's facade is designed to maximize natural light while maintaining privacy, featuring a layered structure. -Different materials with varying light transmission properties—glass, stone, and metal—are used in these layers. -The facade includes movable panels that residents can adjust throughout the day, allowing for dynamic interactions with light and shadow. -The facade should incorporate transparent and semi-transparent glass, natural stone, and perforated metal surfaces. -These materials not only ensure modern aesthetics but also resonate with the historical context of the area. -The building has a relatively small footprint of 71 m². -Beyond the commercial space on the ground floor, the building is residential, designed to meet contemporary living standards with a focus on efficiency and modern comfort.	-The building is located in one of Istanbul's most historic districts. . The design should capture the modern yet harmonious integration of the building within its historic surroundings. 1.Environment: Surrounding the building are narrow streets and historic stone buildings, primarily 1st-degree protected historical structures. Building Characteristics: 2.Facade Design: The building's facade is designed to maximize natural light while maintaining privacy, featuring a layered structure. -Different materials with varying light transmission properties—glass, stone, and metal—are used in these layers. -The facade includes movable panels that residents can adjust throughout the day, allowing for dynamic interactions with light and shadow. -The facade should incorporate transparent and semi-transparent glass, natural stone, and perforated metal surfaces. These materials not only ensure modern aesthetics but also resonate with the historical context of the area. -The building has a relatively small footprint of 71 m². The ground floor is reserved for commercial use. -Beyond the commercial space on the ground floor, the building is residential, designed to meet contemporary living standards with a focus on efficiency and modern comfort.	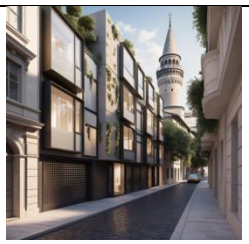 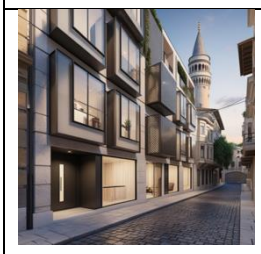  	   

5 Findings and Results

In the visualization made with Leonardo.ai, it was observed that some basic architectural features of Emre Arolat's Sancaklar Mosque were not adequately reflected. For example, although the concept of 'buried underground' was stated in the prompt, the structure was not positioned completely underground in the visuals generated by the AI. This situation shows that one of the most important architectural features of the mosque was not sufficiently

understood. Although the design language of the mosque, which integrates with nature and is oriented towards topography, is partially captured in the artificial intelligence visualization, the architectural details that form the underground-surface transitions in Arolat's original design appear not to have been processed in detail. Thus, it is realized that artificial intelligence has not yet been able to perceive the context and environment of the project or create the desired environment by sending a terrain image. This is a shortcoming of artificial intelligence at the moment because at this stage it can only produce indoor and outdoor images and visuals for what you need. Since it does not perceive the environment correctly, the desired result and the given result are very different from each other.

At the same time, despite the modern, concrete, and minimalist design of the Sancaklar mosque, some characteristic elements of traditional mosque architecture, such as the dome, can be seen in the examples designed with AI. This situation reveals that artificial intelligence has difficulty achieving a fine balance between traditional architectural elements and contemporary interpretation. In the AI-generated Microloft Bulut Project visuals, it is observed that there is a similarity with the original design. The abstract and minimalist language that is at the core of the project seems to have been successfully perceived and reproduced by the AI. The geometric simplicity and minimalist approach of the Microloft Bulut Project were reflected in the visuals produced by Leonardo.ai. This shows that AI can produce more consistent results in designs with clear forms and clean lines. The success of AI in interpreting geometrically simple, abstract designs such as the Microloft Bulut Project shows that such architectural languages have mathematically definable features that can be processed more easily by algorithms. The abstract nature of the original design appears to have been effectively conveyed in the illustrations of the Galata Apartment project made with Leonardo.ai. The project's modern architectural language and integration strategy into the urban fabric have been remarkably accurately replicated by artificial intelligence. The consistency in the visuals produced for the Galata Apartment project highlights the potential of artificial intelligence in contemporary urban architecture projects.

The ability of artificial intelligence to recognize and interpret architectural aesthetic qualities through various factors is demonstrated by these three projects, which were revisualized using Leonardo.ai. Artificial intelligence analyzes the Sancaklar Mosque, Microloft Bulut Project, and Galata Apartment projects differently because they each have unique architectural specifications and aesthetic approaches. When these three projects are evaluated together, they provide important clues about how AI interprets the basic parameters of architectural aesthetics, such as proportion, scale, rhythm, balance, and harmony. It is observed that these parameters are captured more accurately by AI, especially in designs with high geometric definability. This comparison also reveals that there are still certain limitations in the processing of more complex aesthetic parameters of architectural design, such as spatial depth, material texture, light-shadow relationship, and contextual integration by AI. These limitations become especially apparent in projects that use such parameters intensively, such as the Sancaklar Mosque.

6 Discussion

Concerns like the homogeneity of architecture and the loss of creative and individual vision are brought up in criticism of artificial intelligence's role in architecture. This is somewhat accurate, however, modern cities are essentially the same due to structures that would not classify as design or architecture. Are today's architectural designs highly innovative unique and valued?, since each architectural design should tell a unique story[60]. On the other hand, many scientific studies argue that today's cities lack design and aesthetics. This could lead to a physical environment that is monotonous and undifferentiated, failing to capture the variety and cultural backgrounds. On the other hand, artificial intelligence provides at least four distinct designs with precisely identifiable probes for every subject. This makes it possible for urban planners and designers to concentrate on important problems, offer a variety of solutions, investigate performance, carry out generative design and optimization, and foster teamwork. This can be applied to socioeconomic data, disaster mapping, urban development, and urban safety[61]. On the other hand, forming an urban design and planning depends on different political levels, with a certain aim and vision, while taking into account a multitude of interconnected interests, incredibly complicated framework circumstances, and in-depth knowledge of the local context. This is what is officially written and what is discussed in the literature. However, unfortunately, we do not see the development and consideration of these concepts in rapidly developing cities.

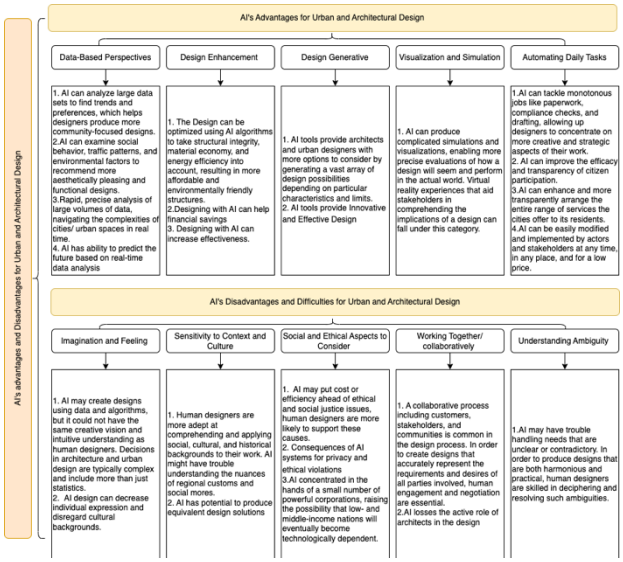

Figure 2. AI advantages and disadvantages in design area (by author, August 2024).

Completely making use of its many advantages besides creating and designing 3D modeling may bring us more identifiable, sustainable, and aesthetic cities. Better outcomes for cities and their citizens result from the integration of artificial intelligence (AI) and data analysis

into urban planning, which improves the capacity to anticipate and address urban difficulties.

7 Conclusion

To effectively utilize a wide range of data and make accurate decisions, developing more architect-effect-centric designs using AI systems necessitates tight collaboration between humans as stakeholders and a variety of architects as actors. Governments, especially developing governments, should include AI strategies in their development especially sustainable development plans and programs. Related governments should assist in supporting local creativity networks, enhance their project delivery capabilities, and draw attention to hazards. This at the same time will be a more participatory approach since considers the opinions of those who use and reside in cities. As Kaatz-Dubberke, and Kehl[62] mentioned human-centric AI should be an architect and urban designer-centric AI in the field of urban design and planning and becoming an ever more important issue. Though it's unlikely to replace human architects and urban designers completely, AI offers a lot of potential to improve the design process and aesthetic outcomes in these fields. In conclusion, artificial intelligence (AI) can greatly improve and complement the work of architects and urban designers, but it will probably perform best as a tool rather than a substitute. However, this study demonstrates that a new form of creative dialogue between architects and AI tools is possible. This dialogue carries the potential for interaction that enriches designers' creative processes rather than restricting them, allowing them to quickly explore different possibilities. The designer can consider the interpretations that the AI produces outside of what is expected as a starting point to question and enrich his or her creative process. However, it seems that no AI design can replace the connection that architects establish with their emotions and designs. In our world, where AI is rapidly developing, it is, of course, possible that we will encounter more powerful, more realistic, and more creative AI designs in the future. Combining AI's advantages with human designers' creativity, empathy, and contextual awareness frequently yields the best results.

Acknowledgements

The author would like to thank the Architect Merve Ayaz (who graduated from Istanbul Arel University, Department of Architecture) for this research. This research would not have been possible without her participation and feedback. Finally, the author would like to thank the unknown reviewers for their insightful comments and valuable improvements to the research.

Declaration

Ethics committee approval is not required.

References

[1] Yigitcanlar, T., Kankanamge, N., Regina, M., Ruiz, A., Rowan, M. B., & Ry, A. (2020). Artificial intelligence technologies and related urban planning and development concepts: How are they perceived and utilized in Australia? *Journal of Open Innovation: Technology, Market, and Complexity*, *6*(87), 1–21.

[2] Guterres, A. (2022). Envisaging the future of cities. *World Cities Report*, UN-Habitat, For a Better Urban Future, 3. ISBN: 978-92-1-133395-4.

[3] Kochskämper, E., Glass, L. M., Haupt, W., Malekpour, S., & Grainger-Brown, J. (2024). Resilience and the sustainable development goals: A scrutiny of urban strategies in the 100 resilient cities initiative. *Journal of Environmental Planning and Management*, 1–27. Kristensen, N. G. (2024). Consequential urban development of sustainable strategies. *Urban Geography*. Urrutia-Mosquera, J. A., Florez Calderon, L. A., & Paredes, D. (2024). 15-min Cities: The potential of a medium-sized polycentric Latin American city. *Journal of Urban Health*.

[4] Lacilla, E., & Ordeig Corsini, J. M. (2016). Waterfront public realm design: Towards a sustainable identity urban projects in Vancouver and Portland. *Journal of Sustainable Development*, *9*(2).

[5] Valls, F., Redondo, E., Fonseca, D., Torres-Kompen, R., Villagrasa, S., & Martí, N. (2018). Urban data and urban design: A data mining approach to architecture education. *Telematics and Informatics*, *35*(4), 1039–1052.

[6] Batty, M. (2018). Artificial intelligence and smart cities. *Environment and Planning B: Urban Analytics and City Science*, *45*(1), 3–6.

[7] Quan, S. J., Park, J., Economou, A., & Lee, S. (2019). Artificial intelligence-aided design: Smart design for sustainable city development. *Environment and Planning B: Urban Analytics and City Science*, *46*(8), 1581–1599. Campbell, S. (1996). Green cities, growing cities, just cities? Urban planning and the contradictions of sustainable development. *Journal of the American Planning Association*, *62*(3), 296–312. He, W., & Chen, M. (2024). Advancing urban life: A systematic review of emerging technologies and artificial intelligence in urban design and planning. *Buildings*, *14*(3), 835.

[8] Son, T. H., Weedon, Z., Yigitcanlar, T., Sanchez, T. H., Corchado, J., & Mehmood, R. (2023). Algorithmic urban planning for smart and sustainable development: Systematic review of the literature. *Sustainable Cities and Society*, *94*, 104562.

[9] Sanchez, T. W., Shumway, H., Gordner, T., & Lim, T. (2022). The prospects of artificial intelligence in urban planning. *International Journal of Urban Sciences*.

[10] Kaatz-Dubberke, T., & Kehl, L. (2020). Artificial intelligence in urban development: Opportunities, challenges and ideas for the German development cooperation. *Deutsche Gesellschaft für Internationale Zusammenarbeit (GIZ) GmbH*, 1–25.

[11] Kaatz-Dubberke, T., & Kehl, L. (2020). Artificial intelligence in urban development: Opportunities, challenges and ideas for the German development cooperation. *Deutsche Gesellschaft für Internationale Zusammenarbeit (GIZ) GmbH*, p. 25.

[12] Yigitcanlar, T. (2020). Artificial intelligence technologies and related urban planning and development concepts. p. 21.

[13] Emaminejad, N., North, N. M., & Akhavian, R. (2022). Trust in AI and implications for the AEC research: A literature analysis. In *ASCE International Conference on Computing in Civil Engineering 2021*. Proceedings paper formatting instructions.

[14] Lewis, M. (2023). AIxArtist: A first-person tale of interacting with artificial intelligence to escape creative block. In *1st International Workshop on Explainable AI for the Arts (XAIxArts), ACM Creativity and Cognition (C&C)*, 1–6.

[15] Gummesson, J. (2023). Urban planning & governance in the age of AI: A study of the potential benefits and risks. *Degree Project in Urban and Regional Planning, KTH Royal Institute of Technology*, 10–50.

[16] Rezafar, A. (2022). Urban environmental aesthetic and identity: The case of Masouleh, Iran. *ART-SANAT, 17*, 397–418.

[17] Oppenlaender, J. (2023). A taxonomy of prompt modifiers for text-to-image generation. *Behaviour and Information Technology*.

[18] Kuzior, A., & Kwilinski, A. (2022). Cognitive technologies and artificial intelligence in social perception. *Management Systems in Production Engineering, 30*(2), 109–115.

[19] Good, I. J. (1966). Speculations concerning the first ultraintelligent machine. In F. L. Alt & M. Rubinoff (Eds.), *Advances in Computers* (Vol. 6, pp. 31–88). Elsevier.

[20] Borglund, C. (2022). Artificial intelligence in architecture and its impact on design creativity – A study on how artificial intelligence affects creativity in the design process. *Degree Project in the Built Environment, KTH Royal Institute of Technology, Real Estate and Construction Management*.
Haenlein, M., & Kaplan, A. (2019). A brief history of artificial intelligence: On the past, present, and future of artificial intelligence. *California Management Review, 61*(4), 5–14.

[21] Nikitas, A., Michalakopoulou, K., Njoya, E., & Karampatzakis, D. (2020). Artificial intelligence, transport and the smart city: Definitions and dimensions of a new mobility era. *Sustainability, 12*(7), 2789.

[22] Mehr, H. (2017). Artificial intelligence for citizen services and government. *Harvard Ash Center for Technology and Democracy*.

[23] Yigitcanlar, T. (2020). Artificial intelligence technologies and related urban planning and development concepts. p. 21.
Caprotti, F., Cugurullo, F., Cook, M., Karvonen, A., Marvin, S., McGuirk, P., & Valdez, A. M. (2024). Why does urban artificial intelligence (AI) matter for urban studies? Developing research directions in urban AI research. *Urban Geography*.
Jiang, M. Z. (2020). Urban planning reform trend based on artificial intelligence. *ICAIIT Journal of Physics: Conference Series, 1533*, 032020.

[24] Pellegrin, J., Colnot, L., & Delponte, L. (2021). Research for REGI Committee – Artificial intelligence and urban development. *European Parliament, Policy Department for Structural and Cohesion Policies*, 14–20.

[25] Gummesson, J. (2023). Urban planning & governance in the age of AI: A study of the potential benefits and risks. p. 10.

[26] Palmini, O., & Charting, F. C. (2023). AI urbanism: Conceptual sources and spatial implications of urban artificial intelligence. *Discover Artificial Intelligence, 3*(1), 15.

[27] Gummesson, J. (2023). *Urban planning & governance in the age of AI: A study of the potential benefits and risks*. p. 10.

[28] Palmini, O., & Cugurullo, F. (2023). *Charting AI urbanism*. p. 5.

[29] Kaatz-Dubberke, T., & Lennard, J. (2020). *Artificial intelligence in urban development*. p. 18.

[30] El Tantawy, H., Abobeah, R., Attia, M., & Abdelaziz, M. (2024). Applications of artificial intelligence in urban design. *Journal of Al-Azhar University Engineering Sector, 19*, 111–126.

[31] Sukkar, A. W., Fareed, M., Moohammed, W., Yahia, M., Mushtaha, E., & Giosa, S. L. (2024). Artificial Intelligence Islamic Architecture (AIIA): What is Islamic architecture in the age of artificial intelligence? *Buildings, 14*, 781. Retrieved August 19, 2024, from https://www.researchgate.net/publication/378949344_Artificial_Intelligence_Islamic_Architecture_AIIA_What_Is_Islamic_Architecture_in_the_Age_of_Artificial_Intelligence

[32] Oppenlaender, J., Silvennoinen, J., Paananen, V., & Visuri, A. (2023). Perceptions and realities of text-to-image generation. In *Mindtrek '23: Proceedings of the 26th International Academic Mindtrek Conference* (pp. 279–288).
Liu, Y. E., & Huang, Y. M. (2024). Exploring the perceptions and continuance intention of AI-based text-to-image technology in supporting design ideation. *International Journal of Human–Computer Interaction*.

[33] Bresciani, S. (2019). Visual design thinking: A collaborative dimensions framework to profile visualizations. *Design Studies, 63*, 92–124.

[34] Chiou, L., Hung, P., Liang, R. H., & Wang, C. T. (2023). Designing with AI: An exploration of co-ideation with image generators. In *DIS '23: Proceedings of the 2023 ACM Designing Interactive Systems Conference* (pp. 1941–1954).

[35] Mrosla, L., & von Both, P. (2019). Quo vadis: AI in architecture? Survey of the current possibilities of AI in the architectural practice. *Blucher Design Proceedings*.

[36] Popelka, S., Narvaez, L., & Beroche, Z. H. (2023). *Urban AI Guide*, 10–90. Retrieved from https://urbanai.fr/wp-content/uploads/2023/03/Urban-AI-Guide-2023-V2.pdf

[37] Zhang, F., Salazar-Miranda, A., Duarte, F., Vale, L., Hack, G., Chen, M., Liu, Y., Batty, M., & Ratti, C. (2024). Urban visual intelligence: Studying cities with artificial intelligence and street-level imagery. *Annals of the American Association of Geographers, 114*(5), 876–897.

[38] Lee, S., Lee, J., Bae, C. H., Choi, M. S., Lee, R., & Ahn, S. (2024). Optimizing prompts using in-context few-shot learning for text-to-image generative models. *IEEE Access, 12*, 2660–2673.

[39] Leonardo.ai. (2024). *Leonardo AI: All you need to know*. Retrieved August 19, 2024, from https://www.linkedin.com/pulse/leonardo-ai-all-you-need-know-blockchaincouncil-lk2pe

[40] Mertyürek, S., & Demirbaş, G. U. (2024). Modern and traditional representation in mosque architecture: Analytic comparison of three mosques in Ankara, Turkey. *GRID Architecture, Planning and Design Journal, 6*(2), 745–773.

[41] Ozalogh, S. (2017). An attempt to transform popular religious images into contemporary mosque architecture: Ahmet Hamdi Akseki Mosque. *Journal of Architectural and Planning Research, 34*(2), 114–132.

[42] Akbulut, N., & Erslan, A. (2017). Türkiye'de çağdaş cami mimarisi tasarımında yenilikçi yaklaşımlar. *İstanbul Aydın Üniversitesi Dergisi, 35*, 33–59.

[43] Şahin, F., & Sennou, Y. (2023). Mimaride imgenin sarsılması: Sancaklar Cami örneği. *Yalvaç Akademi Dergisi, 8*(2), 46–61.

[44] Gür, B. F. (2017). Sancaklar Mosque: Displacing the familiar. *International Journal of Islamic Architecture, 6*(1), 165–193.

[45] Tanyeli, U. (2024). *Profession of faith: Mosque in Sancaklar, Turkey by Emre Arolat Architects*. Retrieved February 15, 2024, from https://www.architectural-review.com/today/profession-of-faith-mosque-in-sancaklar-turkey-by-emre-arolat-architects

[46] Şahin, F., & Sennou, Y. (2023). Mimaride imgenin sarsılması: Sancaklar Cami örneği. *Yalvaç Akademi Dergisi, 8*(2), 46–61.

[47] Leonardo.ai. (2024). *Leonardo AI: All you need to know*. Retrieved August 19, 2024, from https://www.linkedin.com/pulse/leonardo-ai-all-you-need-know-blockchaincouncil-lk2pe
[48] Leonardo.ai. (2024). *Leonardo AI: All you need to know*. Retrieved August 19, 2024, from https://www.linkedin.com/pulse/leonardo-ai-all-you-need-know-blockchaincouncil-lk2pe
[49] Hızlı, N., & Mızrak, B. (2015). Re-thinking loft buildings in the scope of housing production in Turkey. *MEGARON, 10*(4), 479–493.
[50] Tuğlu Karslı, U., & Özker, S. (2021). Loft living and gentrification: A case for Istanbul Galata District reading change through loft designs. *Mimarlık ve Yaşam Dergisi – Journal of Architecture and Life, 6*(2), 553–563.
[51] Geçkili Karaman, P. (2020). Kalıcılığın yıkımı üzerine: Esneklik ve aidiyet. *Tasarım Kuram, 16*(30), 77–95.
[52] Gür, B. F. (2017). Evin topografyası, Çinici Mimarlık'ın MikroLoft projeleri. *Mimarlık, 398*, 36–42.
[53] ARKIV. (2020). *Microloft Bulut projesi*. Retrieved October 5, 2020, from https://www.arkiv.com.tr/proje/microloft-bulut/4100
[54] Gür, B. F. (2017). Evin topografyası, Çinici Mimarlık'ın MikroLoft projeleri. p. 42.
[55] Çinici Mimarlık. (2021). *Mikroloft-2 Bulut-2 projesi tanıtımı*. Retrieved November 12, 2021, from https://www.cinicimimarlik.com/tr/mikroloft-2-bulut-2/
[56] Leonardo.ai. (2024). *Leonardo AI: All you need to know*. Retrieved August 19, 2024, from https://www.linkedin.com/pulse/leonardo-ai-all-you-need-know-blockchaincouncil-lk2pe
[57] Natura Dergi. (2021). *NATURA 53 – Mart-Nisan sayısı*. Retrieved July 3, 2021, from https://www.naturadergi.com/wp-content/uploads/2021/06/NATURA-53-MART-NISAN-3.pdf
WE'RE Mimarlık. (2022). *Galata Apartmanı proje sayfası*. Retrieved April 2, 2022, from https://werearch.com/proje-detay/galata-apartmani/
[58] Leonardo.ai. (2024). *Leonardo AI: All you need to know*. Retrieved August 19, 2024, from https://www.linkedin.com/pulse/leonardo-ai-all-you-need-know-blockchaincouncil-lk2pe
[59] Leonardo.ai. (2024). *Leonardo AI: All you need to know*. Retrieved August 19, 2024, from https://www.linkedin.com/pulse/leonardo-ai-all-you-need-know-blockchaincouncil-lk2pe
[60] Kwon, C., & Ahn, Y. (2024). Critical views on AI (artificial intelligence) in building design. *International Journal of Sustainable Building Technology and Urban Development, 15*(2), 240–246.
[61] Batty, M. (2018). Artificial intelligence and smart cities. *Environment and Planning B: Urban Analytics and City Science, 45*(1), 3–6.
[62] Kaatz-Dubberke, T., & Kehl, L. (2020). *Artificial intelligence in urban development: Opportunities, challenges and ideas for the German development cooperation*. p. 24.

International Journal of Innovative Engineering Applications

Journal homepage: https://dergipark.org.tr/ijiea

EXPERIMENTAL ANALYSIS OF FLOW RATES IN GROUND SOURCE HEAT PUMPS FOR HEATING: A CASE STUDY SOUTHEASTERN ANATOLIA, TURKEY

***Umut Ercan*[*1], *Adem Yılmaz*[2]**

[1]*Besiri OSB Vocational School, Batman University, 72060, Batman,Turkey*
[2]*Faculty of Technology, Batman University, 72060, Batman, Turkey*

Abstract

Original scientific paper

Geothermal energy offers considerable potential for use in buildings and infrastructure. This research investigates the application of a Horizontal Type Ground Source Heat Pump system to reduce energy consumption in buildings. The study assesses the energy efficiency and operational characteristics of ground source heat pump systems under the specific climatic conditions of the Batman region. To conduct this analysis, a horizontal ground source heat pump and an underground circuit were installed in a container at Batman University's West Raman Campus. Experimental data revealed that soil temperatures below two meters remained constant at 21°C. Tests were carried out in December 2020 at three flow rates: maximum (0.19 m³/h), medium (0.12 m³/h), and minimum (0.09 m³/h). During the experiments, measurements were taken for the internal and external temperatures of the heat pump, the inlet and outlet temperatures of the water-monoethylene glycol mixture, and the temperatures of the cooling liquid components. The highest coefficient of performance for the heat pump was recorded at 2.43, while the overall system coefficient of performance reached 2.23.

Keywords: *CSA, COP, energy, heat pump, heating season.*

TOPRAK KAYNAKLI ISI POMPALARINDA AKIŞ HIZLARININ DENEYSEL ANALİZİ: GÜNEYDOĞU ANADOLU, TÜRKİYE'DE BİR VAKA ÇALIŞMASI

Özet

Orijinal bilimsel makale

Jeotermal enerji, binalarda ve diğer altyapılarda uygulamalar için önemli bir potansiyele sahiptir. Bu çalışmada, binalarda enerji tüketimini en aza indirmek için Yatay Tip Yeraltı Kaynaklı Isı Pompası sisteminin uygulanması incelenmektedir. Araştırma, Batman bölgesinin iklim koşulları altında yeraltı kaynaklı ısı pompası sistemlerinin enerji performansını ve çeşitli özelliklerini değerlendirmektedir. Bunu kolaylaştırmak için Batman Üniversitesi Batı Raman Kampüsü'nde bir konteyner içerisine yatay yeraltı kaynaklı ısı pompası ve yeraltı devresi kuruldu. Deneysel ölçümler, iki metrenin altındaki derinliklerde toprak sıcaklığının 21°C'de sabit kaldığını gösterdi. Testler Aralık 2020'de üç farklı hacimsel debide gerçekleştirildi: maksimum (0.19 m³/h), orta (0.12 m³/h) ve minimum (0.09 m³/h). Deneyler boyunca ısı pompasının iç ve dış sıcaklıkları, su-mono etilen glikol karışımının giriş ve çıkış sıcaklıkları ve soğutma sıvısı bileşen sıcaklıkları kaydedildi. Isı pompası için gözlemlenen en yüksek performans katsayısı 2.43 olurken, genel sistem performans katsayısı ise 2.23 olarak hesaplanmıştır.

Anahtar Kelimeler: *CSA, COP, enerji, ısı pompası, ısıtma sezonu.*

1 Introduction

Energy has played a crucial role in human life since its earliest use, significantly enhancing quality of life and welfare. Initially, energy was utilized for basic needs such as heating and cooking, but with technological advancements, its applications have expanded across numerous fields. Today, energy is a cornerstone of technological progress and is deeply intertwined with global political and economic dynamics. In Turkey, 45% of total energy consumption occurs in residential buildings, with 28%, 18%, and 4% used in industry, transportation, and agriculture, respectively (TUİK, 2024) [1]. Nearly half of residential energy is dedicated to heating, primarily relying on fossil fuels. However, fossil fuel reserves are finite, necessitating a shift toward renewable energy sources. This transition is inevitable as the world seeks sustainable energy solutions.

Heat pump systems, which enable both heating and cooling, are a focus of global research and development.

*Corresponding author.
E-mail address: umut.ercan@batman.edu.tr (U. Ercan)
Received 08 February 2025; Received in revised form 20 May 2025; Accepted 16 June 2025
 Doi: https://doi.org/10.46460/ijiea.1635913

These systems transfer heat from the ground or air to regulate indoor temperatures. During summer, heat is expelled to cool the air, while in winter, heat is extracted from the ground to warm indoor spaces. The ground maintains relatively stable temperatures year-round, making it an efficient heat source or sink. By circulating antifreeze solutions through underground pipes, heat pumps can significantly reduce electrical energy consumption, offering an economical and sustainable solution for heating and cooling. Ground source heat pumps (GSHPs) are particularly efficient, consuming less energy than conventional air conditioners.

GSHPs can be installed horizontally or vertically, depending on land availability. Horizontal systems are typically buried 1-2 meters deep and are suitable for areas with sufficient land, such as gardens. The performance of heat pumps depends on factors like refrigerant type, system pressure loss, efficiency, flow rate, source temperature, and installation location. Numerous experimental, theoretical, and simulation studies have explored heat transfer, heat exchangers, and heat pump systems, highlighting their potential for energy efficiency.

Recent studies have investigated hybrid systems combining solar energy with GSHPs to enhance performance, particularly in regions with challenging soil conditions. Simulations programs have shown that integrating solar collectors with GSHPs can reduce annual energy consumption and increased efficiency [2,3]. Other research has evaluated multiple heat pump systems, including solar-assisted ground source, solar-assisted air source, and ground-air source heat pumps, with coefficients of performance (COP) improved. [4,5,6,7,8,9,10,11,12].

Ground Source Heat Pumps (GSHPs) utilize shallow geothermal energy from the Earth's surface for heating, cooling, and hot water production. They operate through underground loops that circulate a heat transfer fluid, efficiently exchanging thermal energy with the ground, which maintains relatively stable temperatures year-round [13-17]. This stability results in higher energy efficiency, lower operating costs, and reduced maintenance compared to Air Source Heat Pumps (ASHPs) and traditional fossil fuel systems [18]. Additionally, GSHPs produce no direct emissions, offering a clean, sustainable option that significantly reduces greenhouse gas emissions, aligning well with climate change mitigation goals [19].

Geographical and climatic factors significantly influence the design and performance of vertical GSHPs, with studies highlighting the importance of geology and climate in system optimization [20]. Monitoring of large-scale GSHP systems has revealed ground heat exchanger loads of up to 50 W/m in heating mode and 20–210 W/m in cooling mode [21]. Hybrid GSHP systems have been optimized for various building types, demonstrating their versatility [22]. Quasi-three-dimensional models of vertical U-bend ground heat exchangers have shown strong agreement with experimental data, with mean relative errors of 5.5% [23].

Experimental setups in Turkey have evaluated the energy, exergy, and economic performance of solar-assisted GSHPs, highlighting their potential in heating and cooling applications [24,25,26,27].

Horizontal ground source heat pump systems (HTGSHPs) are particularly suitable for regions with cold or extremely hot climates, such as Rome (Italy) and Barcelona (Spain). This study provides an overview of HTGSHPs, reviews relevant literature, and presents experimental methods and results to evaluate system performance. Overall, the integration of renewable energy sources with heat pump systems offers a promising pathway toward sustainable energy solutions.

2 System Description (Experimental Setup)

The experimental system was set up in Batman, Turkey, in an experiment room of 27 m^2 within the West Raman Campus area of Batman University. Figure 1 shows the installation diagram of a HTGSHP. The external view of the system is given in Figure 2 [28].

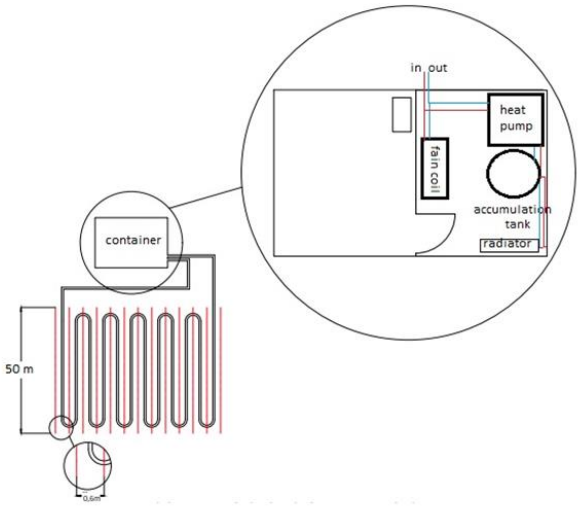

Figure 1. Diagram of ground source heat pump system.

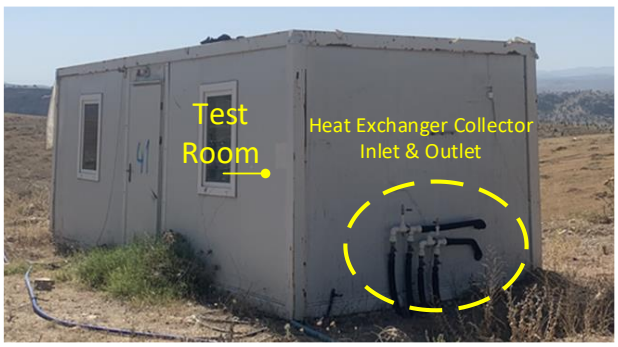

Figure 2. External view of the system.

The GSHP system consists of three main parts: undersoil circuit, heat pump, and heating elements. The ground heat exchanger consists of a polyethylene PE100 type pipe resistant to 10bar pressure at a depth of 2 meters. The length of the ground heat exchanger is 600m. A mixture of monoethylene glycol (10%) and water (90%) was used as the fluid in the ground heat exchanger. The mixture was prepared for the freezing problem of the brine entering the heat pump mixture. The ground heat exchanger is shown in Figure 3.

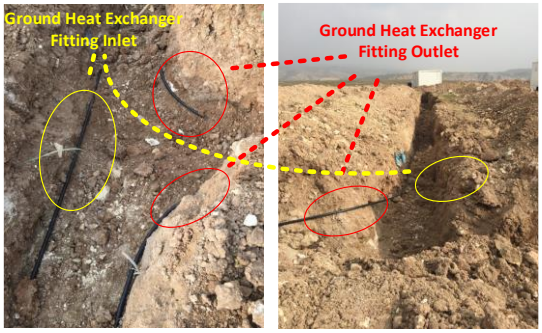

Figure3. Ground heat exchanger.

As the heat pump device, a 9kW Thermia Villa Classic heat pump was preferred (packet system). A 60 cm panel radiator was used in the heating circuit. The system is shown in Figure 4.

Figure 4. Heat pump system Indoor.

Temperature, pressure, flow rate and electrical power values were measured and recorded at certain time intervals in the test system. During the test, a fluid was passed through the undersoil circuit at a flow rate of 0.19 m^3/h; a fluid with a flow rate of 0.12 m^3/h was passed through the undersoil circuit and finally, a fluid with a flow rate of 0.09 m^3/h was passed through the undersoil circuit.

3 Energy Analysis

Machines that transfer thermal energy from a low-temperature environment to another high-temperature environment are called cooling machines. Machines that transfer heat from one place to another for heating or cooling are called heat pumps. Refrigeration machines and heat pumps perform the same cycle. The most used system in refrigeration machines and heat pump systems is vapor compression refrigeration (VCR) cycles. In vapor compression cycles, some refrigerant is sequentially condensed and evaporated. Figure 5 shows p-h diagram of the system with vapor compression. As is seen in Figure 5, The pressures during the condensation and evaporation processes during the cycle are called the condensing pressure (P_c), the evaporation pressure (P_e), respectively. Again, the temperatures during the condensation and evaporation processes during the cycle are called the condensation temperature (T_c), the evaporation temperature (T_e).

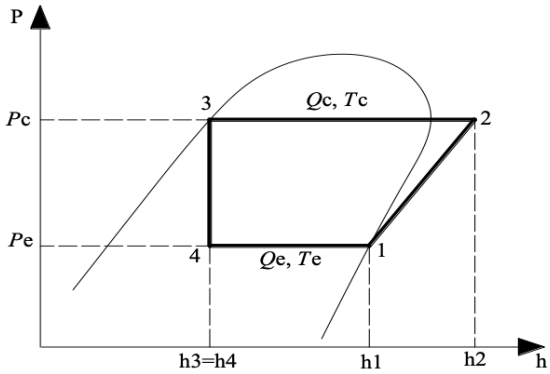

Figure 5.P-h Diagram of a vapor compression system.

There are elements with continuous flow in the VCR cycle. The conservation of energy (TD 1st law per unit mass) is expressed by Equation 1 for a continuous flow open system with one inlet and one outlet.

$$q - W = \Delta h + \Delta E_k + \Delta E_p \quad (1)$$

q and w respectively mean heat transfer and performance for unit mass while ΔE_p and ΔE_k respectively represent potential and kinetic energy. The potential and kinetic energy changes of the refrigerant circulating in the VCR can be neglected as they are very low compared to the work and heat transfer values. At this stage, the conservation of energy per unit mass of the open system with continuous flow is expressed by Equation 2.

$$q - W = h_{out} - h_{in} \quad (2)$$

For this case, Equation 2 can be rearranged, and the energy drawn by the compressor, W_k, can be calculated with Equation 3.

$$W_k = \dot{m}(h_2 - h_1) \quad (3)$$

In this equation, $(\dot{m})$ is refrigerant flow rate circulating in the system; (h_1) is Compressor inlet enthalpy value of the fluid; (h_2) is output enthalpy value. As is understood by Figure 3, compressor as adiabatic draws current from the outside.

There is no energy interaction in condenser and evaporator $W = 0$.

So, energy discharged from the condenser to the external environment (Q_c) and amount of energy absorbed in the evaporator (Q_e) can be computed by Equation 4 and Equation 5.

$$Q_c = \dot{m}(h_2 - h_3) \quad (4)$$

$$Q_e = \dot{m}(h_1 - h_4) \quad (5)$$

In Equation 4, enthalpy of the fluid at the condenser outlet is represented by (h_3) and enthalpy of the fluid at the inlet of the evaporator is represented by (h_4).
The cooling performance coefficient (COP) of VCR is the ratio of the energy absorbed in the evaporator to the energy consumed in the compressor. Related coefficient can be seen in Equation 6.

$$COP = \frac{Q_e}{W_{cp}} \quad (6)$$

3.1 Energy Analysis for the Heating Season

Heating performance coefficient of the heat pump unit,COP_{Hp}, is calculated by Equation 7 while coefficient of heating performance of the system, COP_{SIS}, is computed by Equation 8.

$$COP_{Ip} = \frac{Q_e}{W_{cp}} \quad (7)$$

$$COP_{SIS} = \frac{Q_e}{W_k + W_{p1} + W_{p2}} \quad (8)$$

In the Equation 8, the power drawn (W_k) by the compressor from the mains and the power drawn by the circulation pump from the mains (W_{p1}) were measured by the power analyzer connected to the system. The amount of heat transferred from the condenser to the air (Q_c) is computed by Equation 9.

$$Q_c = \dot{m} c_p (T_{out} - T_{in}) \quad (9)$$

In Equation 9, (m) is the air flow (kg/s), (c_p) is specific heat of air (kj/kg°C), (T_{out}) is the outlet temperature of air from evaporator (°C), (T_{in}) is the air inlet temperature to the evaporator (°C).The amount of heat withdrawn from the ground (Q_{TID}) by the water-antifreeze mixture circulated in the ground heat exchanger is calculated by Equation 10.

$$Q_{GHE} = \dot{m}_{mix} c_{p,mix} (T_{mix,out} - T_{mix,in}) \quad (10)$$

In this equation, the flow rate of the water-antifreeze mixture is (m_{mix}); the specific heat of the water-antifreeze mixture is ($c_{p,mix}$); the temperature of the water-antifreeze mixture going from the evaporator to the soil is ($T_{mix,in}$). Figure 6.a and Figure 6.b. show measurement points.

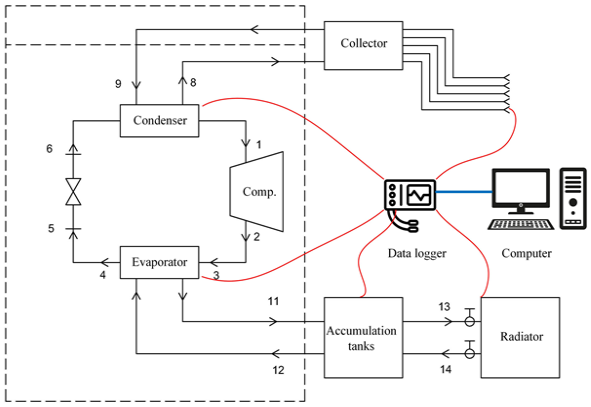

Figure 6.a. Horizontal type of ground source heat pump (HTGSHP) diagram and measurement points.

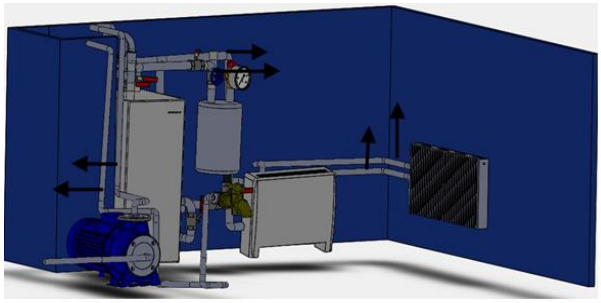

Figure 6.b. Horizontal type of ground source heat pump (HTGSHP) measurement points ((1) GHE (compressor, evaporator, condenser, (2) storage tank, (3) radiator heating system and (4) climate test room.).

3.2 Climate Data

The HTGSHP system was installed in Batman University in Batman, 41°40′ east longitudes latitude and 37°50′ Nort, located in Turkey, it has a mild climate with a dry hot summer and cold winter even through it is influenced by the Mediterranean climate.

4 Results and Discussion

The experiments were conducted in December, as it is the coldest month in the region where the study was carried out. This timing allowed for an evaluation of the system's performance under the most challenging climatic conditions. The system's performance was analyzed using the average of the test results. Figure 7 illustrates the variations in ambient temperature (T_{out}), indoor temperature (T_{in}), and soil temperature (T_{source}) over time while the HTGSHP system was operational.

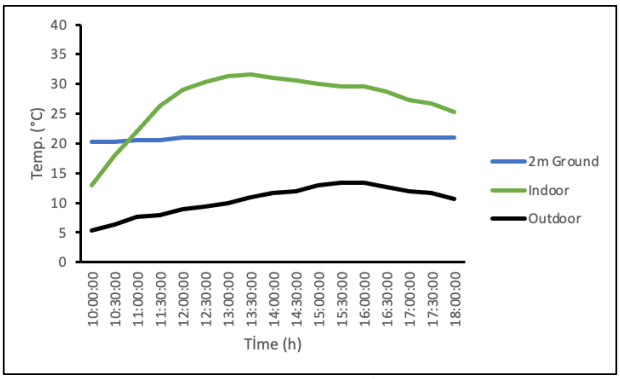

Figure.7. Indoor- outdoor - depth of 2m soil temperature.

In December 2020, the outside temperature ranged from a minimum of 5°C to a maximum of 14°C, with an average daytime temperature of 10–11°C. The initial indoor temperature was measured at 11°C, but during the day, it averaged between 29–30°C, indicating effective heating by the system. At a depth of 2 meters, the soil temperature remained constant at 22°C, demonstrating its stability as a reliable heat source.

Figures 8, 9, and 10 illustrate the time-dependent variations in the inlet ($T_{in,mix}$) and outlet ($T_{out,mix}$) temperatures of the water-antifreeze mixture circulating through the HTGSHP system. The tests were conducted at three flow rates: maximum (0.19 m³/h), medium (0.12 m³/h), and minimum (0.09 m³/h). These figures also show the system's ability to maintain consistent performance

under varying flow rates. The results confirm that the GSHP system successfully met the heating energy requirements of the climate test room and ensured thermal comfort throughout the operational period. This demonstrates the system's effectiveness in maintaining stable and comfortable indoor temperatures, even under varying external conditions.

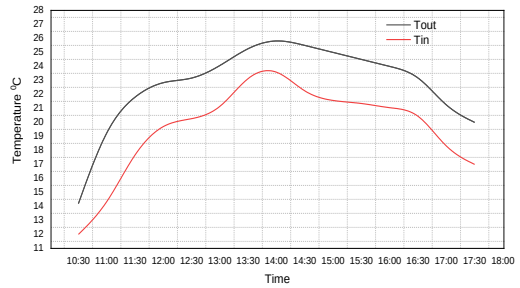

Figure 8. Max Flow rate inlet and outlet water-antifreeze mixture temperatures.

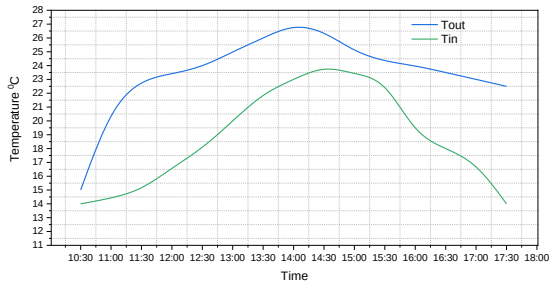

Figure 9. Mid flow rate inlet and outlet water-antifreeze mixture temperatures.

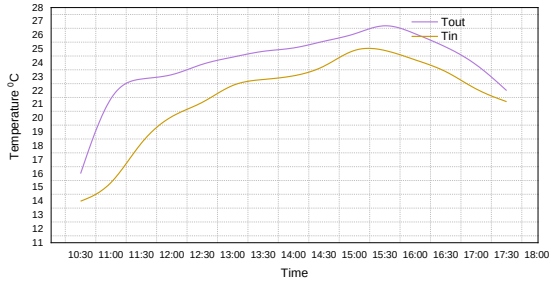

Figure 10. Min flow rate inlet and outlet water-antifreeze mixture temperatures.

The coefficient of performance (COP) of the overall system (COP_{SIS}) was calculated by dividing the heat transferred by the system (Q_{hp}) by the power input to the GSHP system. Figures 11, 12, and 13 present the COP values for both the heat pump unit (COP_{HP}) and the overall soil source heat pump system (COP_{SIS}).

The experiments revealed the following results:

The highest COP_{HP} value of 2.43 was achieved at the maximum flow rate (0.19 m³/h).

At the medium flow rate (0.12 m³/h), the maximum COP_{HP} value was 2.40.

At the minimum flow rate (0.09 m³/h), the highest COP_{HP} value was 2.36.

For the overall system (COP_{SIS}):

The maximum COP_{SIS} value of 2.26 was recorded at the maximum flow rate.

At the medium flow rate, the highest COP_{SIS} value was 2.23.

At the minimum flow rate, the maximum COP_{SIS} value was 2.20.

During the measurement period, the compressor operated intermittently. On the first day, over a 7-hour period, the compressor ran six times. On the second day, during a 4.5-hour period (13:00–17:30), the compressor ran twice. This intermittent operation highlights the system's ability to maintain thermal comfort while optimizing energy use, as the compressor only activates when necessary to meet heating demands.

These results demonstrate the efficiency of the GSHP system in transferring heat and maintaining stable performance across different flow rates, while also ensuring energy-efficient operation through controlled compressor activity.

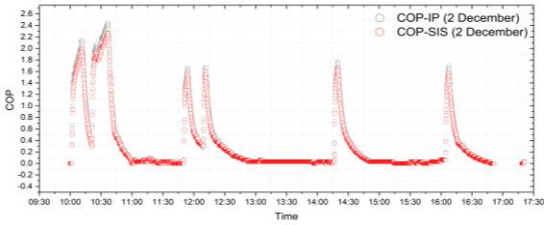

Figure 11. Max flow rate cop heat pump unit.

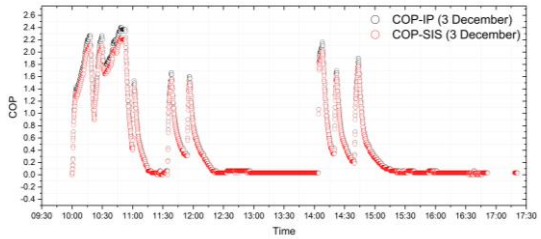

Figure 12. Mid flow rate cop heat pump unit.

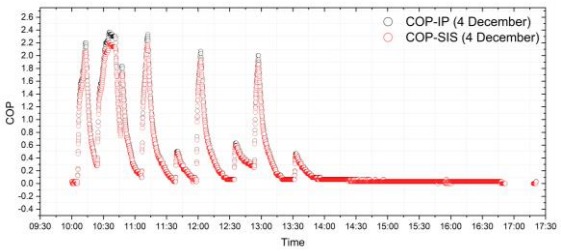

Figure 13. Min flow rate cop heat pump unit.

According to the literature review, there is a notable gap in research on horizontal-type ground source heat pump (HTGSHP) systems in the Southeastern Anatolia region of Turkey. Furthermore, studies on HTGSHP in Turkey as a whole are quite limited. Figure 14 presents a comparison of coefficient of performance (COP) efficiency values from several experimentally examined studies. The COP values in these studies range from 2.16 to 3.18, with the highest efficiency of 3.18 reported.

Mass flow rates in these studies vary significantly, ranging from 0.035 kg/s to 0.900 kg/s, reflecting differences in system designs, configurations, and operational conditions across the studies. This variability highlights the diversity in experimental setups and the influence of factors such as soil properties, climate conditions, and system design on the performance of ground source heat pump systems.

The findings from this study contribute to filling the research gap in the Southeastern Anatolia region and provide valuable insights into the performance of horizontal-type ground source heat pumps under specific climatic and operational conditions. The results align with the broader range of COP values reported in the literature, demonstrating the potential of HTGSHP systems as an efficient and sustainable heating and cooling solution.

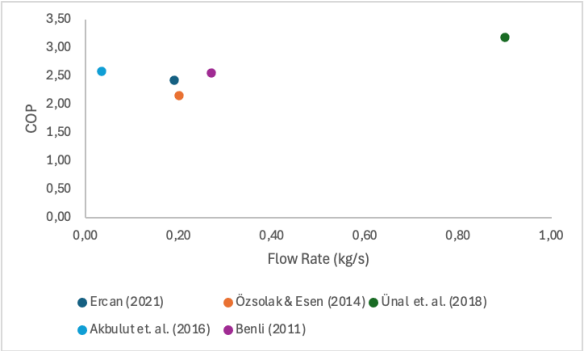

Figure 14. Flow rate-cop heat pump unit literature review.

5 Conclusions

This study focused on analyzing a ground source heat pump system that utilizes the ground as an energy source. An experimental setup was designed and installed to evaluate the system's heating performance and conduct energy analysis. The energy analysis was performed using mass and energy balance equations. The key findings of this study are summarized as follows:

This study represents the first implementation of a HTGSHP system in Batman, under specific climatic conditions. The system is expected to perform with similar efficiency in regions with comparable climates (CSA classification).

Performance Metrics: The highest Coefficient of Performance for the Heat Pump (COP_{HP}) value of 2.43 was achieved during experiments conducted at the maximum flow rate (0.19 m³/h).
The highest Coefficient of Performance for the Overall System (COP_{SIS}) value of 2.26 was also recorded at the maximum flow rate.

Flow Rate and Heat Transfer: Increasing the mass flow rate of the water-antifreeze mixture enhanced heat transfer, leading to higher COP values for both the heat pump and the overall system.

Effectiveness in Batman's Climate: The results demonstrate that GSHP systems are highly effective for heating purposes in the climatic conditions of Batman province. The system was designed to address the freezing problem of the brine mixture entering the heat pump, ensuring reliable operation even in low ambient temperatures.

Advantages Over Conventional Systems: The GSHP outperforms conventional air-source heating systems, particularly in low ambient temperature conditions. Notably, the system did not require an auxiliary heat source, highlighting its self-sufficiency and efficiency.

The study confirms that HTGSHP systems are a viable and efficient solution for heating in regions with climates similar to Batman, Turkey. The system's ability to operate without auxiliary heating and its superior performance compared to conventional systems make it a promising option for sustainable heating applications. These findings contribute to the growing body of research on GSHP systems and support their adoption in regions with comparable climatic conditions.

Declaration

The authors declare that the ethics committee approval is not required for this study.

References

[1] Türkiye İstatistik Kurumu. (2024, July 8). TEİAŞ. *Retrieved July 8, 2024, from https://www.tuik.gov.tr*
[2] Buyukzeren, R., & Kahraman, A. (2024). A comparative study on the application of solar thermal collector and photovoltaic combinations to assist an air source heat pump. *Journal of Thermal Analysis and Calorimetry*, *149*(17), 9413–9428.
[3] Bae, S., Chae, S., & Nam, Y. (2022). Performance analysis of integrated photovoltaic-thermal and air source heat pump system through energy simulation. *Energies*, *15*(2), 528.
[4] Dikici, A., & Akbulut, A. (2011). An exergetic performance evaluation of multiple source heat pump systems. *Energy Sources, Part A: Recovery, Utilization, and Environmental Effects*, *33*(12), 1117–1138.
[5] Shoeibi, H., Mehrpooya, M., Assareh, E., Izadi, M., & Pourfayaz, F. (2022). Transient simulation and exergy analysis of heat-pump systems integrated with solar compound parabolic collector. *Iranian Journal of Chemistry and Chemical Engineering*, *41*(6), 2121–2134.
[6] Zhong, X., Yang, H., Yang, K., & Xu, J. (2019). Development of a new-type multiple-source heat pump with two-stage compression. *Journal of Thermal Science*, *28*, 635–642.
[7] Zheng, Z., Zhou, J., Xu, F., Zhang, R., & Deng, G. (2022). Integrated operation of PV assisted ground source heat pump and air source heat pump system: Performance analysis and economic optimization. *Energy Conversion and Management*, *269*, 116091.
[8] Zhang, W., Wang, K., Guan, C., Yao, H., Li, W., Gao, Y., & Cui, P. (2023). Analysis and optimization of the performance for the ground source heat pump system with the middle-deep U-type well. *Applied Thermal Engineering*, *219*, 119404.
[9] Bae, S., & Nam, Y. (2022). Feasibility analysis for an integrated system using photovoltaic-thermal and ground source heat pump based on real-scale experiment. *Renewable Energy*, *185*, 1152–1166.
[10] Li, T., Wang, X., Li, G., Liu, Y., Liu, Q., Gong, Y., ... & Mao, Q. (2024). Thermal performance and energy flow analysis of a PV/T coupled ground source heat pump system. *Applied Thermal Engineering*, *240*, 122265.
[11] Maghrabie, H. M., Abdeltwab, M. M., & Tawfik, M. H. M. (2023). Ground-source heat pumps (GSHPs): Materials, models, applications, and sustainability. *Energy and Buildings*, *299*, 113560.
[12] Cui, Y., Zhu, J., Twaha, S., Chu, J., Bai, H., Huang, K., ... & Soleimani, Z. (2019). Techno-economic assessment of the horizontal geothermal heat pump systems: A comprehensive review. *Energy Conversion and Management*, *191*, 208–236.

[13] Duarte, W. M., Paulino, T. F., Tavares, S. G., Maia, A. A., & Machado, L. (2021). Feasibility of solar-geothermal hybrid source heat pump for producing domestic hot water in hot climates. *International Journal of Refrigeration, 124*, 184–196.

[14] Arghand, T., Javed, S., & Dalenbäck, J. O. (2022). Combining direct ground cooling with ground-source heat pumps and district heating: Borehole sizing and land area requirements. *Geothermics, 106*, 102565.

[15] Karabacak, R., & Acar, Ş. G. (2010). The experimental thermal performance analysis of the ground source heat pump system dependent on environmental conditions. *Energy Sources, Part A: Recovery, Utilization, and Environmental Effects, 32*(12), 1142–1158.

[16] Usta, H. (2009). The modeling of the efficiency of the heat pump supported by heat pipe with solar energy. *Energy Sources, Part A: Recovery, Utilization, and Environmental Effects, 32*(3), 232–245.

[17] Karytsas, S. (2018). An empirical analysis on awareness and intention adoption of residential ground source heat pump systems in Greece. *Energy Policy, 123*, 167–179.

[18] Zheng, Z., Zhou, J., Xu, F., Zhang, R., & Deng, G. (2022). Integrated operation of PV assisted ground source heat pump and air source heat pump system: Performance analysis and economic optimization. *Energy Conversion and Management, 269*, 116091.

[19] Cheng, F., Xia, J., Ajo-Franklin, J. B., Behm, M., Zhou, C., Dai, T., ... & Zhou, C. (2021). High-resolution ambient noise imaging of geothermal reservoir using 3C dense seismic nodal array and ultra-short observation. *Journal of Geophysical Research: Solid Earth, 126*(8), e2021JB021827.

[20] Blum, P., Campillo, G., & Kölbel, T. (2011). Techno-economic and spatial analysis of vertical ground source heat pump systems in Germany. *Energy, 36*(5), 3002–3011.

[21] Michopoulos, A., Zachariadis, T., & Kyriakis, N. (2013). Operation characteristics and experience of a ground source heat pump system with a vertical ground heat exchanger. *Energy, 51*, 349–357.

[22] Alavy, M., Nguyen, H. V., Leong, W. H., & Dworkin, S. B. (2013). A methodology and computerized approach for optimizing hybrid ground source heat pump system design. *Renewable Energy, 57*, 404–412.

[23] Yang, W., Liang, X., Shi, M., & Chen, Z. (2014). A numerical model for the simulation of a vertical U-bend ground heat exchanger used in a ground-coupled heat pump. *International Journal of Green Energy, 11*(7), 761–785.

[24] Ünal, F., Temir, G., & Köten, H. (2018). Energy, exergy and exergoeconomic analysis of solar-assisted vertical ground source heat pump system for heating season. *Journal of Mechanical Science and Technology, 32*, 3929–3942.

[25] Benli, H. (2011). Energetic performance analysis of a ground-source heat pump system with latent heat storage for a greenhouse heating. *Energy Conversion and Management, 52*(1), 581–589.

[26] Özsolak, O., & Esen, M. (2014). Performance investigation of Slinky heat exchanger for solar assisted ground source heat pump. *E-Journal of New World Sciences Academy, 84*.

[27] Akbulut, U., Utlu, Z., & Kincay, O. (2016). Exergy, exergoenvironmental and exergoeconomic evaluation of a heat pump-integrated wall heating system. *Energy, 107*, 502–522.

[28] Ercan, U. (2021). *Batman ili iklim şartlarında toprak kaynaklı ısı pompası için enerji ve ekserji analizi* (Doctoral dissertation, Batman University, Graduate School of Education).

International Journal of Innovative Engineering Applications

Journal homepage: https://dergipark.org.tr/ijiea

INVESTIGATION OF THE BENEFITS OF THE FLOATING SOLAR POWER PLANT TO BE ESTABLISHED ON KEBAN DAM LAKE USING PENMAN, LINACRE AND ARTIFICIAL NEURAL NETWORKS METHODS

Savaş Kurt*[*1], Hikmet Esen[2], Ünal Toka[3]

[1]Department of Renewable Energy Systems, Faculty of Technology, Fırat University, Elazığ, Turkey
[2]Department of Mechanical Engineering, Institute of Science and Technology, Fırat University, Elazığ, Turkey
[3]Internal Audit Unit, Munzur University, Tunceli, Turkey

Abstract

Original scientific paper

In this study, it will be calculated how much water evaporation will be prevented if a Floating Solar Power Plant (FSPP) is installed on a certain part of the Keban Dam lake in Elazığ (38.41˚N, 39.14˚E), Türkiye by using the Penman and Linacre methods and the Artificial Neural Networks (ANN) method, which are widely used in evaporation calculation. Thus, it will be calculated how much energy can be produced with this saved water. Keban Hydroelectric Power Plant (HPP), examined in this study, is Türkiye's 3rd largest hydroelectric power plant with an installed power of 1.330 MWe. It is the fourth largest lake in Türkiye and the second largest dam lake after the Atatürk Dam. Keban Dam meets the electrical energy needs of 1.750.733 people in their daily lives with an average electricity production of 5.794.927,279 kWh.

It has been calculated that thanks to a floating photovoltaic power plant that will cover 10% of the dam lake, a total of 31.305.282 m^3 of water in normal water code will be prevented from evaporating annually, and thanks to this water, energy benefit will be provided with the power plant with an installed power of 6.624,84 MWe. In addition, it has been analyzed that 11.297.018 kWh of electricity can be produced from the dam turbines with the water prevented from evaporating thanks to FSPP. Approximately 72.39 MWe energy is needed for the Ağın, Pertek, Serince, Palu-Kovancılar, Uluova, Kuzova irrigation projects around the Keban Dam lake. It has been determined that the amount of water and energy needed for irrigation of these plains can be obtained thanks to FSPP.

Keywords: *Floating solar power plant, Keban Dam Lake, irrigation system, evaporation, energy efficiency gains.*

Abbreviations

ASKI	:	Ankara Water and Sewerage Administration General Directorate
FPVF	:	Floating Solar Photovoltaics
FSSPF	:	Floating Solar Power Plant
HDPE	:	High Density Polyethylene
MGM	:	General Directorate of Meteorology
MEVBİS	:	Meteorological Data Information Presentation and Sales
LSTM	:	Long Short-Term Memory
RNN	:	Recurrent Neural Network
CNN	:	Convolutional Neural Networks
GRU	:	Gated Recurrent Unit
SGD	:	Stochastic Gradient Descent
SPP	:	Solar Power Plant

1 Introduction

FSPP is a relatively new form of renewable energy and is experiencing rapid growth in use today. FSPP decarbonizes the energy supply while reducing land use pressure, offers higher electricity generation efficiency compared to ground-based systems, and reduces water body evaporation [1]. Another potential benefit of floating photovoltaic panel systems is that they can outperform traditional photovoltaic (PV) systems in terms of energy efficiency due to the cooling effect of water. Open system designs, where the floating system's PV panels are extensively exposed to the water surface, lead to an increase in the heat loss coefficient (a measure for the cooling effect) of the floating PV panels by up to 22 W/m^2K [2].

Annual specific efficiencies of PV systems compared to reference PV systems were estimated by the measured irradiance-weighted temperature difference and a PVsyst model containing inputs of heat loss coefficients. Based on these calculations, it has been observed that the gain in energy efficiency from the cooling effect of FSPP systems compared to reference PV systems is up to 3% in the Netherlands and 6% in Singapore. A prototype modeled on the concept of evaporation pans has been built to mimic the situation of solar panels floating on reservoirs. Observations are made regarding the evaporation rate and compared to a control. Experimental results have shown that floating solar panels on water bodies have the effect of reducing evaporation rates by approximately 30% [2,3]. FSPPs on water prevent heating and make it easier for

*Corresponding author.
E-mail address: s.kurt@firat.edu.tr (S. Kurt)
Received 27 February 2025; Received in revised form 20 May 2025; Accepted 10 June 2025
 Doi: https://doi.org/10.46460/ijiea.1647566

them to move and turn, which helps achieve higher levels of efficiency [4]. Floating PV systems can contribute to irrigation stability and synergy between the agriculture and energy production sectors, given their ability to prevent surface evaporation while simultaneously generating power [5]. While the floating photovoltaic industry is in its infancy, it is growing at an incredible pace. Floating PV systems have many benefits such as higher efficiency, less evaporation, and less erosion [6].

Floating solar photovoltaic systems were first developed in 2000-2010; the first small-scale system was built in Japan in 2007, and the first commercial system was built in California in 2008 [7]. Installations larger than 1 MWp were not developed until 2013. As of the end of 2019, the total installed capacity of floating PV systems exceeded 2 GWp [8]. By 2030 there will be an estimated 62 GWp of floating PV systems globally. Today, Asia dominates the FSPP market with 87% of global capacity [9].

Conditions taken into account in FSPP site selection; solar radiation, climate conditions, buildable water area and reservoir conditions, bathymetry of the reservoir, reservoir depth, intra-annual water level change, wind and wave conditions, ground structure of the reservoir, shading and pollution, environmental conditions and finally the distance to the grid connection point. By examining these data, the suitable physical installation area will be determined. Depending on this, the float type to be selected, the layout plan with the photovoltaic panel is drawn up, and then the panel-inverter configuration and system power are determined [10]. Floating solar energy system components: consists of floating structure, mooring system, PV solar module, cabling and grid connection station [11]. In floating PV systems; It is important to investigate the use of pre-existing electrical infrastructure of a hydroelectric power plant. FSPP systems have shown that the existing electricity production and transmission infrastructure of the hydroelectric power plant can be technically integrated into the hydroelectric power plant. It is more economically feasible than applying it in other water bodies such as natural lakes, ponds or canals [12]. The electrical infrastructure of the dams has the capacity to support an additional energy production unit such as a Floating Solar Plant. Floating PV systems are modular and can reduce the cost of electricity transmission when combined with a hydroelectric power generation facility. Its modular structure enables easy installation and provides convenience in terms of both production and transmission infrastructure [13]. The future FSPP proposed for sea and large lake areas envisages laminated thin film PV, which will ensure that the structure is flexible and resilient to incoming waves, and designs that will withstand harsh weather conditions and be submerged [14]. Taking environmental factors into account, energy production prediction models based on regression analysis and neural networks are presented and their accuracy is compared. This comparison confirms that the accuracy of the energy production prediction model using neural networks is approximately 2.59% higher than that of the regression analysis method [15]. Regarding the type of water, the use of fresh water (lakes, artificial and natural basins, rivers) has many advantages over sea water, for example, limited corrosion problems, reduced effect of waves and wind, limited algal bloom. On the other hand, seaside space is much more available, but of course the cost of support rafts and moorings may be higher [16]. The supporting structures for a FSPP system with rigid PV modules differ from conventional ones (coastal systems) because they do not have a fundamentally solid fixing (the problem of wind folding) and have an uneven surface (due to waves). Rigid PV modules, when exposed to wind and water loads, may suffer from cell crack formation due to their limited flexibility and mechanical properties [17]. So far, the development of floating GESs has been focused mainly on onshore deployments, as it is thought that the harsh marine environment may compromise the long-term stability of such structures. Typhoon Faxai, which affected Japan in 2019 and caused a fire in one of the floating solar power plants, although rare, still posed a real risk that could deter investment in this technology [18].

Türkiye is in a better situation than Germany, one of the leading countries in the solar industry, in terms of sunshine duration and total solar radiation. Although Sinop province is at lower levels in terms of solar radiation (1400-1500 kWh/m^2), it is higher than Germany's highest center of solar potential, the State of Bavaria [19]. The estimated power we will obtain when 1% of the surface area of the water reserves of hydroelectric power plants in Türkiye is used is 512.69 GW, and this capacity is approximately 214 times the power of the Atatürk dam. In addition, for this 1% surface area, an average of 30.761.400 tons of water is prevented from evaporating annually with the shading effect of FSPPs [20]. It has been announced that if the FSPP planned to be built on Eğirdir Lake in Isparta province is put into operation and photovoltaic panels cover approximately 75% of the installed area, it will help reduce the evaporation problem in the lake. Additionally, it has been determined that it is possible to produce 992 MWh of electricity per year by utilizing the sun [21]. There are 944 dams currently in operation in Türkiye that are not intended for drinking water purposes. These dams have a reservoir surface area of 5300 km^2. It is estimated that if FSPPs are installed on 10% of the surface area of this reservoir, 1/4 of Türkiye's electrical energy needs can be met. It has also been stated that it works 10% more efficiently than terrestrial FSPPs and enables the utilization of unused reservoir surface areas and bringing them into the economy [22].

ASKI General Directorate announced that work is being carried out for the installation of floating solar power plants on the Bayındır Dam. It has been announced by the institution that a on-grid floating solar power plant installation with a photovoltaic panel capacity of 990 kWp is planned on the Bayındır Dam [23]. When the costs of the FSPP built on the Büyükçekmece Lake are examined, it is more expensive than terrestrial solar power plants. The most important reason for this is that these systems are R&D projects and have not reached mass production level. However, not using any soil surface and protecting drinking water by reducing evaporation will cause FSPPs to be preferred [24]. Floating GESs working 10 % more efficiently than terrestrial GES; It provides the evaluation of the reservoir surface areas in the case of the economy. Floating GESs can be installed in all dam reservoirs,

except for drinking water purposes. Türkiye is in a very lucky position in terms of floating GES potential. In our country, there are 944 dams in the form of drinking water in the form of drinking water, 5 thousand 300 kilometers of square such as a very wide reservoir surface area. If the floating GES is installed in 10 %of this surface area, it is foreseen that 53 thousand MW installed power and 79 billion 500 million kilowatt hours (about one quarter of our country's electrical energy needs) can be produced. It is estimated that the amount of water to be saved by preventing evaporation thanks to the floating GESs will be at a level of 540 million cubic meters annually. Moreover, thanks to these facilities, the amount of carbon dioxide to be released into the atmosphere will be reduced by over 51 million tons [25].

2 Material and Methodology

2.1 Preparation of Data Set

The data needed to calculate the amount of evaporation was obtained by requesting an official letter from the Turkish General Directorate of Meteorology (MGM) Meteorological Data Information Sales and Presentation System (MEVBİS). The data set was taken from a total of 13 meteorological observation stations around the Keban Dam lake in the MGM 13th Elazığ region, taking into account the points on the map shown in Fig. 1. These stations have meteorological parameters measured between 2014 and 2023. These parameters are given in detail in Table 1.

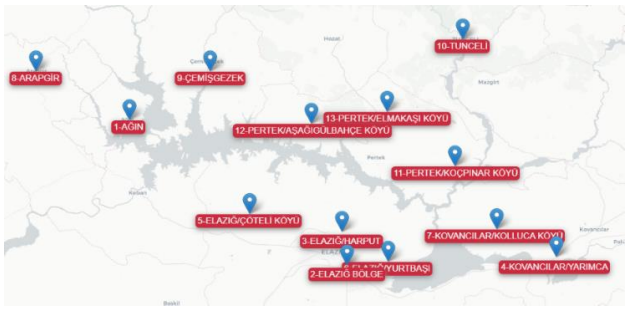

Figure 1. The geographical locations of the 13 weather stations around the Keban Dam Lake [26].

Daily total open surface evaporation, daily total evaporation evapotranspiration, daily total global solar radiation, daily total insolation intensity, daily total insolation intensity global and daily total precipitation (manual) parameters are measured only in Elazığ center and Tunceli meteorological station. These data were prepared by MGM in Excel format, with parameter values as month and day cross tabulation. With the Python programming language, these Excel tables were converted into appropriate formats to be used in calculations and transferred to the Mysql database.

While there are very few empty or invalid values in the basic meteorological parameters such as temperature, pressure, humidity and wind in the data set, there are many empty or invalid values in parameters such as evaporation and solar radiation. There are no values between 2014-2017 in the parameters especially related to solar radiation, measured only in Elazığ Center and Tunceli. Fig. 2 shows the change in solar radiation values of these two stations over time.

Table1. Weather parameters used in this study.

Parameter	Unit	Weather Stations
Daily Vapor Pressure	hPa	All
Daily Duration of Sunshine	hour	All
Daily Maximum Wind Speed	m/s	All
Daily Maximum Wind Direction and Speed	(°)-(m/s)	All
Daily Maximum Wind Hour	UTC	All
Daily Maximum Temperature	°C	All
Daily Mean Soil Temperature (5 cm depth)	°C	All
Daily Minimum Temperature	°C	All
Daily Mean Actual Pressure	hPa	All
Daily Mean MSLP	hPa	All
Daily Mean Relative Humidity	%	All
Daily Mean Temperature	°C	All
Daily Aboveground Temperature	°C	All
Daily Total Open Surface Evaporation	mm	Elazığ Center and Tunceli
Daily Total Evapotranspiration	mm	Elazığ Center and Tunceli
Daily Total Global Solar Radiation	kWh/m²	Elazığ Center and Tunceli
Daily Total Intensity of Solar Radiation	Cal/cm²	Elazığ Center and Tunceli
Daily Total Intensity of Global Solar Radiation	W/m²	Elazığ Center and Tunceli
Daily Total Precipitation - MANUEL	mm=kg/m²	Elazığ Center and Tunceli
Daily Total Precipitation - Automatic Weather Stations	mm=kg/m²	All

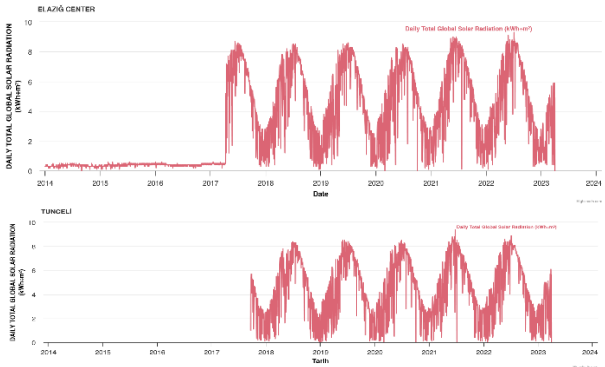

Figure 2. Daily Total Global Solar Radiation values by years (Elazığ Center - Tunceli).

Similarly, open surface evaporation values in mm were measured only between 1 April and 30 October each year. Fig. 3 shows the change in daily total open surface evaporation values of these two stations over time.

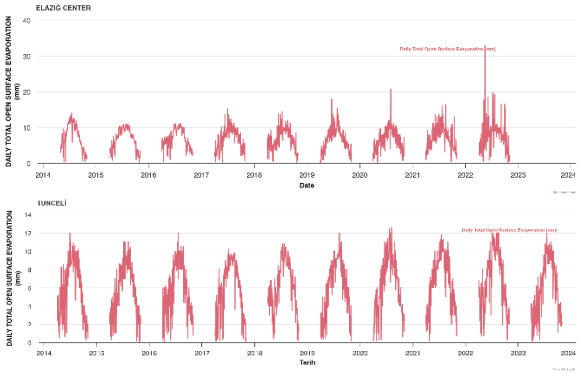

Figure 3. Daily Total Open Surface Evaporation values by years (Elazığ Center - Tunceli).

The parameters needed in the calculations were completed using various interpolation methods.

2.1.1 Evaporation Calculation

Evaporation is the process of liquid water turning into gas and can occur at any temperature. Moving water molecules gain energy by colliding and when they reach enough energy, they move away from the water surface.

There are many meteorological parameters that affect evaporation at different levels. Temperature, pressure, wind and humidity are some of these parameters. Increasing temperature will cause water molecules to move faster and reach higher kinetic energy. As a result, they will separate from the water surface. There is a direct proportion between temperature and the amount of evaporation. Air pressure acts on the water surface and puts pressure on the molecules trying to separate. For this reason, high pressure causes less evaporation. There is an inversely proportional relationship between them. Humidity and evaporation are inversely proportional. Humidity refers to the water vapor in the air. A high level of water vapor means that the air is saturated with water vapor and cannot carry any more. For this reason, it becomes difficult for water molecules to escape into the atmosphere and evaporation occurs slowly. Wind allows the vapor on the water surface to be transported and water molecules that have enough energy to separate to rise more easily into the atmosphere. For this reason, there is a directly proportional relationship between wind and evaporation. Surface area and depth of water are other factors that affect evaporation.

In Table 2 below, the wind directions at the eight stations where measurements were taken are given together with their numbers [27].

Pyet, an open source Python package, was used to calculate the daily evaporation in Keban Dam Lake. The Pyet module calculates daily PET (Potential Evapotranspiration) using eighteen different methods. Detailed information about the content of the Pyet module is given in Table 3 [28].

Table 2. Wind directions and numbers taken from 8 weather stations for the period 2014-2024.

	N	NNE	NE	ENE	E	ESE	SE	SSE	S	SSW	SW	WSW	W	WNW	NW	NNW
AĞIN	20	13	36	92	286	323	203	63	24	70	184	251	336	829	776	43
ELAZIĞ MERKEZ	34	10	23	116	326	469	394	201	138	57	39	86	428	665	609	49
ELAZIĞ -HARPUT	403	269	162	115	180	124	66	148	298	207	265	210	225	207	383	196
KOVANCILAR-YARIMCA	81	191	110	58	40	119	393	383	273	148	363	645	470	202	105	55
ELAZIĞ -YURTBAŞI	92	87	122	305	259	90	69	34	92	100	187	209	304	223	139	104
ARAPGİR	96	158	154	119	158	227	444	175	279	401	259	421	78	101	429	75
ÇEMİŞGEZEK	950	215	31	20	40	111	119	127	594	451	178	53	166	153	137	227
TUNCELİ	91	61	144	98	49	25	92	114	510	265	277	183	207	717	751	67

Table 3. Evaporation calculation methods and input parameters in the Pyet module.

Method name	Pyet function	T	RH	R	U2	Lat.	El.	Benchmark
Penman	penman	✓ [a]	✓ [b,c]	✓[d]	✓	✓ [d]	✓ [e]	✓
Penman-Monteith	pm	✓ [a]	✓ [b,c]	✓ [d]	✓	✓ [d]	✓ [e]	✓
ASCE-PM	pm_asce	✓ [a]	✓ [b,c]	✓ [d]	✓	✓ [d]	✓ [e]	✓
FAO-56	pm_fao56	✓ [a]	✓ [b,c]	✓ [d]	✓	✓ [d]	✓ [e]	✓
Priestley-Taylor	priestley_taylor	✓	✓ [h]	✓ [h]	-	✓ [h]	✓ [e]	✓
Kimberly-Penman	kimberly_penman	✓ [a]	✓ [b,c]	✓ [d]	✓	✓ [d]	✓ [e]	-
Thom-Oliver	thom_oliver	✓ [a]	✓ [b,c]	✓ [d]	✓	✓ [d]	✓ [e]	-
Blaney-Criddle	blaney_criddle	✓	- [i]	- [i]	- [i]	✓	-	✓
Hamon	hamon	✓	-	-	-	✓	-	✓
Romanenko	romanenko	✓	✓	-	-	-	-	✓
Linacre	linacre	✓ [j]	-	-	-	-	✓	✓
Haude	haude	✓	✓ [k]	-	-	-	-	✓
Turc	turc	✓	✓	✓	-	-	-	✓
Jensen-Haise	jensen_haise	✓	-	✓[l]	-	✓ [l]	-	✓
McGuinness-Bordne	mcguinness_bordne	✓	-	-	-	✓	-	✓
Hargreaves	hargreaves	✓ [m]	-	-	-	✓	-	✓
FAO-24 radiation	fao_24	✓	✓	✓	✓	-	✓ [e]	-
Abtew	abtew	✓	-	✓	-	-	-	✓
Makkink	makkink	✓	-	✓	-	-	✓ [e]	✓
Oudin	oudin	✓	-	-	-	✓	-	-

T: Daily Mean Temperature [°C]
R: Solar Radiation [MJ m-2 d-1]
Lat: Latitude [rad]
El: Elevation [m]
RH: Daily Mean Relative Humidity [%]
U2: Daily Mean Wind Speed [m/s]

(a) *Daily Maximum Temperature or Daily Minimum Temperature can also be provided.*

(b) *Daily Maximum Relative Humidity or Daily Minimum Relative Humidity can also be provided.*

(c) *If actual vapor pressure is provided, Relative Humidity is not needed*

(d) *Input for radiation can be (1) Net radiation, (2) solar radiation or (3) sunshine hours. If (1), then latitude is not needed. If (1, 3) latitude and elevation is needed.*

(e) *One must provide either the atmospheric pressure or elevation.*

(f) (h) *If net radiation is provided, RH and Lat are not needed.*
(g) *If method==2, Daily Mean Wind Speed, Daily Minimum Wind Speed and sunshine hours are required.*
(h) (j) *Additional input of Daily Maximum Temperature and Daily Minimum Temperature, or Dew Point Temperature.*
(i) (k) *Input can be Daily Mean Relative Humidity or actual vapor pressure*
(j) (l) *If method==1, latitude is needed instead of incoming solar radiation*
(k) (m) *Daily Maximum Temperature and Daily Minimum Temperature also needed*

In this study, Penman and Linacre methods in the Pyet module were chosen to calculate the daily evaporation in Keban Dam Lake. Python programming language was used for calculation and the open source and free PyCharm 2023.2.2 (Community Edition) package was used as the code development environment.

2.1.1.1 Penman Method

The Penman method is a method developed by Howard Penman in 1948 to calculate evaporation on an open water surface using temperature, wind speed, air pressure and solar radiation parameters [29]. The Penman equation is as follows [30]:

$$E_{pan} = \left(\frac{\Delta}{\Delta+\gamma}\right) x(R_n - G) + \left(\frac{\gamma}{\Delta+\gamma}\right) x \frac{6.43(1+0.53u_2)(e_s-e_a)}{\lambda} \quad (1)$$

In the equation:

E_{pan}: daily pot evaporation amount (mm/day),
Δ: slope of the saturated vapor pressure curve at the current temperature of the air (kPa / °C),
γ: psychometric value (kPa / °C),
R_n: daily net radiation (MJ/m^2 day)
G: Heat flux density of the soil (MJ/m^2 day),
λ: latent heat of evaporation of water,
u_2: wind speed at 2 m above the ground (m/s),
e_s: saturated vapor pressure (kPa),
e_a: actual (current) vapor pressure (kPa).

2.1.1.2 Linacre Method

Linacre is another method used to calculate evaporation from open water surfaces; It uses air temperature, latitude and altitude parameters [31]. To estimate evaporation and potential evaporation values, Linacre developed the following relations.

$$E_{pan} = \frac{\left(\frac{500T_m}{100-A}\right)+15(T-T_{dp})}{80-\mathrm{T}} \quad (2)$$

$$T_m = T - 0.0006h \quad (3)$$

In equality;

E_{pan}: daily container evaporation amount (mm/day),
A: degree of latitude (°),
T: daily average air temperature (°C),
T_m: temperature coefficient decreasing with altitude
h: altitude (m),
T_{dp}: daily average dew point temperature (°C).

Linacre is another method used to calculate evaporation from open water surfaces; It uses air temperature, latitude and altitude parameters [32].

Meteorology station information and parameter data, which were previously read and written to the database with the Python openpyxl module, were read from the database with the MySQLdb module, missing data were filled in with the linear interpolation method using the Pandas module, and were prepared as input to the Pyet module for evaporation calculation. Then, the evaporation values calculated by the Penman method of the Pyet module were written back to the database for easier querying and visualization.
The Python code that performs this operation is given below:

```
import pandas as pd
import MySQLdb
import numpy as np
import pyet

db = MySQLdb.connect(host="localhost", user="****", passwd="****", db="meteo")
cur = db.cursor()
cur.execute("SELECT * FROM station WHERE istno='17165' or istno='17201'")

for row in cur.fetchall():
    cur.execute("SELECT * FROM params WHERE istno='"+row[0]+"'")
    result = list()
    for rowdt in cur.fetchall():
        result.append([rowdt[2], rowdt[0], rowdt[12], rowdt[9], rowdt[16], rowdt[3], rowdt[4], rowdt[20]])

    data = pd.DataFrame(result, columns=['station','time','rad','rel','t','tmax','tmin','vv'])
    meteo = pd.DataFrame({"time":data.time,

"tmean":data.t.interpolate(method='linear', limit_direction='forward'),

"tmax":data.tmax.interpolate(method='linear', limit_direction='forward'),

"tmin":data.tmin.interpolate(method='linear', limit_direction='forward'),

"rh":data.rel.interpolate(method='linear', limit_direction='forward'),

"wind":data.vv.interpolate(method='linear', limit_direction='forward'),

"rs":(data.rad*3.6).interpolate(method='linear', limit_direction='forward'),
                    })
    time, tmean, tmax, tmin, rh, wind, rs = [meteo[col] for col in meteo.columns]
    lat = float(row[3])*np.pi/180
    elevation = int(row[7])

    pet_u = pd.DataFrame()
```

```
        pet_u["tarih"] = time
        pet_u["penman"] = pyet.penman(tmean, wind,
rs=rs, elevation=elevation, lat=lat, tmax=tmax,
tmin=tmin, rh=rh).fillna(0)
        pet_u["linacre"] = pyet.linacre(tmean,
elevation=elevation, lat=lat, tmax=tmax, tmin=tmin,
rh=rh).fillna(0)

        for count, pn in enumerate(pet_u["penman"]):
            sql = "UPDATE params SET penman =
"+str(pn)+" WHERE tarih =
'"+str(pet_u["tarih"][count])+'" and istno=
'"+row[0]+""
            cur.execute(sql)
        db.commit()

        for count, pn in enumerate(pet_u["linacre "]):
            sql = "UPDATE params SET linacre =
"+str(pn)+" WHERE tarih =
'"+str(pet_u["tarih"][count])+'" and istno=
'"+row[0]+""
            cur.execute(sql)
        db.commit()

db.close()
```

Meteorological parameters prepared to be used in evaporation calculations and their statistical information are given in Table 4.

Table 4. The main statistical parameters of weather parameters [2014-2024].

Station name: Elazığ Center						
	Solar Radiation	Relative Humidity	Mean Temperature	Max. Temperature	Min. Temperature	Wind Speed
Total Number of Observations	3378	3611	3648	3649	3649	3645
Mean	3.19	50.85	14.74	21.32	8.54	8.58
Standard Deviation	2.89	22.08	9.95	11.54	8.18	3.43
Minimum	0.00	10.80	-9.70	-5.40	-15.40	2.30
25%	0.40	30.00	6.10	11.10	2.00	6.00
50%	2.40	49.90	14.40	21.20	8.30	8.20
75%	5.90	70.40	23.80	32.00	15.60	10.60
Maximum	9.30	99.00	33.30	42.40	30.50	26.30
Station name: Tunceli						
	Solar Radiation	Relative Humidity	Mean Temperature	Max. Temperature	Min. Temperature	Wind Speed
Total Number of Observations	2219	3652	3652	3652	3652	3652
Mean	4.00	55.25	13.93	21.29	7.55	6.43
Standard Deviation	2.66	20.87	9.87	11.50	8.24	2.03
Minimum	0.00	15.00	-14.50	-8.00	-19.20	0.00
25%	1.70	36.68	5.40	11.10	1.00	5.10
50%	4.00	53.80	13.80	21.40	7.30	6.20
75%	6.40	72.00	22.80	31.70	14.50	7.20
Maximum	9.40	99.40	32.10	41.80	25.50	18.50

Since solar radiation data for the Penman method is available at only two stations and must be given as input in the calculations, this code was run using Elazığ Central and Tunceli Meteorology station data. The daily values of the calculated evaporation results obtained from the Penman and Linacre programs between 2014 and 2023 are given in Fig. 4 in mm.

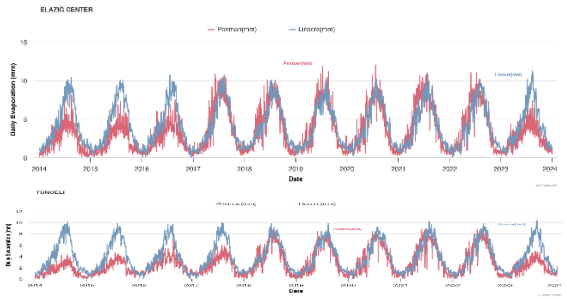

Figure 4. Daily evaporation computed by the Penman and Linacre methods.

In the Penman method, since solar radiation values are missing in these two stations in the first years, the evaporation amounts calculated from the interpolated values are lower than they should be. Evaporation values calculated with the Penman method are closer to their real values between 2018 and 2023. Since the Linacre method does not use solar radiation in the calculation, the results obtained are closer to the actual open surface evaporation values.

In the following sections, these values will be evaluated together with the measured daily total open surface evaporation values and the evaporation values estimated with artificial neural networks (ANN).

2.2 Artificial Neural Networks

ANN are an approach used in many decision-making processes, thanks to their flexible and powerful structure provided by their learning and generalization capabilities. ANN is an effective system in solving different and complex problems depending on its many features. There are different network structures suitable for solving each problem. It is up to the decision maker to decide which solution network is suitable for these problems. This may vary depending on the problem being studied [33, 34].

ANN generally consists of the following three layers. It is the input, hidden and output layer. An ANN model may have more than one hidden layer. ANN processes the information coming from the input layer in the middle layer and converts it into output. A general layer structure of ANN is given in Fig. 5.

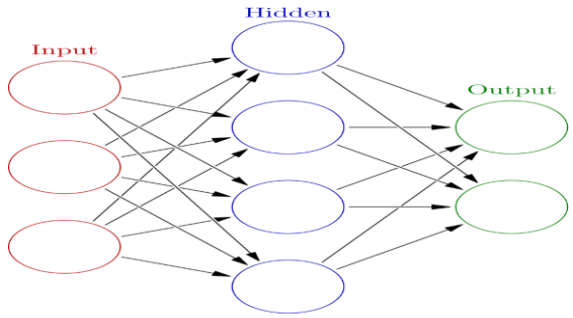

Figure 5. Neural network architecture [35].

2.2.1 Deep Learning

It can be defined as training multilayer artificial neural networks with the backpropagation algorithm. There are many different deep learning models such as CNN, RNN, LSTM and GRU [36, 37].

The long short-term memory model (LSTM) we use in predictions is a recurrent RNN developed by Hochreiter and Schmidhuber in 1997 [38]. The problems experienced in training RNN neural networks are completely eliminated in LSTM. LSTM is widely used in time series problems because it can learn long-term dependencies [39].

Tensorflow and Pytorch are two of the widely used deep learning modules in the Python programming language. In this study, daily evaporation amounts were tried to be estimated using the LSTM model of the Pytorch module (Fig. 6) and the temperature, humidity, pressure, wind and relative humidity data obtained from MGM.

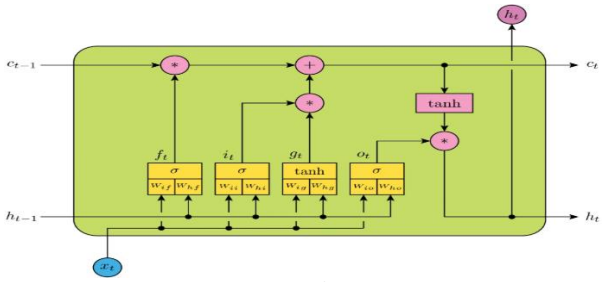

Figure 6. An annotated illustration of the LSTM cell in PyTorch [40].

2.2.2 Correlation

The correlation between meteorological parameters that are input to LSTM is shown in Fig. 7.

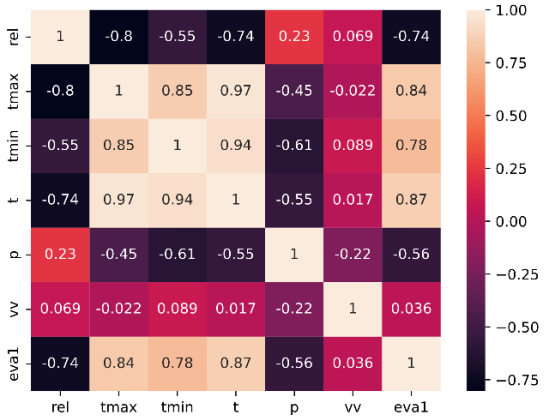

Figure 8. Correlation values of meteorological parameters.

The correlation graph is divided into 2 diagonally in the middle. With a different color palette, colors can mean different things. In the graph, colors that start from 0 and turn black, starting from -1, show negative correlation, and colors that start from 0, and go towards 1, turn red, show positive correlation.

The correlation matrix function of the Pandas module is corr(), the default analysis value is set to "Pearson". There is a very strong correlation (0.8 to 1 or -0.8 to -1.0) between evaporation (eval) and temperature (t) (0.87) and maximum temperature (tmax) (0.84). There is a strong correlation (0.6 to 0.8 or -0.6 to -0.8) between evaporation (eval) and minimum temperature (tmin) (0.78) and relative humidity (rel) (-0.74). There is a moderate correlation (0.4 to 0.6 or -0.4 to -0.6) between evaporation (eval) and pressure (p) (-0.56).

The correlation between evaporation (eval) and wind speed (vv) appears to be very low. There may be different reasons for this. There may not actually be a relationship between the parameters, or pairs of variables may not satisfy the assumptions of Pearson correlation analysis. One or both pairs of variables may not have a continuous data type. The variables are not normally distributed or there is no linear relationship between the variables.

SGD was used as the optimization algorithm in the model. MSE was chosen as the loss function. The epochs value was determined as 200, the stacked LSTM (multiple LSTM) model value was determined as 2, the output size was determined as 1, and the number of hidden features (hidden size) was determined as 512. The data is divided into 60% training and 40% testing.

The nn.MSELoss function in PyTorch was used as the loss function to measure the error rate of the model and therefore its performance. The graph showing the training and testing loss of the model is given in Fig. 8. When the Figure is examined, it is seen that the training loss and test loss both decrease and stabilize after a certain point. Since the loss function of the model is examined, it can be said that it has a good fit.

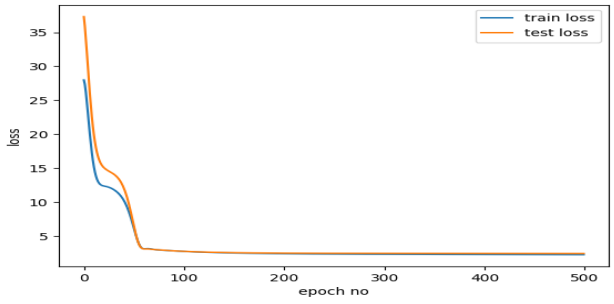

Figure 8. Training and testing loss.

3 Analysis and Evaluation

Annual total open surface evaporation values measured for Elazığ Central and Tunceli Meteorology stations, evaporation estimates of the LSTM model, and the change in evaporation values calculated by the Penman and Linacre method between 2014 and 2023 are given in Fig. 9.

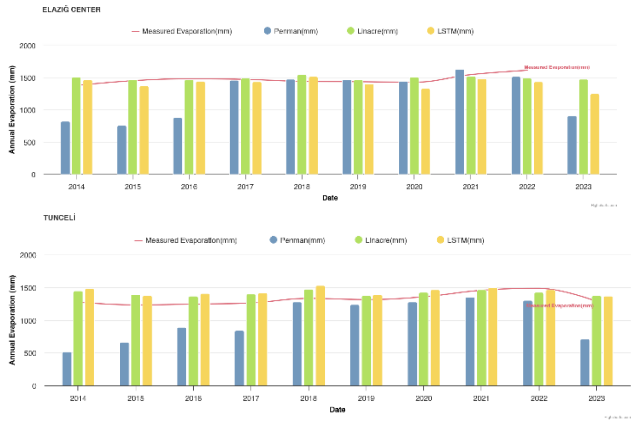

Figure 9. Comparison between calculated from Linacre , Penman, LSTM and the measured evaporation (Elazığ Center - Tunceli).

The change in annual total open surface evaporation values estimated using data obtained from synoptic stations and automatic observation stations around Keban Dam Lake is also given in Table 5.

When Table 5 is examined, it is seen that daily total open surface evaporation values are available for only two stations (Elazığ Center and Tunceli), and likewise, daily total global solar radiation measurement values for only these two stations in Penman are calculated accurately since they are available after 2018. In addition, when Fig. 3 is examined, it is evaluated that outlier values have occurred after 2019 for the daily total open surface evaporation values for Elazığ center, which causes erroneous results in the observed annual total evaporation values. For this reason, especially in recent years, the annual total evaporation values observed for Elazığ center have been very close to or greater than the predicted values. In fact, it is expected that the annual total evaporation observation values will be smaller than expected since evaporation observations for Elazığ center and Tunceli stations are not made from November to April. For these reasons, it was decided to use data from Tunceli station when calculating the Keban Dam lake evaporation estimate.

For Tunceli station, the Linacre average for the last 10 years is 1415 mm, Penman (between 2018-2023 due to missing values) is 1290 mm, LSTM average is 1441 mm and finally the average measured from the evaporation pool is 1323 mm.

Evaporation occurring in evaporation ponds is higher than evaporation occurring in deep waters such as lakes or dams. For this reason, the values measured in evaporation ponds are multiplied by a coefficient to estimate the evaporation amounts in lakes or dams. This coefficient varies between 0.6 and 0.8. For Türkiye, this estimation coefficient is usually taken as an average of 0.7 [41].

In Table 6, the actual or predicted values in the evaporation pond were multiplied by this coefficient and the amount of water evaporated per square meter in the dam lake was calculated in mm. In addition, since Keban Dam has a reservoir area of 408.28 km^2 at a minimum water elevation of 820.00 m and a reservoir area of 676.14 km^2 at a normal water elevation of 845.00 m, the annual total evaporation values in the dam were also calculated for these reservoir areas.

Table 5 Comparison between the calculated and measured evaporation (mm).

		2014	2015	2016	2017	2018	2019	2020	2021	2022	2023
AĞIN	Linacre	1595	1513	1493	1541	1574	1478	1529	1524	1532	1499
	LSTM	1276	1311	1446	1457	1414	1381	1320	1456	1460	1225
ELAZIĞ CENTER	Linacre	1508	1467	1470	1493	1549	1464	1504	1522	1496	1473
	Penman	820	755	879	1457	1477	1465	1446	1627	1514	913
	LSTM	1467	1375	1442	1438	1512	1406	1328	1487	1433	1250
	Measured (MGM)	1377	1450	1478	1470	1440	1434	1427	1544	1611	
ELAZIĞ -HARPUT	Linacre	1797	1627	1397	1441	1400	1309	1362	1353	1341	1309
	Penman								343	743	521
	LSTM	1036	1285	1307	1122	1202	1118	1196	1336	1297	1103
KOVANCILAR-YARIMCA	Linacre	1490	1452	1469	1463	1534	1435	1469	1516	1489	1441
	LSTM	1460	1418	1300	1340	1480	1420	1308	1496	1429	1251
ELAZIĞ -ÇÖTELİ KÖYÜ	Linacre	136	1430	1423	1454	1499	1437	1486	1474	1465	1429
ARAPGİR	Linacre	1395	1361	1337	1395	1414	1351	1404	1383	1409	1350
	LSTM	1450	1355	1382	1425	1459	1370	1292	1446	1269	1197
ÇEMİŞGEZEK	Linacre	1537	1479	1442	1410	1550	1471	1504	1519	1512	1451
	LSTM	1506	1219	1398	1316	1466	1399	1330	1483	1456	1229
TUNCELİ	Linacre	1453	1393	1366	1399	1475	1373	1426	1463	1427	1373
	Penman	519	660	892	840	1277	1235	1283	1352	1301	716
	LSTM	1478	1380	1412	1413	1533	1393	1466	1499	1462	1371
	Measured (MGM)	1272	1231	1244	1261	1331	1313	1356	1455	1484	1284
PERTEK-AŞAĞIGÜLBAHÇE KÖYÜ	Linacre	142	1478	1455	1488	1534	1458	1525	1506	1490	1442
ELAZIĞ -YURTBAŞI	Linacre			504	1486	1532	1449	1535	1569	1485	1463
	LSTM								1305	1356	1183
PERTEK-ELMAKAŞI KÖYÜ	Linacre			543	1353	1382	1339	1401	1367	1355	1330
KOVANCILAR-KOLLUCA KÖYÜ	Linacre					1522	1443	1532	1470	1498	1480
PERTEK-KOÇPINAR KÖYÜ	Linacre					1460	1387	1441	1459	1434	1393

Table 6. The estimated annual evaporation of the Keban Dam Lake.

	Evaporation Gage (mm)	Keban Dam Lake (mm)	Keban Dam Lake Minimum Water Level (m^3)	Keban Dam Lake Normal Water Level (m^3)
Linacre	1.415	991	404.605.480	670.054.740
Penman	1.290	903	368.676.840	610.554.420
LSTM	1.441	1.009	411.954.520	682.225.260
Measured (MGM)	1.323	926	378.067.280	626.105.640

It has been observed that if the water surface is covered with solar energy panels in natural lakes and ponds, evaporation decreases by 33%, and in artificial lakes and dams by 50% [42].

Keban Dam has a reservoir area of 408.28 km^2 and a water volume of 15.820.000 m^3 at a minimum water elevation of 820 m, and a reservoir area of 676.14 km^2 and a water volume of 29.414.669 m^3 at a normal water elevation of 845 meters. How much evaporation will be prevented and how much energy can be produced with this water prevented from evaporating in case a floating solar power plant is installed to cover 3%, 5% and 10% of the surface area of Keban Dam at minimum and normal water elevation is calculated in Table 7.

The amounts of water used and energy obtained in the Keban Dam Lake in Elazığ for the year 2023 are given in Figs. 10 and 11, respectively.

Table 7. The total annual water saving.

	Total Surface Area of Dam Reservoir Covered with PV Panels					
	3%	5%	10%	3%	5%	10%
	The estimated annual total evaporation of the Keban Dam Lake Minimum Water Level (m^3)			The estimated annual total evaporation of the Keban Dam Lake Normal Water Level (m^3)		
Linacre	6.069.082	10.115.137	20.230.274	10.050.821	16.751.369	33.502.737
Penman	5.530.153	9.216.921	18.433.842	9.158.316	15.263.861	30.527.721
LSTM	6.179.318	10.298.863	20.597.726	10.233.379	17.055.632	34.111.263
Measured (MGM)	5.671.009	9.451.682	18.903.364	9.391.585	15.652.641	31.305.282

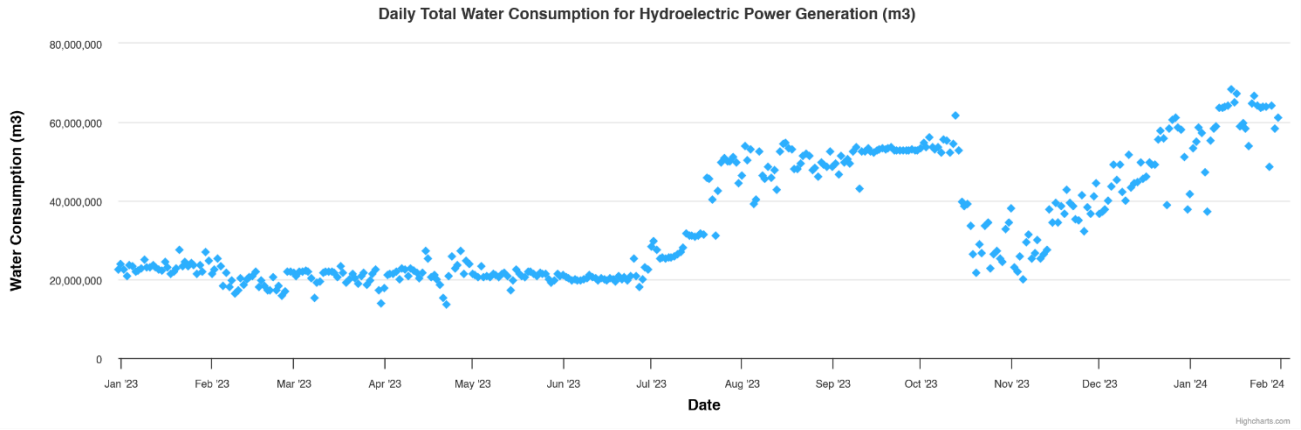

Figure 10. Daily total water consumption for hydroelectric power generation from Keban Dam Lake (Jan 2023 – Feb 2024).

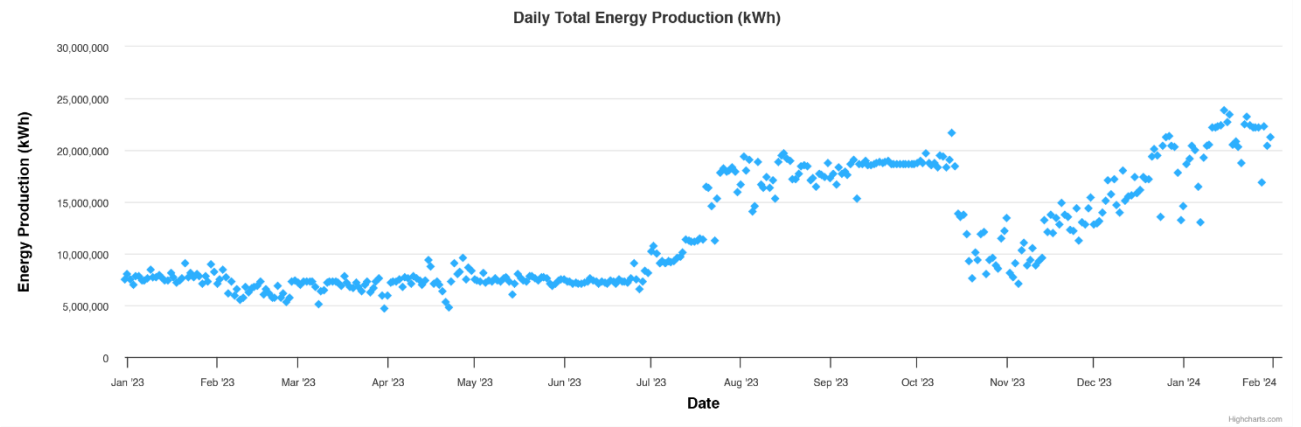

Figure 11. Daily total electrical energy produced from Keban Dam Lake (Jan 2023 – Feb 2024).

Keban Dam meets the electrical energy needs of 1.750.733 people in their daily lives with an average electricity production of 5.794.927,279 kWh. It has been calculated that a total of 31.305.282 m^3 of water in normal water code will be prevented from evaporating annually, thanks to a FSPP that will cover 10% of the dam lake. It has been analyzed that thanks to this water, energy benefit will be provided by the power plant with an installed power (10% floating solar power installed capacity) of 6.624,84 MWe, and 11.297.018 kWh of electricity can be produced from the dam turbines with the water prevented from evaporating thanks to FSPP.

Approximately 72.39 MWe energy is needed for the Ağın, Pertek, Serince, Palu-Kovancılar, Uluova, Kuzova irrigation projects around the Keban Dam lake. Thanks to this study, it has been determined that the amount of water and energy needed for irrigation of these plains can be obtained thanks to FSPP.

4 Results

Türkiye's average annual rainfall is 643 mm. Approximately 501 billion m^3 of this amount of precipitation corresponds to water. 274 billion m^3 of this precipitation returns to the atmosphere through evaporation from rivers, lakes, streams and seas, and from plants. 158 billion m^3 of the water that falls to the ground through precipitation is carried to lakes or seas by streams. The remaining 69 billion m^3 consists of groundwater [43]

With the amount of water per capita of 1.519 m^3, Türkiye is classified as a country suffering from water shortage. Turkish Statistical Institute (TUIK) estimates that Türkiye's population will reach 100 million in 2030. In other words, the amount of water per capita is estimated to be 1.120 m^3/year. Our country is facing the situation of being "water poor" with its increasing population, growing cities and developing economy. Additionally, it has been determined that precipitation in the Mediterranean basin has decreased by 20% in the last 25 years due to global climate change [44].

Floating solar power plants are a structure consisting of solar panel systems mounted on the water surface. These systems are usually built on artificial water reservoirs such as dams, ponds or irrigation ducts.

Solar panels used in floating GES are mounted on platforms floating on the water surface. These systems are usually made of light and water -resistant materials such as HDPE (high density polyethylene). The panels contain photovoltaic cells to capture sunlight and convert them into electricity. The generated electricity is then moved to the land by cable and is either used for direct energy needs or transferred to the electricity network.

Floating GESs, first, the cooling effect of water increases the efficiency of the panels. Secondly, these systems; It reduces the evaporation of water by covering the water surface and contributes to the protection of water resources. Thirdly, floating GESs are beneficial for land use and are especially preferred in areas with land shortage.

For irrigation projects, these irrigation needs to be made with the pumping system, that is with an energy, in terms of the elevation between the buildings to be irrigated with water from dam reservoir. This means an additional cost of about 40 percent.

In addition to providing energy from renewable energy sources for economic development, Türkiye must use water resources effectively, economically and efficiently. In this study, thanks to the FSPP to be built on the Keban Dam lake, overheating of photovoltaic panels will be prevented and electrical energy will be obtained with higher efficiency. Thanks to FSPP, water evaporation in the dam lake is reduced, how much water is prevented from evaporating by using artificial intelligence methods, and thanks to this water, more energy will be obtained from the turbines in the power plant, and thanks to the non-evaporated water, the water needs of the plains around the dam lake and the promoted irrigation systems will be met. determinations were made.

Thanks to a FSPP that will cover 10% of the Keban Dam lake, which is the subject of the study, it has been calculated that a total of 33.502.737 m^3, 30.527.721 m^3 and 34.111.263 m^3 of water in normal water code will be prevented from evaporating annually using Linacre, Penman and LSTM methods, respectively. It was calculated that the evaporation of the measured 31.305.282 m^3 of water was prevented and thanks to this water, energy benefit was provided by the Solar Power Plant with an installed power of 6.624,84 MWe. Additionally, it has been analyzed that 11.297.018 kWh of electricity can be produced from the dam turbines with the water prevented from evaporating thanks to FSPP.

There are 968 dams in Türkiye. In this study, using artificial neural networks and Penman and Linacre methods, which are widely used in evaporation calculations, it has been seen that the amount of water evaporation in the Keban Dam lake with FSPP and the benefit of energy production thanks to water will be significant. In addition, it has been determined that much more energy will be obtained by passing the water flowing after these turbines through the turbines in Karakaya Dam, Atatürk Dam, Birecik Dam and Karkamış Dam. It is thought that this study will create a model for FSPPs to be built on all dams in Türkiye.

Declaration

Ethics committee approval is not required.

References

[1] Exley, G., Armstrong, A., Trevor, P., Page, T., & Jones, I. D. (2021). Floating photovoltaics could mitigate climate change impacts on water body temperature and stratification. *Solar Energy, 219*, 24–33.

[2] Dörenkämper, M., Wahed, A., Kumar, A., Jong, M., Kroon, J., & Reindl, T. (2021). The cooling effect of floating PV in two different climate zones: A comparison of field test data from the Netherlands and Singapore. *Solar Energy, 214*, 239–247.

[3] Melvin, G. K. X. (2015). *Experimental study of the effect of floating solar panels on reducing evaporation in Singapore reservoirs* (Master's dissertation, National University of Singapore).

[4] Redón Santafé, M., Torregrosa Soler, J. B., Sánchez Romero, F. J., Ferrer Gisbert, P. S., Ferrán Gozálvez, J. J., & Ferrer Gisbert, C. M. (2014). Theoretical and experimental analysis of a floating photovoltaic cover for water irrigation reservoirs. *Energy, 67*, 246–255.

[5] Tsoutsos, T., Frantzeskaki, N., & Gekas, V. (2005). Environmental impacts from the solar energy technologies. *Energy Policy, 33*(3), 289–296.

[6] Farfan, J., & Breyer, C. (2018). Combining floating solar photovoltaic power plants and hydropower reservoirs: A virtual battery of great global potential. *Energy Procedia, 155*, 403–411.

[7] Reindl, T., et al. (2019). *Where sun meets water: Floating solar market report*. Retrieved April 10, 2020, from https://esmap.org/where_sun_meets_water_floating_solar_market_report

[8] Intersolar Europe. (2022). *Floating PV: On the rise in Europe*. Retrieved January 1, 2022, from https://www.intersolar.de/market-trends/floating-pv-europe

[9] Farrar, L. W., Bahaj, A. S., James, P., Anwar, A., & Amdar, N. (2022). Floating solar PV to reduce water evaporation in water stressed regions and powering water pumping: Case study Jordan. *Energy Conversion and Management, 260*, 115598.

[10] Işık, A. H., Arıcı, B., & Alhelali, S. *Floating solar power plants technical guide*. Clean Creative Technologies Consultancy and Engineering Inc.

[11] Bulut, M., Kaplanoğlu, İ., & Geylani, V. (2018). Development of world hydro-floating SPP projects and their potential in Turkey. *Power Systems Conference*, Ankara, Turkey.

[12] Huzaifa, R., Gull, M. S., & Arshad, N. (2019). Integrating floating solar PV with hydroelectric power plant: Analysis of Ghazi Barotha reservoir in Pakistan. *Energy Procedia, 158*, 816–821.

[13] World Bank Group, ESMAP, & SERIS. (2019). *Where sun meets water: Floating solar market report*. Retrieved April 10, 2020, from https://www.worldbank.org/en/topic/energy/publication/where-sun-meets-water

[14] Trapani, K., & Santafé, M. R. (2014). A review of floating photovoltaic installations: 2007–2013. *Progress in Photovoltaics: Research and Applications, 22*(4), 689–716.

[15] Jeong, H. S., Choi, J., Lee, H. H., & Jo, H. S. (2020). A study on the power generation prediction model considering environmental characteristics of floating photovoltaic system. *Applied Sciences, 10*(13), 4527.

[16] Aquilina, M., Mule` Stagno, L., Grech, M., & Sant, T. (2016). Determining the optimum shape and size of a platform for an offshore floating photovoltaic system. In *3rd Offshore Energy & Storage Symposium (OSES)*, Valletta, Malta.

[17] Kajari-Schröder, S., Kunze, I., Eitner, U., & Köntges, M. (2011). Spatial and directional distribution of cracks in silicon PV modules after uniform mechanical loads. In *Proceedings of the 37th IEEE Photovoltaic Specialists Conference*, Seattle, WA, USA.

[18] Bellini, E. (2019). Japan's largest floating PV plant catches fire after Typhoon Faxai impact. *PV Magazine International*. Retrieved September 9, 2019, from https://www.pv-magazine.com/2019/09/09/japanslargest-floating-pv-plant-catches-fire-aftertyphoon-faxai-impact/

[19] Alcan, Y., Demir, M., & Duman, S. (2018). Examination of Sinop Province's electricity production potential from solar energy in comparison with our country and Germany. *El-Cezeri Journal of Science and Engineering, 5*(1), 35–44.

[20] Bolat, B. (2022). *Investigation of the energy production potential of hydroelectric power plants and dam lakes with floating solar power plants* (Master's dissertation, Yıldız Technical University)

[21] Güner, S., & Özgür, A. E. (n.d.). Investigating the applicability of Eğridir Lake Solar Power Plant. *Süleyman Demirel University YEKARYUM e-Journal, 8*(2), 80–93.

[22] TRT Haber. (2024). Türkiye yüzer GES'lerden elektrik alacak. Retrieved May 14, 2024, from https://www.trthaber.com/haber/ekonomi/turkiye-yuzer-geslerden-elektrik-alacak-857398.html

[23] ASKİ. (2024). Türkiye'de ilk: ASKİ, baraj üzerinde yüzer GES kurarak elektrik üretecek. Retrieved March 14, 2024, from https://www.aski.gov.tr/tr/HABER/Turk%C4%B1yede-Ilk-Ask%C4%B1-Baraj-Uzer%C4%B1nde-Yuzer-Ges-Kurarak-Elektr%C4%B1k-Uretecek/569

[24] Kaymak, M. K. (2021). *Design and application of adaptive floating solar power plant to weather-environmental conditions* (Doctoral dissertation, Istanbul Technical University, Graduate Education Institute).

[25] State Hydraulic Works (DSİ). (2024). Both clean energy and water savings with floating GES. Retrieved March 10, 2025, from https://www.dsi.gov.tr/Haber/Detay/12128

[26] Ministry of Environment, Urbanisation and Climate Change & Turkish State Meteorological Service. (n.d.). [Institutional source – no specific title available].

[27] Turkish State Meteorological Service. *Official web site: Forecast cities*. Retrieved January 9, 2025, from https://www.mgm.gov.tr/eng/forecast-cities.aspx

[28] PyET Project. *Estimation of potential evaporation*. Retrieved from https://pypi.org/project/pyet/

[29] Terzi, Ö. (2004). *Development and application of evaporation models for Lake Eğirdir* (Unpublished doctoral thesis, Süleyman Demirel University, Institute of Science and Technology, Isparta).

[30] Efthimiou, N., Alexandris, S., Karavitis, C., & Mamassis, N. Comparative analysis of reference evapotranspiration estimation between various methods and the FAO56 Penman–Monteith procedure. [Conference or journal info not provided].

[31] Hiroyuki, M., & Kazzutoshi, O. (2023). Alternative net longwave radiation equation for the FAO Penman–Monteith evaporation equation and the Penman evaporation equation. *Theoretical and Applied Climatology, 153*, 1355–1360.

[32] Emerine, C. N., Isagba, E. S., & Idehen, O. F. (2018). Linacre derived potential evapotranspiration method and effect on supplementary irrigation water needs of tomato, cabbage, and carrot. *Nigerian Journal of Environmental Sciences and Technology, 2*(1), 108–117.

[33] Karaatlı, M., Helvacıoğlu, Ö., Ömürberk, N., & Tokgöz, G. (2012). Automobile sales forecasting with artificial neural networks method. *International Journal of Management Economics and Business, 8*(17), 87–100.

[34] Esen, H., & İnallı, M. (2009). Modelling of a vertical ground coupled heat pump system by using artificial neural networks. *Expert Systems with Applications, 36*(7), 10229–10238.

[35] Wikipedia. Neural network (machine learning). Retrieved June 23, 2025, from https://en.wikipedia.org/wiki/Neural_network_(machine_learning)

[36] Çakmak, E., & Selvi, İ. H. (2022). Protein secondary structure prediction using deep learning (CNN, RNN, LSTM, GRU). *Acta Infologica, 6*(1), 43–52.

[37] Esen, H., İnallı, M., Sengur, A., & Esen, M. (2008). Performance prediction of a ground-coupled heat pump system using artificial neural networks. *Expert Systems with Applications, 35*(4), 1940–1948.

[38] Hochreiter, S., & Schmidhuber, J. (1997). Long short-term memory. *Neural Computation, 9*(8), 1735–1780.
[39] Akın, E., & Şahin, M. E. (2024). A review on deep learning and artificial neural network models. *EMO Scientific Journal: Scientific Refereed Journal of Electrical, Electronics, Computer, Biomedical, Control Engineering, 14*(1), 27–38.
[40] Medium.LSTM cells in PyTorch. Retrieved June 23, 2025, from https://medium.com/@andre.holzner/lstm-cells-in-pytorch-fab924a78b1c
[41] Yıldız, F. E., & Güler, İ. (2014). Comparison of evaporation methods for Sultan Sazlığı wetland. *Gazi University Journal of Science and Technology Part C: Design and Technology, 2*(3), 247–254.
[42] Alok, S., Neha, Y., & Sudhakar, K. (2016). Floating photovoltaic power plant: A review. *Renewable and Sustainable Energy Reviews, 66*, 815–824.
[43] Tokuşlu, A. (2022). Assessing the impact of climate change on Turkish basins. *International Journal of Environment and Geoinformatics, 9*(1), 103.
[44] Devlet Su İşleri. Toprak ve su kaynakları. Retrieved April 3, 2015, from http://www.dsi.gov.tr/toprak-ve-su-kaynaklari
[45]WWF–Türkiye.Türkiye'de su kaynaklarının güncel durumu raporu. Retrieved April 10, 2025, from https://www.wwf.org.tr/kesfet/tatli_su/turkiyede_su_kaynaklarinin_guncel_durumu/

.

International Journal of Innovative Engineering Applications

Journal homepage: https://dergipark.org.tr/ijiea

PRODUCTION AND CHARACTERIZATION OF COMPOSITE POWDER FROM MEDIUM ENTROPY ALLOYS PRODUCED USING W, Mo, Nb – Fe, Ni, Co POWDERS

Muhammet Gökhan Albayrak*[1]

[1]*Firat University, Faculty of Engineering, Department of Metallurgical and Materials Engineering, Elazig/Turkey*

Abstract

Original scientific paper

Todays, Middle Entropy Alloys (MEA) are a relatively new production method and have extraordinary advantages over classical methods. The biggest advantage is defined as the production of complex compounds that cannot be combined with known methods. MEAs prepared with transition metals such as Fe, Ni, Co have an important place due to their superior properties such as anti-oxidation, corrosion and wear behavior. Metals with refractory properties such as W, Mo, Nb are interesting due to their high hardness as well as high temperature applications. In this study, which aims to characterize two different MEA powders produced, MEA powders were produced using refractory metals such as W, Mo and Nb and transition metal powders such as Fe, Ni and Co. The difference of this publication is that all powders are not brought together at once during production, but W, Mo, Nb and Fe, Ni, Co powders are produced separately and combined later. Mechanical Alloying (MA) was preferred as the production method due to its advantages such as reducing grain size and ensuring chemical homogenization. XRD, SEM and EDS (mapping) analyses were performed for the characterization of the obtained medium entropy alloy composite. Thanks to the MA technique, the powder sizes were reduced and both MEA powders were successfully distributed homogeneously within each other.

Keywords: *Characterization, complex compounds, FeNiCo, middle entropy alloy, WMoNb.*

W, Mo, Nb – Fe, Ni, Co TOZLARI KULLANILARAK ÜRETİLEN ORTA ENTROPİ ALAŞIMLARINDAN KOMPOZİT TOZ ÜRETİMİ VE KARAKTERİZASYONU

Özet

Orijinal bilimsel makale

Orta Entropi Alaşımları (MEA) günümüzde oldukça yeni bir üretim metodu olup klasik üretimlere göre sıradışı avantajlara sahiptir. Bilinen yöntemlerle bir araya gelemeyen kompleks bileşiklerin üretilmesi en büyük avantajı olarak tanımlanmaktadır. Fe,Ni, Co gibi geçiş metalleriyle hazırlanan MEA 'lar anti-oksidasyon, korozyon ve aşınma davranışı gibi üstün özellikleri sebebiyle önemli bir yere sahiptir. Refrakter özellikleri bulunan metaller örneğin W, Mo, Nb, yüksek sıcaklık uygulamalarının yanısıra sahip oldukları yüksek sertlikten dolayı ilgi çekicidir. Üretilen iki farklı MEA tozlarının karakterizasyonunu amaçlayan bu çalışmada W, Mo ve Nb gibi refrakter metaller ile Fe, Ni ve Co gibi geçiş metal tozları kullanılarak MEA tozları üretilmiştir. Üretim esnasında bütün tozların tek seferde bir araya getirilmeyip sırasıyla W, Mo, Nb ve Fe, Ni, Co tozlarının ayrı ayrı üretilip sonradan birleştirilmesi bu yayının farkını oluşturmaktadır. Tane boyutunun düşürülebilmesi ve kimyasal olarak homojenizasyonun sağlanabilmesi gibi üstünlüklerinden dolayı üretim yöntemi olarak Mekanik Alaşımlama (MA) tercih edilmiştir. Elde edilen orta entropi alaşım kompozitinin karakterizasyonu için XRD, SEM ve EDS (haritalama) analizleri yapılmıştır. MA tekniği sayesinde, toz boyutları azaltılmış ve her iki MEA tozu birbiri içerisinde homojen olarak başarıyla dağıtılabilmiştir.

Anahtar Kelimeler: *FeNiCo, karakterizasyon, kompleks bileşikler, orta entropi alaşımı, WMoNb.*

1 Introduction

Traditionally, an alloy is composed of a dominant primary element and modicum amounts of secondary ones added [1]. These additions should not be random, but should be determined and processed according to a certain knowledge or experience, resulting in improved material properties for different industries. Because it is the secondary ones that give the alloy desired and various differences [2].

A new approach to alloying was mentioned in a study published in 2004 [3]. This new approach focuses on the intermediate regions of the known and traditionally accepted multicomponent phase diagrams, instead of

*Corresponding author.

E-mail address: mgalbayrak@firat.edu.tr (M. G. Albayrak)

Received 27 February 2025; Received in revised form 16 April 2025; Accepted 21 May 2025

 Doi: https://doi.org/10.46460/ijiea.1648175

focusing on their entirety. The fact that the focused regions consist of unexplored compositional areas represents a significant conceptual change due to the risks associated with phase stability. These differences are the most unique aspect of the new approach [4]. Since study published in 2004 is different from conventional methods, it has the feature of inspiring scientists in their studies today. Therefore, in this study, the term "High Entropy Alloys" (HEA) was used for the first time. HEAs are defined on two principles. The first of these is the principle of having no atom less than 5% and more than 35% (Eq. 1) on the basis of atomic percentage (X_i), and having a total of 5 major metallic elements (n_{major}).

$$n_{major} \geq 5, \qquad 5 \leq X_i \leq 35 \qquad \text{(Eq. 1)[3]}$$

HEAs' have an arrangement of elements in a particular form and combination entropy, the second one, greater than 1.5 R ($R = 8{,}314 J/mol.K$) in the random solution state. For an alloy with "*n*" elements in a random solution state, the ordered combination entropy per mole (ΔS_{conf}) is calculated by the addition equation (Eq. 2).

$$\Delta S_{conf} = -R \sum_{i=1}^{n} X_i ln X_i \qquad \text{(Eq. 2)[3]}$$

The R value of a HEA containing 5 equiatomic metallic elements is calculated as 1.61. For this reason, the R value of 1.5 is accepted as the lower limit for HEAs containing 5 equiatomic metallic elements [5]. Continuing with this definition, the range of 1-1.5 R is called Medium Entropy Alloy (MEA), and 1 R and below is called Low Entropy Alloy (LEA) [6]. The entropy distribution according to the number of co-atomic elements calculated according to Eq. 3 is given in Table 1. "*n*" indicates the quantity of participants (metallic elements) and "ΔS_{Conf}" indicates the entropy value.

Table 1. ΔS_{Conf} distributions according to the number of co-atomic elements.

n	*1*	*2*	*3*	*4*	*5*	*6*	*7*	*8*	*9*
ΔS_{Con}	0	0.69R	1.1R	1.39R	1.61R	1.79R	1.95R	2.08R	2.2R

All alloys which are high, medium and low entropy should be selected on an appropriate scale to modify the microstructure and to be used in different combinations (non-isoatomic). In non-homoatomic low entropy alloys the microstructure is very variable. All (Single or Multi)-Phase microstructures including equiatomic and non-equiatomic phases are formed by high-entropy alloys [7].

The elements in the periodic table have various effects on entropy alloys. In general, the group 1 alkaline elements (excluding the hydrogen elements) have high levels of reactivity [8]. Group 2 elements (Alkaline Earth Metals), are preferred in lightweight HEAs because they can provide weight savings due to their low density [9]. The elements found in groups 3-12 (except Ac) are called transition metals. In addition to its strengths such as thermal and electrical conductivity, D block (transition metals) also has oxidation resistance. Thus, it is quite successful in preventing corrosion of metal parts in the system in which it is used. Post-transition metals that have high affinity to neighboring metals [10]. Metalloids exhibit both metallic and non-metallic behavior and moreover are generally used in HEAs to increase the strength and ductility of the FCC crystal structure [11]. Metalloids find use in structural improvement and biomedical sector applications [12]. The addition of nonmetals with low atomic radius such as C, N, O, P, S, and Se increases the hardness and decreases the toughness of the Fe alloy system. Due to the presence of 4f electrons with greater bonding strength in nature, Lanthanide group elements known Rare Earth Elements (REE) are used in applications where increased hardness and strength are required.

Based on the results of the studies, one of the most suitable ways to reduce particle size, refine grain size and achieve these without compromising chemical homogeneity is undoubtedly the mechanical alloying (MA) technique [13], [14]. MA, also known as high-energy ball alloying, is formed during mechanical alloying by mechanochemical reactions involving solid-solid and solid-liquid interactions. Based on the two different types of reactions in grinding conditions, the self-propagating combustion reaction promotes high enthalpy during grinding. Another incremental reaction occurs gradually. The important parameters affecting MA are ball-powder ratio, powder volume, container volume, grinding speed, grinding time, ball material, ball diameter, number of balls used and process control agents. In Figure 1, the MA jar and the breaking and re-boiling of the powder particles during MA are also schematically illustrated on the figure. If we need to explain the parameters affecting MA, the ball-powder ratio describes the weight ratio of the ball and powder in the container. Alloying speed and duration form the basis of the process. The material of the ball and the material of the container must not create a pollutant in the dust in case of wear. It is important to choose the same or similar material as the powder as possible. The ball diameter and number affect the weight of the ball used. Process control substances refer to a liquid to be given along with a gas or powder that will fill the space in the container. Increased product life or durability is a result of mechanical alloying or powder crushing aimed at improving mechanical performance. Injecting additives increases their effectiveness in the mechanical alloying process. These additives are called Process Control Agents (PCAs). PCAs are surfactants, sometimes known as surface additives. PCAs can be liquid or solid [10].

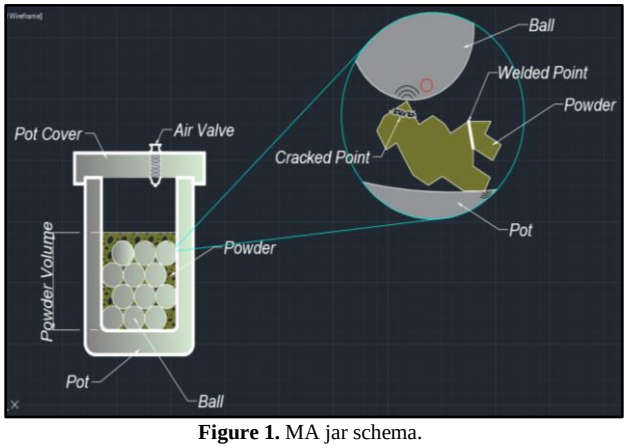

Figure 1. MA jar schema.

Due to the metal term originating from the HEA definition, FeNiCo is frequently used by scientists in MEA production. This combination, which attracts attention due to its mechanical and magnetic properties, is especially investigated in solving energy-related sector problems [15]. Although it has been shown that magnetic properties can be improved by producing FeNiCo-based alloys with different combinations (e.g. FeNiCoMnCu [16], FeNiCoMnAl [17], FeNiCoAlSi [18]), the mechanical properties are not at the desired levels [19]. On the other hand, it has been reported in the literature that composite HEA/MEA produced with particle reinforcements such as oxide or carbide give better results than alloys combined with chemical composition [20], [21]. Until 2010, while alloys based on transition metals such as Fe, Ni and Co were frequently studied in the literature, it is known that HEAs based on refractory composition elements were not discovered [22]. A new window has been opened for scientists with the use of elements such as W, Mo, Nb with refractory characteristics. It is also known that BCC HEAs have higher hardness than FCCs. Additionally, it has been discovered over the years that refractory HEAs have high mechanical properties in addition to their thermal properties [22], [23]. Indeed, providing entropy stability at high temperatures by being added to materials with ductility [24]–[26] and creating wear resistance due to having higher hardness than transition metals [27], [28] are some of the best examples of this new window. It is also becoming worth examining in the exploration of refractory metals. However, it was determined that there was no MEA prepared with W, Nb and Mo, which are among the refractory metals frequently researched in the literature.

In this study, two different MEAs which were FeNiCo and WMoNb, were produced. Then FeNiCo and WMoNb powders were weighed 95% and 5% by weight, respectively. These alloys were subjected to homogenization in a mechanical mill for another 5 hours to ensure both the necessary homogeneity and become a composite. Mechanical alloying (MA) was preferred as the production method in order to benefit from the advantages it provides in both MEA production. Characterization tests of both MEAs were performed and the study was completed by examining the final MEA mixture composite in terms of homogenization. The aim of this study is to produce a composite powder with two different MEAs and to characterize both MEAs and composite powders.

2 Material and Method

The elemental powders to be used in the study were commercially supplied by Nanografi company, provided that they were of high purity. Equal atomic W (Nanografi Company, 99.95% purity, 10µm), Mo (Nanografi Company, 99.99% purity, 10µm), Nb (Nanografi Company, 99.95% purity, 10µm), Fe (Nanografi Company, 99.99% purity, 5µm), Ni (Nanografi Company, 99.99% purity, 10µm) and Co (Nanografi Company, 99.9% purity, 10µm) powders were weighed on a precision balance and then grouped as WMoNb and FeNiCo. RETSCH PM200 device was used in the mechanical alloying process. The pot and balls used were selected as stainless steel, the ball-powder ratio was 10:1, and the rotation speed was 300 rpm, in the Ar atmosphere. The WMoNb group was commanded to work for 120 hours, with a 30-minute break every 30 minutes and the next work to be in the opposite direction, while the FeNiCo group differed from the previous group only in that the process lasted for 30 hours. Due to the presence of high hardness elements such as W, the MA period was determined as a long period of 120 hours in order to reduce the grain size and achieve proper homogenity. For relatively softer powders such as Fe, Ni and Co, MA treatment for a longer time such as 120 h was avoided because it could cause undesirable effects such as agglomeration in the powders. The production phase was completed by subjecting the obtained powder groups to a 5-hour final process under the same environment and conditions as above in order to ensure structural homogeneity. Whole MA process was carried out inert atmosphere (Ar, 99,999% purity) The production process of the study is schematized in Figure 2. Rigaku Miniflex 600 was used for X-Ray Diffraction (XRD) analysis, Hitachi SU3500 for Scanning Electron Microscopy (SEM) analysis and Oxford AZtech for Electron Dispersive Spectroscopy (EDS) analysis for powder characterization.

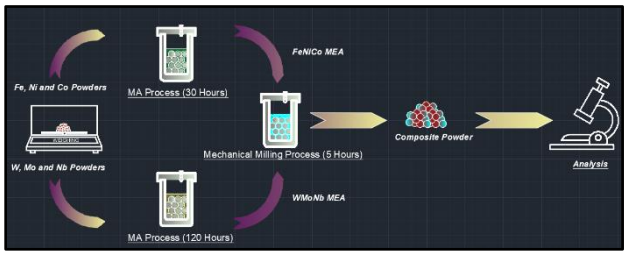

Figure 2. Production process of the study.

3 Results and Discussion

3.1 XRD Analyses of the Samples

During the preparation of the produced powder composite, two different groups were created, then these two different groups were brought together and powder characterizations were performed both as a group and as a single composite. The XRD graph of WMoNb produced as the first group MEA is given in Figure 3. The WMoNb powder mixture prepared as equiatomic was subjected to 120 hours of MA treatment and is named as "*WMoNb MA 120h*" in the figure. The reference codes used in XRD analyses were W *(Ref Code: 00-004-0806)*, Mo *(Ref Code: 00-042-1120)* and Nb *(Ref Code: 00-016-0001)*, respectively. For W, peaks of 40.265° (110), 58.276° (200), 73.198° (211) and 87.024° (220), for Mo, also peaks, 40,516° (110), 58,609° (200), 73,684° (211) and 87,598° (310) were observed. Nb peaks were also detected at 38.610° (110), 55.697° (200), 69.701° (211) and 82.524° (220).

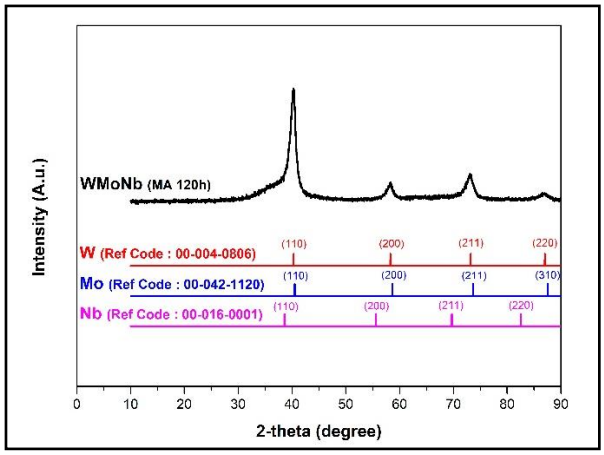

Figure 3: XRD analysis of WMoNb MEA.

The XRD analysis of FeNiCo MEA, which forms the second group of the composite, is given in Figure 4. Just like in the previous group, the results named "*FeNiCo MA 0h*" and "*FeNiCo MA 30h*" are shown before and after the MA process of the FeNiCo powder prepared as identical atoms, respectively. Before the process, the characteristic peaks of Fe (Ref Code: 00-001-1262), Ni (Ref Code: 00-045-1027) and Co (Ref Code: 00-001-1277) are clearly seen. It is observed that there is a decrease in peak intensities after 30 hours of MA treatment. The decrease in peak intensities and angular misalignments required by the MA process are examples of situations encountered in the literature [29]. Although some of the angular differences are based on the device used for measurement, it is generally a phenomenon that is read together with the success of the MA process. Similar situations have been encountered in our previous studies [30]. As seen in Figure 4, before mechanical alloying, FeNiCo powder exhibits pronounced and strong peaks. When looking at *Reference Codes* (Ref Code) to which the XRD data belong, it is seen that the cubic structures are not disrupted. The MA process causes marked alterations in the crystal structure of WMoNb powders. A distinct degredation in the intensity of XRD pattern is observed at all compositions for both the first and second groups. The characteristic peaks of Fe, Ni and Co at 44.6° (110), 44.52° (011) and 47.31° (101), respectively, are still observable, but their intensity has broadened and decreased significantly.

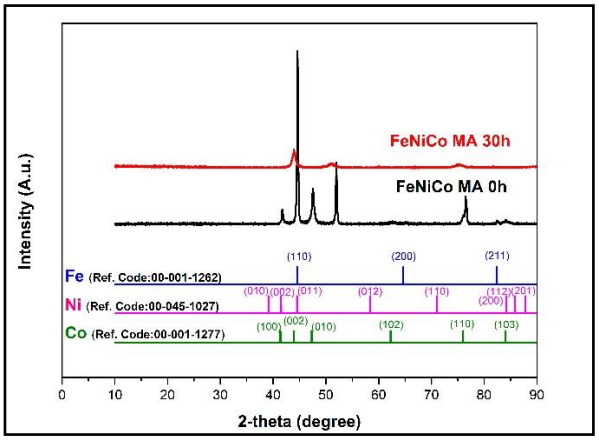

Figure 4. XRD analysis of FeNiCo MEA.

In Figure 5, XRD analyses of WMoNb and FeNiCo powders, in addition to 5% reinforced WMoNb and 95% FeNiCo composite powders are given together. In order to obtain a homogeneous distribution for a total of 5 hours by combining the two groups, the MA process was repeated without altering the environment and circumstances of the first two groups. The composite is named as "WMoNb + FeNiCo". While WMoNb has a very low concentration of 5%, it is inevitable that FeNiCo powder dominates in the XRD analysis of the composite powder. However, the peak of WMoNb around 40 degrees is also seen in the powder composite.

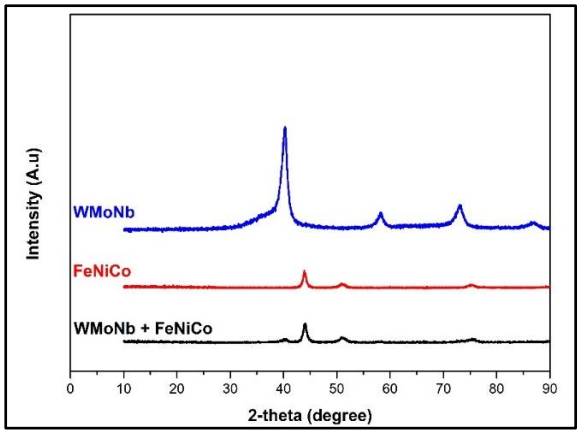

Figure 5. XRD analysis of WMoNb, FeNiCo and WMoNb + FeNiCo MEAs.

This expansion can be explained in two ways. The first one is the reduction in grain size. The second one is the increase in lattice tension. Both explanations are characteristic of the high-energy milling process and indicate that the powders have undergone this process. Angular deviations and expansions are observed at the peak positions. This is a phenomenon reported in the literature. It is considered as repeated fracture and cold welding caused by the powder being stayed in between ball-ball or ball-wall. This repeated randomly oriented fracture and welding process is consistent with previous reports of mechanical alloying, which leads to defect formation and lattice distortion. The substantial decline in peak intensity following MA process (see Figure 3) shows the success of the process related to MA on the crystalline structure of the composite powders. The decline in crystallinity index (see Table 2) is evidence of the mutation from an ordered crystalline to a more disordered possibly named somewhere-amorphous, state due to the high strain induced by mechanical alloying [31], [32]. It is reported in the literature [33] that MA can reduce grain sizes from micron to nano level and cause the emergence of high density dislocations and other defects due to structural deterioration. [30].

Table 2. Average grain size, crystallinity index and average dislocation density belog to all samples.

Samples	***Before MA Process***			***After MA Process***		
	Grain Size	*C. Index*	*D. Density*	*Grain Size*	*C. Index*	*D. Density*
FeNiCo	32.41258	47.84 %	0.000952	8.053712	23.21 %	0.015417
WMoNb	-	-	-	0.138699	57.96 %	51.98204
	Before Mixing for Homogenization			***After Mixing for Homogenization***		
Composite	7.65796	46.61 %	0.059599	0.13867	29.09 %	52.00379

While creating Table 2 containing Average Grain Size and Average Dislocation Density, "*Origin Pro 8.5*" software and "*Scherrer Equation* (Eq.3) [34]" were used. For composite, "*Before Mixing for Homogenization*" sections were calculated by averaging grain size.

$$D = \frac{k.\lambda}{\beta_{hkl}.cos\theta_{hkl}} \quad \text{(Eq.3)}$$

"*D*" symbolizes Grain Size. "*k*" Shape Factor and "λ" Wavelength are constants that are 0,9, and 0,154, respectively. "β" represents the Full Weight at Half Maximum (FWHM) value calculated from the peaks in the XRD image and with "$cos\theta$", it is the radian value of the 2-theta degree of the peak intensity.

The Crystallinity Index (Eq.4) [35] and Dislocation Density (Eq.5) [30] values were also calculated via XRD images. Formulation of these are below (Eq.4 and 5.);

$$\text{Crystallinity Index} = \frac{\text{Area of all the crystalline peaks}}{\text{Area of all crystalline and amorphous peaks}} \quad \text{(Eq.4)}$$

$$\delta = \frac{1}{D^2} \quad \text{(Eq.5)}$$

Average grain size and crystallinity index data have critically decreased after MA process. However, dislocation density has increased as expected. As seen in Table 2, time of MA process is primarily responsible for this situation.

3.2 SEM Analysis of the Composite Powders

SEM images of FeNiCo MEA a) before alloying and b) after alloying are given in Figure 6. It can be clearly seen from the images that the grain size is reduced. This conclusion can be reached as a result of mechanical grinding.

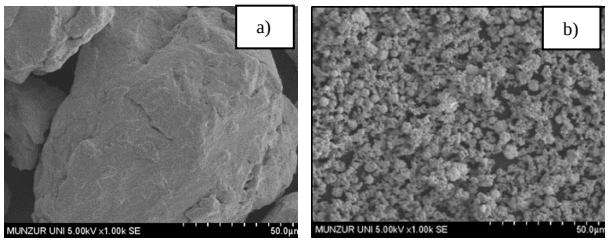

Figure 6. SEM images of FeNiCo MEA a) before alloying and b) after alloying.

Figure 7 shows SEM images of WMoNb MEA a) before alloying and b) after alloying. While it is observed that the powder size decreases with the mechanical alloying process, it is observed that the size distribution within the structure is not homogeneous. This situation is interpreted as the powders starting to agglomerate as a result of the high-energy alloying environment for a long time such as 120 hours. Although non-homogeneous powder particle distribution was mentioned above, this agglomeration is a physical volume increase other than chemical bonding.

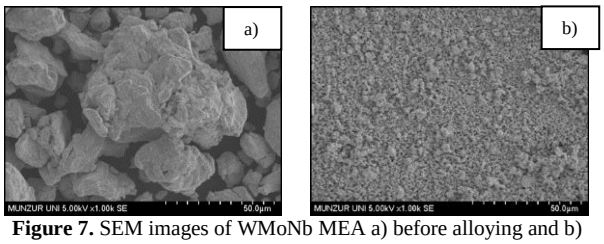

Figure 7. SEM images of WMoNb MEA a) before alloying and b) after alloying.

SEM image of WMoNb + FeNiCo composite is given in Figure 8. The powder, stayed between the ball-ball or ball-wall collusion is broken locally by the energy of the balls (caused by centrifugal force). Then, in another ball-ball or ball-wall collision, cold welding of the powders stayed in randomly between and overlapping each other occurs. By reducing the powder size, an advantage is gained for the sintering process carried out in advanced stages of powder metallurgy [36]–[38]. The possibility of approaching the desired optimum values in mechanical properties with low powder size increases. Lower particle size means lower porosity and therefore improved packing density. In this way, an increase in hardness and strength as well as an improvement in wear resistance can be achieved.

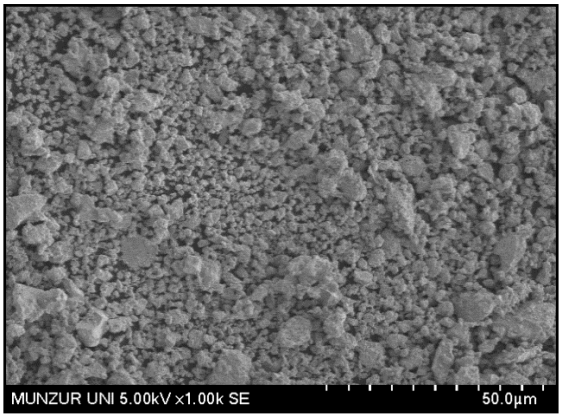

Figure 8. SEM image of WMoNb + FeNiCo composite.

Similar to Figure 7, it is seen in Figure 8 that the particle sizes are not homogeneous among themselves (FeNiCo and WMoNb). This situation can be explained by two reasons. The first of these is the agglomeration that occurs as a result of high-energy alloying, as in the WMoNb powder. In the study conducted by Ji et al. [39], it was stated that agglomerations started at MA times of 60 hours and above. The second is that although the mixing process is carried out for 5 hours under the same conditions for the purpose of homogenization, the grain sizes of the powders may differ from each other due to the different MA times. In addition, the agglomeration of the powders due to the difference in powder grain sizes can be added to the list as a third factor, albeit weak.

3.3 EDS Analysis of the Composite Powders

EDS analysis of FeNiCo MEA is given in Figure 9. It is also seen in the EDS analysis image that the dust size decreases according to the applied MA process. In addition, it is observed that Fe, Ni and Co mixed as elemental powder are mixed homogeneously

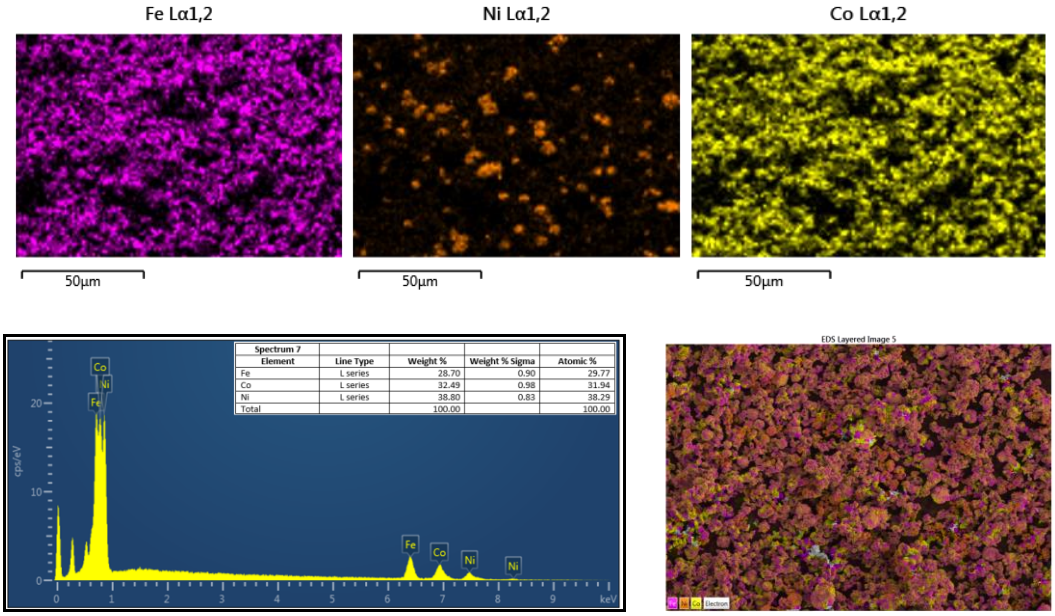

Figure 9. EDS analysis of FeNiCo MEA.

In Figure 10, the EDS analysis of the powder composite of WMoNb and FeNiCo MEA is given. As a result of the 5-hour mixing process in order to ensure a homogeneous distribution in both MEAs, it is seen that the structure is homogeneously distributed in the EDS images.

These findings are in line with the expected results and demonstrate the successful fabrication of the targeted MEA. SEM and elemental mapping analyses elucidate the microstructure of the fabricated MEAs. The dominance of particle sizes below 5 µm and the homogeneous distribution of constituent metals with atomic ratios ranging from 4.5% to 5.5% underline the meticulous control over the fabrication process. With this study, it was seen that homogeneous distributions can be obtained without melting, as in the studies carried out with full melting in the literature [40]–[42]. It is very clear that different advantages can be obtained with this MEA production (with MA process), which enables the metals with low and/or high melting temperatures to be brought together without melting.

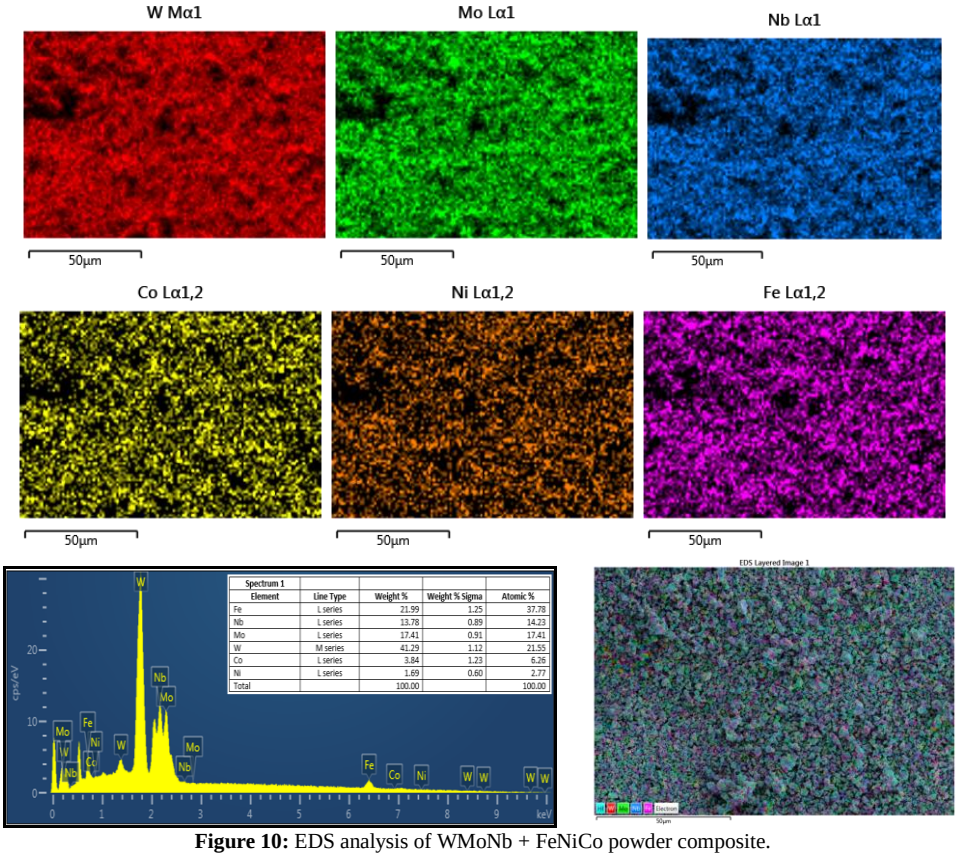

Figure 10: EDS analysis of WMoNb + FeNiCo powder composite.

4 Conclusion

The mechanical production of the powders of both groups (Fe, Ni, Co and W, Mo, Nb) weighed as equal atoms was completed in the MA device. MA process was applied to FeNiCo and WMoNb powders for 30 and 120 hours, respectively, and two different MEA powder productions were successfully completed. Then, a 5-hour Mechanical Milling process was carried out to make these two groups a composite and to homogenize the structure. XRD, SEM and EDS analyses were performed for the powder characterization of the composite. Thus;

In the XRD analysis, it was determined that the dislocation density of both groups increased. It was seen that the peak heights decreased and the openness increased. Thus, it was revealed that the structure started to change from a regular state to an amorphous state with the MA performed. It is also seen that the FeNiCo powder, which is more in weight, is still dominant in the composite. With SEM analysis, it was clearly observed that the MA process reduced the grain size after 120 and 30 hours of MA processing. With EDS analysis, the powders were visualized as elementally homogeneous in both MEA and composite powder production.

As a result, the production of two different MEA powder groups as a composite was successfully achieved. It was revealed that MEA reinforcement can be made instead of particles to particle-reinforced MEAs, which are included in the literature, and that this can be produced successfully.

Declaration

Ethics committee approval is not required.

References

[1] Gorsse, S., Couzinié, J. P., & Miracle, D. B. (2018). From high-entropy alloys to complex concentrated alloys. *Comptes Rendus Physique, 19*(8), 721–736.

[2] Youssef, K. M., Zaddach, A. J., Niu, C., Irving, D. L., & Koch, C. C. (2014). A novel low-density, high-hardness, high-entropy alloy with close-packed single-phase nanocrystalline structures. *Materials Research Letters, 3*(2), 95–99.

[3] Yeh, J. W., Chen, S. K., Lin, S. J., Gan, J. Y., Chin, T. S., Shun, T. T., ... & Chang, S. Y. (2004). Nanostructured high-entropy alloys with multiple principal elements: Novel alloy design concepts and outcomes. *Advanced Engineering Materials, 6*(5), 299–303.

[4] Cabrera, M., Oropesa, Y., Sanhueza, J. P., Tuninetti, V., & Oñate, A. (2024). Multicomponent alloys design and mechanical response: From high entropy alloys to complex concentrated alloys. *Materials Science and Engineering R Reports, 161*.

[5] Yeh, J. W. (2015). Physical metallurgy of high-entropy alloys. *JOM, 67*(10), 2254–2261.

[6] Yeh, J. W. (2013). Alloy design strategies and future trends in high-entropy alloys. *JOM, 65*(12), 1759–1771.

[7] Gupta, M. (n.d.). Multiple component alloys: The way forward in alloy design. *Materials Science Research India, 16*, 1.

[8] Dye, J. L. (2015). The alkali metals: 200 years of surprises. *Philosophical Transactions of the Royal Society A, 373*(2037).

[9] Emsley, J. (2011). *Nature's building blocks: An A–Z guide to the elements* (New edition). London: Oxford University Press.

[10] B. V., & A. X. M. (2024). Development of high entropy alloys (HEAs): Current trends. *Heliyon, 10*(7), e26464.

[11] Wei, D., et al. (2022). Metalloid substitution elevates simultaneously the strength and ductility of face-centered-cubic high-entropy alloys. *Acta Materialia, 225*, 117571.

[12] Sekhon, B. S. (2013). Metalloid compounds as drugs. *Research in Pharmaceutical Sciences, 8*(3), 145–158.

[13] Yang, D., et al. (2020). A novel FeCrNiAlTi-based high entropy alloy strengthened by refined grains. *Journal of Alloys and Compounds, 823*, 153729.

[14] Udhayabanu, V., Singh, N., & Murty, B. S. (2010). Mechanical activation of aluminothermic reduction of NiO by high energy ball milling. *Journal of Alloys and Compounds, 497*(1–2), 142–146.

[15] Gutfleisch, O., Willard, M. A., Brück, E., Chen, C. H., Sankar, S. G., & Liu, J. P. (2011). Magnetic materials and devices for the 21st century: Stronger, lighter, and more energy efficient. *Advanced Materials, 23*(7), 821–842.

[16] Fu, Z., et al. (2019). Exceptional combination of soft magnetic and mechanical properties in a heterostructured high-entropy composite. *Applied Materials Today, 15*, 590–598.

[17] Zuo, T., et al. (2017). Tailoring magnetic behavior of CoFeMnNiX (X = Al, Cr, Ga, and Sn) high entropy alloys by metal doping. *Acta Materialia, 130*, 10–18.

[18] Zhang, Y., Zuo, T., Cheng, Y., & Liaw, P. K. (2013). High-entropy alloys with high saturation magnetization, electrical resistivity, and malleability. *Scientific Reports, 3*, 1–7.

[19] Chu, C., et al. (2023). Unveiling heterogeneous microstructure and good combinations of high yield strength and low coercivity of in-situ formed NbC/FeNiCo medium-entropy composites. *Powder Technology, 419*, 118365.

[20] Song, B., et al. (2020). In situ oxidation studies of high-entropy alloy nanoparticles. *ACS Nano, 14*(11), 15131–15143.

[21] Wu, H., Huang, S., Qiu, H., Zhu, H., & Xie, Z. (2019). Effect of Si and C additions on the reaction mechanism and mechanical properties of FeCrNiCu high entropy alloy. *Scientific Reports, 9*(1), 1–10.

[22] Senkov, O. N., Wilks, G. B., Miracle, D. B., Chuang, C. P., & Liaw, P. K. (2010). Refractory high-entropy alloys. *Intermetallics, 18*(9), 1758–1765.

[23] Zhang, B., Huang, Y., Huang, Z., & Wang, J. (2025). Porous WMoTaNb refractory high entropy alloy fabricated by elemental powder metallurgy. *Materials Today Communications, 45*, 112362.

[24] Senkov, O. N., Wilks, G. B., Scott, J. M., & Miracle, D. B. (2011). Mechanical properties of Nb25Mo25Ta25W25 and V20Nb20Mo20Ta20W20 refractory high entropy alloys. *Intermetallics, 19*(5), 698–706.

[25] Yao, H. W., Qiao, J. W., Hawk, J. A., Zhou, H. F., Chen, M. W., & Gao, M. C. (2017). Mechanical properties of refractory high-entropy alloys: Experiments and modeling. *Journal of Alloys and Compounds, 696*, 1139–1150.

[26] Dangwal, S., & Edalati, K. (2025). Developing a single-phase and nanograined refractory high-entropy alloy ZrHfNbTaW with ultrahigh hardness by phase transformation via high-pressure torsion. *Journal of Alloys and Compounds, 1010*, 178274.

[27] Stepanov, N. D., Shaysultanov, D. G., Salishchev, G. A., & Tikhonovsky, M. A. (2015). Structure and mechanical properties of a light-weight AlNbTiV high entropy alloy. *Materials Letters, 142*, 153–155.

[28] Senkov, O. N., & Woodward, C. F. (2011). Microstructure and properties of a refractory NbCrMo0.5Ta0.5TiZr alloy. *Materials Science and Engineering A, 529*(1), 311–320.

[29] Zhang, K. B., Fu, Z. Y., Zhang, J. Y., Wang, W. M., Lee, S. W., & Niihara, K. (2010). Characterization of nanocrystalline CoCrFeNiTiAl high-entropy solid solution processed by mechanical alloying. *Journal of Alloys and Compounds*, *495*(1), 33–38.

[30] Albayrak, M. G., & Evin, E. (2023). A different approach: Effect of mechanical alloying on pack boronizing. *Journal of Materials Engineering and Performance*, *33*, 9039–9046.

[31] Chen, C. L., & Zeng, Y. (2016). Synthesis and characteristics of W–Ti alloy dispersed with $Y_2Ti_2O_7$ oxides. *International Journal of Refractory Metals and Hard Materials*, *56*, 104–109.

[32] Wang, C., Ji, W., & Fu, Z. (2014). Mechanical alloying and spark plasma sintering of CoCrFeNiMnAl high-entropy alloy. *Advanced Powder Technology*, *25*(4), 1334–1338.

[33] Chen, C. L., & Suprianto. (2019). Effects of nano-dispersoids on synthesis and characterization of low Cr-containing CoNiFeMnCr high entropy alloy by mechanical alloying. *Intermetallics*, *113*, 106570.

[34] Suryanarayana, C., & Norton, M. G. (1998). *X-ray diffraction: A practical approach*. New York: Plenum Publishing Corporation.

[35] Tarani, E., Arvanitidis, I., Christofilos, D., Bikiaris, D. N., Chrissafis, K., & Vourlias, G. (2023). Calculation of the degree of crystallinity of HDPE/GNPs nanocomposites by using various experimental techniques: A comparative study. *Journal of Materials Science*, *58*(4), 1621–1639.

[36] Fang, Z. Z., Wang, H., & Kumar, V. (2017). Coarsening, densification, and grain growth during sintering of nano-sized powders—A perspective. *International Journal of Refractory Metals and Hard Materials*, *62*, 110–117.

[37] Yan, M. F., Cannon, R. M., Bowen, H. K., & Chowdhry, U. (1983). Effect of grain size distribution on sintered density. *Materials Science and Engineering*, *60*(3), 275–281.

[38] Sendi, R. (2022). Grain size and sintering temperatures effects on the mechanical properties of ZnO nanoparticle-based varistor ceramics. *Journal of Umm Al-Qura University for Applied Sciences*, *8*(1–2), 50–56.

[39] Ji, W., et al. (2015). Alloying behavior and novel properties of CoCrFeNiMn high-entropy alloy fabricated by mechanical alloying and spark plasma sintering. *Intermetallics*, *56*, 24–27.

[40] Wang, W., Lyu, T., Choi, H. S., Cheng, C., & Zou, Y. (2025). Wear mechanism transitions in FeCoNi and CrCoNi medium-entropy alloys from room temperature to 1000 °C. *Journal of Materials Science and Technology*, *231*, 151–163.

[41] Cao, F., et al. (2024). Carbon-microalloying enhances strength-ductility synergy of (FeCoNi)90Al10 medium-entropy alloy via tailoring precipitation. *Materials Science and Engineering A*, *916*, 147329.

[42] Wang, X., Suo, H., Zhang, Z., Huangfu, S., & Wang, Q. (2024). Exploring the effect of Cr and Mn on the intrinsic strength of the tensile properties of FeCoNi, FeCoNiMn, FeCoNiCr, and FeCoNiCrMn multi-principal element alloys using in-situ EBSD. *Materials Science and Engineering A*, *918*, 147442.

.

International Journal of Innovative Engineering Applications

Journal homepage: https://dergipark.org.tr/ijiea

COOLING SYSTEM ANALYSIS OF GAS TURBINE BLADES MANUFACTURED USING DIFFERENT MATERIAL TYPES

İbrahim Can[1], *Serdar Mercan*[2], *Doğan Engin Alnak*[1] *Muhammed Sipahi*[*1]

[1]*Department of Manufacturing Engineering, Faculty of Technology, Sivas Cumhuriyet University, Sivas, Turkey*
[2]*Department of Mechatronics Engineering, Faculty of Technology, Sivas Cumhuriyet University, Sivas, Turkey*

Abstract

Original scientific paper

One of the major challenges in gas turbine engines is that the blades operate at temperatures higher than the melting points of the materials they are made of. Researchers have focused on developing materials that can withstand high temperatures and designing effective cooling systems for the blades. Although there are limitations to the improvements that can be achieved through material technology, the importance of cooling is clear, and it is considered a critical factor for achieving high efficiency in turbines. To this end, two cooling models were developed using different materials, and the heat transfer in the blades was analyzed numerically using the SolidWorks package program and Ansys. The study considered titanium carbide (TiC) and third-generation single crystal super-alloy CMSX-10 materials. The blade designs were proposed based on the analysis results. The analysis showed that the enhanced model performed better when used with CMSX-10 material in terms of thermal properties.

Keywords: *Turbine blade, blade cooling, TiC, CMSX-10.*

FARKLI MALZEME TÜRLERİ KULLANILARAK ÜRETİLEN GAZ TÜRBİNİ KANATLARININ SOĞUTMA SİSTEMİ ANALİZİ

Özet

Orijinal bilimsel makale

Gaz türbini motorlarındaki en büyük zorluklardan biri, türbin kanatlarının yapıldıkları malzemelerin erime noktalarından daha yüksek sıcaklıklarda çalışmasıdır. Bu sorunu çözmek amacıyla, araştırmacılar yüksek sıcaklıklara dayanabilen malzemeler geliştirmeye ve kanatlar için etkili soğutma sistemleri tasarlamaya odaklanmışlardır. Malzeme teknolojisi ile elde edilebilecek iyileştirmelerde bazı sınırlamalar olsa da, soğutmanın önemi açıktır ve gaz türbinlerinde yüksek verimlilik sağlamak için kritik bir faktör olarak kabul edilmektedir. Bu amaçla, farklı malzemeler kullanılarak iki soğutma modeli geliştirilmiş ve kanatlardaki ısı transferi, SolidWorks paket programı ve Ansys 18.2 kullanılarak sayısal olarak analiz edilmiştir. Çalışma, titanyum karbür (TiC) ve üçüncü nesil tek kristal süper alaşım CMSX-10 malzemelerini ele almıştır. Kanat tasarımları, analiz sonuçlarına dayalı olarak önerilmiştir. Analiz, iyileştirilmiş modelin, termal özellikler açısından CMSX-10 malzemesi ile kullanıldığında daha iyi performans sergilediğini göstermiştir.

Anahtar Kelimeler: *Türbin kanadı, kanat soğutma, TiC, CMSX-10.*

1 Introduction

Gas turbine engines are mainly thermal engines consisting of a compressor, combustion chamber, and turbines. After fresh air enters through the intake port, the pressure in the compressor is increased, and a mixture is created by injecting fuel into the combustion chamber. High-pressure and high-temperature gases are obtained by burning the mixture in the combustion chamber. These gases pass to the turbine section, and by impacting the blades, they convert the heat energy into mechanical energy. Finally, the exhaust gases are thrown out, completing the cycle. Turbine technology converts fluid motion to useful work. It is a system in which many processes, such as taking atmospheric air, raising the gas temperature, and adding and burning the fuel at constant pressure, continue. A turbine blade is a component of a gas turbine that extracts energy from the high-temperature, high-pressure gases generated by the combustor. The turbine blades represent the limiting component of the gas turbine [1]. Turbine blade materials are generally preferred among nickel alloys, titanium alloys, and super alloys because they operate at high pressures and temperatures. Increasing the turbine rotor

*Corresponding author.
E-mail address: eng.sipahi@gmail.com (M. Sipahi)
Received 08 April 2025; Received in revised form 04 June 2025; Accepted 16 June 2025

Doi: https://doi.org/10.46460/ijiea.1671100

inlet temperature (RIT) has been shown to be an essential approach to increase the thrust performance of aero-gas turbines. [2, 3, 4, 6]. As the turbine inlet temperatures increase, the temperatures of the hot gases often exceed the melting points of the materials.

Fluid movement is used to create useful work using turbine technology. This includes many processes such as capturing atmospheric air. increasing air temperature Filling and burning fuel at constant pressure Turbine blades, which are generally made of nickel alloys titanium alloy or super alloy Considered a limiting element of gas turbines [1], turbine rotor inlet increasing temperature (RIT) has been identified as an important method for improving the thrust efficiency of air gas turbines. But when the temperature of the hot gas passing through the turbine blades increases. It often exceeds the melting point of the materials used in the blades. The development of heat-resistant materials and efficient cooling systems is increasingly important [2-5]. Gas turbine engines are one of the most widely used methods of to produce electricity and power aircraft in the 21st century, the use of heat energy generated during fuel combustion in the combustion chamber has greatly improved the efficiency of these engines. But gas turbine engines operate at very high temperatures, in excess of 1450 degrees Celsius. This can have a negative effect on the blades. This causes distortion and wear on the outer surface of the blade. To fix these problems and maintain the integrity of the blade Researchers are looking at new blade designs that combine metal alloys, blade shapes, and cooling.

Material selection and design procedures are critical in developing an efficient cooling system for turbine blades. To ensure the ability to withstand high pressure and temperature conditions. Researchers have conducted many theoretical and experimental studies on various types of alloys. used in turbine blades Alloys found to be suitable for turbine blades include titanium, chromium, nickel, and steel [7-8]. In this study, the researchers used a combination of single crystals and CMSX-10 super alloy to investigate potential improvements in blade cooling. By choosing these materials. The objective is to increase the durability and efficiency of turbine blades. especially in high temperature environments.

Ni-based single crystal superalloys are becoming increasingly important. To develop a gas turbine engine that meets ecological requirements to improve the thermodynamic efficiency of these engines New single crystal superalloys need to be developed that can withstand high turbine inlet temperatures.... The composition of the new generation superalloy has been modified to provide high resistance to corrosion, oxidation and creep in turbine blades. The amount of tungsten and molybdenum decreased. while the amount of cobalt, tantalum and aluminum increased. This change in the alloy structure is intended to harmonize the tension of the interface between phases A and B, resulting in improved turbine blade performance and durability.

CMSX-10 alloy is a high-performance material used in turbines and engine blades. Known for its high strength at high temperatures. Resistant to creep and fatigue Contains high amounts of rhenium and resistive elements. While the amount of chromium is relatively low, it happens. This alloy was initially developed for use in the air turbine industry. But it has also gained interest in industrial turbine applications because of its excellent long-term robustness at high temperatures. It is considered the third-generation single crystal casting material and has been approved for use in aircraft [14].

This barrier reduces heat transfer to the blade surface and protects the blade from hot air. Panel cooling is generally more effective at reducing the blade surface temperature compared to ventilation. However, its practical implementation is also more complicated and expensive. Therefore, a combination of internal film cooling methods is often used to achieve the optimum cooling efficiency in gas turbine blades. The cooling method used in a typical gas turbine engine depends on a number of factors, such as engine design, operating conditions, and the materials used in the blades.

Convection cooling involves the transfer of cool air through internal passages or tunnels within the blades. The cool air then spreads to the inner surface of the blade to remove the heat generated during operation. This method requires a larger number of blades to support the cooling path. This may affect the overall efficiency of the turbine engine. But it will provide more efficient cooling. and helps to increase the turbine inlet temperature [9].

Blade design is critical in achieving high efficiency and productivity in gas turbine engines. The blades control the flow of hot air to the turbine and convert kinetic energy into mechanical energy, which can be used to generate electricity or, as mentioned above, to power aircraft. The cutting can withstand high temperatures and pressures as well as harsh conditions. Engine operating environment Well-designed, manageable blades can increase engine reliability. Reduce maintenance costs and ultimately leads to better overall performance [4-6].

Development of new materials It is critical to meeting the increasing demand for high-performance, high-performance turbine engines. The use of super alloys has been found to be effective in withstanding high temperatures and pressures. and maintain mechanical properties Researchers have been searching for new superalloy compositions by adjusting the amounts of various alloying elements. appropriately to achieve the desired properties - resistance, high temperature creep and fatigue are also higher as compared to alloys [7].

Titanium carbide and Ni-based single-crystal superalloys were selected because of their excellent mechanical properties and thermal stability. The high melting point (3065°C) and low density (4·93 g cc−1) of Tic make Tic a potential material for high temperature applications [10]. The efficiency of gas turbines and jet engines has been improved. due to temperature. The capacity of Ni-based single crystal superalloy has been improved, which has an exceptionally high heat capacity [11]. Ni-based superalloys generally have 12 alloy compositions. The main component is Ni, which is used as the base material. It has an austenitic crystal lattice (FCC) structure [12].

The addition of other elements such as chromium, cobalt, aluminum, and titanium to the Ni-base super-alloys improves their mechanical properties, high-temperature strength, and resistance to thermal fatigue, creep, and oxidation [13]. These alloys also have excellent castability and weldability. This makes them suitable for

a wide range of applications in the aerospace and energy industries. However, new and improved materials are being developed to meet the increasing demand for higher operating temperatures. And the increasingly critical operating conditions in modern gas turbine engines continue. The study you mentioned investigated the effect of microstructure on the creep performance of superalloy RR3010. The alloy was subjected to different hardening and aging rates. and the microstructure was characterized using scanning electron microscopy. Two different microstructures with different average gamma sizes (γ) were tested for creep at different temperatures and strains. The research results found that the granular structure has a significant impact on the creep performance at low temperatures. Where larger gamma size takes longer to break. But at a higher test temperature. The fine structure has a lesser effect on creep performance. Overall, the study provides valuable insights into the relationship between microstructure and creep behavior of super alloys, which is important for the design and optimization of high-performance materials for gas turbines and jet engines [13].

Efficient cooling of turbine blades is critical for their safe operation and to ensure their longevity. The use of internal and external cooling methods, such as film cooling, helps to maintain safe operating temperatures of the blades, which can exceed the limits allowed for turbine blade materials. However, as you mentioned, the cooling process can impact thermal efficiency, so the design of the cooling system and the fins should be optimized to balance cooling needs with performance goals. It is also important to consider the maximum surface temperature and temperature gradients of the fins in relation to the fin design and material used to prevent thermal stress that could lead to blade failure.

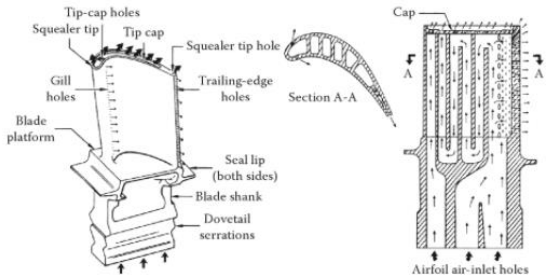

Figure 1. Design of fin with advanced cooling technology.

Figure 1 illustrates the design of the internal cooling channels in a GE CF6 turbofan engine's stage-1 high-pressure turbine rotor blade. Convective cooling, film cooling, rib turbulators, squealer-tip-cap cooling, and pin fins are all used to cool the blade. A combination of these cooling techniques is essential for optimum performance. and to ensure that the blades can work safely at high temperatures. Designing a thermal turbine blade is a very complex process that requires careful consideration of many factors, such as material properties. working environment and cooling efficiency [15, 16].

Accurate modeling of channels and paths in the blades is essential to ensure the most effective and efficient cooling. In addition to the shock from high turbulence. Other factors must also be considered, such as pressure differences and physical properties. By developing a comprehensive understanding of these phenomena and using advanced modeling techniques. Researchers and engineers can optimize turbine blade designs. Improved durability and performance.

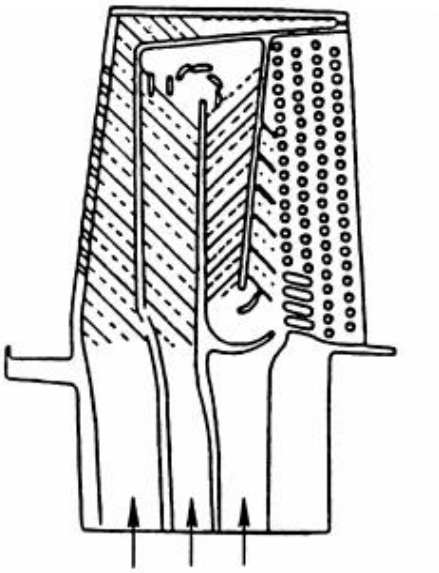

Figure 2 Fin internal cooling channel design using advanced cooling technology [5].

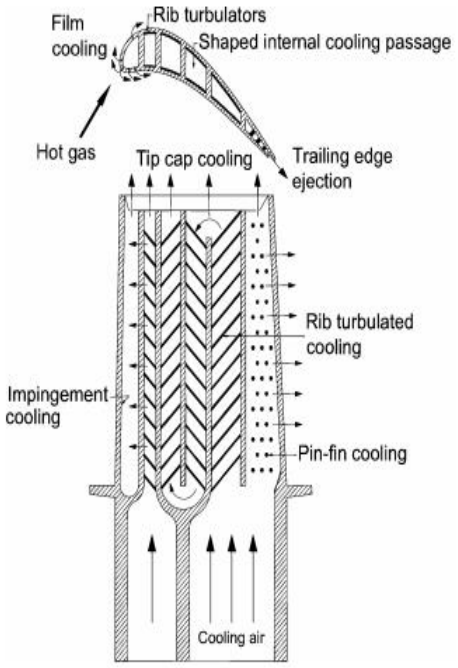

Figure 3 Schematic illustration of a multi-point air inlet fins [5].

Internal cooling channels are generally shown as short channels. square or squares with different aspect ratios Rib table geometry such as rib size, shape, distribution, angle of attack of flow. and the Reynolds number in the flow Its main function is to increase heat transfer in a rectangular cooling channel with a ribbed table. The heat transfer of the rib table by interrupting only the flow near the wall raises the level. As a result, the blade's internal cooling design adopts a reduction in the pressure drop caused by the rib table car.

2 Meterial Method

2.1 Internal Cooling

Internal cooling of the blades is achieved by forcing cool air from the air compressor through the internal cooling channel from the hub to the blade tips. The internal passages may be circular, oval, or spread over the entire surface of the blade. Such blade shape may deviate from the optimal aerodynamic blade profile. Conduction and convection are used to cool the blade; significantly hotter air leaves the blade tips and travels the length of the blade in the cooling passageways. Hollow blades with cores and internal cooling channels can be created. Cool air enters the front area like a jet. then move to the back [13, 14].

2.2 External Cooling

There are two methods of cooling the outside of a turbine blade. From the hub to the tip Cold air enters the interior corridor. during the ascent It can flow through a surface that crosses a number of small faces sloping on the surface. A film forms on the blade surface as a result of cool air escaping from these small holes, reducing heat transfer from the hot gas to the cutting metal. Except for cooling the cutting surface. [15]. SolidWorks is a popular CAD software used for 3D modeling of mechanical components and assemblies, while Ansys is a widely used simulation software for structural analysis, thermal analysis, fluid dynamics, and other engineering simulations. The use of these software packages allows for the creation of a detailed model of the turbine blade and the simulation of its behavior under different operating conditions. This can aid in the optimization of the blade's design and cooling system to improve its performance and durability.

2.3 Material Properties

In this study, we investigated the cooling efficiency of gas turbine blades using two distinct material types. The physical properties of the selected materials are provided in Table 1.

Table 1. Materials physical properties for turbine blade analysis.

Molecular Formula	Thermal conductivity (w/mk)	Poisson's Ratio	Density (kg/m³)	Melting temperature (˚c)	Yield strength (GPa)	Young' Modulus (GPa)	Thermal expansion (˚c)
Titanium Ti	17	0,36	4620	1668	9,3	116	9,10 x 10 e-6
Titanium carbide Tic	21	0,18	4910	3160	20	497	7,60 x 10 e-6
Third-generation single crystal super alloys CMSX-10	26	0,21	8283	-	-	-	15,7 x 10 e-6

2.4 Blades Design

The turbine blade model was created in 3D using the SOLIDWORKS package program as seen in figures 4 and 5. Two different blades are modeled with internal cooling channels. and the generated model was transferred to Ansys program for further analysis. A lattice structure is created. And the simulation was edited using Ansys CFD, which is computational fluid dynamics software used to simulate fluid flow and heat transfer.

FEM is a numerical method used to solve partial differential equations by dividing the problem into smaller components or parts. The network model is then analyzed and simulated to predict system behavior and performance under various conditions. In the case of a model turbine blade, FEM is used to calculate the stress, strain, and temperature distribution across the blade under various operating conditions. The results from the FEM analysis are then used to optimize the design and improve the performance and reliability of the turbine blades [12]. These steps are typical for finite element analysis (FEA) using Ansys software, which is widely used for numerical simulations in the engineering industry. In the first step, a blade model is created in 3D CAD SolidWorks software with internal cooling channels. In the second step, the model is imported into Ansys, where meshes are created in the geometry model to break down the geometry into smaller, finite elements for numerical analysis. and select the mesh density according to the level of precision required for the results. In the third step Boundary conditions are applied to the model, such as temperature and pressure. and the equations of the system are solved to obtain results such as temperature distribution. heat flux and stress distribution.

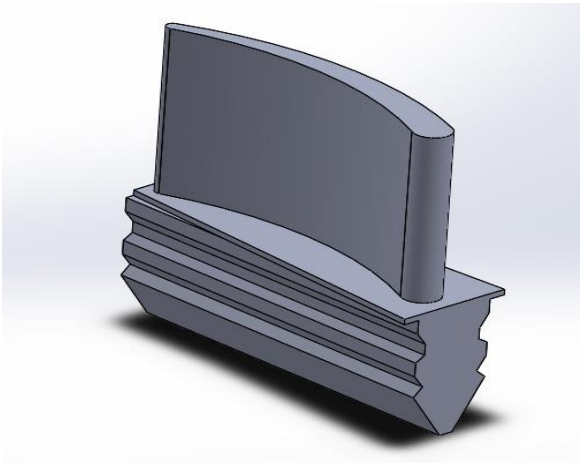

Figure 4. The main design of blade without cooling channels.

The analysis focuses only on the turbine blade cooling system. And the effect of air flowing in the propeller is not taken into account.

In computational fluid dynamics (CFD) simulation, the SIMPLE algorithm for pressure-velocity coupling is used. And the pressure interpolation model implied in the discrete solver is often used. In addition, the first order airflow model is commonly used to differentiate the control equations. The convergence parameters specified for the residuals determine the desired level of precision

in the simulation results. Achieving residues based on these values is important to ensure a convergent and reliable solution.

These values indicate the level of accuracy and convergence of the numerical solutions obtained from the simulations. Residual energy represents the difference between the actual calculated kinetic energy in the system. While the kinetic turbulence and residual kinetic energy represent the difference between the actual calculated kinetic energy and the kinetic energy in the system, respectively. In this case, the residual energy of 10xe-6 and the residual kinetic energy/turbulent energy of 10xe-5 indicates that the simulation achieved a high level of accuracy and convergence.

This three-section turbine blade design is a common method used for internal cooling of gas turbine blades. The first section generally consists of a closed chamber through which cool air enters the blades. while the second section contains internal cooling channels. which is responsible for removing heat from the blades and finally, the third part is usually the exit area. This is where the cool air exits. Blades This three-piece design allows for a more efficient cooling system. Where cool air is distributed evenly and the heat transfer process is optimized.

To get better results, the fixed portion in the blade is discarded as shown in Figure 5 during the analysis process.

Unblocking the constant blocks during the analysis process can provide more precise and accurate results for areas of interest in the cooling path as shown in Figure 6. Because fixed blocks are not directly involved in the cooling process, they may impede ventilation and heat transfer to nearby cooling routes.

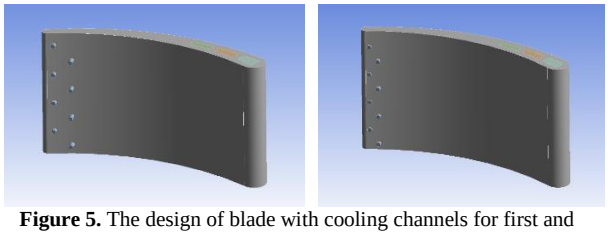

Figure 5. The design of blade with cooling channels for first and enhanced design.

Figure 6. The design of internal cooling channels for first and enhanced design.

3 Analysis and Result

The precise calculation of the heat transfer in turbine blades working at high pressures and temperatures requires a lot of time. The major parameters to increase gas turbine performance and engine life are generally acknowledged to be accurately measuring heat transfer and optimizing the operating temperatures of the fins in light of the acquired values. The development of high-speed computers has made it possible to perform precise calculations for heat transport analyses. The choice of appropriate turbulence models determines the primary challenges in forecasting. Meantime statistical models are used to build turbulence models. Meanwhile and variations in time are used to describe local velocities: U (local velocity) = u (time averaged) + u1 (fluctuating component)

Most turbulence models solve steady-state turbulence with the time averaging of seconds of fluctuating velocity components. Generally, turbulence kinetic energy is the sum of the turbulence energies k and is defined as [16];

Mean Flow Equations:

- Continuity:

$$\frac{\delta}{\delta x_i}(\rho U_i) = 0 \tag{17}$$

- Momentum Transport:

$$\frac{\delta}{\delta x_j}\left(\rho U_i U_j\right) = \frac{\delta P}{\delta x_i} + \frac{\delta}{\delta x_j}\left[\mu\left(\frac{\delta U_i}{\delta x_j} + \frac{\delta U_j}{\delta x_i}\right) - \rho\overline{u_i u_j}\right] \tag{18}$$

- Enthalpy:

$$\frac{\delta}{\delta x_j}(\rho U_i T) = \frac{\delta}{\delta x_j}\left[\frac{\mu}{Pr}\frac{\delta T}{\delta x_j} - \rho\overline{u_i t}\right] \tag{19}$$

- Zonal k-ε model: This consist of the high Re- k-ε in the fully turbulent core:

$$\frac{\delta}{\delta x_j}\left(\rho U_j k\right) = \frac{\delta}{\delta x_j}\left[\left(\mu + \frac{\mu_t}{\sigma_k}\right) - \frac{\delta k}{\delta x_j}\right] + P_k - \rho\varepsilon \tag{20}$$

Where, $P_k = -\rho\overline{u_i u_j}\left(\frac{\delta U_i}{\delta x_j}\right)$ (21)

$$\frac{\delta}{\delta x_j}\left(\rho U_j \varepsilon\right) = \frac{\delta}{\delta x_j}\left[\left(\mu + \frac{\mu_t}{\sigma_\varepsilon}\right) - \frac{\delta_\varepsilon}{\delta x_j}\right] + C_{\varepsilon 1}\frac{\varepsilon}{k}P_k - \rho C_{\varepsilon 2}\frac{\varepsilon^2}{k} \tag{22}$$

Analysis procedures were completed using the Ansys 18.2 program. Figure 7 shows the inlet and outlet domain information. For hot domain:Tinlet = 1200 K, and inlet velocity = 25 m/s.
For cold domain: Tinlet = 300 Kelvin and inlet velocity = 40 m/s

The total numbers of nodes and elements in first and enhanced designs are 417317, 2110027, 452253, 2266075 respectively as shown in Figure 8.

Figures 9 to 14 depict the variation of the resultant thermal gradient at the blade surface and internal cooling domain along the longitudinal distance.

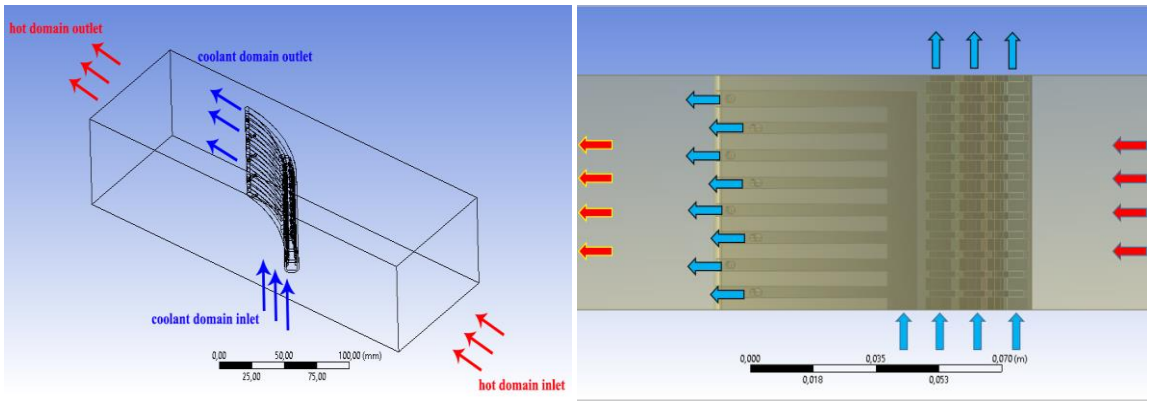

Figure 7. Information about simulation conditions.

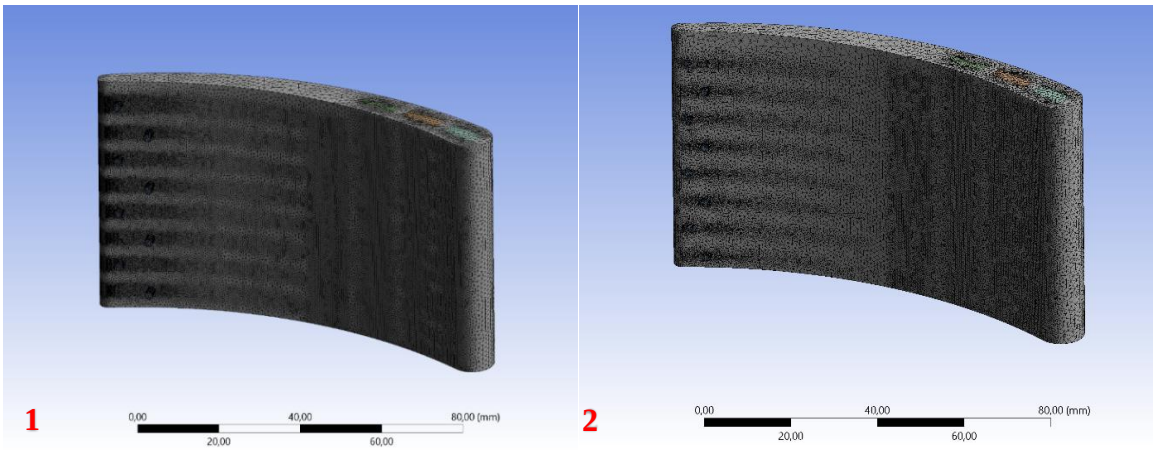

Figure 8. The generated finite element mesh used in the current research.

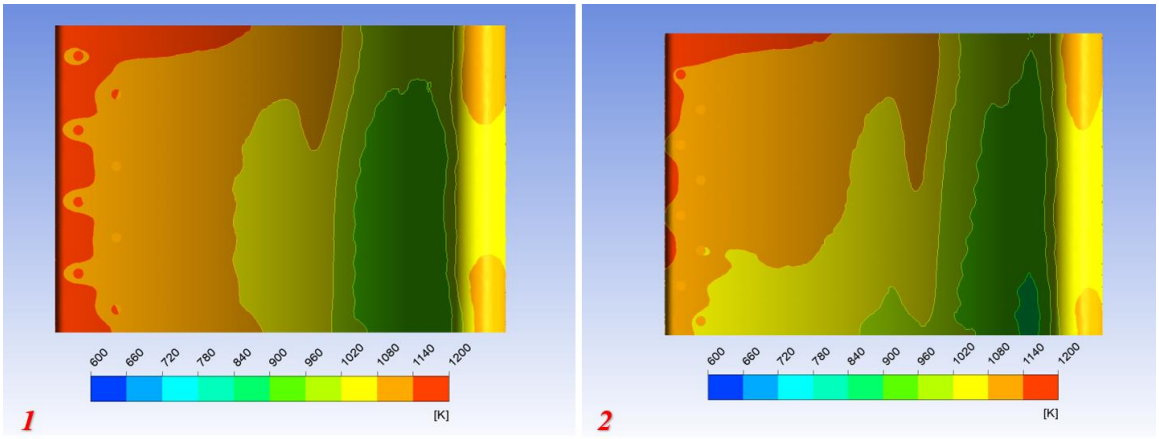

Figure 9. The variation of minimum and maximum temperature observed in blade for Titanium.

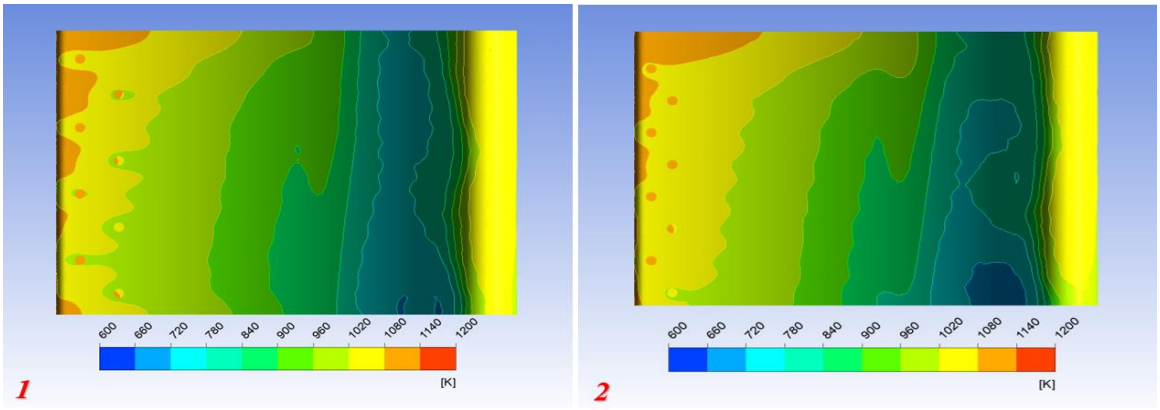

Figure 10. The variation of minimum and maximum temperature observed in blade for Titanium Carbide.

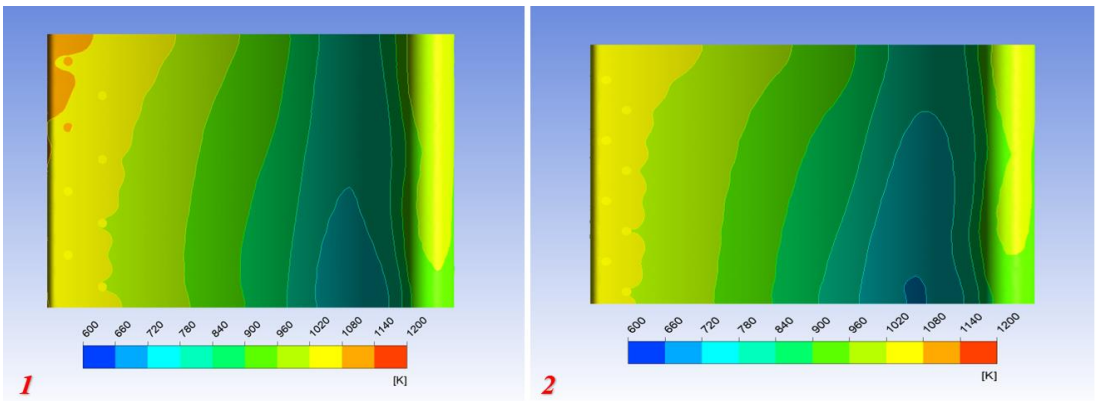

Figure 11. The variation of minimum and maximum temperature observed in blade for CMSX-10.

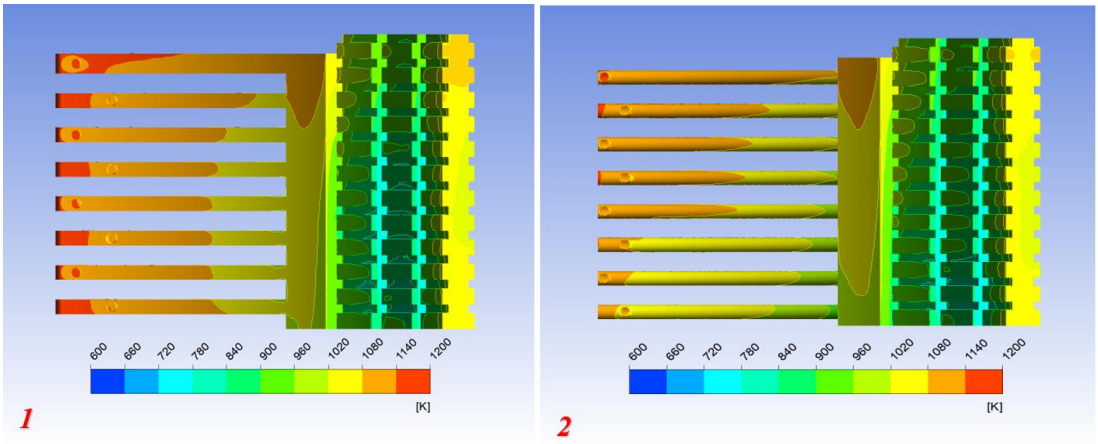

Figure 12. The variation of minimum and maximum temperature observed in cooling channels for Titanium.

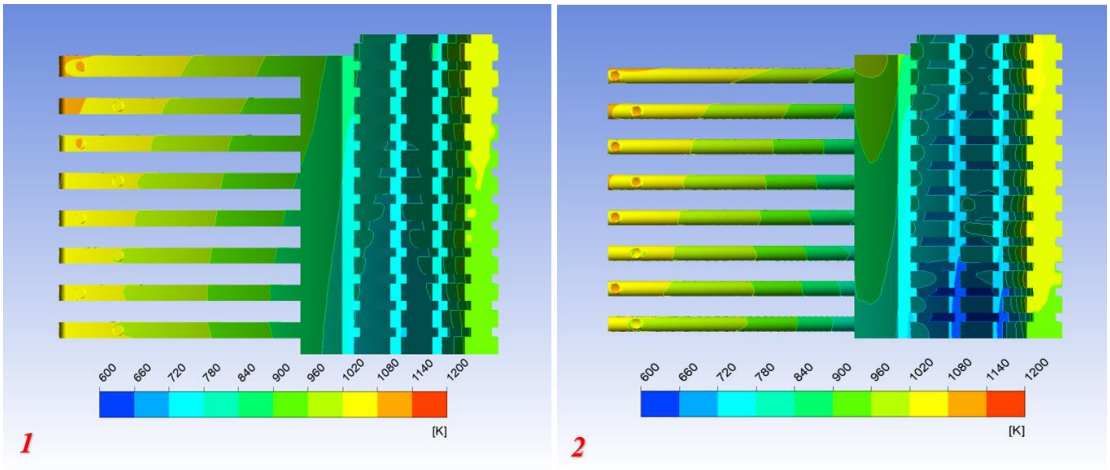

Figure 13. The variation of minimum and maximum temperature observed in cooling channels for Titanium Carbide.

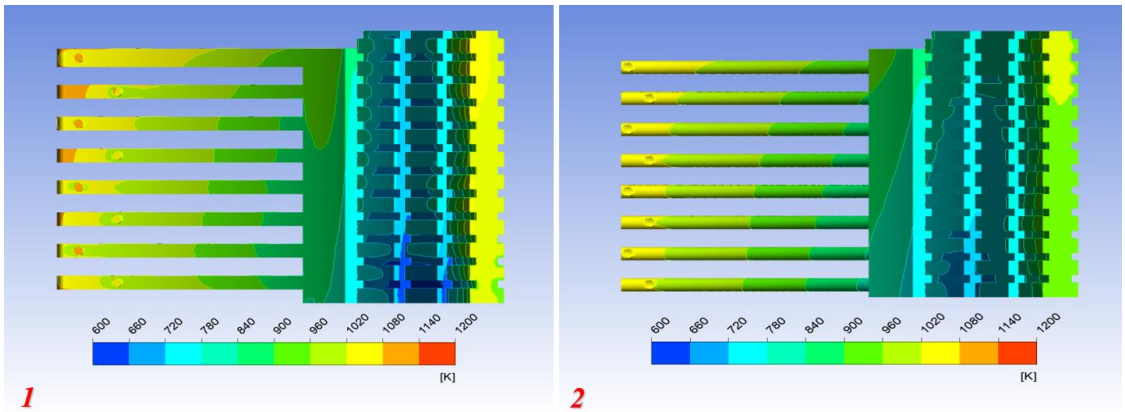

Figure 14. The variation of minimum and maximum temperature observed in cooling channels for CMSX-10.

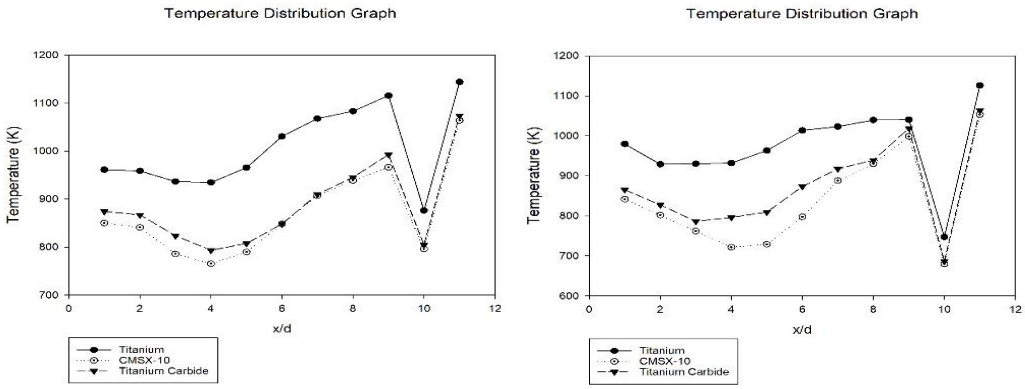

Figure 15. Temperature distribution for first and enhanced blade.

For the first design, a temperature increase is seen because the second and fifth points do not line up with the fin's cooling channels, as mentioned in figure 15.

- A rise in temperature is seen as the 6-7-8-9 points approach the narrow portion of the blade.
- The temperature drops because the 10th point falls on the edge of the film cooling hole.
- The last edge of the 11th-point blade has the greatest temperature value.
- The temperature range for titanium material fluctuates between 900 and 1050 K on a regular basis.
- In the region of the cooling channels, the temperature distribution for titanium carbide and CMSX-10 falls by 750–850 K.

For the enhanced design,

- A temperature increase is seen because 2-3-4 points do not line up with the cooling channels of the blade.
- A rise in temperature is seen as the 6-7-8-9 points approach the narrow portion of the blade.
- The temperature drops because the 10th-point falls on the edge of the film cooling hole.
- The last edge of the 11th-point blade has the greatest temperature value. The temperature range for titanium fluctuates between 900 and 1000 K on a regular basis.

The temperature distribution in the cooling channels' region for titanium carbide and CMSX-10 reduces by 700–800 K.

Among the substances investigated, titanium carbide continually established lower top temperatures in both cooling designs, specifically inside the throat and trailing aspect regions, indicating advanced thermal resistance. While the first layout exhibited a steeper temperature gradient among the main and trailing edges, the enhanced design resulted in a greater uniform thermal distribution—maximum extensively for titanium carbide. However, whilst comparing average surface temperatures across the entire blade, CMSX-10 outperformed the opposite materials, accompanied by means of titanium carbide, whereas titanium exhibited the best ordinary temperatures.

4 Conclusion

Two different cooling models have been designed for a gas turbine engine's turbine blade. Additionally, both models have been numerically analyzed for maximum heat flux values of the gas turbine blade with three different materials. The use of circular-section channels in the obtained models has resulted in better cooling performance.

In addition to internal channels, film cooling, achieved through holes positioned on the channels, has also yielded better results compared to models with only internal channels. It was observed that there was an improvement in both internal-channel and film-cooling models depending on the material, but titanium carbide and single-crystal super-alloy showed better results. This indicates that improving the thermal conductivity properties of materials can provide advantages in cooling.

It is known that the thinness of the blade's trailing edges and the accumulation of heat are challenges. However, thanks to the created channel model and the positioning of film cooling holes, heat flux at the blade's trailing edge has increased. This can help reduce potential thermal damage.

The working temperature of the blade surfaces remained approximately around 900-1000 K. Considering that the materials can withstand working temperatures in the range of 1200-1300 K, the use of the cooling models can increase the temperature of exhaust gases from the combustion chamber, thereby improving the engine's performance.

As indicated by the numerical data of the study, the models obtained can be used in turbine blades, especially with single-crystal super-alloys and circular-section models with film cooling, to achieve better result.

From an engineering application perspective, these thermal characteristics directly affect the blade’s service lifestyles, efficiency, and preservation necessities. For instance, decrease most temperatures and smoother gradients, as seen in CMSX-10 and titanium carbide, are crucial for minimizing thermal fatigue, creep deformation, and oxidation, all of which are crucial failure modes in high-temperature environments which include aircraft engines and electricity-era generators.

CMSX-10’s superior thermal overall performance makes it in particular appropriate for applications in which reliability and persistence are prioritized. However, this material offers huge sensible obstacles: it's far steeply-

priced, tough to device, and can require specialized casting or additive manufacturing techniques. These constraints can increase manufacturing prices and restriction its use to top rate, high-cost components.

Titanium carbide, imparting a stability among performance and cost, suggests promise for mild-duty turbines. However, its brittleness and potential oxidation troubles at extended temperatures may also require protective coatings or composite layering, including complexity to the layout.

Declaration

The authors declare that the ethics committee approval is not required for this study.

References

[1] Ahmed, S. I., Balguri, P. K., & Habeeb, G. S. (2021). Numerical study and heat transfer analysis of nickel-chromium and titanium carbide gas turbine blades cooling. *Materials Today: Proceedings*.

[2] Shin, D. H., Kim, M., Kim, J. S., Lee, B. J., & Lee, J. (2020). Precise infrared thermometry with considering background radiation for gas turbine air cooling application. *International Journal of Thermal Sciences*, 158.

[3] Kim, S. I., Rahman, H., & Hassan, I. (2009). Effect of turbine inlet temperature on rotor blade tip leakage flow and heat transfer. *International Journal of Numerical Methods for Heat & Fluid Flow*, 22(1), 73–93.

[4] Wen, Z. X., Pei, H. Q., Yang, H., Wu, Y. W., & Yue, Z. F. (2018). A combined CP theory and TCD for predicting fatigue lifetime in single-crystal superalloy plates with film cooling holes. *International Journal of Fatigue*, 111, 243–255.

[5] Han, J.-C. (2004). Turbine blade cooling studies at Texas A&M University: 1980–2004. *International Journal of Rotating Machinery*.

[6] Yamamoto, T., Furuhata, T., & Arai, N. (2000). Performances of the chemical gas turbine system and comparison with other gas turbine based cycle. *International Journal of Applied Thermodynamics*, 3(4), 155–162.

[7] Whittaker, M. (n.d.). Status of titanium blading for low-pressure steam turbines. *Final Report*.

[8] Whittaker, M. (n.d.). The effect of tension-torsion loading on low temperature dwell-sensitive fatigue in titanium alloys. In *Titanium in the Gas Turbine Engine*. Swansea University.

[9] Durlu, N. (1999). Titanium carbide-based composites for high temperature applications. *Journal of the European Ceramic Society*, 19(13–14), 2415–2419.

[10] Kawagishi, K., Yeh, A.-C., Yokokawa, T., Kobayashi, T., Koizumi, Y., & Harada, H. (2012). Development of an oxidation-resistant high-strength sixth-generation single-crystal superalloy TMS-238. In *Superalloys 2012*.

[11] Sowa, R., Arabasz, S., & Parlinska-Wojtan, M. (2016). Classification and microstructural stability of high generation single crystal nickel-based super alloys. *Zastita Materijala*, 57(2), 274–281.

[12] Yuan-Jian, Y. (2015). Finite element analysis for turbine blades with contact problems. *International Journal of Turbo and Jet Engines*.

[13] Mohammad, H., Albeirutty, A., Alghamdi, S., & Najjar, Y. S. (2004). Heat transfer analysis for a multistage gas turbine using different blade-cooling schemes. *Applied Thermal Engineering*.

[14] Giovanni, C., Ambra, G., Lorenzo, B., & Roberto, F. (2007). Advances in effusive cooling techniques of gas turbines. *Applied Thermal Engineering*.

[15] Deepanraj, B., Lawrence, P., & Sankaranarayanan, G. (2011). Theoretical analysis of gas turbine blade by finite element method. *Unpublished Manuscript*.

[16] Handrakant, R., Shenoy, S. B., & Sharma, Y. N. (2012). Numerical analysis of gas turbine HP stage blade cooling with new cooling duct geometries. *International Journal of Earth Sciences and Engineering*, 5(4), 1057–1061.

[17] Wagner, J. H., Johnson, B. V., & Kopper, F. C. (1991). Heat transfer in rotating serpentine passages with smooth walls. *Journal of Turbomachinery*, 113, 321–330.

[18] Acharya, S., Dutta, S., Myrum, T. A., & Baker, R. S. (1993). Periodically developed flow and heat transfer in a ribbed duct. *International Journal of Heat and Mass Transfer*, 36(8), 2069–2082.

[19] Abuaf, N., & Kercher, D. M. (1994). Heat transfer and turbulence in a turbulated blade cooling circuit. *Journal of Turbomachinery*, 116, 169–177.

[20] Chyu, M. K., & Naturajan, V. (1995). Surface heat transfer from a three-pass blade cooling passage simulator. *Journal of Heat Transfer*, 117, 650–656.

[21] Kim, Y. W., & Metzger, D. E. (1995). Heat transfer and effectiveness on film cooled turbine blade tip models. *Journal of Turbomachinery*, 117, 12–21.

[22] Prakash, C., & Zerkle, R. (1995). Prediction of turbulent flow and heat transfer in a radially rotating square duct. *Journal of Turbomachinery*, 114(4), 835–846.

International Journal of Innovative Engineering Applications

Journal homepage: https://dergipark.org.tr/ijiea

FREE VIBRATION ANALYSIS OF LAMINATED COMPOSITE BEAMS CONSIDERING DELAMINATION EFFECTS USING GENERALIZED LAMINATION THEORY

Sebahat Şimşek*[1]

[1]Department of Civil Engineering, Faculty of Engineering, Karadeniz Technical University, Trabzon, Turkey

Abstract

Original scientific paper

Laminated composites exhibit highly complex damage mechanisms. One of the most critical failure modes is delamination, which refers to the separation between adjacent layers and can lead to significant reductions in structural stiffness. A major challenge associated with delamination is its invisibility on the material surface, making visual detection difficult. Although vibration-based damage detection methods offer a promising solution for identifying delamination, the effectiveness of such approaches relies on the availability of an accurate numerical model that can capture the behavior of delaminated structures. This study focuses on the modeling of delamination damage in laminated composite beams and the investigation of their free vibration behavior through the generalized lamination theory and finite element analysis. The displacement field within each lamina is assumed to vary linearly based on Lagrange polynomials, while terms accounting for interlayer sliding and separation caused by delamination are explicitly included. The governing equations of motion are derived using Hamilton's principle, and the corresponding mass and stiffness matrices are formulated using the Galerkin method. The influence of delamination length and position on the natural frequencies and mode shapes is examined under various boundary conditions and laminate stacking sequences. The results are compared with existing studies in the literature to validate the accuracy of the proposed model. Additionally, three-dimensional finite element models are developed using ANSYS® software to perform a comparative analysis. Two different modeling strategies for the delaminated interfaces are considered: in the first, nodes on the delaminated surfaces are allowed to move independently; in the second, contact elements are used to constrain the relative motion between layers. The impact of these two modeling approaches on the simulation results is evaluated in detail.

Keywords: *Delamination, free vibration, finite element method, generalized lamination theory, layered composite beam.*

1 Introduction

The rapid advancement in technology and industrial innovation has significantly increased the demand for advanced structural materials characterized by high strength-to-weight ratios, enhanced durability, corrosion resistance, favorable thermal properties, and ease of manufacturing. Composite materials, particularly laminated composites, fulfill these criteria and have consequently become indispensable in various engineering fields, including aerospace, automotive, marine, civil infrastructure, energy production, and mechanical systems.

Despite their numerous benefits, laminated composite structures exhibit unique damage mechanisms due to their heterogeneous and anisotropic nature. Unlike conventional isotropic materials where damage typically manifests visibly as surface cracks, laminated composites predominantly experience internal damage, such as matrix cracking, fiber fractures, and especially delamination—the separation of adjacent layers—before reaching catastrophic structural failure [1], [2]. Such internal damage might initially remain undetected yet significantly degrade the structural integrity, stiffness, and overall load-bearing capacity of composite structures.

Delamination is recognized as a critical failure mechanism in laminated composites, often initiated by interlaminar stress concentrations arising from fatigue loading, transverse impacts, or complex loading conditions [1], [3]. Accurately predicting the onset and progression of delamination is essential for ensuring structural safety and integrity. Consequently, substantial research effort has been dedicated to developing robust and precise numerical modeling approaches to simulate and predict delamination phenomena.

The Finite Element Method (FEM) remains one of the most widely employed numerical tools for analyzing complex damage phenomena, including delamination in laminated composites. The accuracy and reliability of FEM simulations are highly influenced by the underlying theoretical framework and the assumptions utilized to represent the material and structural behavior [4]. To this end, several advanced theories have been proposed, including the Equivalent Single Layer (ESL) theory [5]–[7], the Layerwise theory [7]–[9], the Zig-Zag theory [10]–[13], and the Three-Dimensional Elasticity theory [14], [15].

While ESL theories offer computational simplicity and efficiency, they are inadequate for accurately capturing the complex interlaminar stress fields,

*Corresponding author.

E-mail address: sebahatkaraca@ktu.edu.tr (S. Şimşek)

Received 06 May 2025; Received in revised form 30 May 2025; Accepted 03 June 2025

 Doi: https://doi.org/10.46460/ijiea.1693283

especially in thick laminates or when detailed local damage analyses are required. In contrast, Layerwise theories overcome these limitations by independently modeling each laminate layer, providing detailed descriptions of displacement and stress distributions through the laminate thickness [16], [17]. Recent developments have enhanced Layerwise theory further, notably the Carrera Unified Formulation (CUF), which allows for flexible, high-order expansions to accurately capture multilayered composite behavior [18], [19]. Additionally, integration of advanced numerical methods, such as modified spectral collocation approaches, has significantly improved the predictive capability of Layerwise theories, particularly in complex boundary condition scenarios [17].

Despite these theoretical advancements, a notable gap remains in comprehensive comparative studies between simplified LW-based analytical approaches and fully three-dimensional FEM solutions under delamination conditions, particularly concerning free vibration analyses. Addressing this gap is essential to establish the practical reliability and limitations of simpler analytical frameworks in predicting dynamic structural responses.

Motivated by this need, the present study systematically investigates the free vibration characteristics of laminated composite beams subjected to various delamination scenarios. The analytical model employed is based on Reddy's delaminated beam theory, utilizing linear Lagrange shape functions to represent inter-layer displacement behavior accurately. The model explicitly incorporates interlaminar slip and normal separation effects associated with delamination. The governing equations of motion are derived using Hamilton's principle, while the mass and stiffness matrices are constructed through the Galerkin procedure.

To validate the developed analytical formulation, comparative numerical simulations are conducted using the commercial FE software ANSYS®. The three-dimensional FEM employs SOLID185 elements, modeling delaminated interfaces with two distinct methods: one permitting free separation between layers and another employing contact elements to replicate realistic ply interactions. The resulting free vibration responses under varying delamination configurations are extensively analyzed and compared.

2 Generalized Lamination Theory

2.1 Kinematic Relations and Constitutive Equations

Figure 1 illustrates a schematic view of a composite beam experiencing delamination. In this figure, x_0, z_i and d represent the delamination midpoint's distance from the origin, the interface location of delamination, and the total length of the delamination, respectively. The beam's displacement field is formulated by Equation (1) [20]:

$$\begin{aligned} u(x,z,t) &= u^{LWT}(x,z,t) + u^{DEL}(x,z,t) \\ v(x,z,t) &= 0 \\ w(x,z,t) &= w^{LWT}(x,z,t) + w^{DEL}(x,z,t) \end{aligned} \tag{1}$$

where u^{LWT} and w^{LWT} denote displacements along the longitudinal (x) and transverse (z) axes. The terms u^{DEL} and w^{DEL} define the relative in-plane shear and out-of-plane separation displacements at the delaminated interface. These are further detailed in Equation (2):

$$\begin{aligned} u^{LWT}(x,z,t) &= \sum_{I=1}^{N} U_I(x,t)\Phi^I(z), \\ w^{LWT}(x,z,t) &= \sum_{i=1}^{N} W_I(x,t)\Phi^I(z), \\ u^{DEL}(x,z,t) &= \sum_{I=1}^{ND} {}^{D}U_I(x,t)H^I(z), \\ w^{DEL}(x,z,t) &= \sum_{i=1}^{ND} {}^{D}W_I(x,t)H^I(z) \end{aligned} \tag{2}$$

In this context, *ND* indicates the number of delaminated regions within the beam. The Heaviside unit step function, defined in Equation (3), captures the discontinuity due to delamination:

$$H^I(z) = \hat{H}^I(z - z_i) = \begin{cases} 1 & z \geq z_i \\ 0 & z < z_i \end{cases} \tag{3}$$

Within these equations, z_i signifies the interface location where delamination occurs, and the functions ${}^{D}U_I$ and ${}^{D}W_I$ represent shear slip and normal separation between the respective layers.

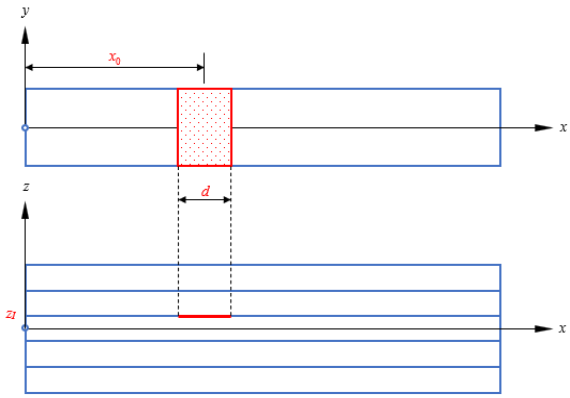

Figure 1. Geometry and coordinate axes of a delaminated beam.

Using the displacement relations provided in Equations (1) and (2), the corresponding strain-displacement relationships are derived:

$$\begin{aligned} \varepsilon_{xx} &= \sum_{I=1}^{N} \frac{dU_I}{dx}\Phi^I + \sum_{I=1}^{ND} \frac{d\,{}^{D}U_I}{dx}H^I, \\ \varepsilon_{yy} &= \gamma_{xy} = \gamma_{yz} = 0, \\ \varepsilon_{zz} &= \sum_{I=1}^{N} W_I \frac{d\Phi^I}{dz}, \\ \gamma_{xz} &= \sum_{I=1}^{N} \left(U_I \frac{\partial \Phi^I}{\partial z} + \frac{\partial W_I}{\partial x}\Phi^I \right) + \sum_{I=1}^{ND} \frac{\partial\, {}^{D}W_I}{\partial x} H^I \end{aligned} \tag{4}$$

$$\begin{Bmatrix}\sigma_{xx}\\ \sigma_{zz}\\ \tau_{xz}\end{Bmatrix}^k = \begin{bmatrix}\tilde{C}_{11} & \tilde{C}_{13} & 0\\ \tilde{C}_{31} & \tilde{C}_{33} & 0\\ 0 & 0 & \tilde{C}_{55}\end{bmatrix}^k \begin{Bmatrix}\varepsilon_{xx}\\ \varepsilon_{zz}\\ \gamma_{xz}\end{Bmatrix}^k \tag{5}$$

Here, the coefficients $\tilde{C}_{ij}^k$ represent the transformed reduced stiffness values for each individual layer [20].

2.2 Equations of Motion

Let δT represent virtual kinetic energy, δU virtual strain energy, and the virtual work by external forces. According to Hamilton's principle [15]:

$$\int_{t_1}^{t_2} \{\delta T - (\delta U + \delta V)\}\, dt = 0 \tag{6}$$

Since the current analysis addresses the beam's free vibration behavior, the term δV becomes zero. Inserting the respective energy formulations into Equation (6) and executing variational procedures leads to the governing equations of motion, expressed as:

3 Finite Element Model

3.1 Finite Element Model Based on the Generalized Lamination Theory

Figure 2 depicts the finite element representation of a beam containing an interfacial delamination. The displacement field within each FE is formulated as:

$$\begin{aligned} U_I(x,t) &= \sum_{j=1}^{2} U_I^j(t)\varphi_j(x),\\ W_I(x,t) &= \sum_{j=1}^{2} W_I^j(t)\varphi_j(x),\\ {}^D U_I(x,t) &= \sum_{j=1}^{2} {}^D U_I^j(t)\varphi_j(x),\\ {}^D W_I(x,t) &= \sum_{j=1}^{2} {}^D W_I^j(t)\varphi_j(x) \end{aligned} \tag{8}$$

In this expression, U_I, W_I, ${}^D U_I$ and ${}^D W_I$ are the generalized coordinates associated with the element's degrees of freedom. The interpolation functions φ_i are linear Lagrange polynomials applied for spatial discretization within the FE context. By substituting the displacement field described in Equation (8) into the motion equations obtained previously (Equation (7)), and subsequently applying the Galerkin method, the elemental FE equation is derived as:

$$M^e + \ddot{U}^e + K^e U^e \tag{9}$$

where, M^e and K^e denote the elemental mass and stiffness matrices, while U^e and $\ddot{U}^e$ represent the element displacement and acceleration vectors, respectively. These vectors are defined as follows:

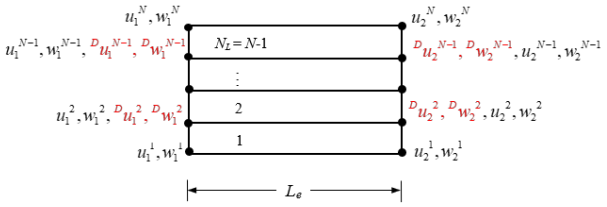

Figure 2. Finite element model with delamination.

$$\mathbf{M}^e = \begin{bmatrix}\mathbf{M}_{11}^{IJ} & \mathbf{0} & \mathbf{M}_{13}^{IJ} & \mathbf{0}\\ \mathbf{0} & \mathbf{M}_{22}^{IJ} & \mathbf{0} & \mathbf{M}_{24}^{IJ}\\ \mathbf{M}_{31}^{IJ} & \mathbf{0} & \mathbf{M}_{33}^{IJ} & \mathbf{0}\\ \mathbf{0} & \mathbf{M}_{42}^{IJ} & \mathbf{0} & \mathbf{M}_{44}^{IJ}\end{bmatrix},\quad \mathbf{K}^e = \begin{bmatrix}\mathbf{K}_{11}^{IJ} & \mathbf{K}_{12}^{IJ} & \mathbf{K}_{13}^{IJ} & \mathbf{K}_{14}^{IJ}\\ \mathbf{K}_{21}^{IJ} & \mathbf{K}_{22}^{IJ} & \mathbf{K}_{23}^{IJ} & \mathbf{K}_{24}^{IJ}\\ \mathbf{K}_{31}^{IJ} & \mathbf{K}_{32}^{IJ} & \mathbf{K}_{33}^{IJ} & \mathbf{0}\\ \mathbf{K}_{41}^{IJ} & \mathbf{K}_{42}^{IJ} & \mathbf{0} & \mathbf{K}_{44}^{IJ}\end{bmatrix},$$
$$\ddot{\mathbf{U}}^e = \begin{bmatrix}\ddot{\mathbf{U}}^J & \ddot{\mathbf{W}}^J & {}^D\ddot{\mathbf{U}}^J & {}^D\ddot{\mathbf{W}}^J\end{bmatrix}^T,\quad \mathbf{U}^e = \begin{bmatrix}\mathbf{U}^J & \mathbf{W}^J & {}^D\mathbf{U}^J & {}^D\mathbf{W}^J\end{bmatrix}^T \tag{10}$$

The evaluation of the submatrices within the global system requires integral expressions, which are provided by:

$$\begin{aligned} M_{11ij}^{IJ} &= M_{22ij}^{IJ} = \int_0^L \{I_1^{IJ}\varphi_i\varphi_j\}\,dx, \quad M_{13ij}^{IJ} = M_{24ij}^{IJ} = \int_0^L \{I_3^{IJ}\varphi_i\varphi_j\}\,dx,\\ M_{31ij}^{IJ} &= M_{42ij}^{IJ} = \int_0^L \{I_2^{IJ}\varphi_i\varphi_j\}\,dx, \quad M_{33ij}^{IJ} = M_{44ij}^{IJ} = \int_0^L \{I_4^{IJ}\varphi_i\varphi_j\}\,dx \end{aligned} \tag{11}$$

$$\begin{aligned} K_{11ij}^{IJ} &= \int_0^L \left\{A_{11}^{IJ}\frac{\partial\varphi_i}{\partial x}\frac{\partial\varphi_j}{\partial x} + \bar{A}_{55}^{IJ}\varphi_i\varphi_j\right\}dx,\\ K_{12ij}^{IJ} &= \int_0^L \left\{\tilde{A}_{13}^{IJ}\frac{\partial\varphi_i}{\partial x}\varphi_j + \bar{B}_{55}^{IJ}\varphi_i\frac{\partial\varphi_j}{\partial x}\right\}dx,\\ K_{13ij}^{IJ} &= \int_0^L \left\{{}^D A_{11}^{IJ}\frac{\partial\varphi_i}{\partial x}\frac{\partial\varphi_j}{\partial x}\right\}dx, \quad K_{14ij}^{IJ} = \int_0^L \left\{{}^D\bar{B}_{55}^{IJ}\varphi_i\frac{\partial\varphi_j}{\partial x}\right\}dx,\\ K_{21ij}^{IJ} &= \int_0^L \left\{\bar{B}_{55}^{JI}\frac{\partial\varphi_i}{\partial x}\varphi_j + \tilde{A}_{31}^{JI}\varphi_i\frac{\partial\varphi_j}{\partial x}\right\}dx,\\ K_{22ij}^{IJ} &= \int_0^L \left\{\bar{D}_{55}^{IJ}\frac{\partial\varphi_i}{\partial x}\frac{\partial\varphi_j}{\partial x} + \hat{A}_{33}^{IJ}\varphi_i\varphi_j\right\}dx,\\ K_{23ij}^{IJ} &= \int_0^L \left\{{}^D\tilde{A}_{31}^{JI}\varphi_i\frac{\partial\varphi_j}{\partial x}\right\}dx, \quad K_{24ij}^{IJ} = \int_0^L \left\{{}^D\bar{A}_{55}^{JI}\frac{\partial\varphi_i}{\partial x}\frac{\partial\varphi_j}{\partial x}\right\}dx,\\ K_{31ij}^{IJ} &= \int_0^L \left\{{}^D\tilde{A}_{11}^{IJ}\frac{\partial\varphi_i}{\partial x}\frac{\partial\varphi_j}{\partial x}\right\}dx, \quad K_{32ij}^{IJ} = \int_0^L \left\{{}^D\tilde{A}_{13}^{IJ}\frac{\partial\varphi_i}{\partial x}\varphi_j\right\}dx,\\ K_{33ij}^{IJ} &= \int_0^L \left\{{}^D\bar{\bar{A}}_{11}^{IJ}\frac{\partial\varphi_i}{\partial x}\frac{\partial\varphi_j}{\partial x}\right\}dx, \quad K_{41ij}^{IJ} = \int_0^L \left\{{}^D\bar{B}_{55}^{JI}\frac{\partial\varphi_i}{\partial x}\varphi_j\right\}dx,\\ K_{42ij}^{IJ} &= \int_0^L \left\{{}^D\bar{A}_{55}^{JI}\frac{\partial\varphi_i}{\partial x}\frac{\partial\varphi_j}{\partial x}\right\}dx, \quad K_{44ij}^{IJ} = \int_0^L \left\{{}^D\bar{\bar{A}}_{55}^{IJ}\frac{\partial\varphi_i}{\partial x}\frac{\partial\varphi_j}{\partial x}\right\}dx \end{aligned} \tag{12}$$

Within these formulations, the matrices *A*, *B* and terms correspond to the laminate's extensional stiffness, coupling stiffness, and bending stiffness matrices, respectively, as established in composite lamination theory [21].

3.2 ANSYS® Finite Element Model

To validate the analytical results derived from the generalized lamination theory, a comprehensive three-dimensional FE model of the delaminated composite beam was developed using ANSYS 16.0, a widely utilized commercial FE analysis software.

For the structural discretization of the laminated composite beam, the SOLID185 element type was employed. SOLID185 is an 8-node hexahedral element capable of modeling nonlinear material behavior, large deformations, and strain-based geometric nonlinearity. Each node has three translational degrees of freedom (UX,

UY, UZ), allowing accurate simulation of deformation in 3D space. To capture the thorough-thickness behavior of the laminated structure with sufficient fidelity, one element per layer was used across the thickness direction. This modeling approach enabled precise characterization of interlaminar stress distributions and deformation gradients, which are particularly significant in the presence of delamination.

The laminate stacking sequence, ply orientation angles, and orthotropic material properties were defined using the SHELL SECTION assignment for layered solids. This ANSYS feature allows users to assign varying fiber orientations, elastic properties, and thicknesses to each ply within a single layered volume, thereby facilitating accurate representation of composite layups without requiring separate meshing for each ply.

A mesh convergence study was performed to determine the optimal element size that balances accuracy with computational cost. Several mesh configurations were analyzed, with natural frequency convergence used as the primary assessment metric. Following this parametric analysis, a refined mesh configuration comprising 1752 elements and 1664 nodes was adopted for all simulations, ensuring consistency across models while maintaining numerical efficiency.

In the FE model, interlaminar continuity was enforced across intact interfaces by coupling the degrees of freedom (DOFs) between nodes of adjacent plies. This constraint condition ensures that no relative displacement occurs in undamaged regions, accurately simulating the perfect bonding assumption typical in composite theory. Conversely, at delaminated interfaces, the nodes were left uncoupled to allow independent movement, thereby replicating the mechanical discontinuity caused by delamination.

To model the delaminated interface behavior, two distinct strategies were implemented:

First Strategy – Free Node Separation: In this simplified method, nodes on opposing delaminated surfaces were left entirely unconstrained. This approach permits full relative motion between the delaminated plies in all spatial directions, offering computational simplicity. However, such an assumption may yield non-physical results under dynamic loading, including excessive separation or even interpenetration of layers, particularly during out-of-plane vibration responses (see Figure 3(a)). Consequently, this method is primarily used for preliminary evaluations or when qualitative behavior is of interest.

Second Strategy – Contact-Based Delamination Modeling: A more realistic and physically robust approach was implemented using contact elements, specifically CONTAC173 and TARGE170. These allow accurate modeling of interface interactions by defining surface-to-surface contact behavior.

TARGE170 represents the target surface and is usually assigned to the stiffer body or underlying layer. CONTAC173 is designated as the contact surface and is applied to the deformable body, enabling interaction with the target during loading.

This strategy permits the model to replicate the asymmetric behavior of delaminated interfaces:

During compressive loading, contact elements transfer normal forces between plies, effectively preventing interpenetration and ensuring realistic mechanical response.

Under tensile conditions, the contact pair automatically deactivates, allowing the delaminated surfaces to separate freely. This behavior reflects the actual physical mechanism of delamination propagation and recovery (see Figure 3(b)).

The contact parameters, including normal stiffness, frictional properties (if applicable), and penetration tolerance, were carefully selected to avoid numerical instabilities while preserving solution accuracy. This contact-based approach significantly enhances the realism of the FE simulations, particularly for vibration and stability analyses of delaminated composite structures.

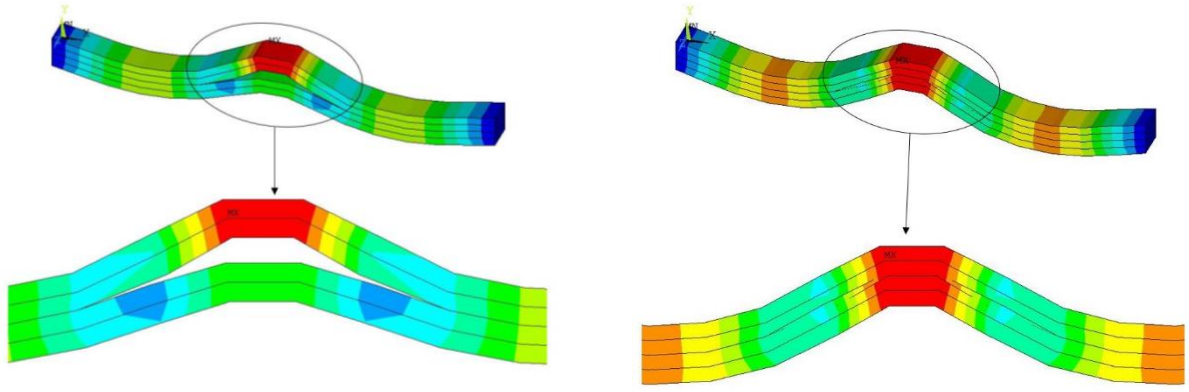

(a) (b)

Figure 3. FE models of delaminated beams created in ANSYS®: (a) without contact elements, (b) with contact elements.

4 Results and Discussion

In order to obtain sufficiently accurate results in the finite element analyses, a mesh convergence study was first conducted. For this purpose, a laminated composite beam with a length of L = 300 mm, width b = 20 mm, and height h = 20 mm was considered. The beam is made of AS3501/6 graphite-epoxy material. The material properties are as follows: E_1 = 144.9 GPa, E_2 = 9.65 GPa, G_{12} = G_{13} = 4.14 GPa, G_{23} = 3.45 GPa, ν = 0.3, and ρ = 1389.23 kg/m³ [22]. Table 1 presents the variation of the first three dimensionless natural frequencies of a clamped–clamped undamaged $(0/90)_2$ beam with respect

to the number of elements. The natural frequencies are expressed in a nondimensional form. As observed, the dimensionless natural frequencies decrease rapidly and converge toward a constant value as the number of elements increases. Based on the table, it is concluded that using N = 80 elements in the finite element analyses is sufficient.

To verify the accuracy of the natural frequencies obtained using the generalized lamination theory and to validate the results for potential damage detection applications, a comparison with existing literature results was performed. Specifically, the non-dimensionalized natural frequencies of a symmetrically delaminated isotropic fixed-fixed beam were considered, based on the study in [23]. The dimensionless frequency parameter Ω was defined as follows:

$$\Omega^2 = \left(\frac{\rho_0 A_0}{E_0 I_0} \right) L_0^4 \omega^2 \tag{13}$$

where ρ_0 is the material density,, A_0 is the cross-sectional area, E_0 is the Young's modulus, I_0 is the second moment of area (moment of inertia), L_0 is the total beam length, and is the angular frequency.

Table 2 presents a comparative summary of the dimensionless natural frequencies obtained in the present study alongside those reported in [23]. The results demonstrate excellent agreement, confirming the validity of the present FE model and analytical approach.

The results clearly show a very strong correlation between the natural frequencies obtained in the present study and those reported in [23] who employed an analytical solution. Particularly for small delamination lengths (a / $L \leq 0.1$), the dimensionless frequencies are nearly identical, indicating the robustness of the modeling approach for slight damage scenarios.

When the results are evaluated internally, as the relative length of the delamination (a / L) increases, a progressive decrease in the natural frequencies is observed, with the higher modes being particularly more affected. While the first natural frequency Ω_1 exhibits a relatively slower reduction, the second and third modes demonstrate greater sensitivity to the presence and growth of delamination. This behavior suggests that higher vibration modes are more effective indicators of delamination damage. Moreover, when the delamination length exceeds a / $L \geq 0.6$, the frequency reduction becomes significantly more pronounced, reflecting substantial stiffness degradation and a corresponding loss of structural integrity.

Table 1. Finite element convergence analysis.

Number of Elements	Natural Frequencies		
	Ω_1	Ω_2	Ω_3
10	3.9395	9.5608	16.8382
20	3.7246	8.8667	15.2230
30	3.6833	8.7352	14.9225
40	3.6687	8.6886	14.8168
60	3.6581	8.6551	15.7410
80	**3.6543**	**8.6433**	**14.7143**
100	3.6526	8.6378	15.7019

Table 2. Non-dimensional natural frequencies of an isotropic fixed-fixed beam with mid-plane delamination.

a / L	Present Study			Analytical [23]		
	Ω_1	Ω_2	Ω_3	Ω_1	Ω_2	Ω_3
0.00	22.6131	61.1880	117.1458	22.39	61.67	120.91
0.05	22.6131	61.1090	117.1447	22.37	61.53	120.90
0.10	22.6126	60.5399	117.1012	22.37	60.76	120.81
0.20	22.5984	56.7449	115.7720	22.35	55.97	118.76
0.30	22.5032	50.7074	108.8308	22.23	49.00	109.04
0.40	22.1713	45.8342	96.1191	21.83	43.87	93.57
0.50	21.3842	43.3365	85.5149	20.88	41.45	82.29
0.60	20.0055	42.7007	80.5521	19.29	40.93	77.64
0.70	18.1395	42.5913	79.7721	17.23	40.72	77.05
0.80	16.0652	41.2531	78.7290	15.05	39.01	75.33
0.90	14.0357	37.9362	73.5082	13.00	69.17	68.84
0.99	12.4029	34.0117	66.2261	11.36	61.36	61.36

To validate the finite element model, a cantilever composite beam with a $(0/-45/45/90)_s$ stacking sequence was considered. The beam has a length of L = 244 mm, while its height and width are given in Table 3. The material properties are as follows: E_1 = 92.5 GPa, E_2 = 8.04 GPa, $G_{12} = G_{13}$ = 2.88 GPa, G_{23} = 2.80 GPa, ν = 0.33, and ρ = 1429.0 kg/m³ [24]. The damage scenarios considered are listed in Table 3. Table 4 presents the first five natural frequencies (Hz) of the beam for both the undamaged case and four different damage scenarios. The results of this study were compared with the experimental data reported in [24]. As can be seen, the results are in good agreement with each other.

Table 3. Dimensions and damage scenarios for cantilever composite beams with (0/−45/45/90)s lay-up [24].

Model	Width (mm)	Thickness (mm)	Delaminated Interface	Delamination Length (mm)	Distance from Support (mm)
Undamaged	19.18	2.27	-	-	-
Case 1	19.25	2.46	4	28	44.9
Case 2	19.09	2.66	3	31	45.3
Case 3	19.36	2.76	2	60.2	105.1
Case 4	18.98	2.69	1	34.5	43

Table 4. First five natural frequencies for undamaged and delaminated cantilever beams with (0/−45/45/90)s.

Method	f_1	f_2	f_3	f_4	f_5
Undamaged					
Present Study	40.6109	253.9843	708.9229	1382.971	2273.114
Zhang et al. (2014) [24]	40	248	698	1362	2244
Case 1					
Present Study	43.6278	266.5954	736.2754	1463.726	2418.190
Zhang et al. (2014) [24]	46	260	724	1482	2434
Case 2					
Present Study	46.88932	284.1747	780.3951	1555.483	2587.254
Zhang et al. (2014) [24]	50	286	792	1610	2636
Case 3					
Present Study	47.9252	295.0304	717.4321	1330.968	2286.246
Zhang et al. (2014) [24]	48	276	704	1434	2402
Case 4					
Present Study	47.4401	290.4456	799.5212	1576.927	2615.020
Zhang et al. (2014) [24]	44	290	804	1564	2665

Following the validation study, numerical results concerning the natural frequencies and mode shapes of a laminated composite beam under various delamination scenarios are presented. The beam considered has a $[0/90]_2$ stacking sequence, with both ends fixed, and equal layer thicknesses are assumed. The material properties for a single ply are taken as: E_1 = 144.9 GPa, E_2 = 9.65 GPa, $G_{12} = G_{13}$ = 4.14 GPa, G_{23} = 3.45 GPa, Poisson's ratio ν = 0.3 and density ρ = 1389.23 kg/m^3. The beam dimensions are considered as L/h =15, $b = h$ = 1 unit.

Table 5 summarizes the delamination scenarios considered in the analysis. In all cases, a single delamination is located at the mid-span of the beam. Variations in delamination position across different interfaces and changes in delamination length are investigated to assess their effects on the natural frequencies and mode shapes. In the first three scenarios (S1–S3), the delamination length is L/5, while in the last three scenarios (S4–S6), it is increased to L/3. In both sets, the delamination is positioned sequentially at different interlaminar interfaces.

Numerical results were obtained using a FE code developed in FORTRAN and compared against results obtained from a 3D FE model created in ANSYS®. In the ANSYS® simulations, contact elements were employed along delaminated surfaces to realistically capture opening and sliding effects between layers. It was observed that the inclusion of contact elements did not significantly alter the natural frequencies but affected the deformation patterns during vibration.

Table 5. Delamination scenarios considered in the analysis.

Damage Scenario	Variables describing delamination (see Figure 1)		
	Interface, z_I	Length, d	Midpoint, x_0
S1	1	L / 5	L / 2
S2	2	L / 5	L / 2
S3	3	L / 5	L / 2
S4	1	L / 3	L / 2
S5	2	L / 3	L / 2
S6	3	L / 3	L / 2

Table 6. First four natural frequencies (Hz) obtained from Reddy's Theory and ANSYS® for different delamination scenarios.

Damage Scenario	f_1		f_2		f_3		f_4	
	Reddy	ANSYS®	Reddy	ANSYS®	Reddy	ANSYS®	Reddy	ANSYS®
S1	2633.67	2667.07	5430.13	6366.64	10399.47	11019.80	12929.54	16151.90
S2	2632.64	2663.77	5409.83	5587.51	10342.91	10869.89	12914.37	13782.94
S3	2623.31	2663.76	6213.01	5595.65	11185.41	10869.93	14814.82	13785.87
S4	2579.53	2666.09	4542.21	6319.76	9005.38	10987.01	12460.03	15864.43
S5	2573.47	2617.85	4518.34	4651.17	9002.69	9559.01	12455.67	13295.84
S6	2308.58	2618.57	5911.20	4668.30	11015.27	9571.07	15670.04	13299.48

The first four natural frequencies obtained for each damage scenario are listed in Table 6, showing results from both Reddy's theory-based FE model and the ANSYS® simulations. It can be observed that the presence of delamination significantly affects the natural frequencies of the composite beam. An increase in delamination length leads to a noticeable reduction in the natural frequencies across all modes. Specifically, for

shorter delaminations (scenarios S1–S3 with $d = L/5$), the natural frequencies from both methods are relatively close, with only minor differences. However, as the delamination length increases to $L/3$ (scenarios S4–S6), the reduction in frequency becomes more pronounced, and the differences between the two approaches tend to increase, particularly for the third and fourth modes. This behavior can be attributed to the growing influence of localized stiffness degradation, which affects the dynamic response more severely at higher frequencies.

Figures 4 and 5 illustrate the first four bending mode shapes for the beam with a delamination located at the second interface (Scenario S2), obtained using the proposed FE approach and ANSYS® simulations, respectively. In Figure 4, which corresponds to Reddy's theory-based model, discontinuities in the slope of the mode shapes are clearly visible at the start and end points of the delamination, indicating the localized stiffness reduction. These discontinuities are more pronounced in higher modes, consistent with the greater sensitivity of higher modes to local defects.

In contrast, Figure 5, showing the ANSYS® results, reveals additional physical phenomena. Relative sliding between the separated layers is clearly observed during vibration, a behavior captured due to the use of contact elements. While separation (opening) between the layers is less evident in lower modes, it becomes noticeable in the fourth mode, as the deformation becomes sufficiently large to induce contact opening. This observation confirms that the proposed numerical approach accurately captures key deformation characteristics while maintaining computational efficiency.

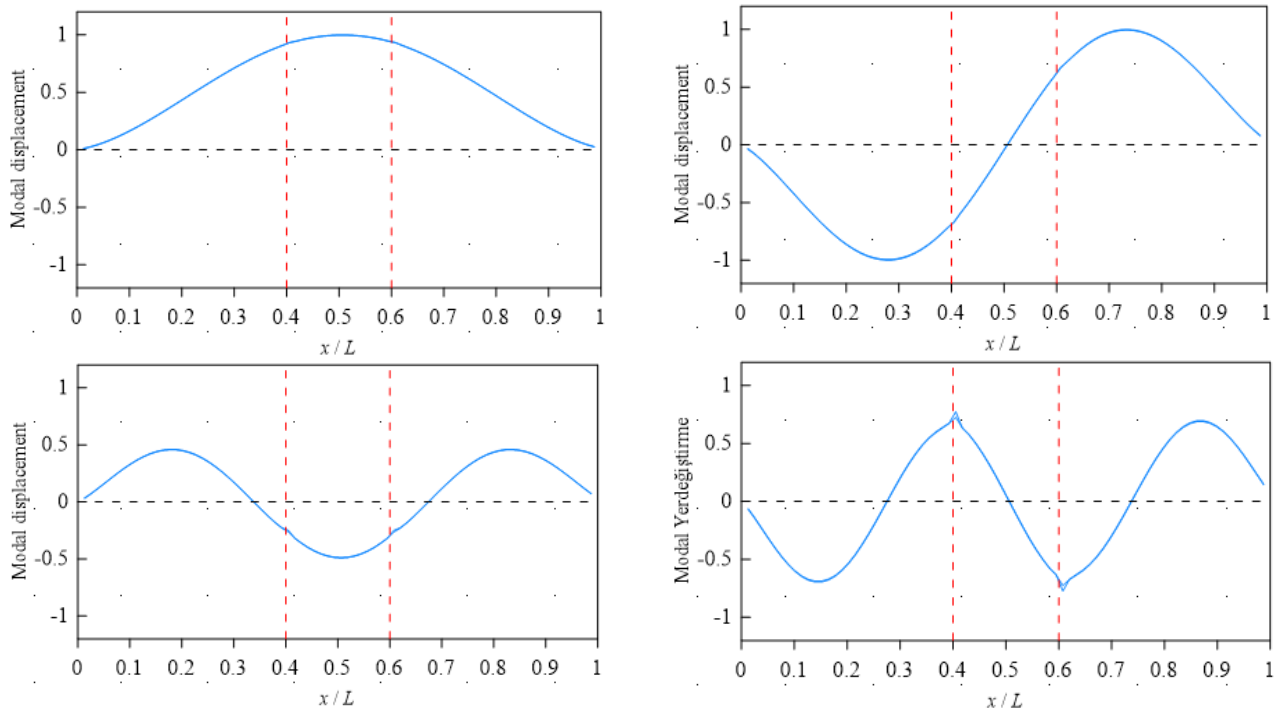

Figure 4. First four mode shapes of the fixed-fixed laminated composite beam obtained from the FE model based on Reddy's Theory (Scenario S2).

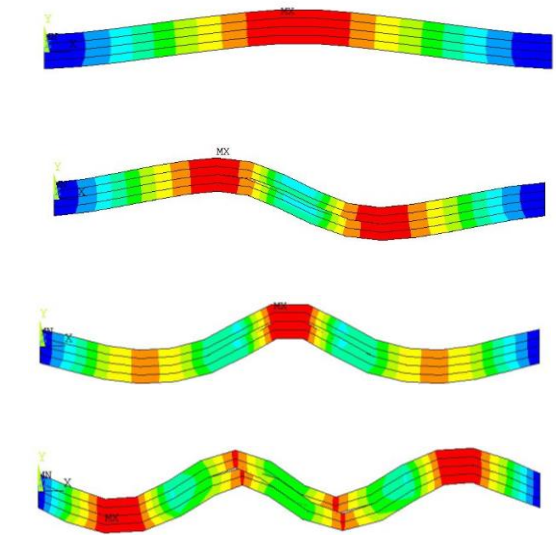

Figure 5. First four mode shapes of the fixed-fixed laminated composite beam obtained from ANSYS® Simulations (Scenario S2).

5 Conclusions

This study examined the free vibration behavior of laminated composite beams under various delamination scenarios using an FE formulation based on Reddy's delaminated beam theory. The displacement field within each ply was approximated by linear Lagrange polynomials, and interlaminar sliding and separation due to delamination, along with Poisson's effects, were considered. Equations of motion were derived via Hamilton's principle, and FE matrices were constructed using the Galerkin method.

Validation was performed against analytical results and three-dimensional FE simulations conducted using ANSYS®. The developed model exhibited excellent agreement with analytical solutions, particularly for smaller delamination, and maintained consistency as delamination length increased. ANSYS® simulations with SOLID185 elements employed both free-separation and contact-element modeling approaches.

- Increasing delamination length significantly reduces natural frequencies, highlighting the sensitivity of dynamic response to structural damage.
- Reddy's theory-based FE model efficiently simplifies the three-dimensional problem into a two-dimensional approach, achieving accurate predictions with lower computational effort.
- The developed model demonstrates strong agreement with both analytical and comprehensive 3D numerical solutions, confirming its accuracy and reliability.
- This approach provides a flexible and computationally efficient tool suitable for vibration-based damage detection in laminated composite structures.

Overall, the proposed FE methodology effectively captures delamination effects and represents a reliable approach for dynamic structural analyses of laminated composite beams.

Acknowledgments

The author would like to express their sincere gratitude to Prof. Volkan Kahya for his valuable comments in preparation of this work.

Declaration

Ethics committee approval is not required.

References

[1] Ghobadi, A. (2017). Common type of damages in composites and their inspections. *World Journal of Mechanics, 7*(2), 24–33.

[2] Li, D. (2021). Layerwise theories of laminated composite structures and their applications: A review. *Archives of Computational Methods in Engineering, 28*, 577–600.

[3] Torabi, K., Shariati-Nia, M., & Heidari-Rarani, M. (2016). Experimental and theoretical investigation on transverse vibration of delaminated cross-ply composite beams. *International Journal of Mechanical Sciences, 115–116*, 1–11.

[4] Della, C. N., & Shu, D. (2007). Vibration of delaminated composite laminates: A review. *Applied Mechanics Reviews, 60*(1), 1.

[5] Goyal, V. K., & Kapania, R. K. (2007). A shear-deformable beam element for the analysis of laminated composites. *Finite Elements in Analysis and Design, 43*(6–7), 463–477.

[6] Aguiar, R. M., Moleiro, F., & Mota Soares, C. M. M. (2012). Assessment of mixed and displacement-based models for static analysis of composite beams of different cross-sections. *Composite Structures, 94*(2), 601–616.

[7] Sayyad, A. S., & Ghugal, Y. M. (2017). Bending, buckling and free vibration of laminated composite and sandwich beams: A critical review of literature. *Composite Structures, 171*, 486–504.

[8] Hajianmaleki, M., & Qatu, M. S. (2013). Vibrations of straight and curved composite beams: A review. *Composite Structures, 100*, 218–232.

[9] Li, D. (2020). Layerwise theories of laminated composite structures and their applications: A review. *Archives of Computational Methods in Engineering, 1*(0123456789), 3.

[10] Lansing, E., & Lansing, E. (1999). C^0 zig-zag finite element for analysis of laminated composite beams. *Journal of Engineering Mechanics, 125*(3), 323–330.

[11] Zhen, W., & Wanji, C. (2008). An assessment of several displacement-based theories for the vibration and stability analysis of laminated composite and sandwich beams. *Composite Structures, 84*(4), 337–349.

[12] Khan, A. A., Alam, M. N., & Wajid, M. (2016). Finite element modelling for static and free vibration response of functionally graded beam. *Latin American Journal of Solids and Structures, 13*(4), 690–714.

[13] Filippi, M., & Carrera, E. (2016). Bending and vibrations analyses of laminated beams by using a zig-zag-layer-wise theory. *Composites Part B: Engineering, 98*, 269–280.

[14] Chen, W. Q., Lv, C. F., & Bian, Z. G. (2003). Elasticity solution for free vibration of laminated beams. *Composite Structures, 62*(1), 75–82.

[15] Kant, T., Gupta, A. B., Pendhari, S. S., & Desai, Y. M. (2008). Elasticity solution for cross-ply composite and sandwich laminates. *Composite Structures, 83*(1), 13–24.

[16] Liew, K. M., Pan, Z. Z., & Zhang, L. W. (2019). An overview of layerwise theories for composite laminates and structures: Development, numerical implementation and application. *Composite Structures, 216*, 240–259.

[17] Ji, M., Sekiguchi, Y., Naito, M., & Sato, C. (2025). A modified spectral collocation method for vibration of sandwich beams based on a higher-order layer-wise beam theory. *Thin-Walled Structures, 209*, Article 112949.

[18] Filippi, M., Giusa, D., Pagani, A., Zappino, E., & Carrera, E. (2020). Assessment of classical, advanced, and layer-wise theories for the vibration of rotating composite anisotropic blades. *Composite Structures, 245*, Article 112315.

[19] Augello, R., Carrera, E., & Saputo, S. (2025). Component-Wise measure of elastic energy contributions in laminated composite beams. *Composite Structures, 355*, Article 118842.

[20] Reddy, J. N. (2003). *Mechanics of laminated composite plates and shells: Theory and analysis* (2nd ed.). CRC Press/Balkema.

[21] Na, W. J. (2008). *Damage analysis of laminated composite beams under bending loads using the layer-wise theory* [Doctoral dissertation, Texas A&M University].

[22] Dinh-Cong, D., Vo-Duy, T., Nguyen-Minh, N., Ho-Huu, V., & Nguyen-Thoi, T. (2017). A two-stage assessment method using damage locating vector method and differential evolution algorithm for damage identification of cross-ply laminated composite beams. *Advances in Structural Engineering, 20*(12), 1807–1827.

[23] Wang, J. T. S., Liu, Y. Y., & Gibby, J. A. (1982). Vibrations of split beams. *Journal of Sound and Vibration, 84*(4), 491–502.

[24] Zhang, Z., Shankar, K., Morozov, E. V., & Tahtali, M. (2016). Vibration-based delamination detection in composite beams through frequency changes. *Journal of Vibration and Control, 22*(2), 496–512.

International Journal of Innovative Engineering Applications

Journal homepage: https://dergipark.org.tr/ijiea

SPREAD EMBEDDING OF FRAGILE COPYRIGHT INFORMATION TO PROTECT AUDIO SIGNAL

Hüseyin Bilal Macit*[*1]

[1]*Burdur Mehmet Akif Ersoy University, Dept. of Information Systems and Technologies, Bucak ZTYO, Burdur*

Abstract

Original scientific paper

Nowadays, millions of gigabytes of new data are generated every second and a large part of it is multimedia data. The security of this large amount of data is an important problem as well as its transmission and storage. Data without proven authenticity should not be distributed or used without permission. Audio data, unlike other types of multimedia, is quite weak in terms of copyright protection. Industrial practices generally prioritize the quality of audio data over the security of copyright data, contrary to academic recommendations. In this study, a spread hash-supported copyright embedding algorithm is proposed to ensure the copyright protection of audio data. The proposed algorithm is tested on a total of 92.017 seconds of dataset consisting of 516 music files and the results are presented. The algorithm successfully performs copyright verification of any 2-millisecond fragment of the audio in any clipping attack. Despite the changes made to the entire audio data, a 6% Bit Error Rate and 0.9999 Normalized Correlation values are obtained. According to international standards for perceptual evaluation of audio quality, a score of ~-1.7 is obtained in the objective evaluation. All performance evaluations are presented with tables and graphs, and comparisons are made with similar models in the literature. This study is one of the first to use a spread-hashing technique for audio copyright protection and has shown high performance, especially against clipping attacks.

Keywords: *Copyright protection, cyber security, data security, hash function.*

SES SİNYALİNİ KORUMAK İÇİN KIRILGAN TELİF HAKKI BİLGİLERİNİN YAYGIN GÖMÜLMESİ

Özet

Orijinal bilimsel makale

Günümüzde her saniye milyonlarca gigabayt yeni veri üretilmektedir ve bunun büyük bir kısmı multimedya verisidir. Bu büyüklükte verinin iletilmesi ve depolanması kadar güvenliği de önemli bir problemdir. Aidiyeti kanıtlanmamış veri izinsiz dağıtılmamalı ve kullanılmamalıdır. Ses verisi, diğer multimedya türlerinin aksine telif hakkı korunması konusunda oldukça güçsüzdür. Endüstriyel uygulamalar genellikle akademik önerilerin aksine telif hakkı verisinin güvenliğinden ziyade ses verisinin kalitesine önem verir. Bu çalışmada, ses verilerinin telif hakkı güvenliğini sağlamak için hash destekli yaygın bir telif hakkı gömme algoritması önerilmiştir. Önerilen algoritma 516 müzik dosyasından oluşan toplam 92,017 saniyelik bir veri seti üzerinde test edilmiş ve sonuçları sunulmuştur. Algoritma herhangi bir kırpma saldırısında sesin herhangi 2 milisaniyelik parçasından bile telif doğrulamasını başarıyla gerçekleştirmiştir. Tüm ses verisinde yapılan değişikliğe rağmen %6 Bit Hata Oranı ve 0,9999 Normalize Korelasyon değerleri elde edilmiştir. Uluslararası ses kalitesinin algısal değerlendirmesi standartlarına göre nesnel değerlendirmede ~-1,7 skor elde edilmiştir. Tüm performans değerlendirmeleri tablolar ve grafikler ile sunulmuş, literatürdeki benzer modeller ile karşılaştırma yapılmıştır. Bu çalışma, ses sinyalinin telif hakkını korumak için bir yaygın-çırpı tekniği kullanan ilk çalışmalardandır ve özellikle kırpma saldırılarına karşı yüksek performans göstermiştir.

Anahtar Kelimeler: *Çırpı fonksiyonu, telif hakkı koruması, siber güvenlik, veri güvenliği.*

1 Introduction

The amount of data production and distribution has grown tremendously with the widespread use of the Internet in the 21st century. It is estimated that an average of 4.6 million GB of data will be produced per second in 2024 [1], and the vast majority of it will be multimedia data [2]. Ensuring the security of digital media is becoming increasingly difficult as computer networks are extremely susceptible to external attacks [3]. Although unauthorized access to multimedia data is prevented by cryptography [4], once the data is decrypted, it becomes vulnerable again to various attacks such as re-sampling, re-quantization, compression, and echo injection. A multimedia object that

*Corresponding author.

E-mail address: hbmacit@mehmetakif.edu.tr (H. B. Macit)

Received 24 February 2025; Received in revised form 21 April 2025; Accepted 16 June 2025

 Doi: https://doi.org/10.46460/ijiea.1645813

appears to be vulnerable can be made to protect itself in an undetectable manner. For this purpose, data hiding methods such as labeling, digital signing, digital watermarking, and steganography methods [5] based on ancient times have been adapted to the 21st century digital world. In addition to these methods, the security of multimedia is also protected by laws. For example, according to the laws of the United States; the developer of a story, picture, song or any other original work automatically owns the copyright from the moment this work is recorded in physical form [6]. However, if the authors wish to distribute their work, they must add a copyright notice to the work. In Turkey, Article 22 of the Law on Intellectual and Artistic Works No. 5846 clearly states the rights of the author: "The right to reproduce the original or copies of a work, in whole or in part, directly or indirectly, temporarily or permanently, by any means or method, belongs exclusively to the author. Making a second copy of the original work or recording the work on any known or future means that are used for signal, sound and image transmission and repetition, any sound and music recordings, and the implementation of plans, projects and sketches of architectural works are also considered copies.". Despite the laws, copyright violations are increasing, especially with the spread of mobile devices. Manufacturers are developing new algorithms for copyright protection. Most of these methods add an imperceptible piece of information representing the producer to the digital multimedia object [7] as shown in figure 1.

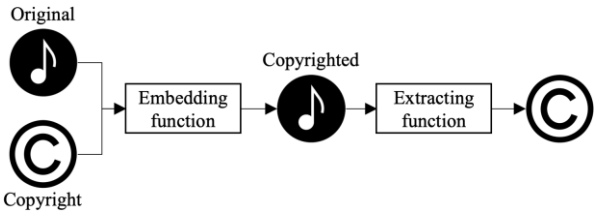

Figure 1. Overview of the basic multimedia copyright protection scheme.

However, the biggest risk of these methods is that the person who made the unauthorized copy is able to cut the copyright embedded part of the object. In this case, the person who purchased the multimedia object may not be able to decide whether it is the original or a pirate copy. In today's digital world, the best way to check copyright information is to consult a copyright database, which is a collection of copyrighted works and related information such as authors, publishers, publication dates, and copyrights. The General Directorate of Copyrights of the Ministry of Culture and Tourism of Turkey has provided access to the Database of Intellectual and Artistic Works via eser.telifhaklari.gov.tr [8]. This includes information such as registration and banderol information regarding processed works, repertoire records of some music workers' associations, names of works, authors, publishers and producers, years of publication and production. The performance of a copyright protection algorithm is calculated according to four criteria: Imperceptibility, robustness, payload and low computational time. Imperceptibility refers to the similarity of the original multimedia with copyright information added version [9]. A copyrighted audio data should not be distinguishable by the human auditory system. The ability of copyrighted multimedia to protect copyright during transfer and storage is called robustness. A malicious distributor can perform various transformations on the digital multimedia object to destroy copyright data [10]. In some applications, multimedia is expected to retain most of the copyright data despite these transformations. Payload is defined as the data embedding capacity of the algorithm and is measured as the number of bits embedded in one second of the audio signal (bps) [11]. The ideal amount of data payload is 1kbs for every 1kHz [12]. An algorithm cannot be expected to satisfy all four criteria at the same time [13]. Depending on the type of multimedia object, the distribution/storage medium and the distributor's demands, it can be decided which criterion is the priority. To date, many copyright protection algorithms have been proposed and used for audio. The biggest problem of most of them is the quality loss that may occur in the original audio data [14].

In this paper, a copyright protection method with an ideal payload of 1 bit per Hertz is proposed, which is almost imperceptible for the Human Auditory System (HAS). The Royalty-Free Audio (RFA) Dataset [15] downloaded from kaggle.com website was used to implement the method and test its results. The reasons for choosing this experimental dataset in this study are that it contains freely distributed sounds, all files have detailed copyright information, and they have a wide variety of file lengths. The dataset contains a total of 92,017 seconds of audio data sampled from Youtube Royalty-free videos. There are 516 music files, and a table including copyright texts, ranging from 104 characters to 386 characters. The shortest music file is 68 seconds, and the longest one is 1792 seconds. The proposed method is implemented with all elements in this dataset and the performance results are shown mathematically with various metrics, and visually with graphs.

2 Method

The proposed method consists of two phases: Embedding copyright information and extracting it. The schematic of the method is shown in figure 2.

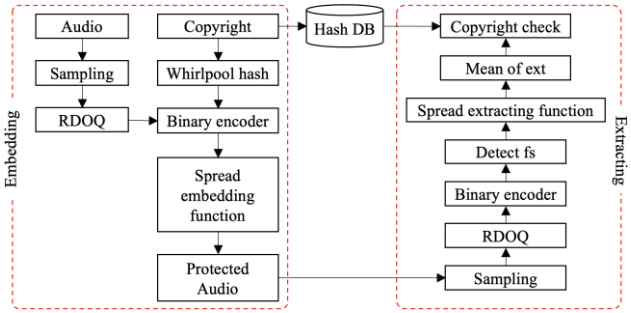

Figure 2. Overall schematic of the proposed method.

2.1 Copyright Embedding Phase

The number of sound samples recorded in 1 second of an audio signal is called sampling rate and is measured in Hertz or samples/sec. For example, a 44.1kHz audio signal has 44100 digital sound samples per second. In the first step, the audio signal is sampled and the continuous-time

signal is reduced to a discrete-time signal. In other words, the analog signal is converted into a series of "samples". Each sample is the value of the signal in time space. The sample set is obtained by sampling the audio signal s(t) and multiplying it by the impulse sequence $\delta(t)$:

$$\delta(\mathrm{t}) = [\frac{1}{T_s} + \sum_{n=1}^{\infty} \frac{2}{T_s} cosn\omega_s t] \quad (1)$$

Here, ω_s is the value of each sample, T_s is the sample time, and n is the index number of corresponding samples. Sampled audio $y(t)$ is calculated in equation (2):

$$\begin{aligned} y(t) &= s(t).\delta(\mathrm{t}) \quad (2)\\ &= s(t).[\frac{1}{T_s} + \sum_{n=1}^{\infty} \frac{2}{T_s} cosn\omega_s t] \\ &= \frac{1}{T_s}[s(t) + 2cos\omega_s t.s(t) + 2cos2\omega_s t.s(t) + \cdots] \end{aligned}$$

Fourier Transform is performed on both sides of $y(t)$:

$$\begin{aligned} y(\omega) &= \frac{1}{T_s}[s(\omega) + s(\omega - \omega_s) + s(\omega + \omega_s) + s(\omega - 2\omega_s) + \cdots] \\ &= \frac{1}{T_s}\sum_{n=-\infty}^{\infty} s(\omega - n\omega_s) \quad (3) \end{aligned}$$

$y(\omega)$ is the sample set of s. Quantization process is performed to convert the amplitude values indicated by the sample set $y(\omega)$ into a numerical sequence. Thus, a finite number of output values are obtained from a continuous set. In this study, the quantization process is coded by 8 bits regardless of the size of the input data. During coding, a sequence of numbers called quantization noise is produced, which is sometimes modeled as an additive random signal called quantization noise. After adding copyright protection, Rate Distortion Optimized Quantization (RDOQ) was applied as a solution method for the problem of "minimum number of bits per symbol" [16] to reconstruct the same s signal. Thus, it was aimed to find the most appropriate set of transformation coefficients [17]. Because, RDOQ finds the optimal quantized level of each transform coefficient by minimizing the rate and distortion of s. The scale factor f_s is used to transform the resulting decimal number elements into their corresponding integers.

$$f_s = argmin|s - S|^2 \quad (4)$$

Here, S is the corresponding 8-bit transformed element of s. So, $S(t)$ is the optimized quantized array. Copyright information detects any unauthorized change or tampering, ensures the verification of the audio source, and ensures data integrity. Thus, the intellectual property rights of content creators are protected [18]. However, there is no global standardization for copyright information. Therefore, the copyright of each work is of different length and formation. The RFA Dataset used in this study contains 516 music files with copyright text varying from 104 characters to 386 characters. The shortest music file is 68 seconds and the longest one is 1792 seconds long, as shown in Table 1.

Table 1. Copyright information of the shortest and longest music in the RFA Dataset.

Audio	Copyright data	Character count
Far Away – MK2	Far Away - MK2 | Royalty Free Music - No Copyright Music | YouTube Music, No license provided/CC0 License	104
Enchanted Valley - Kevin MacLeod	Dnchanted Valley - Kevin MacLeod | Royalty Free Music - No Copyright Music | YouTube Music, Enchanted Valley by Kevin MacLeod is licensed under a Creative Commons Attribution license(https://creativecommons.org/licenses/by/4.0/)Source: http://incompetech.com/music/royalty-free/index.html?isrc=USUAN1200093Artist: http://incompetech.com/Support by RFM - NCM: https://youtu.be/RC4W3GDGZMg	386

Variable copyright text length makes it difficult to hide copyright information in audio data with a standard model. Many studies hide copyright information from the first sample of audio data. However, in this case, copyright information is lost by trimming the first seconds of the audio. When reading copyright data, the data length must be known in advance, which creates a standard data length requirement for adding copyright. In the proposed method, a hash function is used, and the copyright information is spread over the entire audio data to avoid these problems. A hash function maps data of different dimensions to fixed-size and irreversible values [19]. The most commonly used hash algorithms today are MD5 and SHA variants [20]. SHA-256 and SHA3-256 both have an output size of 256 bits (32 bytes) whereas MD5 has an output size of 128 bits (16 bytes). In this study, The Whirlpool Secure Hash Function [21], which is the hash algorithm with the longest output (512 bits) that can be used with SHA [22], I s used. Let's assume that C_o is the initial copyright text, and C_h is the encrypted hash data.

$$C_{int} = W(C_{i-1}, m_i) \oplus C_{i-1} \oplus m_i \quad (5)$$

C_{int} is the intermediate value where $m_1, m_2, \ldots, m_t$ are the time-based blocks of C_o. Each C_i is the value of iteration i, and C_{i-1} is the previous value. W is the Whirlpool block cipher function, which operates similarly with AES. Figure 3 shows the general structure of W.

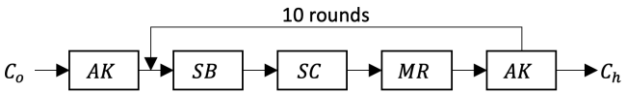

Figure 3. Whirlpool Cipher

C_o is transformed to 8x8 matrix as an input data to the first AK function. This input is called $CState$. The 8x8 matrix produced as a result of each AK function is called $KState$. In short, the first AK input is called $CState$. Let r represent the round number:

$$CState = KState_r, \text{ where } r = 1 \quad (6)$$

$KState$ is the input key for AK when $2 \leq r \leq 10$. A 16x16 Substitution box (S-box) table is used for the SB function. This table contains all possible 8-bit values. S-box is used

for nonlinear mapping of $CState$ by taking four leftmost bits and place them as the column indexes:

$$KState_r = SB(KState_{r-1}), b_{i,j} = S[a_{i,j}] \quad (7)$$

Here, $b_{i,j}$ is the value of the S-box, i,j represents the individual byte of CState. SC function:

$$KState_r = SC(KState_{r-1}) \leftrightarrow b_{i,j} = a_{(i-j)mod8,j} \quad (8)$$
$$0 < i,j < 7, 2 \leq r \leq 10$$

The MR function is a linear diffusion layer. Diffusion is a cryptographic property [23] that hides the statistical properties of the input key. For this purpose, it uses a standard transformation matrix M.

$$M = \begin{bmatrix} 01 & 01 & 04 & 01 & 08 & 05 & 02 & 09 \\ 09 & 01 & 01 & 04 & 01 & 08 & 05 & 02 \\ 02 & 09 & 01 & 01 & 04 & 01 & 08 & 05 \\ 05 & 02 & 09 & 01 & 01 & 04 & 01 & 08 \\ 08 & 05 & 02 & 09 & 01 & 01 & 04 & 01 \\ 01 & 08 & 05 & 02 & 09 & 01 & 01 & 04 \\ 04 & 01 & 08 & 05 & 02 & 09 & 01 & 01 \\ 01 & 04 & 01 & 08 & 05 & 02 & 09 & 01 \end{bmatrix} \quad (9)$$

For example, $KState_i$, which is obtained in round i is:

$$KState_i = KState_{r-1}.M \quad (10)$$

The AK function XORs the bits of the round associated with the $KState$. The AK function:

$$KState_{r-1} = AK[Key_i](A) \leftrightarrow b_{i,j} = a_{i,j} \oplus k_{i,j}, 0 \leq i,j \leq 7 \quad (11)$$

Here, Key_i is the round key, and round Constant rc is calculated to produce it in the corresponding round:

$$rc[r]_{0,j} = Sbox[8(r-1)+j] \quad (12)$$
$$0 \leq j \leq 7, 1 \leq r \leq 10$$

$$rc[r]_{i,j} = 0, 1 \leq i \leq 7, 1 \leq r \leq 10 \quad (13)$$

Key_i is calculated by obtained rc:

$$Key_r = RF[rc[r]](Key_{r-1}) \quad (14)$$

RF function in any r round using these values:

$$RF(K_r) = AK[K_r] \odot MR \odot SC \odot SB \quad (15)$$

Here, the operator $\odot$ indicates the iteration of the composition function with index r, and running from 1 through 10. The entire W function can be summarized as in equation 16:

$$W(K) = \left(O_{r=1}^{10} RF(Key_r)\right) \odot AK(Key_0) \quad (16)$$

The 128 character C_h array obtained with the C_0 copyright input to the Whirlpool hashing function is a hexadecimal array. However, $S(t)$ obtained with RDOQ is a binary array. To embed the hash data into $S(t)$, it is also encoded in binary form. Binary encoder converts C_h to 1-dimension binary array which contain 512 elements consisting of 1s and 0s.

$$C_h(t) = \{C_h(1), C_h(2), \ldots, C_h(512)\} \quad (17)$$

Least Significant Bit (LSB) modification was applied for copyright embedding, which is popular for data hiding due to its simplicity and readability [24]. LSB preserves the audio quality after copyright embedding, but is not robust against attacks such as noise and clipping [25]. LSB modification basically replaces the last bit of each 8-bit sample of $S(t)$ with the last bit of $C_h(t)$. So, LSB modification can change the numeric value of the corresponding sample of $S(t)$ by a maximum of ±1.

$$S(t)_i = \begin{cases} 1, C_h(t)_i = 1 \\ 0, C_h(t)_i = 0 \end{cases} \quad (18)$$

Most of the traditional methods hide the copyright information into the audio header. However, some methods hide it from the first second of the audio data. In this case, if a part of the first seconds of the audio is cut, copyright is lost. The proposed method divides $S(t)$ into equal parts of 512-bit size and embeds $C_h(t)$ into the LSBs of each part of it as shown in figure 4. Thus, even if any random part of the audio is clipped, copyright information can still be accessed.

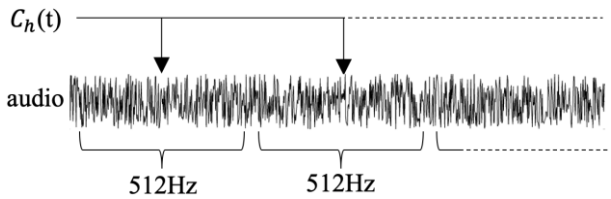

Figure 4. Spread embedding of binary encoded hash data into the audio.

The generated copyright protected signal is a discrete-time signal. It should be formed with the same sample rate of the original input signal. For example, if the original signal was 44.1kHz, the copyright embedded signal is also formed back as 44.1kHz.

2.2 Copyright Extracting Phase

This phase is the stage of reading the encrypted copyright information in the copyrighted audio. The main purpose is to compare the information extracted from the copyrighted audio with the encrypted copyright data in the hash database. In the first step, the copyrighted audio $S(t)$ is sampled using the method in the copyright embedding phase to obtain $y(\omega)$ samples. RDOQ is applied to convert the amplitude values indicated by the $y(\omega)$ sample set into a numerical array. Thus, a protected audio sequence $P(t)$ consisting of t samples is obtained. The possible problem here is that the audio may have been subjected to a clipping attack. In this case, it is not possible to detect which sample the copyright data starts from, but the proposed method offers a solution to this problem. $P(t)$ is divided into 512-bit pieces starting from the first sample and the $\forall(m, 512)$ matrix is created, with each piece being a row:

$$P(t) \to \forall(m,512) = \begin{bmatrix} \forall_{1,1} & \cdots & \forall_{1,512} \\ \vdots & \ddots & \vdots \\ \forall_{m,1} & \cdots & \forall_{m,512} \end{bmatrix} \quad (19)$$

$$= \begin{bmatrix} P(t)_i & \cdots & P(t)_{512+i} \\ \vdots & \ddots & \vdots \\ P(t)_{512m+i} & \cdots & P(t)_{513m-1} \end{bmatrix}, 1 \le i < 512$$

If the copyright information is placed starting from the ith sample of $P(t)$, each row of the $\forall$ must be identical or largely similar to each other. To evaluate this, each column is selected in turn and the standard deviation of the selected column is taken as $\sigma\forall(i)$:

$$\sigma\forall(i) = \sqrt{\frac{1}{m}\sum_{j=1}^{m}(\forall(j) - \overline{\forall})^2} \quad (20)$$

The column with the smallest standard deviation is actually considered to be the starting point $pos(C_e(t))$ of the section where all the rows are most similar to each other, which theoretically contains the new copyright information C_e.

$$pos(C_e(t)) = \min(\sigma\forall) \quad (21)$$

Starting from $pos(C_e(t))$, the average of 512 columns is taken one by one and the extracted copyright C_e is obtained.

$$C_e(i) = \frac{\sum_{j=1}^{m} \forall_{i,j}}{512}, 1 \le i < 512 \quad (22)$$

C_e is compared with the data in the hash database to check the ownership of the sound. Here, the similarity between the C_h retrieved from the database and the extracted C_e is evaluated. The desired similarity rate can be determined by experimental studies or by the threshold value determined by the user using the algorithm. Since both vectors are of the same type of data, Bit Error Rate (BER) and Two-dimensional correlation analysis (CC) were calculated to determine their experimental similarity rate. BER is a bitwise calculation metric which is used to measure the number of bits that change between two signals. As the BER value decreases, the probability of C_e being copyrighted increases.

$$BER = \frac{C_e \oplus C_h}{512} \quad (23)$$

Here, the $\oplus$ operator indicates the number of bits that differ between two vectors. CC analysis is a mathematical technique that shows the amount of change between two signals. CC is also referred to as covariance or correlation in classical mathematics. Let $\tilde{d}(C)$ be the reference difference between C_e and C_h:

$$\tilde{d}(C) = C_e - C_h \quad (24)$$

Synchronous spectrum is calculated in:

$$\phi(C_e, C_h) = \frac{1}{n-1}\sum_{i=1}^{n}\left(\tilde{d}(C) - C_e\right)\left(\tilde{d}(C) - C_h\right) = \frac{1}{511}\sum_{i=1}^{512}\left(\tilde{d}(C) - C_e\right)\left(\tilde{d}(C) - C_h\right) \quad (25)$$

Here, ϕ is the CC value and as it approaches to 1, the similarity between C_e and $C_h$increases. Therefore, low BER and high CC results were targeted in the test results of the proposed algorithm.

3 Experimental Results

The RFA Dataset was used to test the performance of the proposed method. The method was run on all 516 music files in the dataset and all statistical results obtained were shown with tables and graphs. Avalanche effect test was performed with Dataset inputs to measure the encryption performance of the hash algorithm. Segmental Signal to Noise Ratio (SSNR) test was performed to mathematically measure the quality of the copyrighted audio produced. Random Simulation was performed to monitor the amount of noise caused by the method. Additionally, Objective Difference Grade (ODG), which is an international sound quality measurement standard, was measured.

A hash function should be able to change at least 50% of the output data even with a 1-bit change in the input data [26]. This feature is called Avalanche Effect [27] and is calculated in the proposed implementation as in Equation (26).

$$Avalanche\ Effect = \frac{Modified\ bits\ (or\ hex')\ of\ hash}{Total\ bits\ (or\ hex')\ of\ copyright} \quad (26)$$

Each character of the hash text is 1 hex long. Therefore, the avalanche effect test was performed both bitwise and hexwise. Copyright data character length and avalanche effect graphs for a total of 516 audio files in the RFA Dataset are shown in figures 5 and 6.

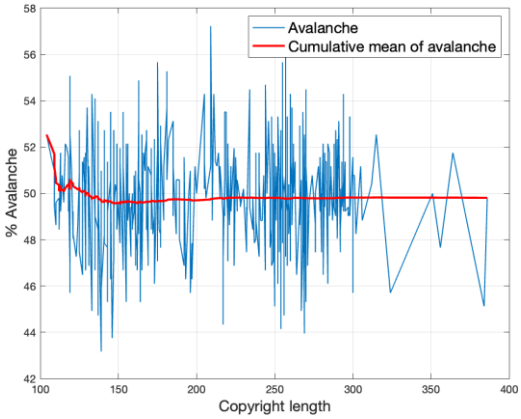

Figure 5. Avalanche effect percentage of 1-bit modification.

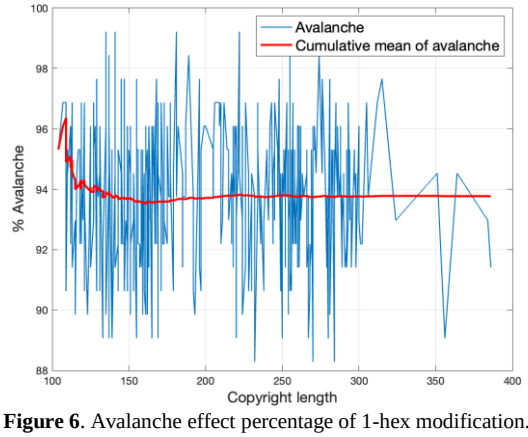

Figure 6. Avalanche effect percentage of 1-hex modification.

As seen in the graphs in figures 5 and 6, there is no relationship between Copyright Length (CL) and avalanche effect. Table 2 shows the maximum, minimum and average results of bitwise and hexwise avalanche tests performed on RFA Dataset.

Table 2. Avalanche test results of RFA dataset.

	1-bit modification	1-hex modification
Min percentage	43.16%	88.28%
Min count	221	113
Avg percentage	49.81%	93.77%
Avg count	255.02	120.02
Max percentage	57.23%	99.22%
Max count	293	127

It is clearly seen in the table that the hash data changes by approximately 50% on average in 1-bit modification and by approximately 95% on average in 1-hex modification. In other words, even if 50% of the C_e is similar to the C_h, this audio data is likely to be copyrighted.

SSNR is one of the widely used objective methods for measuring sound quality [29]. To calculate SSNR, copyright embedded signal is first divided into m segments with n samples each. Then SSNR is calculated in Equation (28):

$$SSNR = 10log_{10}\left\{\frac{1}{m}.\sum_{i=1}^{m}\left(\frac{\sum_{j=1}^{n}[x_i(j)]^2}{\sum_{j=1}^{n}[x_i(j)-s_i(j)]^2}\right)\right\} \quad (28)$$

Here, $x(i)$ and $s(j)$ are the original and copyright embedded signals, respectively. $\sum[x_i(j)-s_i(j)]^2$ is the noise power, which refers to mathematical difference of two signals. As shown in figure 7, as the SSNR value increases in the positive direction, the mathematical similarity between the original sound and the copyrighted sound increases, and as it decreases in the negative direction, the similarity decreases.

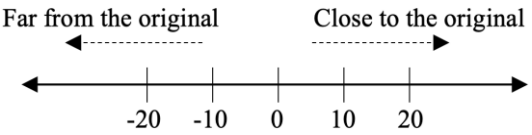

Figure 7. SSNR Scale [29].

In some special cases, such as phase encoding, SSNR measurement is meaningless. Because the waveform of the embedded signal changes a lot due to the phase change, SSNR is underestimated. The proposed method is extremely suitable for SSNR measurement, because it applies LSB modification.

In the early years of digital technology, there were no International Standards for measuring sound quality. Quality measurement was done with listening tests relying on human perception. The first methods for testing telephone band speech signals were standardized within ITU-T (International Telecommunication Union-Telecommunication Standardization Sector) Recommendation P.800 in 1993 [30]. Between 1994 and 1998, the Perceptual Evaluation of Audio Quality (PEAQ) method was proposed to objectively measure perceived sound quality [31] and this method was accepted as a standard. PEAQ simulates the human ear's perceptual properties. The model uses a metric called Subjective Difference Grade (SDG). This metric measures the distance between two sound signals and produces a reference score. The SDG score and the ODG score are produced as shown in table 3.

Table 3. PEAQ Scoring [9].

Audio quality	SDG	ODG
Imperceptible	5	0
Perceptible, but not annoying	4	-1.0
Slightly annoying	3	-2.0
Annoying	2	-3.0
Very annoying	1	-4.0

Copyright embedding was performed with the proposed method on all sounds in the RFA Dataset and the maximum, minimum, and average mathematical and perceptible high precision results obtained are shown in table 4.

Table 4. Performance test results of the proposed method.

	Worst	Average	Best
SSNR	12.12885955	23.97756593	33.05281978
BER	0.061658518	0.062416802	0.062965252
CC	0.998574061111926	0.99990356	0.999971083931624
ODG	-3.9049	-3.4719	-1.7073

The proposed method was applied to random audio in the RFA Dataset to simulate the amount of noise it causes. To show the amount of noise, the amplitude versus time graph of a small section of the original audio and the copyrighted audio were plotted over each other, as shown in figure 8.

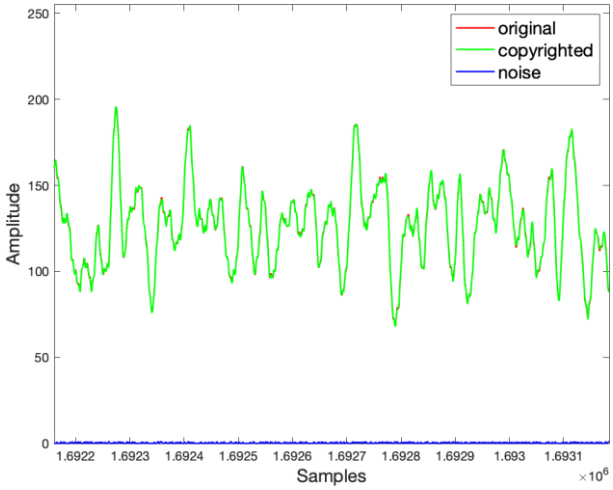

Figure 8. Noise graph of the proposed method on a random section of a random audio from the dataset.

The signal shown in the graph is approximately 2 milliseconds random piece of a random sound in the RFA dataset. The original signal is plotted in red, and the embedded signal is in green. The amount of difference is also plotted in blue. As can be seen, the perceptual difference between the signals is quite low, which can also be shown with Spectrograms. Spectrograms are the visual representations of audio, which are very detailed and accurate images that have been widely used in audio classification tasks [32]. Very similar sounds can be distinguished by a spectrogram. A spectrogram is typically produced using a short-time Fourier transform with a fixed window size, the square of which gives the magnitude of

the spectrogram [33]. The y-axis of the spectrogram simply represents the time, the x-axis represents the frequency, and the color of each point represents the amplitude of that point. The spectrogram of the audio whose amplitude/time graph is given in figure 8 is shown in figures 9 and 10.

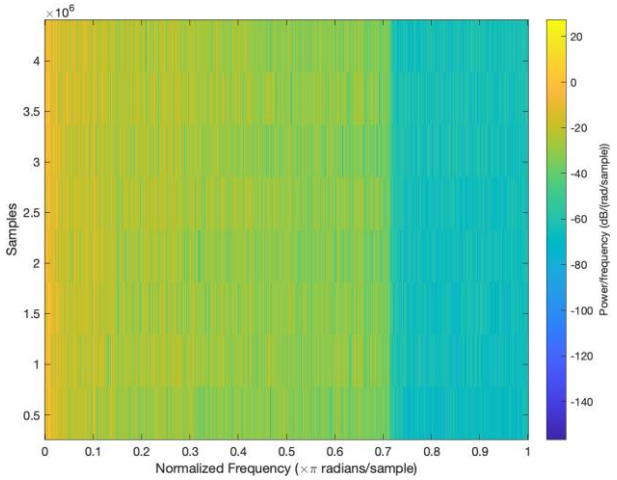

Figure 9. Spectrogram of the original audio.

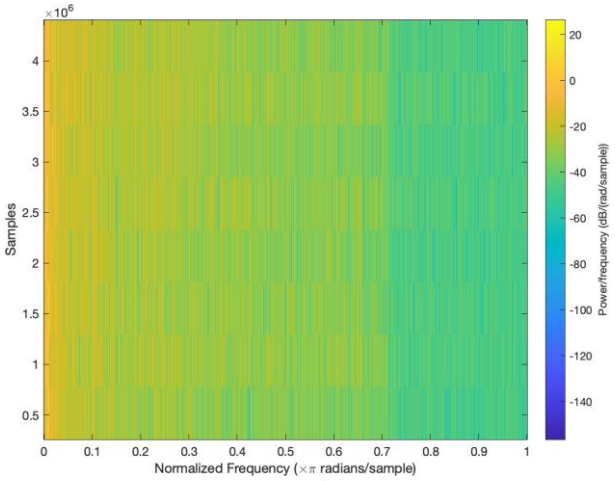

Figure 10. Spectrogram of the copyrighted audio.

The proposed method was performed on 516 sound files in the RFA dataset. The sound files that have minimum and maximum features and that are produced maximum and minimum results in mathematical measurements and the results obtained from them are shown in table 5.

Table 5. Audio files with marginal features and results in RSA Dataset.

Feature	Name	Duration (sec)	CL	BER	CC	SSNR	ODG
Min duration	Prelude No 1 - Chris Zabriskie	68	351	0,062243754	0,999038298	23,47209493	-2,615307505
Max duration	Top 10 Songs Of Ikson	1792	187	0,06247304	0,999936699	22,26100438	-2,43847257
Min CL	Far Away - MK2	105	104	0,062380556	0,999944469	21,21885178	-2,746567625
Max CL	Enchanted Valley - Kevin MacLeod	190	386	0,062425941	0,999631367	28,51836632	-3,643323121
Min BER	Lilac Skies - Corbyn Kites	109	283	0,061658518	0,999959743	16,89904238	-3,674572915
Max BER	Hot Coffee - Patrick Patrikios	194	153	0,062965252	0,999944051	21,42182483	-3,869273264
Min CC	Shattered Paths - Aakash Gandhi	178	155	0,062441933	0,998574061	20,91147021	-3,597474417
Max CC	First Of The Last - Silent Partner	127	177	0,062546669	0,999971084	12,12885955	-3,811454725
Min SSNR	First Of The Last - Silent Partner	127	177	0,062546669	0,999971084	12,12885955	-3,811454725
Max SSNR	Take Your Pick - Aaron Lieberman	109	157	0,062367196	0,999886119	33,05281978	-3,573908485
Min ODG	Forgiveness - Patrick Patrikios	203	155	0,062533817	0,999909641	30,64274854	-3,904917952
Max ODG	Mirror Mirror - Diamond Ortiz	185	145	0,062443396	0,999948195	22,49870419	-1,707289275

The shortest sound duration in the RFA Dataset is 68 seconds, and the longest one is 1792 seconds. The mathematical results obtained in the proposed method are expressed according to the sound duration in figures 11 to 15.

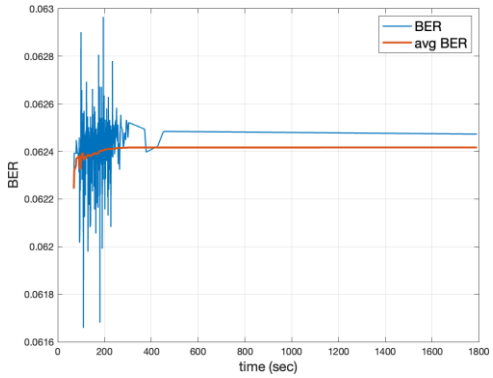

Figure 11. BER-duration.

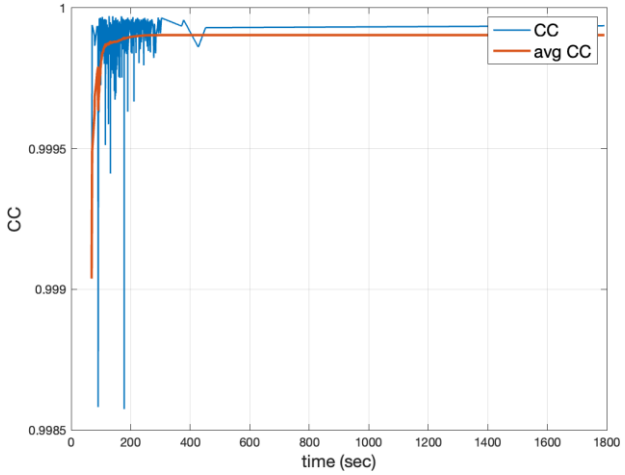

Figure 12. CC-duration.

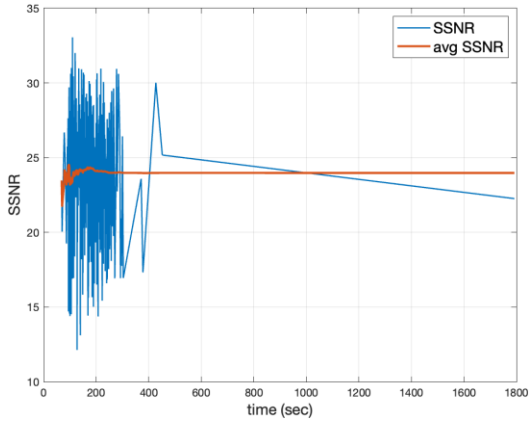

Figure 13. SSNR-duration.

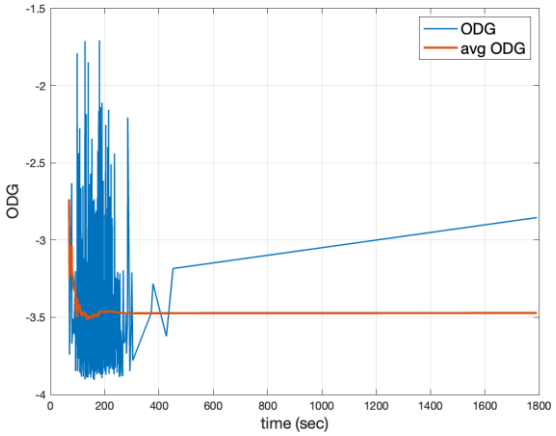

Figure 14. ODG-duration.

While the mathematical measurements are far apart for shorter audio files, the longer ones appear to be quite close to the cumulative average. However, it is not possible to infer that the audio file duration directly affects the mathematical scores in the proposed method. There are many methods of embedding some kinds of data into audio files in the literature. Many of them have been tested on different data sets. Since there is no standardized metric for testing these methods, each has performed tests with its own chosen metric. Therefore, it is not possible to directly compare the proposed method in this study with the literature. However, a state-of-the-art comparison is shown in table 6, based on all metrics between the best and worst results declared. Another important point to note that almost all of these studies are not spread. Therefore, they cause interference only in a limited area of the audio. This also makes it difficult to compare the methods with each other. Moreover, as it is obvious, no method can be successful in all criteria at the same time. In order to approach an objective comparison result, the best and worst experimental results of the studies are shown in table 6. However, each study used different mathematical performance metrics to express experimental results. When the best and worst results are averaged, the proposed method is ranked second in three studies that give BER scores, and second in five studies that give CC scores. The obtained SSNR score was compared with the average of the state-of-the-art Peak Signal to Noise Ratio (PSNR) score, the proposed method ranked first in eight studies. Both methods express perceptual performance in signal processing methods. The proposed method is ranked third in three studies in the ODG standard. However, all of these methods do not have as much bit density as the proposed method because they do not spread copyright data to whole signal. The main goal of the proposed method is to obtain copyright information even when a large part of the audio data is cropped.

Table 6. State-of-art comparison.

Paper	Method	Value	Metric				
			BER	CC	PSNR	SSNR	ODG
Proposed	-	Best	0.061658	0.99997	NA	33.0528	-1.7073
		Worst	0.062965	0.99857	NA	12.1288	-3.9049
[18]	DCT	Best	NA	NA	41.5638	NA	NA
		Worst	NA	NA	3.21	NA	NA
[9]	SVD-DWT based	Best	NA	NA	39.02	NA	-0.67
		Worst	NA	NA	37.5	NA	-0.91
[12]	M16M	Best	NA	1.0000	72.0019	NA	NA
		Worst	NA	0.9743	37.3739	NA	NA
[2]	Iterative Filtering	Best	NA	0.9999	40.05	NA	NA
		Worst	NA	0.8698	NA	NA	NA
[3]	FFT	Best	NA	0.9999	37.98	NA	NA
		Worst	NA	0.9995	35.78	NA	NA
[34]	M-SW-LSC	Best	0.0035	0.9931	37.8132	NA	-0.53
		Worst	0.0257	0.9557	37.8113	NA	-1.9599
[35]	LPC	Best	0.0000	NA	39	NA	-1.02
		Worst	8.76	NA	33	NA	-3.68

4 Conclusion

Digital audio protection methods have been applied to industry applications since the early development stage in late 1990s [36]. Most of them were the incorporation and modifications of existing techniques from other research areas, e.g., spread spectrum from communication theory [37], and patchwork methods from image watermarking [38]. Most of the proposed methods are based on signal processing techniques. These methods are generally classified whether copyright data is placed in the time domain or the frequency domain. Real time industrial methods differ from academic solutions. They consider more on imperceptibility than robustness. The reason is that each industry solution defines a specific application, in which the attacks may not need to be exhausted [36]. This study implemented an irreversible copyright data using a hash algorithm for audio security. An unlimited

sized copyright data has been reduced to a fixed size and spread from the first to the last bit of the audio signal. Thus, the clipping attack, which is the easiest to apply by attackers, has been rendered ineffective. This feature shows that proposed method can be applicable in the industry.

According to the results of the avalanche effect tests, the fact that even 50% of the copyright data can be extracted has shown that the originality of the sound is guaranteed. This has shown that preserving even half of the LSBs in any interfered sound is sufficient to prove the ownership. The proposed method works independently of the length of the copyright text. The mathematical performance of the method was measured with SSNR, BER, CC, and ODG measurements made on the entire dataset. The results are shown as maximum, minimum, and average values. In addition, all other scores of the sound data that produced a marginal score in the dataset are also shown. In order to see the relationship between the mathematical performance of the method and the duration of the audio, duration-performance analysis graphs are presented. Accordingly, the length of the audio is not a constraint for the method, that is, the method produced consistent results for all lengths of audio in the dataset. The obtained results show the applicability of the proposed method in the real world. The spread embedding ability of the method and the ability to detect the starting point of hashed copyright information show that it is extremely robust against all clipping attacks.

Decleration

Ethics committee approval is not required.

References

[1] Duarte, F. (2024). Amount of data created Daily. Retrieved September 07, 2024 from https://explodingtopics.com/blog/data-generated-per-day

[2] Naqash, K. I., Malik, S. A., & Parah, S. A. (2024). Robust audio watermarking based on iterative filtering. Circuits *Syst Signal Process*, (43), 348–367.

[3] Salah, E., Amine, K., Redouane, K., & Fares, K. (2021). A fourier transform based audio watermarking algorithm. *Appl. Acoust*, (172).

[4] Kwon, O. J., Choi, S., & Lee, B. (2018). A watermark-based scheme for authenticating JPEG image integrity. *IEEE Access*, (6), 46194–46205.

[5] Yalman, Y., & Ertürk, İ. (2009). Gerçek zamanlı video kayıtlarına veri gizleme uygulaması. *XI. Akademik Bilişim Konferansı Bildirileri/Harran University, Şanlıurfa,* (pp. 545-552).

[6] Macit, H. B. (2019). Mobil cihaz görüntüleri için entropi tabanlı kırılgan damgalama metodu geliştirilmesi (Publication No. 566003) [*Doctoral dissertation, Süleyman Demirel University, Isparta*].

[7] Arnold, M., Schmucker, M., & Wolthusen, S. D. (2003). Techniques and applications of digital watermarking and content protection. *Artech House. London*.

[8] Arseven, M. (2019). Turkey provides access to copyright database. *MA Gazette Edition*, (78).

[9] Al-Haj, A. (2014). An imperceptible and robust audio watermarking algorithm. *J Audio Speech Music Proc.*, (37).

[10] Wu, C. P., Su, P. C., & Kuo, C.-C. J. (2000). Robust and efficient digital audio watermarking using audio content analysis. *Proceedings of SPIE 12th International Symposium Electronic Imaging, San Jose, CA*, (pp. 382-392).

[11] Tseng, H. W., & Leng, H. S. (2014). High-payload block-based data hiding scheme using hybrid edge detector with minimal distortion. *EURASIP Journal on Audio, Speech, and Music Processing*, (8)11, 647-654.

[12] Bhattacharyya, S., Kundu, A., & Sanyal, G. (2011). A novel audio steganography technique by M16MA. *International Journal of Computer Applications*, (30)8, 26-34.

[13] Acevedo, A. (2003). Digital watermarking for audio data in techniques and applications of digital watermarking and content protection. *Artech House, USA*. (75–114).

[14] Rachid, R. S. (2014). Binary image watermarking on audio signal using wavelet transform (Publication No. 386090) [*Master's thesis, Çankaya University, Ankara*]

[15] Deshpande, D. (2021). Royalty-Free Audio Dataset. Retrieved September 02, 2024 from https://www.kaggle.com/datasets/darshan1504/royaltyfree-audio-dataset

[16] Blau, Y., & Michaeli, T. (2019). Rethinking lossy compression: The rate-distortion-perception tradeoff. *Proceedings of the International Conference on Machine Learning*, (pp. 675–685).

[17] Stankowski, J., Korzeniewski, C., Domański M., & Grajek, T. (2015). Rate-distortion optimized quantization in HEVC: Performance limitations. *2015 Picture Coding Symposium (PCS)/Cairns, QLD, Australia*, (pp. 85-89).

[18] Al-Darrat, K., & Abushaala, A. (2024). Copyright protection based on hybrid image watermark (DCT) with audio watermark (EMD). *The International Journal of Engineering & Information Technology (IJEIT)*, 12(1), (pp. 84–89).

[19] Aggarwal, K., & Verma, H. K. (2015). Hash_RC6 — Variable length Hash algorithm using RC6. *Proceedings of 2015 International Conference on Advances in Computer Engineering and Applications, Ghaziabad, India*, (pp. 450-456).

[20] Pittalia, P. P. (2019). A comparative study of hash algorithms in cryptography. *International Journal of Computer Science and Mobile Computing*, (8)6, 147-152.

[21] Barreto, P., & Rijmen, V. (2003). The Whirlpool hashing function, *First open NESSIE Workshop, Leuven, Belgium*, (pp. 13- 14).

[22] Stallings, W. (2006). The Whirlpool secure hash function. *Cryptologia*, (30), (pp. 55–67).

[23] Shannon, C. (1949). Communication theory of secrecy systems. *Bell Systems Technical Journal*, 28 (4), (pp. 656–715).

[24] Kashifa, S., Tangeda, S., Sree, U. K., & Manikandan, V. M. (2023). Digital image watermarking and its applications: A detailed review. *Proceedings of IEEE Int. Students' Conf. Electr., Electron. Comput. Sci. (SCEECS)*, (pp. 1–7).

[25] Ramyashree, Venugopala, P. S., Raghavendra, S., & Ashwini, B. (2024). CrypticCare: A strategic approach to telemedicine security using LSB and DCT steganography for enhancing the patient data protection. *IEEE Access*, (12), (pp. 101166 – 101183).

[26] Chi, L., & Zhu, X. (2018). Hashing techniques: A survey and taxonomy. *ACM Comput. Surveys*, (50)1, (pp. 1–36).

[27] Upadhyay, D., Gaikwad, N., Zaman, M., & Sampalli, S. (2022). Investigating the avalanche effect of various cryptographically secure hash functions and hash-based applications. *IEEE Access*, (10), (pp. 112472-112486).

[28] Prodeus, A. (2015). Reducing sensitivity of segmental signal-to-noise ratio estimator to time-alignment error. *International Journal of Electrical and Electronic Science*, 2(2), (pp. 31-36).

[29] Alsaad, S., & Hashim, E. (2013). A speech scrambler algorithm based on chaotic system. *Al- Mustansiriyah J. Sci.*, (24), 357-372.

[30] Salovarda, M., Bolkovac, I., & Domitrovic, H. (2005). Estimating perceptual audio system quality using PEAQ algorithm, *18th International Conference on Applied Electromagnetics and Communications*, Dubrovnik, Croatia, 1-4

[31] Thiede, T., Treurniet, W. C., Bitto, R., Schmidmer, C., Sporer, T., Beerends, J. G., Colomes, C., Keyhl, M., Stoll, G., Brandenburg, K., & Feiten, B. (2000). PEAQ the ITU standard for objective measurement of perceived audio quality. *J.Audio Eng.Soc.*, (48)1/2, 3-29.

[32] Zeng, Y., Mao, H., & Peng, D. (2019). Spectrogram based multi-task audio classification. *Multimed Tools Appl*, (78), 3705–3722

[33] Kalantarian, H., Alshurafa, N., Pourhomayoun, M., Sarin, S., Le, T., & Sarrafzadeh, M. (2014). Spectrogram-based audio classification of nutrition intake, *2014 Health Innovations and Point-of-Care Technologies Conference*, Seattle, Washington USA, 161-164.

[34] Zhang, G., Zheng, L. Su, Z., Zeng Y., & Wang, G. (2023). M-Sequences and sliding window-based audio watermarking robust against large-scale cropping attacks. *IEEE Transactions on Information Forensics and Security*, (18), 1182-1195.

[35] Korany, N. O., Elboghdadly, N. M. & Elabdein, M. Z. (2024). High capacity, secure audio watermarking technique integrating spread spectrum and linear predictive coding. *Multimed Tools Appl*, (83), 50645–50668.

[36] Hua, G. Huang, J. Shi, Y.Q., Goh, J., Thing, V.L.L. (2016). Twenty years of digital audio watermarking-a comprehensive review, *Signal Processing*, (128), 222-242.

[37] Cox, I.J., Kilian, J., Leighton, F.T., Shamoon, T. (1997). Secure spread spectrum watermarking for multimedia, *IEEE Trans. Image Process.*, 6(12), 1673-1687.

[38] Yeo, I.K., Kim, H.J. (2003). Modified patchwork algorithm: a novel audio watermarking scheme, *IEEE Speech Audio Process.*, 11(4), 381–386.